DAMAGE AND FRACTURE OF BRITTLE VISCOELASTIC SOLIDS WITH APPLICATION TO ICE LOAD MODELS

JING XIAO

DAMAGE AND FRACTURE OF BRITTLE VISCOELASTIC SOLIDS WITH APPLICATION TO ICE LOAD MODELS

by

© Jing Xiao, B.Eng. M.Eng.

A thesis submitted to the School of Graduate Studies
in partial fulfillment of the requirements for the degree of
Doctor of Philosophy

Faculty of Engineering and Applied Science
Memorial University of Newfoundland
August, 1997

St. John's Newfoundland Canada

Abstract

In this work a multiaxial constitutive theory for brittle, viscoelastic materials is presented based on viscoelasticity, continuum damage theory and fracture mechanics. The microstructural nature of the material and micromechanical processes have been modelled by damage mechanics using averaging procedures with a finite collection of state variables. The change in the state variable is directly related to the individual deformation process. The constitutive model includes the effects of damage including microcracking, dynamic recrystallization and pressure melting on the reduction in elastic modulus and the enhancement in creep deformation. Damage evolution is based on Schapery's approach using the generalized J integral theory. The influence of confining pressure on damage progress is included. Volumetric deformation under compression is also investigated, which is mostly dilatation due to microstructural changes (damage).

A triaxial test program has been carried out in the laboratory at Memorial University. A description of the test program, specimen preparation, test equipment and procedure used has been presented. The experimental observations and results have been discussed and are summarized. Triaxial tests were designed to investigate the deformation of ice and the influence of damage on the mechanical properties of ice. These tests have also served to verify the constitutive modelling. The theoretical model provides good agreement with test results.

The role of fracture and spalling in ice-structure interaction has been investigated. Fracture analysis, using the J-integral, has been carried out in the numerical scheme, which is based on finite elements and the computer program ABAQUS. This analysis is consistent with the damage mechanics and has been carried out on the basis of plane strain assumptions and the direction of crack propagation was calculated by maximizing the strain energy release rate. The direction of maximum tensile stress was also considered. Available data for ice on the tensile and shearing modes (I and II) of crack propagation were taken into account.

Analysis showed that localization of damage occurs if the geometry leads to stress concentration at the structure-ice interface. Calculations indicate that the load on a structure would be high if the failure in the ice was by distributed damage only. Initial analysis showed that a small crack near the interface would propagate at loads about one-half of those found using damage analysis only. The analysis included crack propagation and removal of material. These initial results are very promising for a realistic analysis of ice-structure interaction.

Load oscillations induced by ice crushing failure against a structure have also been investigated. Evidence of pressure melting has been reported from both laboratory and medium-scale field indentation tests. Possible effects of pressure melting on ice-induced vibrations are presented. A simplified damage model using only one Maxwell unit is proposed for the highly damaged materials. Two trial test cases are carried out using the simplified damage model to simulate the extrusion of crushed ice in the laboratory and field indentation tests. Preliminary analyses have shown promising results in the light of experimental programs where load oscillations have been observed.

Acknowledgments

I am very grateful to the faculty of Engineering and Applied Science that, in many ways, provided assistance in the completion of this project. Without their active collaboration and cooperation this project would have remained an unfulfilled dream. In particular, I am greatly indebted to Dr. Ian J. Jordaan, my supervisor, who not only helped at every stage of the development, reading through all of the early drafts of the manuscript time and time again, but who also had a profound influence on my academic training through scholarship, and whose constructive comments and meticulous criticism have been a constant source of inspiration and encouragement during the writing of this thesis. Special thanks are also to the members of the supervisory committee: Dr. Stephen J. Jones, the Institute for Marine Dynamics, NRC and Dr. A.S.J. Swamidas, Faculty of Engineering, MUN, for their support during this study.

The author would like to gratefully acknowledge the financial support from the School of Graduate Studies, and the Faculty of Engineering, Memorial University, the Government of Newfoundland and Labrador.

Special thanks go to Dr. Sanjay K. Singh who not only provided me with much assistance as well as valuable suggestions and discussions during the process of completing this project, but who also introduced me to many relevant readings and materials. I also want to extend my gratitude to Mr. Barry Stone, whose concrete help and contribution in my laboratory experiments are gratefully acknowledged.

I wish to especially thank my friends and colleagues, Dr. Richard McKenna, Dr. Bin Zou, Dr. Mark Fuglem and Dr. Irine Meglis for their countless academic discussions, as well as sincere concerns, very helpful suggestions and criticisms throughout my research.

Finally, a special word of thanks goes to my wife, Yang Meng, and our sons, Ted and Brian, for their constant encouragement, patience and above all, for their love.

Contents

List of Figures

List of Tables

Nomenclature

C_{ijkl}	forth order compliance tensor
D	damage parameter
$D(t)$	creep compliance
E	elastic modulus (MPa)
E_k	elastic stiffness in Kelvin unit
E_m	elastic stiffness in Maxwell unit
E_R	reference elastic modulus (MPa)
$E(t)$	relaxation modulus
G	shear modulus (MPa)
G_c	critical strain energy release rate
J	J integral
K	bulk modulus (MPa)
K_{IC}	critical stress intensity factor
K_{ijkl}	forth order stiffness tensor
N	crack density
P	hydrostatic pressure
Q	activation energy
S	damage parameter (Schapery's definition)
T	temperature
T_m	melting temperature
T_{ij}	surface tractions
U	potential energy
W	strain energy
W^c	complementary strain energy
a	one half of the crack length (m)
d	average grain size (m)
e	equivalent strain
e_{ij}^e	elastic strain deviator
e_{ij}^d	delayed elastic strain deviator
e_{ij}^c	secondary creep strain deviator
m	creep exponent for Maxwell unit

n	creep exponent for Kelvin unit
s	von Mises stress (MPa)
s_{ij}	stress deviator (MPa)
t	time (s)
β	creep enhancement parameter
δ_{ij}	delta function
$\dot{\epsilon}_0^d$	delayed elastic strain reference rate
$\dot{\epsilon}_0^c$	secondary creep strain reference rate
ϵ_{ij}	strain tensor
ϵ_{ij}^e	elastic strain components
ϵ_{ij}^d	delayed elastic strain components
ϵ_{ij}^c	secondary creep strain components
ϵ_v	volumetric strain
μ	viscosity coefficient (MPa·s)
μ_k	viscosity in Kelvin unit
μ_m	viscosity in Maxwell unit
ν	Poisson's ratio
σ_c	critical stress for crack nucleation (MPa)
σ_{ij}	stress tensor (MPa)
σ_v	volumetric stress (MPa)
ψ	reduced time

Chapter 1

Introduction

The deformation of solids under load often results in changes to the structure of the material. These changes, to a large degree, will depend on the combined effects of geometry, loading, and most importantly, the development of micro-scale changes in the structure. The accumulation of these changes, is often termed "the process of damage" and is associated with changes in the mechanical behavior of the material and the dissipation of strain energy. The mechanism of energy dissipation determines the material response and failure process. Solids like ceramics, rocks, concrete and ice, can be failed in two typical modes, ductile or brittle, depending on the loading rate and temperature. For the analysis of these two types of failures, classical theories, like plasticity, viscoelasticity and fracture mechanics, are well established. Plasticity and viscoelasticity focus on the material behaviour associated with the propagation of dislocations, and the material failure is distributed over a plastic zone. Fracture mechanics, on the other hand, is focused on a very small fracture process zone at the crack tip. Upon reaching a critical value of stress intensity, the initial crack may propagate throughout the structure resulting in a sudden failure, manifested by spalling, breaking or splitting. But in many cases, brittle solids will fail neither by collapse due to brittle fracture nor by plastic deformation, especially under moderate loading rates. Failure often involves the nucleation and growth of microcracks at the

grain boundaries or between grains, due to possible mechanisms including dislocation pileup as well as the elastic anisotropy of the material. These are all effective sources of stress concentration. The nucleation and growth of microcracks are associated with the release of elastic strain energy from the material. The energy is largely dissipated but some is stored as surface energy of the crack. For certain materials under favorable loading conditions, other mechanisms such as dynamic recrystallization and pressure melting could be the dominant sources of structure destruction in the material which will result in the dissipation of energy. The presence of these structure changes will effectively reduce the strength of the material and also enhance the deformation process. In this case, the failure of brittle material is a very complex process associated with the transition from ductile to brittle behaviour. A great deal of research has been done to study the influence of distributed cracks and other structure changes on the mechanical properties of solid materials. Damage mechanics was introduced to recognize the difference between plastic flow and cracking. It is based on the averaging procedures that will take into account only the averaged effects of all structure changes using a set of kinematic state variables. These variables represent different processes in the change of material structure. It should be noted that fracture mechanics can be included as a special case of damage mechanics, and these two theories can be applied to a failure analysis in different situations.

1.1 Nature of the Problem

In the present study a constitutive theory for brittle, viscoelastic materials has been developed based on damage and fracture mechanics, as well as viscoelasticity theory. Special attention has been given to ice deformation processes applicable to ice indentation problems. These problems are encountered in determination of ice forces on a

structure.

1.1.1 The Challenge of Ice Environment

Increased exploration for energy resources and marine transportation in the arctic and subarctic offshore areas has focused attention on the engineering problems of designing and building large structures in ice-covered waters. It requires that methods be developed to design various structures to resist ice forces. Safety, environmental protection and economy are of great importance, and a practical approach to ice load estimation is advocated to obtain a balance between these objectives. Recent research on ice-structure interactions shows that safety can be achieved by a combination of good systems design and a rational approach to design criteria and structural response. For design purposes and the operation of arctic and subarctic offshore structures and vessels, such as, the Hibernia GBS structure and oil shuttle tankers, reliable estimation of the global and local ice loads as well as the frequency and amplitude of load fluctuations are required. The development of accurate and reliable methods for the prediction of such ice loads is a great challenge in ice research.

1.1.2 Ice Forces on Offshore Structures

Ice is a viscoelastic material, but under high loading rates, it behaves as a very brittle solid. Due to a wide range of loading conditions in engineering practice, the prediction of ice loads on structures can be very difficult. Both heterogeneity and distributed flaws in natural ice can produce a significant number of microcracks in the loading zones. When ice impacts with a structure, the ice near the interface will be damaged and pulverized forming a crushed layer. This layer of crushed ice will then be extruded out of the interface resulting in a crushing failure (Jordaan and Timco, 1988). In zones where the stress state and flaw size are favourable, a crack

may propagate to the surface of the ice feature, and a piece may spall off. In the extreme, splitting of a large feature such as a floe can take place.

Ice forces are limited either by the deformation failure and clearing of the ice in front of the structure, or by the environmental driving forces on the ice. The modes of ice failure are varied and complex, such as crushing, spalling, buckling, bending, shearing and splitting. Ice load can be static, but in most cases, it is dynamic in character. It can cause severe dynamic responses to the structure. This has been observed in field programs (Jefferies and Wright, 1988). The other important aspect of ice loads is the high local pressure induced by the impact of ice feature against structure. The local pressures have been measured as high as 70 MPa in field test programs (Frederking et. al., 1990a, b). Reliable prediction of ice loads requires an good understanding of the formation of local pressure and the process of disintegration and clearing of ice at the ice-structure interface.

1.2 Objectives

The design of structures and vessels for arctic and subarctic waters requires knowledge of ice loads and their distribution in space and time. In turn, this requires analysis of the interaction between the structure and the ice at the appropriate rate, and here only the interaction at rates fast enough to cause brittle failure of ice in both micro- and macro-scale is concerned, and concentration is on the areas where the ice is under predominantly compressive stresses. This situation will typically occur in ice-vessel interaction or the interaction of icebergs with fixed or floating structures.

Under these circumstances, the ice will fail mostly in two types of processes. The first corresponds to the formation of macrocracks and consequent spalling of ice pieces. The second includes an intense shear-damage process in zones where high pressures

are transmitted to the structure. These zones are termed critical zones (Jordaan et al., 1990). These two processes can be combined to explain the main features of ice-structure interaction. It is important that the processes described can provide explanations for observations of variation of pressure in time and spaces.

The basic objective of the proposed study is the estimation of ice forces on structures with proposed constitutive theory providing information on local ice pressures and new ice force modelling methods. Key factors to be considered include:

- fracture and damage processes involving microcracking, recrystallization, pressure melting, pulverization and subsequent extrusion, as well as spalling;
- ice-induced vibration and its effect on the ability of a structure to resist ice loads;
- local ice pressures and the large variations in pressure which have been measured over the contact area.

1.3 Approach and Methodology

Medium scale ice indentation tests were conducted on Hobson's Choice Ice Island in April, 1989 (Frederking et al., 1990a, b) and in May, 1990, and also earlier in 1984, at Pond Inlet by Mobil Oil Canada (Geotech, 1985). The experiments have shown a progression of failure from largely creep, at lower rates (3 mm/s), to a combination of spalls with zones of high pressure, at higher rates (20-400 mm/s). High-frequency oscillations in load, which are associated with crushing failure in the contact zones, were observed for loading rates higher than 20 mm/s. Spalls occurred roughly every tenth cycle, leading to drops in load being superimposed on the high-frequency oscillations. The results indicate that global loads on structures are lower

than had been anticipated, whereas the local pressures are higher. These are very significant implications for optimal design from the point of view of economy.

To investigate the ice behaviour under similar loading conditions as in the indentation tests, a special test program has been designed and conducted in the laboratory at Memorial University.

1.3.1 Laboratory Test Program

The test program included triaxial tests conducted under both strain and load control at a variety of rates, confining pressures and damage conditions. These tests will provide the data necessary to calibrate the input constants for analytical modelling over a broad range of conditions. Thermodynamic aspects of ice behaviour have also been investigated to study possible pressure melting during ice indentation processes.

Tests designed to address specifically these features utilize a state-of-the-art digital, dual-axis, servo-hydraulics material test system and triaxial cell. This equipment permits both dependent and independent closed-loop control of both axial load/displacement and triaxial confining pressure. Complex pre-programmed test sequences and data acquisition can be conveniently designed through integrated application software.

Triaxial tests have been performed on laboratory-made freshwater ice. The comparison of the test results on both intact and damaged ice show clear evidence of an enhancement of the creep strain due to crack and damage.

1.3.2 Analytical Model Development

An isotropic damage model is used in the present work based on Schapery's (1981) viscoelastic theory incorporating damage mechanics. This relationship is based on the generalized J integral theory. Additionally, dilatation of ice under compression is

modelled as a function of volumetric stress, creep deformation and von Mises stress. To verify this model, direct comparisons to the triaxial tests have been performed.

The damage model is implemented to simulate the ice failure process in compression, in which the elasticity was degraded and the creep enhanced by the presence of micro-scale structure changes. In addition, a model based on fracture mechanics has been developed to replicate an initial flaw which propagates at a critical value of the strain energy release rate. Laboratory tests provided initial input constants, particularly the modulus of elasticity and creep enhancement factors of damaged ice, and the medium-scale indentation tests have served to verify model output.

1.3.3 Scope of This Thesis

Finite element analysis with damage mechanics is a new and unique approach, for modelling ice behaviour under both triaxial loading and medium scale indentation testing conditions.

As outlined above, the scope of this work may be categorized as follows:

1. a literature review of recent theories on viscoelasticity, damage, fracture mechanics and ice mechanics, as well as experimental observations on ice behaviour.

2. triaxial tests conducted in the laboratory on the freshwater ice to calibrate the material constants for theoretical modelling; description of ice indentation tests carried out on Hobson's Choice Ice Island (1989, 1990).

3. constitutive modelling of damage processes, including creep enhancement due to the development of structure changes, such as microcracking, recrystallization and pressure melting; special attention was given to the effects of high shear stress and confinement on damage processes; finite element implementation and model verification.

4. Finite element modelling of indentation problems including medium scale field ice tests and comparison with the experimental results.

5. Fracture analysis of spalling failures in ice-structure interaction.

6. Investigation of the effects of pressure melting and friction in ice-structure contact problems based on the information provided from the damage analysis as well as the experiments.

7. Conclusions and recommendations for further studies.

Chapter 2

Literature Review

2.1 Viscoelasticity

2.1.1 Linear Theory

Because of the central role of viscoelasticity in the present study, some basic theories will be reviewed briefly. In general, creep strain can be expressed as a function of stress σ, temperature T and time t, $\epsilon = F(\sigma, T, t)$. Based on the Boltzmann superposition principle, creep expressions of uniaxial stress σ and strain ϵ can be expressed in integral forms for linear viscoelastic materials:

$$\epsilon(t) = \int_0^t D(t-\tau)\frac{d\sigma(\tau)}{d\tau}d\tau, \tag{2.1}$$

$$\sigma(t) = \int_0^t E(t-\tau)\frac{d\epsilon(\tau)}{d\tau}d\tau \tag{2.2}$$

where τ is a point in time in the interval $[0, t]$. When $t < 0$, ϵ and σ are assumed to be zero. The lower limit is in fact assumed to be 0^-, rather than 0. This is to allow for a discontinuity in stress at time equal to zero, as in the case of a creep test under constant stress. $D(t)$ and $E(t)$ are the creep and relaxation functions, and they are memory functions that describe the history dependence of strain and stress, respectively. This integral form was first suggested by Volterra (1909). The

creep function (or compliance) and the relaxation function (or modulus) are inversely related as follows:

$$s^2\bar{D}(s)\bar{E}(s) = 1 \tag{2.3}$$

where the overbar denotes the Laplace transform and "s" is the transform parameter.

Based on the thermodynamics of irreversible processes (Biot, 1954), the creep compliance and relaxation modulus can be expressed as:

$$D(t) = \frac{1}{E_1} + \frac{t}{\mu_1} + \sum_{i=2}^{N} \frac{1}{E_i}\{1 - \exp(-\frac{E_i}{\mu_i}t)\} \tag{2.4}$$

$$E(t) = E_1 + \sum_{i=2}^{N} E_i' \exp(-\frac{E_i'}{\mu_i'}t) \tag{2.5}$$

where E_i, μ_i, E_i' and μ_i' are material constants. The above equations represent the classical formulation of viscoelastic theory.

All viscoelastic models can be represented by a series of springs and viscous dashpots. Figure 2.1 shows two types of combinations of springs and viscous dashpots, named (a) Kelvin chain; (b) Maxwell chain. The values of E_i, μ_i, E_i' and μ_i' can be interpreted as stiffnesses (moduli) and dashpot viscosities, respectively. The chain (a) is a Kelvin chain plus a Maxwell unit with elements E_1 and μ_1. This chain can be represented by Eq. (2.4). It is found in practice that chains of Maxwell or Kelvin units with a spectrum of values for the springs and dashpots are needed for proper representation of material creep behaviour. For many materials, Eq. (2.4) can be simplified as:

$$D(t) = D_0 + D_1 t + D_2 t^b, \tag{2.6}$$

where D_0, D_1, D_2 and b $(0 < b < 1)$ are material constants. It can be seen that the summation term in Eq. (2.4) is approximated by a power-law term t^b in Eq. (2.6). Under certain conditions, Eq. (2.6) can be very useful in practical applications instead of using the full expression of Eq. (2.4).

2.1.2 Nonlinear Theory

Based on Biot's (1954) thermodynamic analysis for linear behaviour, Schapery (1968, 1969) showed that nonlinearities in time-dependent processes can be taken into account by generalizing Biot's equations. An entropy production coefficient, a_d was introduced. This coefficient can reflect many effects, e.g. due to temperature, and in particular, the nonlinearities in response to stress or strain. The resulting theory is similar to linear viscoelasticity, except that the time t in Eq. (2.1) and (2.2) is replaced by $\psi(t)$, called the reduced time, which is defined as:

$$\psi(t) = \int_0^t \frac{d\tau}{a_d} \tag{2.7}$$

where a_d is a function of stress, temperature or other related effects. The uniaxial stress and strain functions in Eq. (2.1) and (2.2) can, be rewritten for nonlinear material as:

$$\epsilon(t) = \int_0^t D(\psi(t) - \psi(\tau)) \frac{d\sigma(\tau)}{d\tau} d\tau, \tag{2.8}$$

$$\sigma(t) = \int_0^t E(\psi(t) - \psi(\tau)) \frac{d\epsilon(\tau)}{d\tau} d\tau. \tag{2.9}$$

An application of this theory was given in Jordaan and McKenna (1988), in which a Burgers body (see Figure 2.2) with linear springs and nonlinear dashpots was analyzed. The viscosity of the dashpot is stress dependent, i.e. $\mu = \mu(\sigma')$, where σ' is the stress in the dashpot. If a constant overall stress σ is applied to the body at time $t = 0$, the stress equilibrium for Kelvin unit is:

$$\sigma = E_k \epsilon^d + \mu_k \dot{\epsilon}^d \tag{2.10}$$

where E_k is the elastic modulus of the spring, and μ_k is the viscosity of the dashpot in the Kelvin unit. Solving the equation, the deformation of the Kelvin unit $\epsilon^d(t)$ can

then be expressed as:

$$\epsilon^d(t) = \frac{\sigma}{E_k}\left[1 - \exp\{-\int_0^t \frac{E_k}{\mu_k(\sigma_d)}\, dt\}\right] \tag{2.11}$$

where σ_d is the stress in the dashpot in Kelvin unit. This equation is similar to the last term of Eq. (2.4) when N equals to 1, provided that t is substituted by $\psi(t)$ in Eq. (2.7), and a_d is assumed equivalent to $\mu_k(\sigma_d)$, i.e. $a_d \equiv \mu_k(\sigma_d)$.

If the dashpot is assumed to follow a power-law relationship with stress, then

$$\mu_k(\sigma_d) = \frac{1}{A_k\, \sigma_d^{n-1}}, \tag{2.12}$$

where A_k is the viscosity parameter; n is a constant. Using the equation of equilibrium for the element of the Kelvin unit, i.e.

$$\frac{\dot{\sigma} - \dot{\sigma}_d}{E_k} = \frac{\sigma_d}{\mu_k(\sigma_d)}.$$

It is then found that

$$\mu_k = (n-1)E_k t + \mu_{k0}. \tag{2.13}$$

where μ_{k0} is the viscosity at time $t = 0$. This equation shows that the viscosity is a linear function of time.

Substituting Eq. (2.13) into Eq. (2.11), the deformation of Kelvin unit is then given by

$$\epsilon^d(t) = \frac{\sigma}{E_k}\left\{1 - [(n-1)\omega t + 1]^{1/(1-n)}\right\} \tag{2.14}$$

where, $\omega = E_k/\mu_{k0}$.

Another nonlinear theory based on generalized linear viscoelastic theory is called modified superposition principle, which will be discussed later.

2.1.3 The Broad-Spectrum Approach

As mentioned in section (2.1.1), chains of Maxwell or Kelvin units with a spectrum of values for the springs and dashpots can often model the behaviour of viscoelastic materials better than a single unit, especially when nonlinearity is involved. But this also increases the difficulty and complexity for modelling and fitting of the experimental results. Schapery (1962) proposed a broad-spectrum collocation method for fitting the experimental data. An example was given to fit the experimental data using the relaxation modulus as given by Eq. (2.5), i.e.

$$E(t) = E_1 + \sum_{i=2}^{N} E_i \exp(-\frac{E_i}{\mu_i} t). \tag{2.15}$$

Let $\tau_i = \frac{\mu_i}{E_i}$, and the above equation can be expressed as:

$$E(t) - E_1 = \sum_{i=2}^{N} E_i \exp(-\frac{t}{\tau_i}) \tag{2.16}$$

where $E_1 = E(\infty)$. First, a set of collocation points for t will be chosen, for example, $t_1 = 0$ and $t_j = 10^{(j-3)}$, (j=2, 3, ... n). Then the values of τ_i will be chosen in a way that is somewhat arbitrary, for example, let $\tau_i = 2t_i$, i.e. $\tau_i = 2 \times 10^{(i-3)}$ (i=1, 2, 3, ... n). By letting $E(t_j)$ equal to the value of experimental data at time t_j (j=1, 2, 3, ... n), this leads to a set of n linear algebraic equations for the unknown variables of E_j (j=1, 2, 3, ... n), i.e.

$$\{b_j\} = \{a_{ij}\}\{E_j\} \tag{2.17}$$

where $b_j = E(t_j) - E_1$ and $a_{ij} = \exp(-\frac{t_j}{\tau_i})$ (i, j=1, 2, 3, ... n). By solving the above equation, the values of E_j can be calculated. Substituting E_j into Eq. (2.15), the model response can be evaluated by comparing with the experimental results. A few iterations may be needed by adjusting t_j and τ_i to achieve satisfactory results. In some cases, very small values of E_j can be found by this approach. This means the

units with small E_j values will make little contribution to total response. Therefore these units can be eliminated to save computation time.

2.2 Dynamic Recrystallization

Dynamic recrystallization is a process involving the formation or migration of grain boundaries (Vernon, 1981). This process will often result in the creation of new grains at the cost of existing ones thus lowering their free energy. When the recrystallization process is associated with the progress of deformation, it is called dynamic recrystallization, otherwise it is called static recrystallization. There are four types of driving forces for dynamic recrystallization: (1) intragranular lattice defect energy; (2) grain boundary (surface) energy; (3) chemical free energy, and (4) elastic energy by external loading (Urai et al., 1980). Dynamic recrystallization will result in the softening of the material and the enhancement of ductility. This in turn will lead to the localization of strain and the development of shear zones. The effect of dynamic recrystallization on mechanical properties has been summarized by Urai et al. (1980) as: (1) changes in grain size; (2) changes in dislocation density and substructure; (3) development of preferred orientation; and (4) changes in impurity concentration and grain boundary structure. The formation or migration of grain boundaries due to dynamic recrystallization can either increase or decrease the grain size. One of the important controlling factors of recrystallized grain size is the flow stress. The decrease of grain size will result in a change of deformation mechanism to diffusive mass transfer. This process will in turn lead to more significant softening of the material. The progress of dynamic recrystallization is a discontinuous process under certain loading conditions. When the strain reaches a critical value, a wave of recrystallization will occur and lead to a wave of accelerated creep deformation (Duval et. al.,

1983). But when loading rates are high, a rapid development of recrystallization will lead to high deformation rates and the discontinuity will disappear. The possibility of dynamic recrystallization in enhancement of ice creep deformation was also discussed by Duval et. al. (1983).

Jonas and Muller (1969) studied the deformation of ice under high stresses. The effect of dynamic recrystallization on the strain rate was proposed to follow the equation:

$$\dot{\epsilon} = \psi \exp(-\frac{\Delta H}{kT}) \exp\{\frac{v(\tau - \tau_B)}{kT}\} \tag{2.18}$$

where ψ is a structure factor; ΔH is the activation enthalpy; v is the activation volume; k is the Boltzmann's constant; T is the temperature; τ is the applied stress, and τ_B is the so-called internal back stress. The development of dynamic recrystallization can significantly reduce the back stress and result in rapid increase in strain rate. From the experimental observations, they concluded that dynamic recrystallization will occur after a critical strain is reached. The critical strain is a function of stress and temperature. Dynamic recrystallization will not be initiated under very low stresses, and it will be periodic under intermediate stresses, which leads to periodic increases in strain rate. Under high stresses, the development of dynamic recrystallization after a period of conventional creep deformation will lead to a rapid increase in strain rate. These conclusions were essentially confirmed by Duval et. al., (1983).

2.3 Damage Mechanics

2.3.1 Introduction

Most of the early work in damage mechanics was based on the original idea that the damage of a structure can be measured by a scalar factor (Kachanov, 1958), which is equal to the ratio of the area of voids to that of the whole cross section, or by the

density of microcracks and voids which would permanently affect either the elastic modulus or shear modulus. This was the guideline for most of the early work of the present group. The importance of this kind of damage model is the establishment of a rational damage law which defines the rate of damage accumulation in terms of the current values of state variables and internal variables.

2.3.2 The Concept of Damage

Based on Kachanov's model (1958), a solid body has an overall section area of A_0 and a fractured (damaged) area of A. In the case of uniaxial loading P without damage, the stress in the body is given as

$$\sigma = \frac{P}{A_0}. \tag{2.19}$$

With isotropic damage, the damage variable D can be defined as

$$D = \frac{A}{A_0};\ 0 \leq D \leq 1 \tag{2.20}$$

and the effective stress σ_a is introduced as

$$\sigma_a = \frac{P}{A_0 - A} = \frac{P}{A_0(1-D)} = \frac{\sigma}{1-D}. \tag{2.21}$$

It is assumed that the strain response of the body is modified by damage only through the effective stress, so the stress-strain relation of the damaged material is

$$\varepsilon = \frac{\sigma_a}{E_0} = \frac{\sigma}{E_0(1-D)} = \frac{\sigma}{E} \tag{2.22}$$

where E_0 is the elastic modulus of virgin material and $E = E_0(1-D)$ can be termed the "effective" modulus. So the behaviour of damaged material can be considered to be equivalent to the behaviour of undamaged material, provided that the original elastic modulus E_0 is replaced by

$$E = E_0(1-D). \tag{2.23}$$

The "effective" modulus will be reduced due to the accumulation of damage.

An application of continuum damage theory in rock mechanics was proposed by Resende and Martin (1983, 1984) for rock-like materials which defines the elastic strain-stress relation of the material as:

$$s = G_0(1 - D)e^e \tag{2.24}$$

and

$$\dot{e} = \dot{e}^e + \dot{e}^p \tag{2.25}$$

where s is the stress invariant; G_0 is the initial shear modulus; D is the damage measure; e is the total shear strain invariant, and e^e and e^p are the elastic and nonlinear components of the strain e, respectively. The rate form of Eq. (2.24) was given as:

$$\dot{s} = G_0(1 - D)\dot{e}^e - G_0 e^e \dot{D}; \text{ for loading } (\dot{D} > 0), \text{ and} \tag{2.26}$$

$$\dot{s} = G_0(1 - D)\dot{e}^e; \text{ for unloading } (\dot{D} = 0). \tag{2.27}$$

The damage evolution law was defined as

$$\dot{D} = \dot{D}(\dot{e}, e, \sigma_m, \dot{\epsilon}_v, \epsilon_v) = A(e, \sigma_m)\dot{e} + B(\epsilon_v)\dot{\epsilon}_v \tag{2.28}$$

where A and B are material constants and depend on the loading situation. The invariant volumetric strain rate $\dot{\epsilon}_v$ was also assumed as

$$\dot{\epsilon}_v = \dot{\epsilon}_v^e + \dot{\epsilon}_v^p \tag{2.29}$$

where $\dot{\epsilon}_v^e$ and $\dot{\epsilon}_v^p$ are the elastic component and inelastic component including damage effects, respectively. The strain ϵ_v^e is defined as a function of volumetric stress, σ_v, $(\sigma_v \leq 0)$ in the form of:

$$\epsilon_v^e = [1 - \exp(A\sigma_v)](W - \epsilon_{vmax}) \tag{2.30}$$

where A and W are constants; ϵ_{vmax} represents the degree of packing of the material. The inelastic component $\dot{\epsilon}_v^p$ is defined as a function of strain and damage and their rates as:

$$\dot{\epsilon}_v^p = (c_1 + c_2 e)\dot{D} + c_3 D\dot{e}, \tag{2.31}$$

where c_1, c_2 and c_3 are constants. This model has also been generalized to include the tensile behaviour and some numerical results were presented.

2.3.3 Effects of Microcracks on Elastic Properties of Solids

A very important aspect of damage mechanics is to relate the concept of damage to the cracks and other flaws in the solid. A great deal of research has been done to investigate the effects of these structural defects on the mechanical properties of solids. Models have been developed to define the evolution of damage as a function of crack density, by introducing averaging procedures to "smear" out the effect of each individual crack.

Budiansky and O'Connell (1976) discussed the reduction of elastic moduli due to the presence of microcracks of a given shape for the three dimensional case. Their solution gives change of elastic properties from the strain energy loss during the nucleation of individual cracks in an elastic brittle body. Their results include interaction between cracks but do not account for traction across crack surfaces; all cracks remain open. Assuming an isotropic array of similarly shaped flat circular cracks, the isotropic damage parameter is simply related to the crack density by $D = a^3 N$, where a is the radius of crack surface and N is the crack density. The properties of the solid as a function of damage are given as

$$E'/E = 1 - [16(1 - \nu'^2)(10 - 3\nu')]/[45(2 - \nu')]\, D \tag{2.32}$$

$$K'/K = 1 - [16(1 - \nu'^2)]/[9(1 - 2\nu')]\, D \tag{2.33}$$

where ν is the Poisson's ratio and

$$D = [45(\nu - \nu')(2 - \nu')]/[16(1 - \nu'^2)(10\nu - \nu'(1 + 3\nu))]. \tag{2.34}$$

where the prime denotes that the property includes the effect of cracks.

Under compression, the effect of traction across cracks cannot be ignored and the above approach needs to be modified. It is clear that the influence of cracks on the elastic properties will be reduced in compression due to the crack closure and difficulty in crack nucleation. Closed cracks can still transmit tractions and shear stress; therefore, in compression, the existence of cracks will not reduce the strength of the solid body as much as in tension. Horii and Nemat-Nasser (1983) developed a general solution for the case of two dimensional, compressive state of stress with a simple frictional relation for plane strain cracks. Their solution is expressed as

$$K'/K = f(D, \sigma_p/s) \tag{2.35}$$

$$G'/G = g(D, \sigma_p/s, \eta) \tag{2.36}$$

where σ_p, s are the applied normal and shear stress respectively; η is the frictional coefficient. Their result is based on an iterative numerical solution and can not be expressed in analytical form. Simple functional forms have been derived to approximate these relations for the two dimensional case:

$$(1 - K'/K)^2 = [1.8\alpha D(\sigma_p/s + 1)] \tag{2.37}$$

$$(1 - G'/G) = 0.9D\{\sigma_p/s + 1 + \exp[\eta(\sigma_p/s - 1)]\}. \tag{2.38}$$

All the cracks are closed when $\sigma_p/s \leq -1$ and all are open when $\sigma_p/s \geq 1$. Their results are only applicable for proportional loading where the ratio of normal and shear stress remains constant. In practice, the assumption of proportional loading is generally reasonable.

The approach taken by Kachanov (1993) also deals with some basic problems in analysis of solids with multiple cracks or other structural defects. The focus is on the important physical effects of crack interactions. His method provides simple solutions for (a) the impact of crack interactions on the behaviour of individual cracks, specially on the stress intensity factors at the tips; (b) the effective elastic properties of solids with multiple cracks; (c) the interactions between a macrocrack and an array of microcracks. His approach is applicable to both two and three dimensional configurations.

Consider an elastic solid with N cracks per unit volume; each crack has a normal n^i. Given an applied stress σ^o at the remote boundary, this configuration can be represented by the problem with crack surfaces loaded by tractions of $f^o = n^i\sigma^o$ and stresses vanishing at infinity. A 3-D solution was proposed by Kachanov (1993) to approximate the effective elastic modulus of noninteracting cracks with isotropic random distribution. The effective moduli are given as:

$$\frac{E}{E_0} = (1 + C_1 N)^{-1} \tag{2.39}$$

$$\frac{G}{G_0} = (1 + C_2 N)^{-1} \tag{2.40}$$

$$\frac{\nu}{\nu_0} = \frac{E}{E_0}(1 + C_3 N) \tag{2.41}$$

where

$$C_1 = \frac{16(1-\nu_0^2)(1-3\nu_0/10)}{9(1-\nu_0/2)}$$

$$C_2 = \frac{16(1-\nu_0)(1-\nu_0/5)}{9(1-\nu_0/2)}$$

$$C_3 = \frac{8(1-\nu_0^2)}{45(1-\nu_0/2)}.$$

These forms can provide accurate results at both low and high crack densities. If the crack density is small, the above equations can be linearized to a form as $\frac{E}{E_0} = (1 - CN)$, which is similar to Eq. (2.23).

Other references on damage mechanics include Krajcinovic (1983, 1989); Krajcinovic and Fonseka (1981); Leckie (1978); Schapery (1981, 1984 and 1988).

2.4 Fracture Mechanics

2.4.1 Introduction

For ideally brittle linear materials , a crack will start to propagate if the stress concentration at the crack tip, i.e. if the stress intensity factor K reaches a critical value, termed K_c, which is called the fracture toughness. The stress intensity factor can be defined as $K = \sigma_{max}/\sigma_n$, where σ_{max} and σ_n are the local maximum stress and the applied nominal stress, respectively. The criterion of crack propagation in a linear elastic solid can also be defined based on the energy-balance approach, i.e. the crack will propagate in an unstable manner when the strain energy release rate G exceeds G_c, the critical value of G. For $G = G_c$, crack growth is stable; this becomes unstable for $G > G_c$. For plane-strain conditions, $G = \frac{K^2}{E}(1 - \nu^2)$, where E and ν are Young's modulus and Poisson's ratio respectively.

2.4.2 J-Integral Theory

For nonlinear elastic materials, the J-integral theory has been proposed by Rice (1968a, b) to characterize the stress-strain field at the crack tip by taking a closed-path integration near the crack tip (see Figure 2.3). The definition of the J-integral is given as:

$$J = \int_C (W dx_2 - \mathbf{T}(\frac{\partial \mathbf{u}}{\partial x}) dS), \tag{2.42}$$

where **T** and **u** are traction and displacement vectors respectively; $W = \int \sigma d\epsilon$ is the strain energy density; dS is a small element of C, the path of integration. The J-integral was also proved to be the energy release rate per unit crack extension (Rice. 1968a, b), i.e.

$$J = -\frac{dU}{da}, \tag{2.43}$$

for unit thickness, where U is the potential energy, and a is the crack length. For linear elastic materials, the J-integral is identical to G. Therefore, for plane-strain conditions, $J = G = \frac{K^2}{E}(1 - \nu^2)$.

A constitutive theory was developed by Schapery (1981, 1984) for nonlinear viscoelastic materials. His study included the influence of distributed damage (flaws) on the mechanical behaviour of the materials. A generalized J-integral theory was also subsequently developed to analyze crack growth in nonlinear viscoelastic materials.

Considering a nonlinear elastic body with distributed cracks, Figure (2.4) shows an idealized crack with planar surfaces near the tip and the crack tip is straight. Assuming the crack has a unit thickness and the failure zone is thin compared with its length α. An arbitrary closed surface C shown in the figure consists two parts, C1 and C2 which covers the failure zone. There are no cracks inside C. For any point inside C, the equilibrium equations are given as:

$$\frac{\partial \sigma_{ij}}{\partial x_j} + F_i = 0 \tag{2.44}$$

The surface tractions T_i are given as

$$T_i = \sigma_{ij} n_j \tag{2.45}$$

where n_j are the normals on the surface C. The stresses σ_{ij} can be expressed by a potential function W as:

$$\sigma_{ij} = \partial W / \partial u_{i,j} \tag{2.46}$$

where $u_{i,j}$ are the displacements.

Assuming the existence of a body force potential W_F, the body forces F_i are then given by

$$F_i = -\partial W_F / \partial u_i. \tag{2.47}$$

Multiplying Eq. (2.44) By $-\partial u_i/\partial x_1$, and integrating the equation over the volume V included by surface C, this gives

$$J \equiv \int_V \left[\frac{\partial}{\partial x_1}(W + W_F) - \frac{\partial}{\partial x_1}\left(\sigma_{ij}\frac{\partial u_i}{\partial x_1}\right)\right] dV. \tag{2.48}$$

Converting the volume integral to surface integral, and using Eq. (2.45), the above equation can be derived as:

$$J \equiv \int_C \left[(W + W_F)n_1 - T_i \frac{\partial u_i}{\partial x_1}\right] dS. \tag{2.49}$$

If the failure zone is very thin in direction x_2 relative to its length α, the normals n_1 on surface C2 can be assumed to be zero. Therefore,

$$\begin{aligned} J &\equiv J_v - J_f \\ &= 0, \end{aligned} \tag{2.50}$$

where

$$J_f = \int_{C2} \left[T_i \frac{\partial u_i}{\partial x_1}\right] dS, \tag{2.51}$$

and

$$J_v = \int_{C1} \left[(W + W_F)n_1 - T_i \frac{\partial u_i}{\partial x_1}\right] dS; \tag{2.52}$$

thus $J_f = J_v$. This condition provides a basic relationship between the failure material at the crack tip and the material outside the failure zone. The integral J_v is also independent of surface C1, i.e. C1 is an arbitrary surface as long as it contains no

cracks inside. The derivation of the integral does not exclude the presence of tractions on the crack surfaces, while Rice's J-integral assumes the crack surfaces to be free of tractions. Eq. (2.52) reduces to Rice's J-integral if body forces are omitted.

2.4.3 Modelling of Crack Growth

To model the material failure due to fracture, the first step is to predict the propagation of cracks based on the theories discussed in the above sections. It is also important to analyze the speed and the stability of crack growth. For some brittle solids, the cracking speed can be very high and unstable, therefore it is difficult to analyze. But under certain loading conditions, stable crack propagation can be achieved, especially for some nonlinear materials. Proceeding from the elastic case to the viscoelastic one requires the inclusion of rates of change with time in the theory. Thus, instead of crack dimension "a" (i.e. half of the crack length) the rate of change with time, $\dot{a}$, is considered. For nonlinear material following a power-law stress-strain relationship, Schapery's analysis (1981, 1984) showed that the crack growth speed $\dot{a}$ is also following the power-law relationship with the J-integral J_v, i.e. $\dot{a} \propto J_v^n$, where n is a constant. Various experimental and semi-empirical studies (eg. Atkins and Mai, 1985) had also found that the rate of crack growth can be expressed as follows:

$$\dot{a} = c_1 J^k \tag{2.53}$$

where c_1 and k are constants.

Assuming a material with a power-law nonlinearity with stress, of degree r, i.e. $\epsilon = A\sigma^r$, Eq. (2.53) will be applied, under certain loading conditions, such as proportional stressing, i.e.

$$\sigma_{ij} = \sigma \sigma'_{ij}, \tag{2.54}$$

where σ represents the proportionality, and σ'_{ij} is a constant tensor.

The complementary strain energy is defined as (see also Figure 2.5):

$$\begin{aligned} W^c &= \int \epsilon d\sigma \\ &= \sigma\epsilon - W, \end{aligned} \tag{2.55}$$

where W is the strain energy $W = \int \sigma d\epsilon$.

Under the loading condition of Eq. (2.54), the complementary strain energy W^c is given by

$$\begin{aligned} W^c &= \int \epsilon_{ij} d\sigma_{ij} \\ &= \int A\sigma_{ij}^r d\sigma_{ij} \\ &= A\sigma_{ij}^{r+1}/(r+1). \end{aligned} \tag{2.56}$$

Substituting Eq. (2.54) into above equation, it is found that

$$\begin{aligned} W^c &= |\sigma|^{r+1} A\sigma_{ij}'^{r+1}/(r+1) \\ &= |\sigma|^{r+1} \int \epsilon_{ij} d\sigma_{ij}', \end{aligned} \tag{2.57}$$

and

$$W^c(\sigma\sigma_{ij}') = |\sigma|^{r+1} W^c(\sigma_{ij}'). \tag{2.58}$$

Based on Schapery (1981), $J = -\partial W/\partial A$ where $dA = da$ for unit thickness. Since $W^c = \sigma\epsilon - W$, the energy release rate J can be derived from the complementary energy:

$$J = \frac{\partial W^c}{\partial a}. \tag{2.59}$$

This indicates that energy decrease would, for a particular crack, correspond to the increase in W^c. Substituting Eq. (2.58), (2.59) into Eq. (2.53), it is found that:

$$\dot{a} = c_1 |\sigma|^{k(r+1)} \left(\frac{\partial W^c}{\partial a} \right)^k, \tag{2.60}$$

For penny-shaped crack of radius a, $\partial W^c/\partial a$ is found to be proportional to a, i.e. $\partial W^c/\partial a \propto a$, (Schapery 1981), therefore

$$\dot{a} = c_1(c_2 a)^k \sigma^q, \tag{2.61}$$

where $q = (\tau + 1)k$, and c_2 is a constant. Integrating Eq. (2.61), it is found that

$$\frac{a}{a_0} = \frac{1}{[1 - (k-1)(c_2 a)^{k-1} S]^{1/k-1}}, \tag{2.62}$$

where a_0 = initial crack length, and

$$S = \int_0^t c_1 \sigma^q d\tau. \tag{2.63}$$

A crack will become unstable when the denominator of Eq. (2.62) tends to zero, i.e. when

$$\begin{aligned} S &= \int_0^{t_f} c_1 \sigma^q d\tau \\ &= \frac{1}{(k-1)(c_2 a)^{k-1}}, \end{aligned} \tag{2.64}$$

the unstability will occur, where t_f is the critical value of time , the failure time. Thus a crack in a viscoelastic material may propagate either if time $t \to t_f$, i.e. Eq. (2.64) is satisfied, or if the crack length is such that $J \to J_c$.

For some polycrystalline materials, such as ice, microcracks often propagate suddenly at high speed and are then arrested at grain boundaries. The time for crack propagation is usually negligible compared to the failure time t_f. And from crack to crack, the failure time can be different. Let t_i be the failure time of ith crack, thus

$$S_i = \int_0^{t_i} c_1 \sigma^q d\tau. \tag{2.65}$$

As mentioned earlier, the decrease of energy due to crack propagation will result in increase of the complementary strain energy, so each microcrack will cause a jump in W^c. Damage mechanics assumes that all the jumps due to microcracking are

small, the effects of individual cracks are smeared out , therefore the damaging of the material is a smooth process. And total damage S can be defined as the summation of S_i and expressed by Eq (2.63). Figure (2.6) shows the increase in W^c as a function of S, where each small jump in W^c represents a crack propagation. In macro-scale the smoothed function can be used. The above approach developed by Schapery (1981, 1984) provides a link between the fracture mechanics and the damage theory for nonlinear materials. A large jump is also shown in the figure which corresponds to a spall or large fracture event (E).

2.4.4 The Trajectory of Crack Propagation

The study of the trajectory of crack propagation is also very important in order to predict the correct spall size and the failure zone as well as the remaining shape of the solid. Extensive studies have been done, e.g. by Sih (1973), Palaniswamy and Knauss (1974), Conrad (1976), Sih and Tzou (1983) and Zou (1997). Three principal criteria have been proposed: first, that the crack will propagate at right angles to the maximum tensile stress, second, that it will propagate in the direction which corresponds to the maximum strain energy release rate (SERR), and third, the crack direction is that which corresponds to the minimum strain energy density (SED). The criterion of maximum strain energy release rate is judged to be most fundamental. It makes sense that a crack would propagate in this direction since the criterion for propagation itself is the very same: that crack which causes the maximum SERR will be the first to propagate. The direction of maximum tensile stress is an attractive and simple rule; it can be tested against the others. Experience has shown that it is close to the maximum SERR criterion.

When modelling of the crack trajectory, all three fracture modes (I, II and III) should be considered. In many cases, it is appropriate to assume that the strain field

at the crack tip corresponds a state of plane strain. This is then the natural mode for analysis using the J-integral method. Only the first two modes of crack propagation, I - tensile and II - shearing, need to be considered. Palaniswamy and Knauss (1974) presented a relationship between the angle of crack propagation and the ratio of stress intensity factors, as shown in Figure 2.7. The angle θ represents the direction of crack propagation, measured from the existing crack direction; the analyses were based on the maximum SERR criterion. A more detailed analysis was conducted by Conrad (1976) based on finite elements, as shown in Figure 2.8. His analysis showed a good agreement with that of Palaniswamy and Knauss (1974), except at low K_I/K_{II}, in which case shear stress predominates. Figure 2.8 has been used in the present study.

Experimental work was also conducted by Shen and Lin (1986) to study the fracture behaviour of ice under mixed-mode (mode I and II) loading conditions. Their test results showed a relationship between K_I and K_{II}, and the data were fitted to the result of maximum SERR analysis based on Palaniswamy and Knauss (1974), as shown in Figure 2.9. The data have been normalized with $K_I = 1$ MPa $m^{1/2}$. Timco and Frederking (1986) found that the value of K_I was in the range of 0.1 to 0.14 MPa $m^{1/2}$ for sea ice, which is consistent with the value 0.107 MPa $m^{1/2}$ from Shen and Lin (1986). Assuming the elastic modulus of ice is $E = 10$ GPa, the critical energy release rate G_{IC} will be in the range of 1-2 J/m^2. In this study $G_{IC} = 1$ J/m^2 has been used, together with the theoretical interaction curve of Figure 2.9.

2.5 Schapery's Approach

A continuum damage theory has been developed by Schapery (1981, 1984, 1988, 1989) using the generalized J-integral theory. His approach offers a rigorous solution to a class of problems involving cracking and damaging of viscoelastic materials.

It includes a proper treatment of energy flux into the crack tip zone, and of the thin layer of damaged material outside the crack tip zone along the crack surface. In the solution, viscoelastic behaviour of material is modelled using the modified superposition principle (MSP).

2.5.1 Modified Superposition Principle

Based on linear viscoelastic theory as discussed in the earlier sections, the modified superposition principle (Findley et al., 1976), is generalized for nonlinear materials. In the case of uniaxial stress state, the modified superposition principle may be written in the following form, based on Schapery (1981):

$$\epsilon(t) = E_R \int_0^t D(t-\tau) \frac{\partial \epsilon^0(\sigma,\tau)}{\partial \tau} d\tau, \tag{2.66}$$

where ϵ^0 is referred to as pseudostrain; $D(t)$ is a linear compliance; E_R is a reference elastic modulus, included so as to give ϵ^0 the units of strain. The applied stress σ is included in the pseudostrain, ϵ^0. Consider the case where $\epsilon^0 = \sigma/E_R$, then the above equation becomes the same as the expression for uniaxial linear viscoelasticity (see Eq. (2.1)) Consider another special case: $D(t-\tau) = 1/E_R$, then $\epsilon(t) = \epsilon^0$, i.e. for the elastic case the strain is equal to the pseudostrain.

Nonlinearity can be included in above equation via the pseudostrain. Assuming that the stress-strain relationship follows a power-law nonlinearity, for instance, $\dot{\epsilon} = A\sigma^n$, where σ =constant $(t \geq 0)$, let $\epsilon^0 = \sigma^n$ and $D(t-\tau) = A(t-\tau)/E_R$, and substitute them into Eq. (2.66), it is found

$$\epsilon(t) = E_R \int_0^t \frac{A(t-\tau)}{E_R} \frac{d(\sigma^n)}{d\tau} d\tau.$$

If σ =constant $(t \geq 0)$, with $\tau = 0$, then the above equation becomes:

$$\epsilon(t) = At\sigma^n.$$

Therefore the expression for power-law relationship can be derived: $\dot{\epsilon} = A\sigma^n$.

The pseudostrain ϵ^0 can be defined as

$$\epsilon^0 = \frac{\partial W^c}{\partial \sigma} \tag{2.67}$$

where W^c is the complementary strain energy. The nonlinear equation can then be summarized by

$$\epsilon(t) = E_R \int_0^t D(t-\tau) \frac{\partial}{\partial \tau} (\frac{\partial W^c}{\partial \sigma}) \, d\tau, \tag{2.68}$$

in which

$$\begin{aligned} \frac{\partial W^c}{\partial \sigma} &= \epsilon^0 \\ &= \frac{1}{E_R} \int_0^t E(t-\tau) \frac{\partial \epsilon(t)}{\partial \tau} \, d\tau, \end{aligned} \tag{2.69}$$

where $E(t)$ is the relaxation function as given in Eq. (2.2).

2.5.2 Modified Superposition Principle with Damage

The modified superposition principle provides a simple method for predicting both linear and nonlinear behaviour of viscoelastic materials. Schapery (1981) also extended this method to include the effects of cracking, and other structural changes on the deformation of the material via the pseudostrain, i.e. ϵ^0 is also a function of damage parameters: $\epsilon^0 = f(\sigma, S_i), (i = 1, 2, 3, ...)$, where S_i represents each individual process in the change of material structure. For uniaxial or more general proportional loading, assuming quasi-static microcracking and the cracking rate follows the power-law in stress, two functions were proposed by Schapery (1981) for the pseudostrain and damage parameter, respectively, in the form of:

$$\epsilon^0 = (\sigma)^r g(S) sgn(\sigma), \tag{2.70}$$

$$S = sgn(\sigma) \int_0^t (\sigma)^q f_1 d\tau \tag{2.71}$$

where r and q are positive constants; $sgn(\sigma)$ is the sign function; f_1 reflects the properties of the material at the crack tip. By using a set of values of q or functions of f_1, different S_i can be defined. Notice that Eq. (2.71) is similar to Eq. (2.63). In many cases, one damage parameter may be sufficient, but for complex loading conditions, so as to the structural changes of the material, more than one parameters may be required.

An exponential form was proposed by Schapery (1981) for the function $g(S)$:

$$g(S) = \exp(\lambda S), \tag{2.72}$$

where λ is a positive constant. The function $g(S)$ is an enhancement factor of damage on the deformation process. This function and the damage parameters will be discussed in detail later.

2.6 Ice Mechanics

2.6.1 Introduction

Ice in nature is a polycrystalline material composed of a large number of crystals usually in different orientations. Michel (1979) provided a detailed description of the structure and classification of ice. Typically, there are two types of polycrystalline ice found in nature:

1. Granular ice, which is randomly oriented polycrystalline ice, can be found in ice features; such as, glaciers and icebergs. The grain size is classified as fine to medium. In the laboratory, this type of ice can be obtained by freezing water seeded with full mould of randomly oriented fine ice crystals, and it can be treated as a statistically isotropic material.

2. Columnar ice is formed with the grains growing parallel to the heat flow and with c-axis perpendicular to the column length. This type of ice is referred to as S2

ice which can be found in lake, river and Arctic sea ice. The mechanical properties of columnar ice are orthotropic, or more usually, transversely isotropic.

Ice is characterized as a viscoelastic material with its deformation response dependent upon the loading rate and temperature; it is also very brittle under high loading rate. The Burgers' model, as shown in Figure 2.2 , is often used for polycrystalline ice. The mechanical properties of ice can be divided into two parts (Sanderson, 1988):

1. Continuum behaviour. This includes elastic and ductile creep deformation, which can be extended to include the uniformly distributed microcracking and damage processes.

2. Fracture behaviour. This includes crack propagation and brittle failure.

2.6.2 Elasticity of Ice

In engineering applications, the elasticity of granular ice is typically treated as isotropic and can be characterized by two constants, the elastic modulus, E, and Poisson's ratio, ν. Following Hooke's law, the elastic strain ϵ_e of ice is given as:

$$\epsilon_e = \frac{\sigma}{E}, \tag{2.73}$$

where σ is the loading stress. For polycrystalline ice of low porosity, the standard range of elastic modulus is approximately 9 to 9.5 GPa in the temperature range of -5 °C to -10 °C (Mellor, 1983). The commonly accepted range for Poisson's ratio is 0.3 to 0.33.

2.6.3 Creep of Ice

A constant stress creep test on polycrystalline ice gives a conventional creep curve as shown in Figure 2.10. The idealized creep curve can be divided into three phases: primary, secondary and tertiary. Sinha (1978) developed a viscoelastic constitutive

equation for columnar ice under uniaxial compression. The total strain ϵ is considered as the sum of three components as shown in Figure 2.10, i.e.

$$\epsilon = \epsilon^e + \epsilon^d + \epsilon^c \tag{2.74}$$

where ϵ^e is the instantaneous elastic component; ϵ^d is the delayed elastic component, or recoverable primary creep, and ϵ^c is the permanent viscous component, or secondary creep strain. The elastic component in Sinha's equation was defined by $\epsilon^e = \sigma/E$, where E is the elastic modulus. An expression for delayed elastic strain under constant stress was given as

$$\epsilon^d(t) = \frac{c_1 d_1}{d}\left(\frac{\sigma}{E}\right)^s [1 - \exp\{-(a_T t)^b\}], \tag{2.75}$$

where c_1, s, b and a_T are all constants depending on the temperature and the grain size, d; where $E = 9.5$ GPa; $c_1 = 9$, is a constant corresponding to the unit grain size d_1 ($d_1 = 0.001$); $s = 1$; $b = 0.34$; $a_T = 2.5 \times 10^{-4} s^{-1}$ ($T = 263K$). The delayed elastic strain corresponds to the deformation of the Kelvin unit.

The secondary creep strain describes the effect of the viscous flow and dislocation movement within the grains, and appears to be independent of the grain size (Cole, 1986). The secondary creep strain corresponds to the deformation in the dashpot of the Maxwell unit. For polycrystalline ice under uniaxial compression or tension, a power-law relation of strain rate and stress was suggested by Glen (1955) of the form

$$\dot{\epsilon}^c = A\sigma^n$$

where n is a constant and A is a function of temperature in the form

$$A = B \exp\left(\frac{-Q}{RT}\right), \tag{2.76}$$

where $R = 8.314$ J mol^{-1} K^{-1} is the universal gas constant; T is the temperature in degrees Kelvin; Q is the activation energy and B is a material constant, both Q and

B are dependent on the ice type. In Sinha's expression for columnar ice, the creep strain rate was given by a similar relationship:

$$\dot{\epsilon}^c = \dot{\epsilon}_0^c \left(\frac{\sigma}{\sigma_0}\right)^n, \tag{2.77}$$

where $n = 3$, and $\dot{\epsilon}_0^c = 1.76 \times 10^{-7} s^{-1}$ $(T = 263K)$, is the viscous strain rate for unit stress σ_0, ($\sigma_0 = 1$ MPa). Note that the above equations, Eq. (2.73) to Eq. (2.77) include only the elastic strain, and primary and secondary creep strains.

Secondary creep can be considered as a transient process between primary and tertiary creep. The whole process of secondary creep may be very short in time.

Tertiary creep was considered due to the effect of microcracking (Gold, 1970), but it was found that cracking is not essential for the occurrence of tertiary creep in polycrystalline ice, even during the transition from primary to tertiary creep (Mellor and Cole, 1982). Duval (1981) and Duval et. al. (1983) suggested that the increase of tertiary creep rate was associated with development of fabrics favouring the glide on basal plane as well as the softening processes due to dynamic recrystallization. Other possible mechanisms, such as pressure melting under high stress and confining pressure, were suggested by Barnes and Tabor (1966), Jones and Chew (1983), Meglis et al. (1997) and Jordaan et al. (1997).

2.7 Cracking of Ice

Ice is a viscoelastic material, but it can be very brittle under certain loading conditions. Crack nucleation in ice is a complex process associated with the transition from ductile to brittle behavior. The mechanism of nucleation depends on the load level and loading rate and temperature. Gold (1972) first described the failure of columnar-grained ice in terms of microcracking during compressive creep tests, with special attention being given to the crack initiation time, strain and crack density de-

velopment. Based on statistical analysis, two types of crack distributions were found. Strain-dependent crack distributions were proposed to be the result of a dislocation pileup mechanism. Strain-independent crack distributions appeared to be related to the elastic anisotropy which causes stress concentrations at grain boundaries.

For fracture of ice in tension, the applied load must be sufficient to nucleate microcracks, and the load must be increased until the crack begins to propagate. Crack nucleation is likely to be associated with critical tensile strain (Seng-Kiong and Shyam Sunder, 1985) or critical delayed elastic strain as proposed by Sinha (1982).

For ice of grain size less than 1 mm, nucleation of cracks may occur at a stress of about 1 to 1.2 MPa and the propagation stress is about 1.2 to 2 MPa. From test data obtained at strain rates $10^{-6}s^{-1}$ to $10^{-3}s^{-1}$ by Schulson et al. (1984, 1989), Schulson (1987, 1989), and Currier et al. (1982), tensile crack nucleation occurs at a critical stress which can be expressed as

$$\sigma_N = \sigma_0 + k\, d^{-1/2} \tag{2.78}$$

where σ_0 is 0.6 MPa and k is 0.02 MPa $m^{1/2}$ and d is the grain size. The criterion for tensile crack propagation is given by

$$\sigma_P = \frac{Y\, K_{IC}}{(\pi a)^{1/2}} \tag{2.79}$$

where K_{IC} is the critical stress intensity factor for mode I loading, a is half of the crack length and Y is a geometrical parameter. Tensile cracks and fracture surfaces are always perpendicular to the tensile stress axis.

In compression, the crack nucleation process is more complicated and highly rate sensitive. Seng-Kiong and Shyam Sunder (1985), Hallam (1986) proposed that crack nucleation occurs when the associated lateral tensile strain induced by the Poisson expansion reaches a critical value. The required compressive nucleation stress should be about 3 times higher than that for tension.

Sinha (1984) used the test results of Gold (1972) to relate crack nucleation to a critical delayed elastic strain associated with grain boundary sliding, i.e., the delayed elastic strain ϵ^d is equal to the strain induced by the grain boundary sliding ϵ_{gbs}, and when ϵ_{gbs} reaches a critical value ϵ'_{gbs}, crack nucleation occurs. The critical value of grain boundary sliding ϵ'_{gbs} is related to the critical stress needed to produce a crack at the end of a sliding interface.

The dislocation pileup mechanism was adopted by Schulson et al. (1984), Cole (1986) and Kalifa et al. (1989). This mechanism is based on the concept that dislocation pileup at grain boundaries may provide a high stress concentration which can induce crack nucleation when the stress reaches a critical level.

More tests were carried out by Sinha (1988) on columnar ice, Hallam et al. (1987) on granular ice at constant load, and by Cole (1986) on granular ice at constant strain rates. Kalifa et al. (1989) performed a series of triaxial compression tests with strain rates varying between $2.5 \times 10^{-5} s^{-1}$ and $10^{-3} s^{-1}$ and confining pressure ranging from 0 MPa to 10 MPa. The test results showed that stress and strain levels for crack nucleation increased with the confining pressure, and so did the standard deviation of the distribution of crack orientation. It should point out that the above observations were mostly based on low loading rates and moderate confinements.

In fact, only when the strain rate is relatively high, about $10^{-3} s^{-1}$, does the ice become brittle and complete fracture failure occurs. In this case cracks extend to the free surface or cracks interact to form a larger crack or shear fracture surface. If the loading rate is low, the stress-strain curve eventually reaches a plateau and ice creeps without sudden failure.

The elastic anisotropy mechanism has also been applied to ice by Cole (1988) and Shyam Sunder and Wu (1990). Their work showed that elastic anisotropy of the ice lattice is an effective source of stress concentration and can be taken as an alternative

for crack nucleation when deformation rate is too high to allow dislocations to pileup. These models gave good agreement with test results.

2.7.1 Fracture of Ice in Indentation Tests

Microcracking and fracture of ice are very common in ice indentation. As addressed in the work of Jordaan and Timco (1988), Timco (1986), Tomin et al. (1986) and Jordaan and McKenna (1988a), when an ice sheet interacts with a flat indenter, a layer of crushed ice is formed in front of the indenter and the microcracks are developed along the maximum shear stress. The ice is idealized into three zones, undamaged virgin ice; partly damaged ice with relatively high density of cracks and reduced stiffness; and crushed ice which eventually will be extruded out but this ice can carry compressive loads due to its frictional properties, i.e. the compressive strength of crushed ice is not zero.

For ice sheet indentation tests, several different failure modes were observed (Timco 1986) depending on the loading rate and the ratio of the indenter width to ice thickness. Generally, at low speed, there is mainly crushing and microcracking in the ice with some short cracks less than a few centimeters in length.

At high speed, there is crushing and spalling right in front of the indenter, but the failure of ice is mainly due to the occurrence of the radial and circumferential cracks and possible buckling. In some cases there are mainly 45° - 60° radial cracks extending from the corners and the cracks would be a couple of meters long. More tests have been carried out in the ice tank in the Institute for Marine Dynamics, Canada, which provides similar evidence of ice cracking in interaction (Finn, 1991). In the case of the cylindrical indentation, crushing, microcracking, radial and circumferential cracks can also be observed similarly to the flat indentation (Hallam, 1986). Both local crushing and large scale fracture (including spalling) failures were recorded in medium scale

indentation tests on Hobson's Choice Ice Island (1989) (Frederking et al., 1990a, b). A possible crushing and damage mode of the spherical indentation tests, as discussed in the work of Jordaan and McKenna (1988a), is illustrated in Figure 2.11. A layer of crushed ice is under the indenter and the ice beyond the crushed zone is partly cracked. The density of the crushed ice is less than the intact ice. Radial cracks could also form and reach the surface, so large flakes would spall away.

2.8 Pressure Melting of Ice

The melting temperature of ice decreases with increasing pressure. When the melting point is lower than the ice temperature, pressure melting will occur, and this will result in changes in mechanical behaviour of ice. Some earlier work on ice pressure melting was presented by Barnes and Tabor (1966) and Hobbs (1974). A theoretical relationship between the melting temperature and pressure was given based on the classical Clausius-Clapeyron equation. When both ice and water are present at a equilibrium temperature of 0°C, it is found that

$$\frac{dT_m}{dP} = -0.0738°\text{C/MPa}, \tag{2.80}$$

where T_m is the melting temperature; P is the hydrostatic pressure.

Evidence of pressure melting and resulting softening of the material was reported by Barnes and Tabor (1966) based on their ice indentation tests. At ice temperature above -1.2 °C, there was a sharp drop in loading pressure when the hydrostatic pressure reached about 20 MPa, presumably due to pressure melting. This was confirmed by a thin section study of the ice structure near the contact zone. When temperature is below -1.2 °C, the loading pressure increases with decreasing temperature. It was concluded that under the experimental conditions, the applied load was not sufficient to produce pressure melting and the dominant process was creep deformation

for lower temperatures. A recent work on pressure melting has been carried out by Nordell (1990). Eq. (2.80) and Nordell's test results are plotted in Fig. 2.12, which shows that Eq. (2.80) is a good approximation for low pressures. Nordell's test results also show that a confining pressure of about 110 MPa is required to lower the melting temperature to -10°C. This is quite high compared to measured pressures at the indentation interface during the medium scale field tests (these tests will be discussed later). This discrepancy can be explained by the fact that the measured pressures are averaged over the area covered by the pressure cells. With rapid loading, high stress concentrations are developed at the grain boundaries or between ice particles. These local pressures would be much higher than the measured values. For the medium-scale indentation and crushed ice tests, the measured pressures at the center of the contact face were usually between 5 - 20 MPa, and the in-situ temperature was about -10°C. Therefore the average local pressure between ice grains or particles needs to be about 5 to 20 times higher than the global pressure or the pressure measured at the interface, in order to produce pressure melting. This kind of stress concentration should be common especially in the area that ice is highly damaged (structurally disordered). This will be discussed later.

2.9 Friction of Ice

Ice friction depends on many factors, such as speed, temperature and the contact material. The bell-shaped pattern of speed dependence of ice friction between ice has been reported by Jones et al. (1991) (see Fig. 2.13). It was found that the friction coefficient generally decreases with both increasing speed and increasing temperature. In most situations the two moving surfaces are not fully contacted over the whole apparent area, but over finite isolated junctions or asperities. At very low sliding

speeds, ice friction is attributed to the combination of creep, recrystallization and adhesion of the asperities (Barnes et al., 1971). With increasing sliding speed, higher shearing stress is required for creep deformation, which results in a higher friction coefficient. At even higher speeds, there will not be enough time for the asperities to creep. Other processes, such as ploughing, shearing or cracking of the asperities on the surfaces will occur, and a higher shearing force is required. This is responsible for the maximum friction coefficient in the medium speed range at low temperature. As the sliding speed increases, frictional heating and melting will result in a layer of lubricating water at the interface. The friction coefficient will decrease rapidly, and eventually becomes constant. This is attributed to the shearing of the lubricant film.

Based on the works of Barnes et al. (1971), Saeki et al. (1986) and Jones et al. (1991), the friction coefficient ranges from 0.01 to 0.3 between ice (sea ice or freshwater ice) and steel, and varies from 0.05 to 0.7 between ice and ice. These test data cover a speed range of 10^{-8} m/s to 100 m/s, and a temperature range from 0°C to -40^{0}C. It was also noted that the structure of the ice does not affect the friction coefficient significantly.

2.9.1 Damage Mechanics in Ice

Damage mechanics has been introduced to ice by Karr (1985), Cormeau et al.(1986), Sjölind (1987), Jordaan and McKenna (1988), McKenna et al. (1989), Karr and Choi (1989), Schapery (1989) and others. Based on thermodynamics, Sjölind (1987) defines damage growth rates in terms of dissipation potentials using tensor theory. The elastic modulus is a function of damage. Karr and Choi (1989) use two damage measures, one for intergranular cracking and one for intragranular cracking. The damage evolution law is defined as a function of existing damage, stress and strain rate. The damage measure is expressed by a second order tensor which also takes

account of the orientation of distributed cracks. An isotropic damage model with a single scalar damage measure has been developed by Jordaan and McKenna (1988), McKenna et al. (1989), Jordaan et al. (1990). It focused on the relation of the extent of damage and the growing network of microcracks which is often assumed to be uniformly (isotropically) distributed and randomly oriented. A rate expression of crack formation was proposed, based on rate theory in the form of

$$\dot{N} = \dot{N}_0 \left(\frac{\sigma - \sigma_c}{\sigma_0} \right)^r, \tag{2.81}$$

where $\dot{N} = 0$, if $\sigma \leq \sigma_c$, σ_c is the threshold stress; σ_0 is a constant(units of stress); r is a constant and $\dot{N}_0$ is a reference rate. Following Budiansky and O'Connell (1976), damage is defined as $D = a^3 N$ and the elastic moduli of the solid are approximated by Eq. (2.37) and (2.38) based on Horii and Nemat-Nasser (1983).

The work mentioned above was focused on the influence of microcracks on the mechanical properties of the material under mostly moderate loading stresses. As discussed in Xiao and Jordaan (1996), the measurement of damage only as a function of crack density may not be appropriate for all brittle solids under complex loading conditions, such as the crushed ice in the center of indentation interface. In this case, the crystal structure of intact ice has been broken down to fine grains, or particles. Figure 2.14 shows the appearance of the crushed layer obtained after medium scale field indentation experiments. The boundary is very distinct for most of the layer and the ice in the layer is fine-grained, contains bubbles and is of lower density than the parent ice. Under high confining pressure, the crushed ice may be sintered into a solid but microstructurally modified ice mass due to pressure melting or recrystallization. It will not be appropriate to use crack density as the measurement of damage for this type of ice. But the ice behind the layer maintains, to a large extent, its original structure, although microcracks can be observed in the thin sections made from the

ice samples (Meaney et al., 1996). This suggests that two or more types of damage measures are needed to characterize the behaviour of damaged ice and other solids. In fact, many micro-processes, such as grain boundary sliding and elastic anisotropy at triple junctions, can cause stress concentrations at grain boundaries, and lead to microcracking (both intergranular and intragranular) therefore damaging the solid. Other processes, if applicable, like pressure melting between grains and recrystallization can also result in changes in the microstructure of the material. So each of the processes can correspond to a damage measure S_i (i=1, 2, 3, ... n). One individual process may play a more significant or important role than others, under certain loading conditions at a given point of time. For instance, in those critical zones with high confining pressure, pressure melting and recrystallization may be more significant and cracking will be suppressed, while at the edges of interface with high shear and low confinement cracking would be the main source of damage.

As discussed in the previous sections, Schapery's continuum damage theory using the generalized J-integral offers a rigorous solution to problems involving cracking and damaging of viscoelastic materials. The damage measure given by Schapery is defined as

$$S = \int_0^t f_1 (\frac{\sigma}{\sigma_0})^q dt \tag{2.82}$$

where σ is overall stress, σ_0 is a unit stress and q is a constant. Parameter f_1 reflects the properties of the crack-tip material and is a function of stress.

It should also be mentioned that the confining pressure will also affect the development of damage, since the nucleation and growth of microcracks would be suppressed under certain confinement. The pressure dependence has been investigated by Singh (1993) based on the data of triaxial tests in laboratory. An expression for damage

measure was proposed as

$$S = \int_0^t f_1(p)(\frac{\sigma}{\sigma_0})^q dt \tag{2.83}$$

where $f_1(p) = f_1/p$; f_1 is a constant and p is the hydrostatic pressure. This model was then adopted by Xiao and Jordaan (1996). A good agreement was achieved between the theoretical results and the experimental results under moderate loading stresses (less than 10 MPa) and confining pressures (less than 20 MPa).

Recent work by Jordaan et al., (1997) and Meglis et al., (1997) have focused on the effects of both high shear stress (15 MPa) and high confinement (up to 60 MPa) on the damage processes of ice. Their work showed that under low pressures microcracking is the dominant damage process which is suppressed by the increasing pressure. At high pressures, recrystallization and pressure melting become the dominant mechanisms leading to the failure of the material. Based on Schapery's theory and the experimental results, a damage model with two state variables, S_1 and S_2 was proposed, where S_1 is related to the damage processes, such as microcracking, shear banding, at lower confining pressures. The second state variable S_2 is mainly related to the pressure-softening processes, e.g. dynamic recrystallization and pressure melting under high pressures. This leads to higher damage rate with increasing pressure. Similar to Eq. (2.83), the damage evolution law was defined as:

$$S = S_1 + S_2 \text{ and} \tag{2.84}$$

$$S_i = \int_0^t f_i(p)(\frac{\sigma}{\sigma_0})^{q_i} dt \quad \text{(i=1,2)} \tag{2.85}$$

where

$$f_1(p) = \begin{cases} 0.712\left(1 - \frac{p}{37}\right)^2 & \text{if } p < 37 \text{ MPa} \\ 0 & \text{if } p \geq 37\text{MPa} \end{cases}, \text{ and} \tag{2.86}$$

$$f_2(p) = 0.1\left(\frac{p}{42.8}\right)^r, \tag{2.87}$$

and q_i and r are constants.

More discussions will be presented on the dependence of damage on loading stress and confining pressure.

2.10 Creep Enhancement due to Damage

The effect of cracks on the steady-state creep rate for the two dimensional case was examined by Weertman (1969) using dislocation theory. Approximate solutions were given for materials obeying the power law creep equation. His result for low crack density was used by Sinha (1988) as

$$\dot{\epsilon}^c = \dot{\epsilon}_0^c(1 + 2\pi N a^2 n^{1/2})(\sigma/\sigma_0)^n;\ a^2 N \ll 1$$

where N is the number of cracks per unit area and a is half of the crack length. The creep strain is enhanced by a factor of $2\pi N a^2 n^{1/2}$. For high crack density ($a^2 N \gg 1$), Weertman noted that the creep rates must be on the order of

$$\dot{\epsilon}^c \sim A\sigma^n (a^2 N)^{n+1}, \tag{2.88}$$

which indicates that the creep enhancement is on the order of $(a^2 N)^{n+1}$. Jordaan and McKenna (1989) proposed a solution for the three dimensional case. The exponential form models the creep enhancement on inelastic strain, which was redefined as $\exp(\beta D)$ in McKenna et al. (1990). This term is actually equal to the series $\sum_{k=0}^{\infty} b_k D^k$, where b_k are constants, so it will approximate the linear solution for small D ($D = Na^3$) and covers all orders of n for $(Na^3)^{n+1}$ at large D. Therefore, it is a more general form of the creep enhancement factor. This exponential form was also adopted in Xiao and Jordaan (1996) to define the enhancement factor as a function of damage S, i.e. $\exp(\beta S)$.

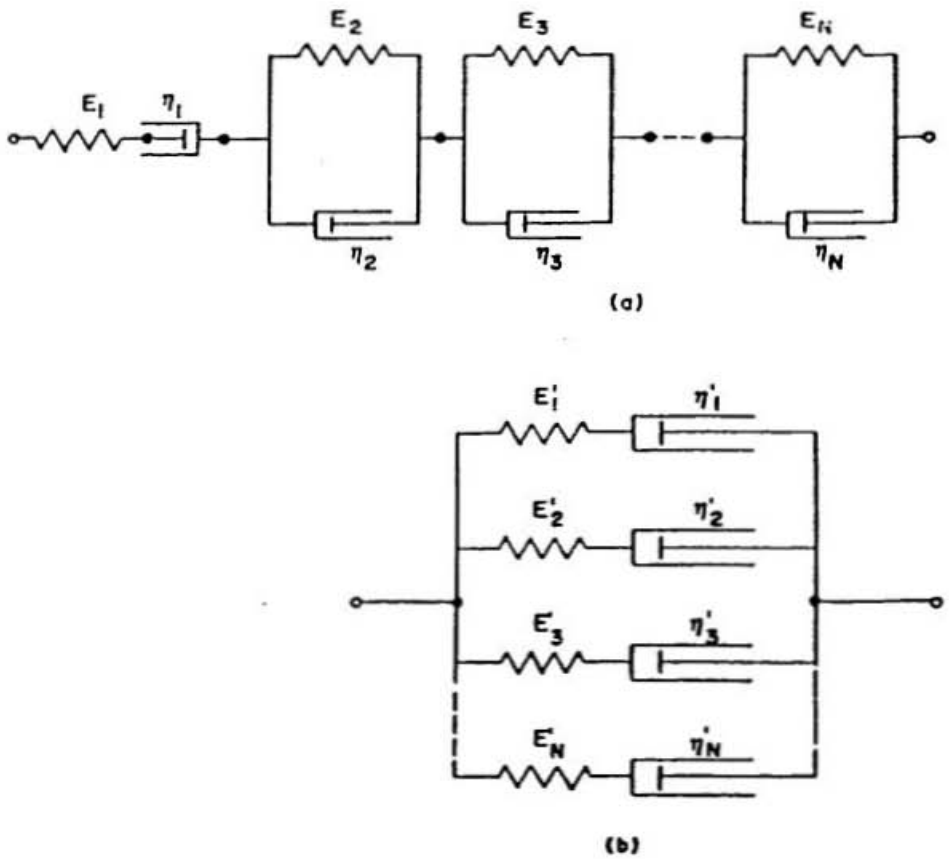

Figure 2.1: Canonic forms of viscoelastic models

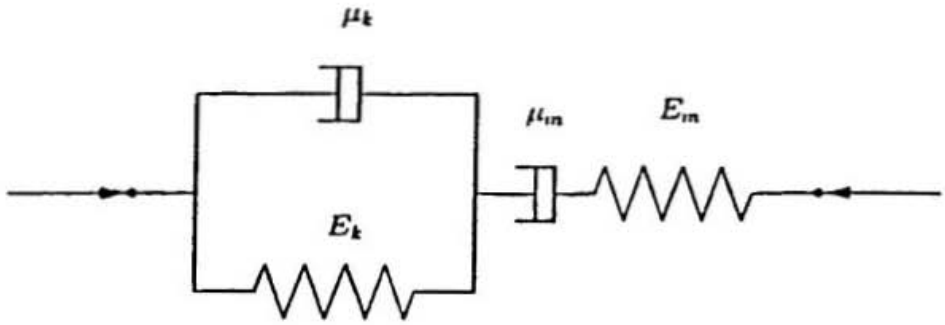

Figure 2.2: Burgers Body; E and μ are elastic modulus and viscosity coefficient, respectively.

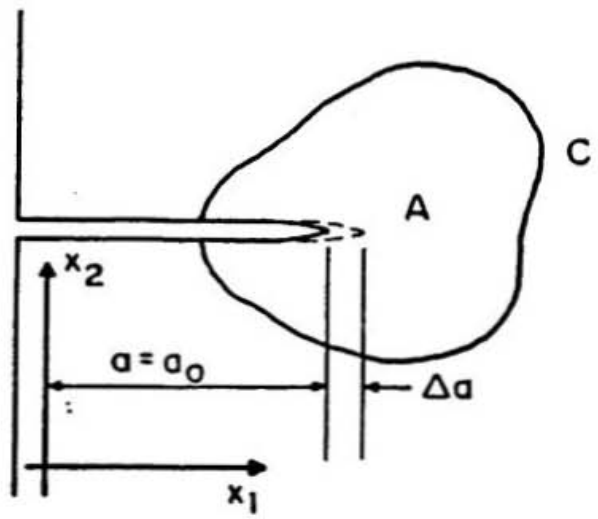

Figure 2.3: Rice's J-integral: Crack and Contour (after Xiao and Jordaan, 1991).

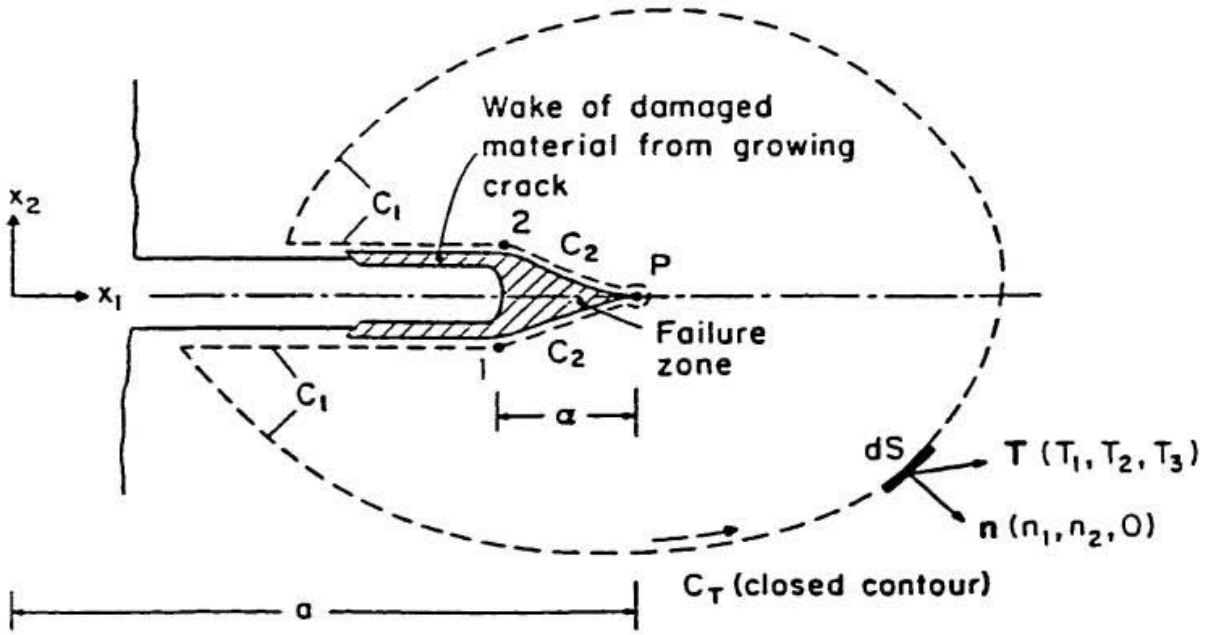

Figure 2.4: Schapery's Idealization of Crack (after Xiao and Jordaan, 1991).

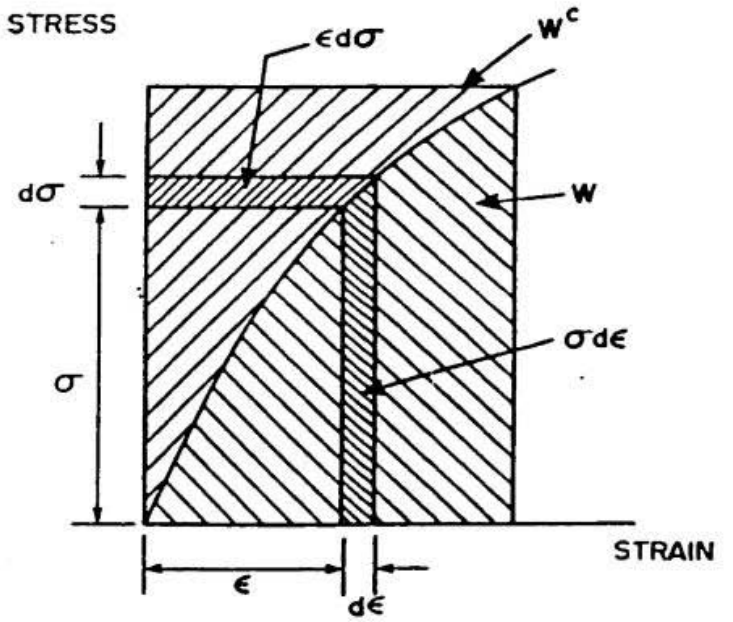

Figure 2.5: Nonlinear Elastic Stress-Strain Curve, Strain Energy W and Complementary Strain Energy W^c (after Jordaan et al., 1990b).

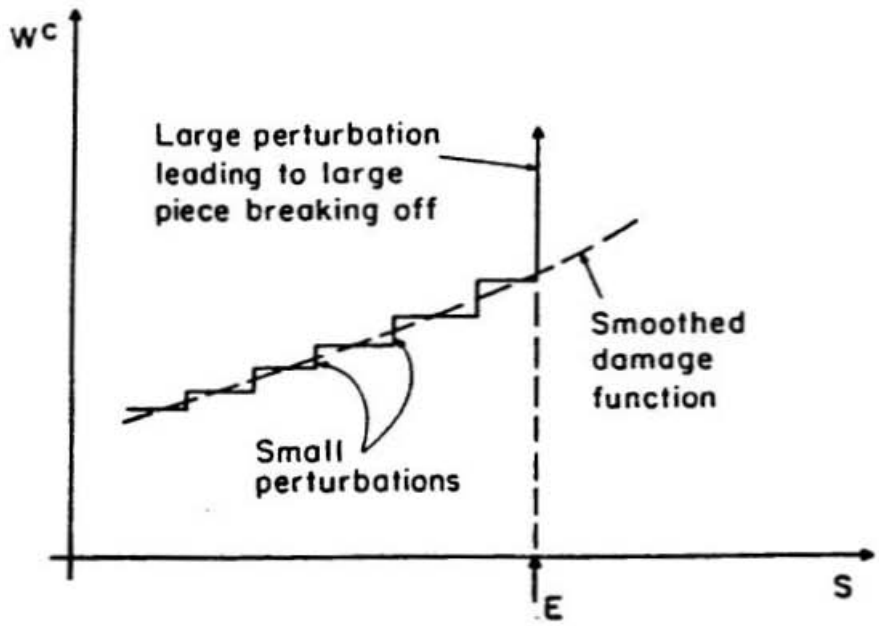

Figure 2.6: Growth of Damage S and Change in Complementary Strain Energy W^c; Event E Represents a Large Flaw that Reaches Critical Size (after Jordaan et al., 1990b).

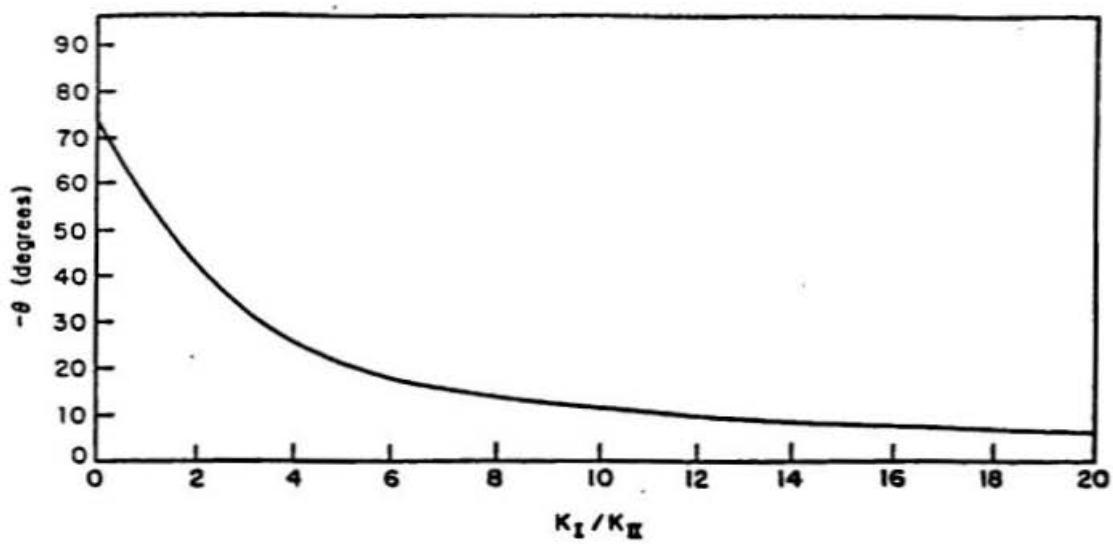

Figure 2.7: Angle of Crack Propagation for Various Ratios of Stress Intensity Factors(K_I/K_{II}) Based on Palaniswamy and Knauss (1974).

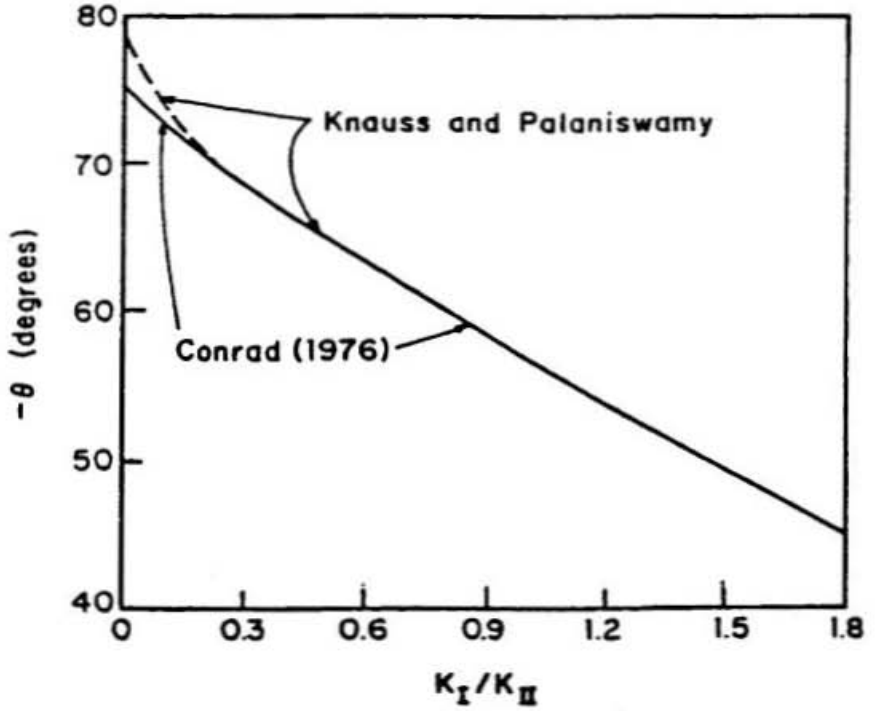

Figure 2.8: Angle of Crack Propagation for Small K_I/K_{II}; see Conrad (1976).

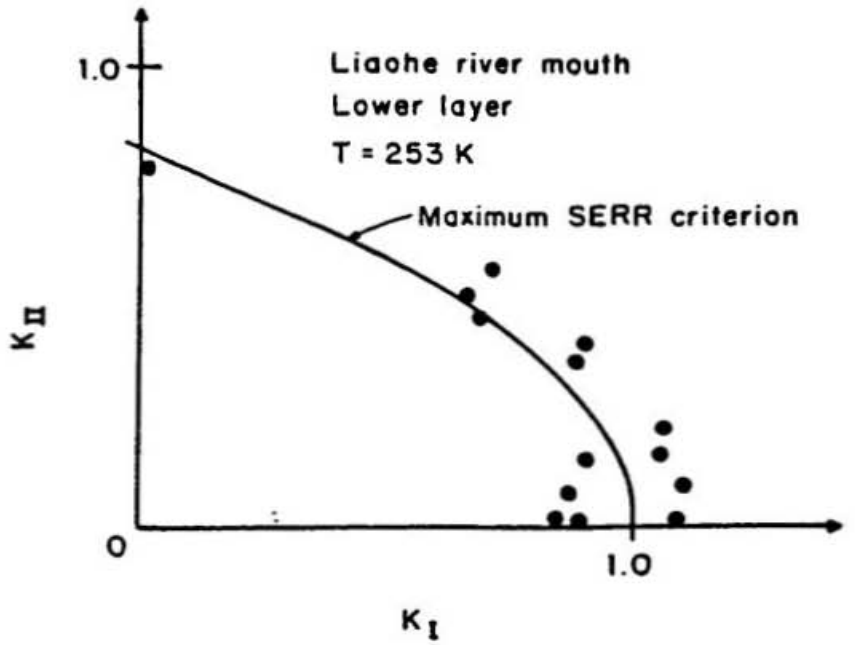

Figure 2.9: Data of Shen and Lin (1986) Fitted to the Maximum SERR Analysis of Palaniswamy and Knauss (1974). Data Normalized with $K_I = 1$ MPa $m^{1/2}$ (after Xiao and Jordaan, 1991).

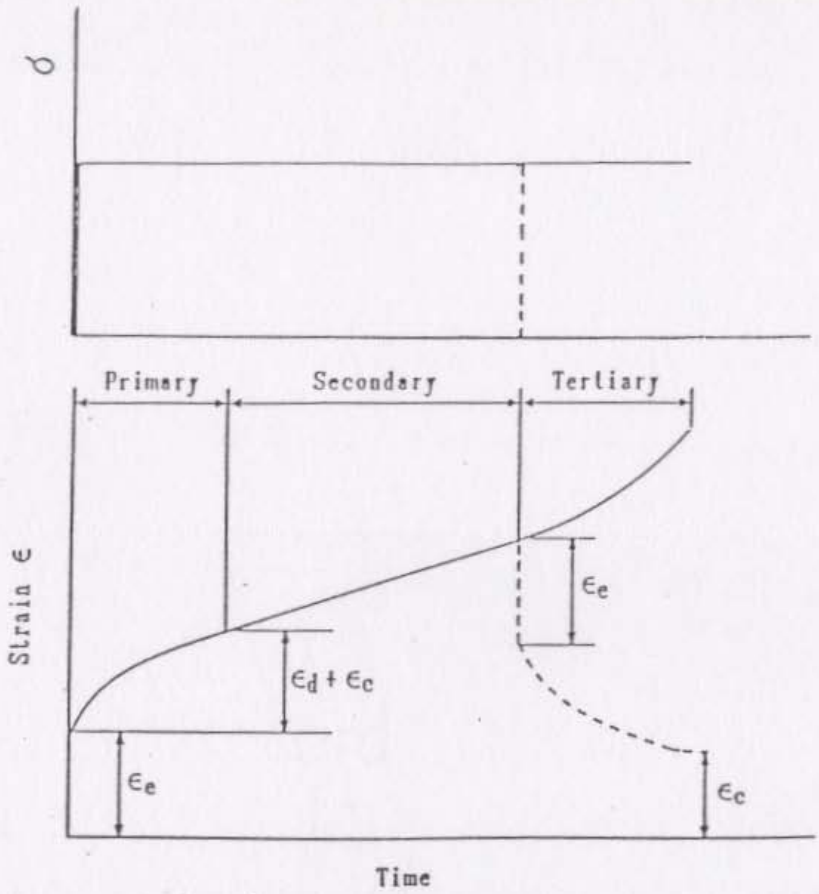

Figure 2.10: The stress-strain history and three phases of constant stress creep test: (I) primary; (II) secondary; (III) tertiary.

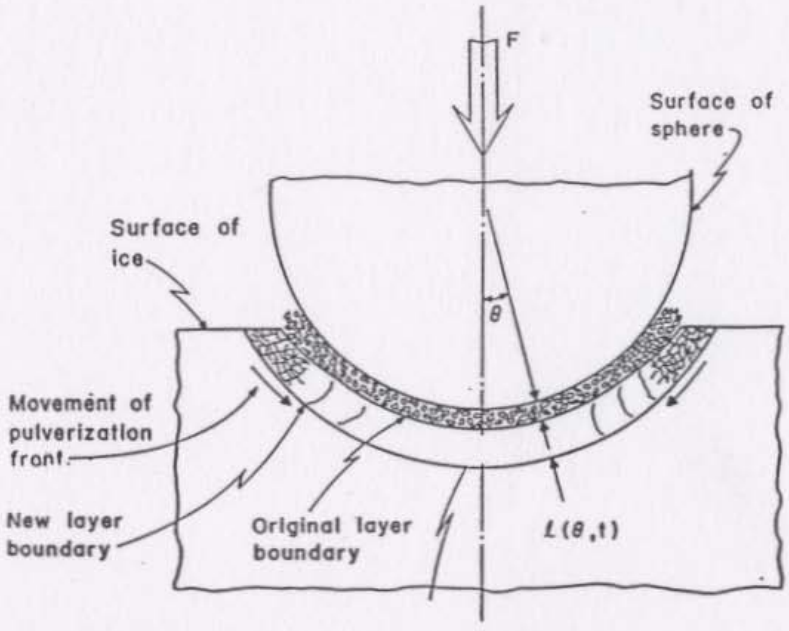

Figure 2.11: Possible mode of pulverization ahead of spherical indenter (Jordaan and McKenna, 1988a).

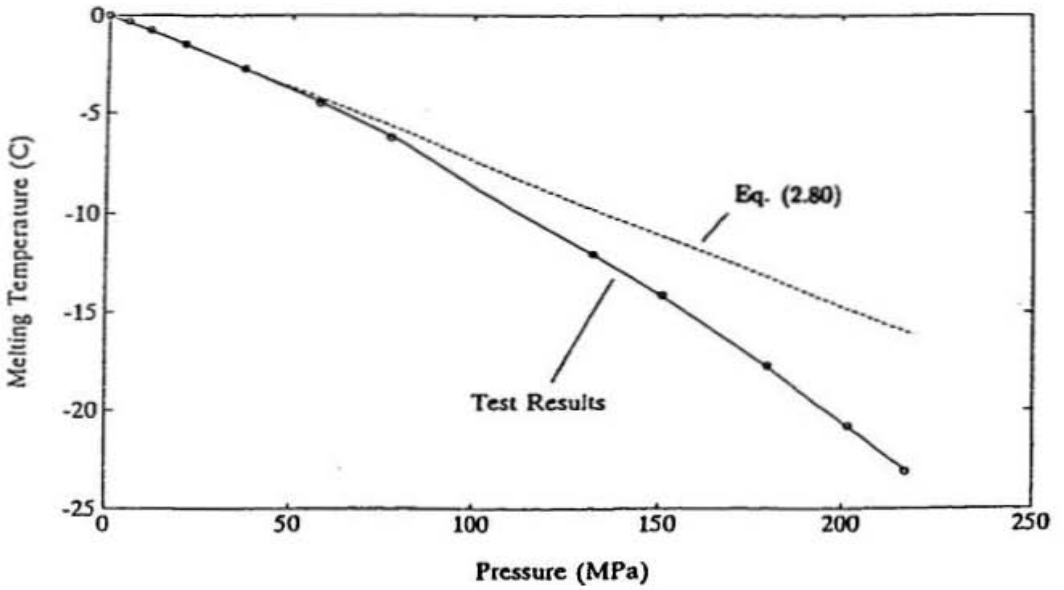

Figure 2.12: Measured Melting-Temperatures and Pressures by Nordell (1990) and Calculated Curve from Eq. (2.80).

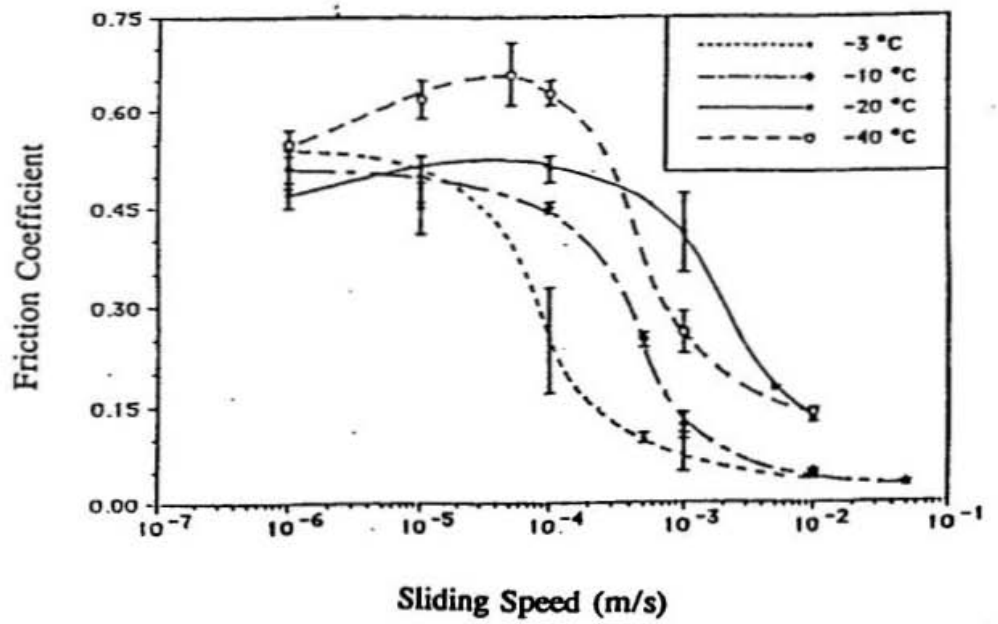

Figure 2.13: Test results of Friction Coefficients Versus Sliding Speed at Different Temperatures (Jones et al., 1991).

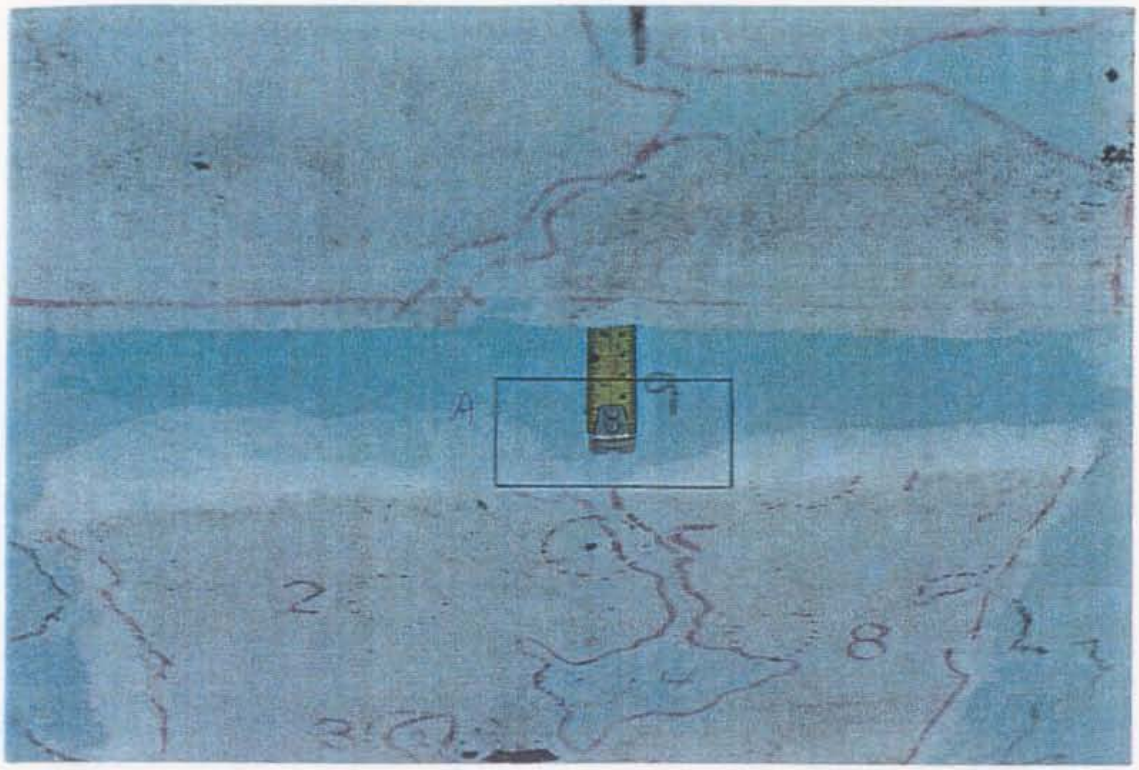

(a)

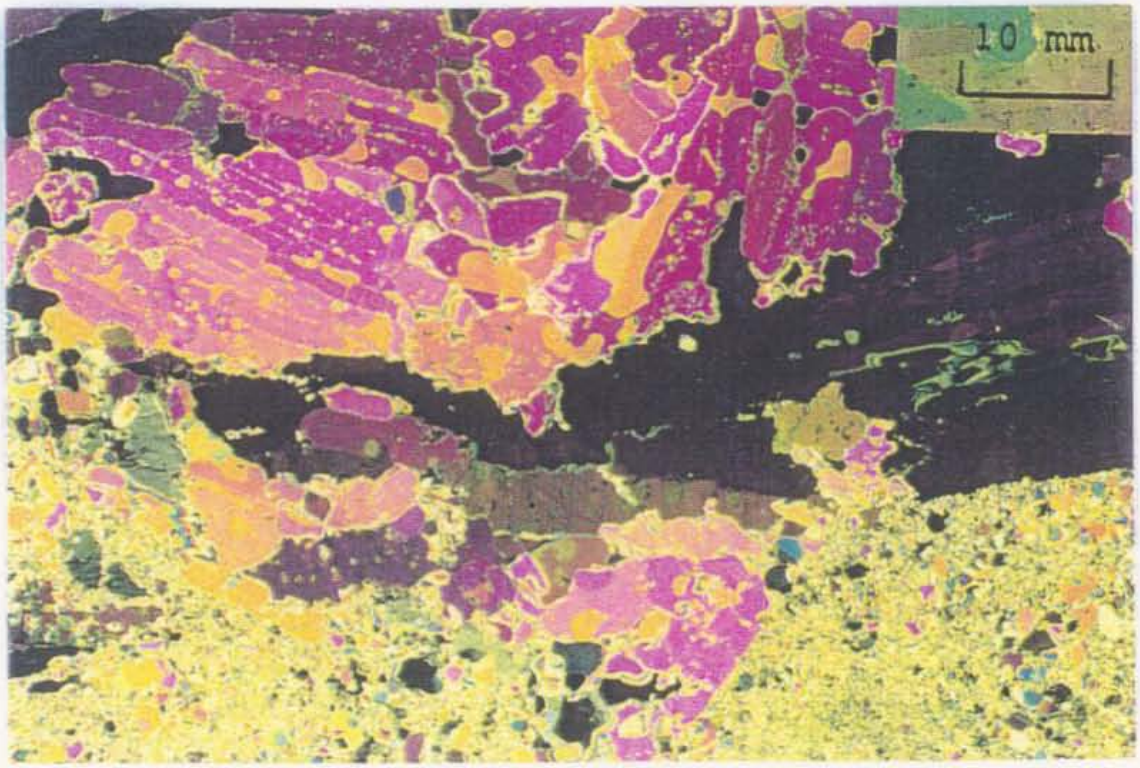

(b)

Figure 2.14: Contact face at end of the test, (a) general view of vertical face and horizontal cross section cut into the ice face, (b) thin section of area A (after Frederking et al., 1990a).

Chapter 3

Experimentation

3.1 Introduction

Two medium-scale test programs were carried out on Hobson's Choice Ice Island Research Station by Memorial University, the National Research Council of Canada (NRC), Canadian Coast Guard (CCG) and Sandwell Swan Wooster (SSW) in April, 1989 and May, 1990. A hydraulic indentation system was utilized with spherical, wedge and flat indenters in different sizes. There were eleven tests in April, 1989 and fifteen successful tests in May, 1990. In most tests (except for very low speed ones), ice crushing was observed in front of the indenter and the thickness of the crushed layer was irregular from 30 mm to 50 mm. There was usually less cracking in the center area due to high confinement and more damage at the edge of the interface. Maximum pressures measured at the center were in the range of 30 to 50 MPa. Pressure melting has also been reported (Gagnon and Sinha, 1991). An ice sheet indentation test program was also conducted in the ice towing basin at the Institute for Marine Dynamics, NRC. This program was designed to investigate the ice failure processes in ship-ice interaction. Different failure modes, including crushing, bending and fracture splitting, were observed (Finn, 1991).

To understand the ice behaviour under such complex loading conditions, espe-

cially the ice in the zones with high confining pressure, a test program, utilizing laboratory prepared granular ice under a variety of triaxial confining pressures, has been conducted at Memorial University (see also Stone et al., 1997). These tests were designed to investigate the deformation of ice, the influence of cracks and level of damage on the creep response, and to obtain the relevant material constants for constitutive modelling. The main focus is on the behaviour of ice in the critical zones, i.e. ice under high triaxial confining pressure and shear stresses. The test results were also used to verify the theoretical model. The objectives of the experimental program were as follows.

- The intrinsic creep response of ice in the undamaged state requires consideration. Tests have been conducted to study this aspect, in particular the question of the minimum creep rate.
- The different types of microstructural changes have been investigated. This included evidence from thin sections, as well as an analysis of stress, and strain response.
- The effect of stress path on the response of ice was studied, particularly under the unloading conditions.
- Thermodynamic aspects were investigated by measuring the temperature at the center of ice sample under triaxial confinement.

3.2 Triaxial Tests

3.2.1 Specimen Preparation

All tests were conducted using laboratory prepared granular ice following the procedure detailed by Stone et al. (1989). To minimize the final air content of the ice while

maintaining control over grain size, the following equipment and procedure was used (Figure 3.1). Bubble free columnar grained ice was crushed and sieved to produce 2.00 to 3.36 mm seeds. A cylindrical, acrylic mold, 229 mm diameter, 303 mm length, was filled with this seed. The mold, with seed ice and connecting tubing, was placed under a vacuum of 270 to 400 Pa (2.0 to 3.0 torr) for a period of 1.5 to 2 hours. After evacuation, distilled and deionized water cooled to 0°C was transferred to the deaerator and deaerated for 15 minutes. The mold was then completely flooded with this deaerated water. After flooding, the freezing process began and it was primarily unidirectional from the bottom up, and was completed in approximately 3 days, at a cold room temperature of -10°C.

Typically, the freezing procedure produced larger than desired grains near the bottom and outside perimeter and a higher density of bubbles near the top. To ensure consistent repeatable ice quality, the top and bottom 30 mm were removed and discarded. The specimens were machined to the desired diameter using a lathe. The final test specimens were measured 70 $\pm$ 0.05 mm in diameter and 175 $\pm$ 1.0 mm in length.

The crystal structure of each batch of four specimens was checked by taking a thin section at the immediate top and bottom of random specimens throughout a given batch. The average number of grains per diameter of 70 mm of the specimens used was 22 to 29. The ice produced by the above procedure is transparent through the 70 mm diameter with minimal bubble content.

3.2.2 Test Equipment and Procedure

An MTS Test System integrated with a Structural Behaviour Engineering Laboratories triaxial cell was used for all tests (Figure 3.2). The dual axis (axial load frame and triaxial cell pressure intensifier) digital control system permitted full uninterrupted

closed loop feedback control across the full range of control modes for the complete test sequence.

Two LVDT's were mounted directly on the specimen, over a gauge length of approximately 120 mm. The two LVDT outputs were averaged to provide the in-situ measure of axial strain as well as a closed-loop feedback control signal to the MTS servo-valve. Lateral strain was also measured to find evidence of compaction or dilatation during deformation process. For this purpose, three specially designed strain gauges were mounted on the two sides of the sample and approximately on a line. Another technique of measuring the volumetric strain is the fluid displacement method, which measures the volume of the fluid displaced from the triaxial cell, by means of an LVDT which was built into the confining pressure intensifier.

Several hours before each test, the specimen was placed in the cold room to allow temperature equalization. During the test, the temperature on the surface of the specimen were measured. For some specially designed tests, the temperature at the center of the specimen were also measured to provide evidence of pressure melting under high confining pressure. A maximum inside temperature of -9.3°C was measured right after the pressurization for a -10°C tests, i.e. the approximate cold room temperature.

All the test data were recorded on a microcomputer via a multifunction data acquisition board. An acquisition rate of 20 sample/sec/channel was used for the loading and unloading phases of the test. Between each unloading and loading, i.e., during the period of relaxation, where the deformation rate is very low, the acquisition rate will be set to 10 times lower than that of loading phases, so to reduce greatly the amount of data stored in the computer without losing all important characteristics.

Data recorded included:

- Confining stress by a pressure transducer mounted on a port of the triaxial cell;
- Stress difference by a load cell between piston and cross-head;
- Axial displacement (strain) by averaging of two LVDTs;
- Diametral displacement at mid-height of the sample by three specially designed strain gauges;
- Time;
- Stroke;
- Ice temperature on the surface, and inside of the sample for some tests.

3.2.3 Test Program and Summary of Results

The test series undertaken considered four aspects: the intrinsic creep properties of intact (i.e. undamaged) ice, the enhancement of creep and changes in microstructure due to damage, the effects of different stress paths, and thermodynamic aspects of triaxial compression testing.

(1) Intrinsic Creep Properties

The creep properties characteristic of intact (i.e. undamaged) granular ice as defined by a small stress difference applied over a long duration of time was demonstrated by an extended creep test. A 2 MPa stress difference was applied to an intact specimen under 20 MPa triaxial confinement for a period of 8 hours. This pulse load (instant load and unload) was followed by an 8 hour relaxation period. The 8 hour load, 8 hour relaxation sequence was repeated immediately following the "initial" test. The creep response of both the initial and repeat tests are shown in Figure 3.3.

The initial test sequence resulted in a maximum total strain of about 2% at the end of the initial 8 hour, 2 MPa pulse load. Tertiary creep, a gradual increase in creep

rate following secondary creep, occurs after about 250 min. Beyond the instantaneous recovery of elastic strain upon unloading at 480 min. (8 hours), the time dependent recovery of delayed elastic strain occurs at a low rate over the 8 hour relaxation period.

Transition from delayed elastic strain, through secondary creep, to the tertiary creep stage has been associated with the occurrence of microstructural change resulting from crack formation (Gold, 1972) and, potentially, dynamic recrystallization (Sanderson, 1988). The repeat load pulse, relaxation sequence immediately following the initial test indicates that the specimen has undergone significant change. Maximum total strain at the end of the 8 hour load pulse is 5%, 2.5 times that of the initial test, with tertiary creep occurring earlier at about 160 min. Typical cross-polarized horizontal thin sections of the ice prior to testing (Figure 3.4a) and after initial and repeat tests (Figure 3.4b) shows a change in grain size from a mean grain diameter of 3 mm to 2.4 mm. A number of small voids between crystals were also observed in the after test thin section during microtoming.

Compression tests on intact ice utilizing a number of sequential pulse loads of short duration of 20 seconds and duplicating tests conducted on damaged specimens provided the creep properties of ice uniaxially and under different triaxial confinement conditions. These test results form the basis of comparison with damaged ice. Conducted on an intact ice sample and with a confinement of 10 MPa, Figure 3.5a shows the applied stress history and strain response of a constant stress creep test, which is, in fact, a series of creep tests. Each creep test consisted of a 20 second load pulse. The reason for loading only 20 seconds is that these tests were designed to investigate the short-time responses of ice, such as, elastic and delayed elastic strain components. Figure 3.5b shows a creep test conducted on a damaged sample with the same confinement. The sample was damaged by subjecting to a constant strain rate

loading of $10^{-4}s^{-1}$ to a total strain of 2% under uniaxial loading condition. Figure 3.6 shows two thin section photos of intact and damaged ice samples. It can be seen that the grain structure of intact ice has been broken down due to damage. The average grain size of damaged ice is much smaller than that of its original dimension.

(2) Damaged Ice and Creep Enhancement

Compression tests were conducted on both intact and damaged specimens under uniaxial conditions and triaxial confining pressures (5, 10, 20 MPa). A variety of damage levels were created by compressing otherwise undamaged intact samples at a strain rate of 10^{-4} s^{-1} to a total strain of 2 or 4% under either uniaxial or the triaxial confinement conditions (5, 10, and 20 MPa) to be applied in the particular test. Typical stress-strain curves for each of the 4% total strain damage steps are shown in Figure 3.7. Following the damage step, the test sequence involved the application of a number of 1, 2, and 3 MPa pulse loads (instant load and unload) for a period of 20 seconds, followed by either a 200 or 400 seconds of relaxation period. In most cases, this initial stress sequence was common for all tests was followed by a sequence of higher pulse loads, up to 10 MPa, for a longer duration (100 s) which were followed by a longer relaxation period (800 s). A summary listing of compression tests conducted is given in Tables 3.1 to 3.3 for each of the triaxial confining pressures applied.

Jordaan et al. (1992) introduced the effect of stress history and related changes in material constants on the creep response of intact (i.e. undamaged) and damaged ice (to 2% of total strain at strain rate of 10^{-4} s^{-1}) under uniaxial conditions (Figure 3.8). Comparison of the creep response of intact and 2% uniaxial damaged ice shows that elastic strain was not significantly influenced by the damage state, whereas delayed elastic strain and its time dependent recovery were increased by several orders of magnitude. The stress pulses used for these tests (0.25, 0.5, and 0.75 MPa) were smaller than those used in the triaxial tests presented later resulting in negligible

Table 3.1: Test Matrix, 5 MPa Triaxial Confinement (// indicates change from 20 sec. pulse loads to 100 sec. pulse loads).

Intact Ice (Zero Damage)		
Test No.	Damage %	Load Pulse Sequence (MPa)
IT230793	-	1/2/3/1/5/1//3/1/5/1/7/1

Uniaxial Damage		
Test No.	Damage %	Load Pulse Sequence (MPa)
DT150193	2	1/2/3/1
DT121193	2	1/2/3/1

Triaxial Damage		
Test No.	Damage %	Load Pulse Sequence (MPa)
DT200793	2	1/2/3/1//3/1/5/1
DT180194	4	1/2/3/1//3/1/5/1

Table 3.2: Test Matrix, 10 MPa Triaxial Confinement (// indicates change from 20 sec. pulse loads to 100 sec. pulse loads).

Intact Ice (Zero Damage)		
Test No.	Damage %	Load Sequence (MPa)
IT290193	-	1/2/3/1/5/1/7/1/10/1
IT110194	-	1/2/3/1/5/1/7/1/10/1

Uniaxial Damage		
Test No.	Damage %	Load Pulse Sequence (MPa)
DT170792	2	1/2/3/1
DT200792	2	1/2/3/1
DT300792	2	1/2/3/1
DT030892	2	1/2/3/1
DT250193	2	1/2/3/1/5/1/7/1
DT270193	2	1/2/3/1/5/1/7/1
DT211293	2	1/2/3/1/5/1/7/1
DT120293	4	1/2/3/1//3/1/5/1

Triaxial Damage		
Test No.	Damage %	Load Pulse Sequence (MPa)
DT190393	4	1/2/3/1//3/1/5/1

Table 3.3: Test Matrix, 20 MPa Triaxial Confinement (// indicates change from 20 sec. pulse loads to 100 sec. pulse loads).

Intact Ice (Zero Predamage)		
Test No.	Damage %	Load Pulse Sequence (MPa)
IT050293	-	1/2/3/1/5/1/7/1/10/1/20/1
IT061293	-	1/2/3/1/5/1/7/1/10/1

Uniaxial Damage		
Test No.	Damage %	Load Pulse Sequence (MPa)
DT091092	2	1/2/3/1
DT171292	2	1/2/3/1
DT181292	2	1/2/3/1
DT160293	4	1/2/3/1//3/1/5/1/10/1

Triaxial Damage		
Test No.	Damage %	Load Pulse Sequence (MPa)
DT230693	2	1/2/3/1//3/1/5/1/7/1
DT240693	2	1/2/3/1//3/1/5/1/7/1
DT090393	4	1/2/3/1//3/1/5/1/10/1
DT110393	4	1/2/3/1//3/1/5/1/10/1
DT180593	4	1/2/3/1//3/1/5/1/10/1
DT251193	4	1/2/3/1//3/1/5/1/7/1

additional damage after repeated loadings.

Figures 3.9 to 3.11 show the creep response of intact ice, and 2% and 4% uniaxially damaged ice, tested under triaxially confining pressures of 5, 10, and 20 MPa. As in the previous uniaxial tests the damage state has a small effect on the elastic component under each of the three confining pressures. At a confining pressure of 5 MPa there is virtually no difference in the creep response of intact and 2% uniaxially damaged ice for all three pulse loads. This is also the case for the 1 MPa pulse load under 10 and 20 MPa triaxial confinement. The 4% damage state produces a small increase in delayed elastic creep under a 1 MPa stress difference, and 10 and 20 MPa confinement. The 2 MPa and 3 MPa load pulse at 10 and 20 MPa, confinement does illustrate an increasing creep rate as a function of increasing damage state (2% to 4%) and decreasing confinement (20 MPa to 10 MPa). Unlike the large increases shown in the previous uniaxial tests, only fractional increases in delayed elastic creep as a function of uniaxial damage state were observed under triaxial confinement.

Figures 3.12 to 3.14 show the creep response of 2% and 4% triaxially damaged ice along with that of the intact ice previously shown. In these tests the 2% and 4% total strain at 10^{-4} s^{-1} damage step was executed under the same triaxial confining pressure as the pulse loads of the particular test. As previously discussed, there is a small effect on instantaneous elastic creep occurring immediately upon loading. The delayed elastic component of creep has increased for the triaxial damage state versus the previous uniaxial damage state. This would indicate that a specimen compressed to 2% and 4% total strain at a strain rate of 10^{-4} s^{-1} under triaxial confinement results in increased damage over that imposed under uniaxial conditions.

The acceleration of creep rates as a function of damage state has been associated with microcracking increasing as total strain increases and with recrystallization, the rearrangement of dislocations resulting in the formation of new grains and the

reoccurrence of an increasing creep rate. A smaller grain size is apparent in the thin sections shown in Figure 3.4, taken at the end of an extended creep test on an intact specimen under 20 MPa confining and 2 MPa stress difference. Figure 3.15a shows the thin section of a specimen have undergone a 2% uniaxial damage step and a 1, 2, 3, 1 MPa 20 sec. pulse load sequence under triaxial confinement of 10 MPa. Cracks along and across grain boundaries, with fine particles dispersed throughout the section, are readily apparent on the magnified section (Figure 3.15b).

The creep tests provide information on the viscosity of the ice. Comparing the creep responses (delayed elastic strain plus secondary creep strain, $\epsilon^d + \epsilon^c$) of the tests of intact to damaged ice under 10 MPa confinement in Figure 3.16, it shows that the presence of cracks and damage significantly influence creep strain. The creep strain of damaged ice is more than 3 times that of intact ice. As shown in Figure 3.13, the strain response of the intact ice has been mostly recovered, especially for those under lower stresses. This suggests that the elastic and delayed elastic components in intact ice dominate for short loading period. The strain response of damaged ice has a significant percentage of secondary creep, and the creep strain rate, $\dot{\epsilon}^d + \dot{\epsilon}^c$ (which is the slope of the strain versus time curve in Figure 3.13 and 3.16) is much higher than that of intact ice. This implies that cracking and damage can significantly enhance the creep response of ice (see also Stone et al., 1989; Jordaan et al., 1990a, b). Figure 3.17 shows the strain responses of damaged ice under same stress difference $(\sigma_1 - \sigma_3)$ of 3 MPa, but with different confinement, 10 MPa and 20 MPa. It shows clearly that the increase of confinement will suppress the cracks and close them so that the ice would become stiffer and less creep strain would be developed.

(3) Pressure Reduction Test

Crushed ice extrusion and spalling may result in sudden reductions in confining

pressures and a corresponding increase in stress difference. In addition to compression tests to characterize creep enhancement, a preliminary investigation of the effect of sudden confinement pressure drops on creep rate has been started. A 7 MPa pulse load for 100 sec. was applied to a specimen damaged to 2% total strain at a triaxial confining pressure of 10 MPa. Twenty seconds after the initiation of the load pulse, triaxial confinement pressure was instantaneously dropped from 10 MPa to 5 MPa for the remaining duration of the pulse load (or to transducer operational limits). This pressure drop was executed without a corresponding drop in applied axial stress effectively increasing the stress difference load pulse to 12 MPa triaxial at a 5 MPa confining pressure.

Figure 3.18 shows the strain-time curve for the stress difference load pulse of 7 MPa. At 20 sec. the drop in confinement from 10 MPa to 5 MPa resulted in a substantial increase in deformation rate from a total strain of 0.5% at 20 sec. to a total strain of 4.0% at 42 sec. A seven fold increase in deformation rate for a 1.71 fold increase in stress difference. At 50 sec. it has been estimated that total strain for a 7 MPa pulse load at 10 MPa confinement would be 1.1% (ϵ). The pressure drop and resulting stress difference increase has resulted in a total strain of 7.3% (or $\Delta\epsilon$ = 6.2%).

(4) Thermodynamic Aspects

The triaxial cell confining fluid temperature at the start of each test was -10°C ± 0.9°C. Pressurization of the cell resulted in a warming of the fluid by: 0.7°C for 5 MPa, 1.4°C for 10 MPa, and 2.6°C for 20 MPa. To establish the effect of pressurization on sample temperature fast response RTD elements were placed in the confining fluid, on the sample wall and in the sample center. As in all tests the specimen was sealed in a latex membrane with the center RTD element output being passed through a specially designed platen and high pressure electrical feed through. Output was recorded on a

Table 3.4: Temperature Measurements at Specific Peaks Under 40 MPa Triaxial Confinement.

	Prior to Pressurization °C	Peak After Pressurization °C	Peak After Secondary Warming °C
Sample Center	-9.9	-9.3	-7.8 @1002 sec.
Sample Wall	-9.7	-6.5	-
Fluid	-10.2	-4.5	-

stripchart.

All three RTD elements showed an immediate increase in temperature upon pressurization to a confining pressure of 40 MPa. (Figure 3.19, Table 3.4). The 40 MPa pressurization at a rate of 4 MPa/sec. warmed the solid ice by 0.6°C and the liquid confining fluid by 5.7°C. After peaks had been reached, cooling from the -10°C cold room began immediately with sample center temperature reaching -9.0°C at 5400 sec. just prior to depressurization.

A second temperature test to a confining pressure of 20 MPa with a 4% total strain damage step showed similar results (Table 3.5). The RTD element at the sample centre failed at the completion of the damage step.

Table 3.5: Temperature Measurements at Specific Peaks Under 20 MPa Triaxial Confinement.

	Prior to Pressurization	Peak After Pressurization
Sample Center	-10.5° C	-10.1° C
Sample Wall	-10.0° C	-8.1° C
Fluid	-10.3° C	-7.3° C

3.2.4 Discussion

As mentioned earlier, the elastic strain is not strongly influenced by the damage state, whereas the delayed elastic and secondary creep strain are significantly enhanced by several orders of magnitude, especially when initial damage is introduced under a triaxial stress state. The creep strain response of uniaxially damaged ice is much smaller than that of triaxially damaged ice. This effect is shown in the figures 3.9 to 3.14. If the ice is damaged under uniaxial loads and then subjected to triaxial confinement, the initially introduced cracks (damage) will be suppressed and closed, therefore the effects of cracks on the deformation of ice is very limited. If the ice is damaged under triaxial loads, and the confinement is kept on when the constant stress pulses are applied to the ice sample, the initially introduced cracks (damage) will be not suppressed and closed, therefore the effects of cracks on the deformation of ice is very significant.

Figure 3.20 shows two strain history curves for creep tests on damaged samples. Sample I was tested under 10 MPa confinement with triaxial initial damaging, i.e., the 10 MPa confining pressure was applied at the beginning of the test and kept constant throughout the test. The strain history from O to A is the damage period. ¿From A to B is the creep test period. Sample II was also tested under 10 MPa confinement, but with uniaxial damaging, i.e., the initial damaging was done under uniaxial conditions. The 10 MPa confinement was applied after the initial damaging, i.e., at point A. Due to the uniaxial damaging, microcracks were developed along the direction of loading stress, therefore introducing anisotropy to the material properties. Upon the application of confinement, sample II was compressed close to the original volume, which indicates most of the cracks were closed, or nearly closed, the creep response would also be smaller due to the closure of cracks. In fact, ice with most of its cracks closed (due to confinement) can behave similarly to intact ice. The friction between the crack surfaces plays an important role in this type of ice. The effect of friction between closed crack surfaces may also explain why under 5 MPa confinement, the creep strain of damaged ice was almost the same as the intact ice. When the confinement was increased to 10 or 20 MPa, due to possible pressure melting between grains or crack surfaces, the effect of friction is reduced and creep response of uniaxially damaged ice is increased.

Sample I was tested after triaxial damaging. Thin sections of the sample after the test show less evidence of preferred crack orientation. Since the confinement was applied at the beginning of the test and kept constant thereafter, once the crack is opened, it will stay open so there are no frictional tractions cross the crack surfaces during the deformation process, and the creep will be larger than that of uniaxially damaged ice, as well as intact ice under the same confinement.

As mentioned earlier, temperature at the center of the ice sample was measured

for two triaxial situations. During the 40 MPa pressurization, the ice was warmed by 0.6°C at the center, and 0.4°C for the 20 MPa pressurization. Since the temperature was measured at the center of ice, and the sample was covered with a latex membrane, the pressurization period can be assumed as an adiabatic process, and a thermodynamic formula can be derived to calculate the increase of temperature in the form of:

$$\Delta T = \frac{T}{C_p}(\frac{\partial v}{\partial T})_p \Delta P \tag{3.1}$$

where T is ice temperature; C_p is specific heat; $\frac{\partial v}{\partial T}$ is the thermal expansion and ΔP is the applied pressure. Calculated temperature increases are 0.86°C for 40 MPa and 0.43°C for 20 MPa. The calculated temperature increases are higher than that of measured ones. This may be explained by possible pressure melting which will absorb heat during melting process.

The above sections discussed the experiments for ice under triaxial stress states with low to moderate pressures. Both intact and damaged samples were used under a varity of loading conditions, such as loading path and temperature. The tests provide useful information on the effects of cracks and level of damage on the creep response. The influence of confining pressure on the development of damage and the deformation of ice is also investigated. The proposed damage model was calibrated using the test results.

3.3 High Stress Triaxial Tests

Creep tests were conducted by Jones and Chew (1983) on polycrystalline ice under a combination of axial compressive stress (deviatoric stress) of 0.47 MPa, and hydrostatic pressures up to 60 MPa. The test results showed that the secondary creep rate was decreasing when hydrostatic pressure was increased from 0 to 15 MPa, and

reached a minimum rate under a pressure of around 20 MPa. and then the creep rate was increasing rapidly when the pressure was between 30 to 60 MPa. Their conclusion from the test results indicated that more than one mechanism was contributing to the creep deformation. One possible mechanism was the pressure melting at the grain boundaries under high pressures. The liquid phase formed between the grains would result in increasing deformation rate. Recent work by Meglis et al., (1997) presented some test results on polycrystalline ice under high deviatoric stress (15 MPa) and high confining pressures (up to 60 MPa). The primary purpose of this work is to study ice behaviour under impact conditions with structures, in which case high stresses and large strains associated with high deformation rates can be involved. The measured strain rates were mostly on the order of $10^{-3}s^{-1}$ at the beginning of the testing. The strain rates went up to the order of $10^{-1}s^{-1}$ near the end of the testing. These rates were much higher than those presented by Jones and Chew (1983), which were on the order of $10^{-8}s^{-1}$. The difference in strain rates indicates that the damage mechanisms for high stresses may be different from that of low stresses. The preliminary results showed that at low pressures, the dominant process of ice failure is microcracking, and the creep strain rate is decreasing when confining pressure is increasing; while at high pressures, microcracks are suppressed, the dominant mechanisms of ice failure are dynamic recrystallization and pressure melting, and the creep strain rate is increasing rapidly with pressure. Thin sections of ice samples after testing show that at low pressures, microcracks are present at the grain boundaries as well as within the grains, while the primary ice crystal structures remain largely unchanged. At high pressures, microcracks mostly disappeared and ice crystal structures were destroyed. Replacing them are fine grains and much smaller sized particles. The test program also indicates that both high deviatoric stress and confining pressure are needed in order to develop high normal loads and rapid growth, highly damaged ice samples.

This will also lead to the formation of pulverized, fine grained materials as seen in the contact zones of medium scale indentation tests. Some test results are shown in Figure (3.21). Those tests were done under 15 MPa constant deviatoric stress and various confining pressures and temperatures. Figure (3.22) shows a test curve of strain rate in logarithm scale versus time. This was done under 15 MPa deviatoric stress and 50 MPa confinement. The curve has been linearized into three portions: minimum, linear, and maximum portion. Each of them represents a different stage of deformation progress. The test curve also shows a rapid increase in deformation rate. This implies that the test sample has been undergoing a significant softening process. Figure (3.23) shows the relationship of strain rate (in logarithm scale) versus hydrostatic pressure. Three strain rates, minimum, linear and maximum rate from each test were plotted.

3.4 Medium Scale Indentation Experiments

3.4.1 Test Setup

In April, 1989, a total of eleven tests were performed on Hobson's Choice Ice Island. Three of them were flat-rigid indentation tests with speeds ranging from 10 mm/s to 80 mm/s. In May, 1990, there were five flat-rigid tests with two loading speeds 100 mm/s and 400 mm/s. The insitu ice temperature was about -10 to -14 °C. The tests were carried out in an area of 8 m thick multiyear ice which was attached to the edge of the ice island. A trench 3 m wide, 4 m deep and 100 m long was excavated to conduct the tests. The walls of the trench were roughly smoothed with a chain saw and the test areas were specially machined with a vertically mounted circular saw. The wall opposite the test face was also machined and made parallel to the test face.

The ice indentation system consists of a hydraulic actuator (some tests in May,

1990 used three actuators) mounted upon a large mobile skid of beam and strut construction, as shown in Figure 3.24a. The actuator was powered by a bank of pressure accumulators and controlled by a servo-control system which provided a constant displacement rate. The indentation speeds could be assumed approximately constant over the whole test period. A flat back plate was attached to the rear end of the actuator to support the system. This back plate had a larger contact area than the indenter to force crushing failure on the indentation face only. Eight pressure cells for measuring local pressures were mounted to the front of the flat rigid indenter in the 1989 program (see also Figure 3.24b). The truncated wedge ice face is shown in Figure 3.25. For 1990 test program, the flat rigid indenter was larger and had a dimension of 1220 × 1500 mm^2. A multi-element pressure panel with an area of 150 × 480 mm^2 and a grid of 36 pressure sensors was utilized. The ice failure was also recorded with a video camera through a special video window of 160 × 340 mm^2 area at the center. In addition, 12 individual pressure cells with a piston diameter of 12.7 mm were spaced in a pattern over an approximate area of 400 × 400 mm^2. The ice contact faces was shaped as pyramids with a slope of 1 : 3 and an initial contact area of either 100 × 100 mm^2 or 400 × 400 mm^2.

3.4.2 Results and Discussion

Test results of 1989 program were discussed in Frederking et al. (1990a, b). Both large scale and local crushing under the indenter face typically accompanied the indentation tests. Low speed tests allowed sufficient time for creep deformation and microcracks to extend into the ice, and the total load versus time curves were relatively smooth, while high speed tests appeared to produce localized failure near the indenter and dynamic ice forces on the indenter were recorded. Analysis of crushed layer profiles after the indentation tests showed that the layer thickness was irregular. The thickness of the

crushed layer was typically about 20 mm to 50 mm. There was a clear boundary between the parent ice and crushed ice. For the low speed tests, the ice under the indenter was partly damaged with short cracks and the interface was smooth. These observations can also be applied to the 1990 test program.

In the present work, attention is focused on two flat indentation tests, No. 6 and No. 7 tests (NRC06 and NRC07) of 1989 program. The load-time results of the two tests are shown in Figure 3.26a, b. The loading rate for test NRC06 was about 20 mm/s. The indenter came in contact with the ice at point A and the system stopped at point C. The loading rate for test NRC07 was 68 mm/s.

Figure 3.26 shows regular load oscillations. The slower test, NRC06 has lower peak loads than that of faster test, NRC07, especially the first peak load (first oscillation) of test NRC07 is about 3 MN, much high than that of test NRC06. This shows the typical ice behaviour that, under low loading rates it is more like a ductile material than a brittle one. Under high loading rates, it will fail mostly by fracturing in a much shorter time and less creep deformation, therefore much high peak loads.

From the pressure measurements, the maximum pressures were recorded at the center of the indenter and the average pressures were in the range of 5 MPa to 20 MPa. Around the edge of the interface, there is less confining pressure and higher shear stress, so the ice has become more damaged and the crushed layer is thicker. Near the center of the interface, recrystallization and possible pressure melting has also been reported during indentation tests (Frederking et al., 1990, Gagnon and Sinha, 1991), which means that friction between the indenter and the ice may be small.

3.5 Ice sheet Indentation Experiments

A series of experiments was carried out by Memorial University and the Institute for Marine Dynamics, NRC in 1989 (Finn, 1991 and McKenna et. al., 1991). Freshwater ice sheets were indented with a variety of indentation speeds, ice thicknesses and indenter angle, using vertical and downward sloping surfaces. The widths of all indenters were 120 mm. Nominal ice thicknesses were 30 mm, 40 mm and 50 mm. Indentation speeds (10 mm/s to 400mm/s) covered a range of ice behaviour, from essentially pure crushing to situations where both flexural failure and crushing took place. Fracture splitting due to the formation of radial and circumferential cracks were also evidence of many tests. Axial forces were measured in the vertical and in two horizontal directions, detailed video imaging of the zone around the indenter was performed, ice piece size distributions were measured and detailed thin sections of the damaged zone were analyzed. The ice was observed to be damaged and subsequently cleared out from the face of indenter and, particularly at the slower speeds and for the sloping indenters, flexural failures were also present and dominated the dynamic forces that were measured.

In this study a vertical indentation test is modelled, using proposed constitutive theory and finite elements to investigate the damage and crushing processes, during ice sheet indentation. The test speed is 50 mm/s, indenter width = 120 mm and the ice thickness = 35.6 mm. The test result of force vs time trace is shown partially in Figure 3.27.

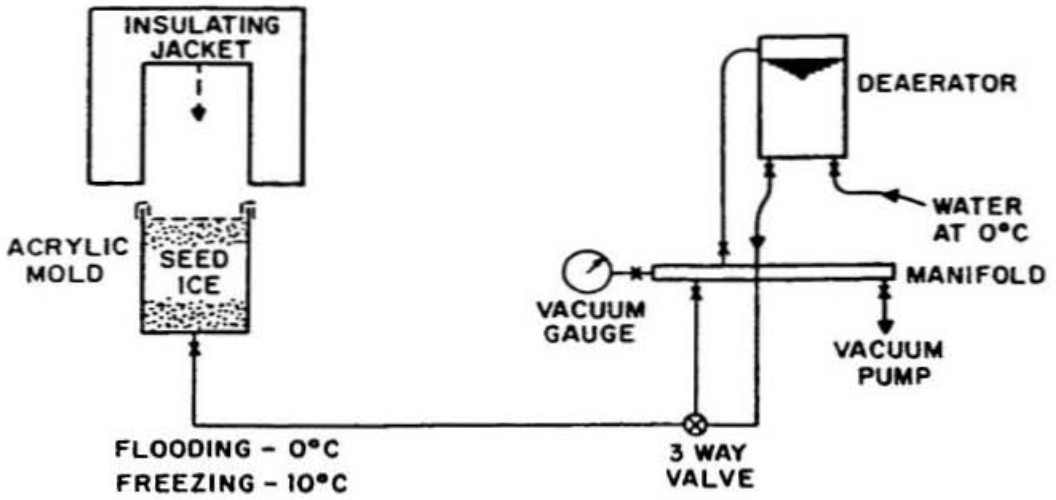

Figure 3.1: Equipment and procedure, laboratory prepared granular ice.

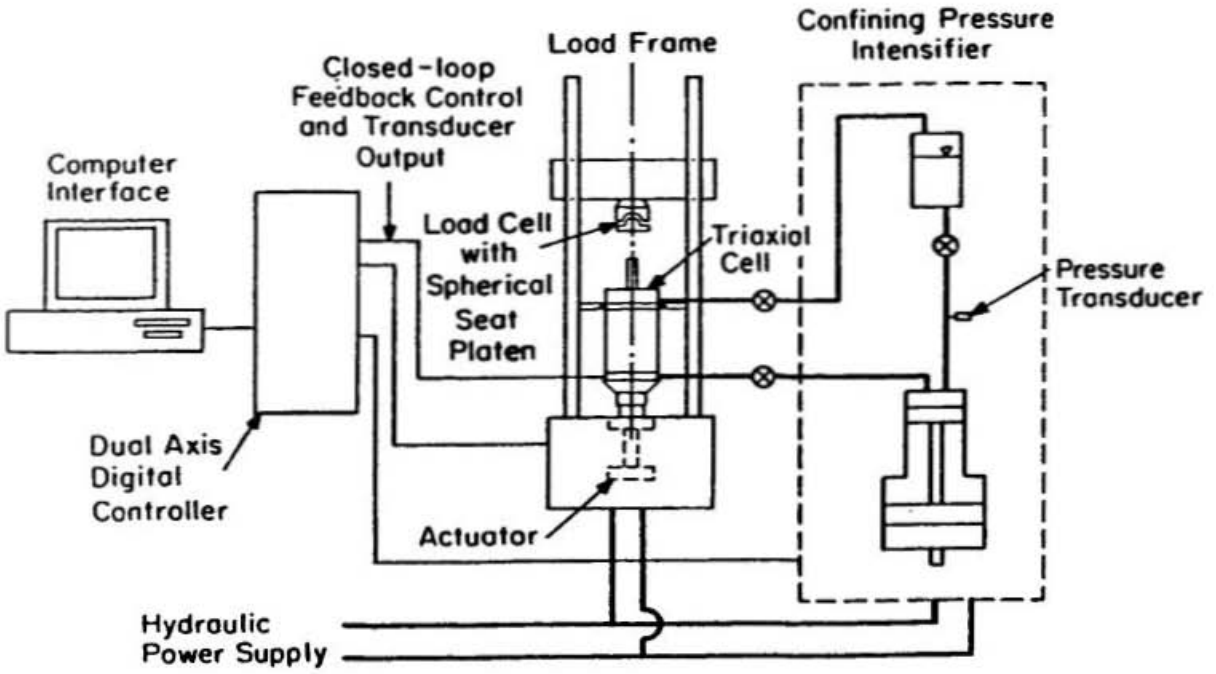

Figure 3.2: Test apparatus, MTS dual axis Teststar system with SBEL triaxial cell.

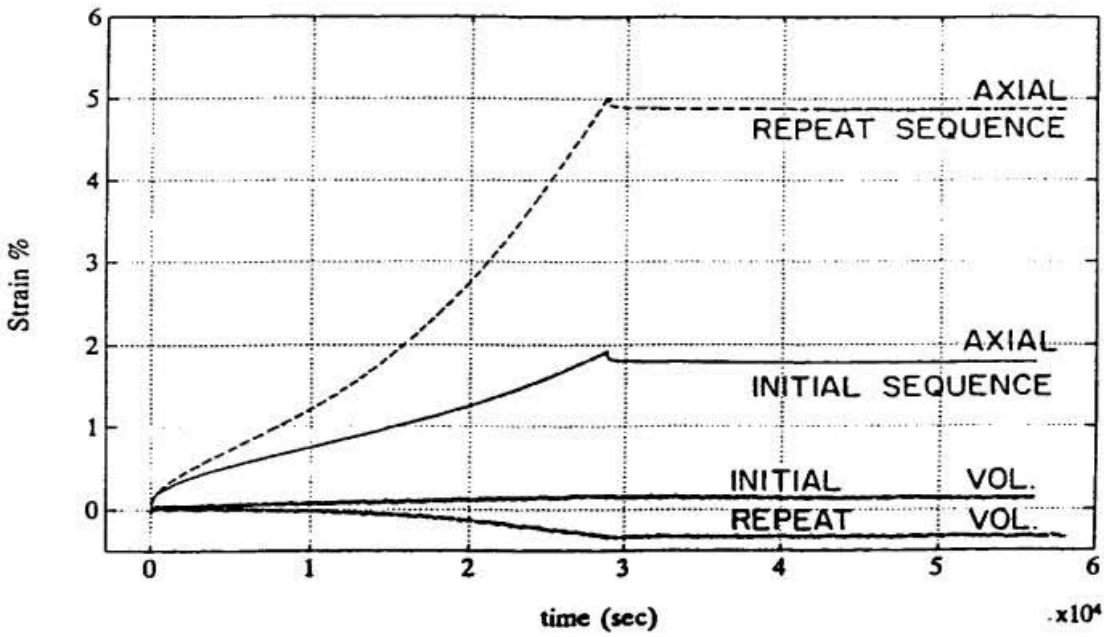

Figure 3.3: Axial and volumetric strain of initial and repeat 8 hour 2 MPa pulse load, 8 hour relaxation sequence under 20 MPa triaxial confinement.

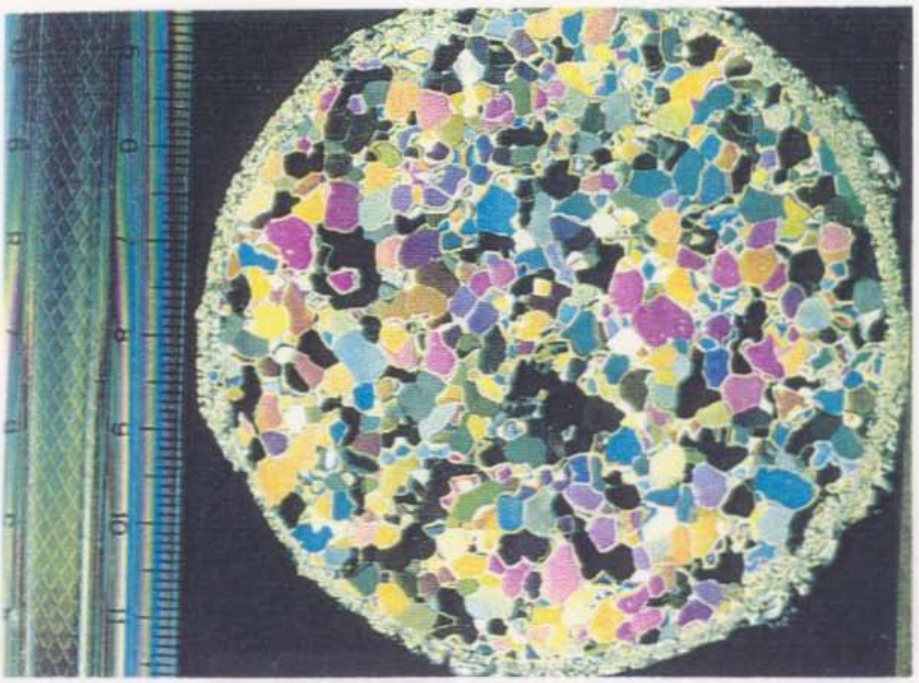

(a)

(b)

Figure 3.4: Thin sections (a) prior to testing and (b) after extended creep test.

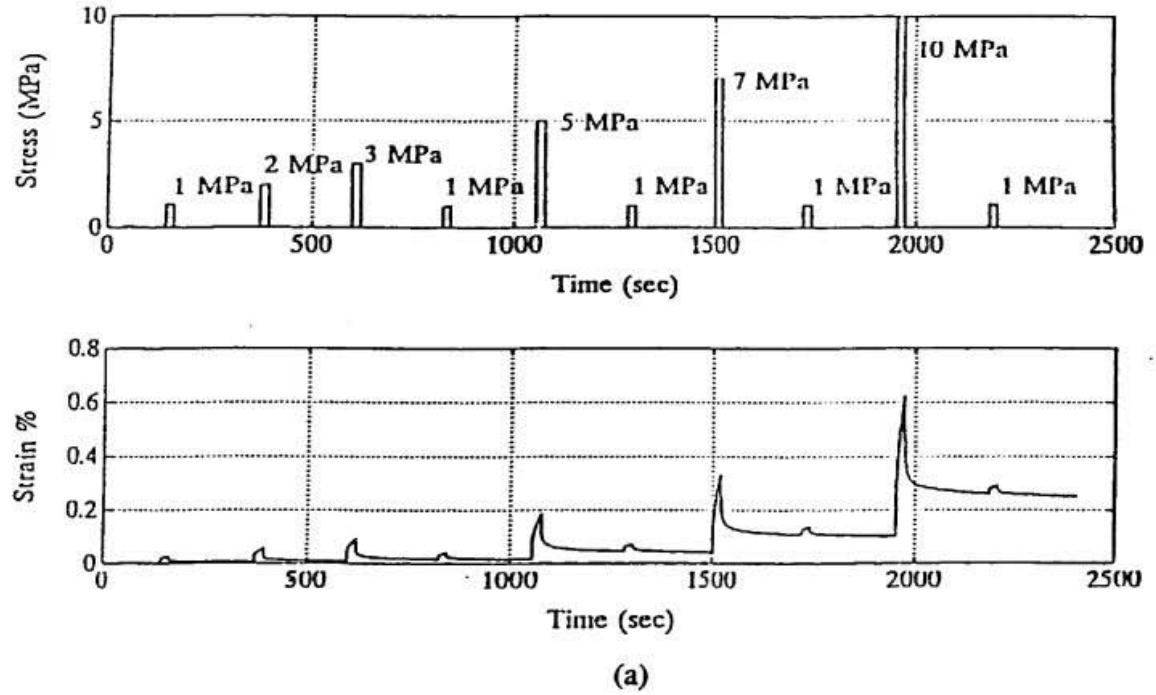

(a)

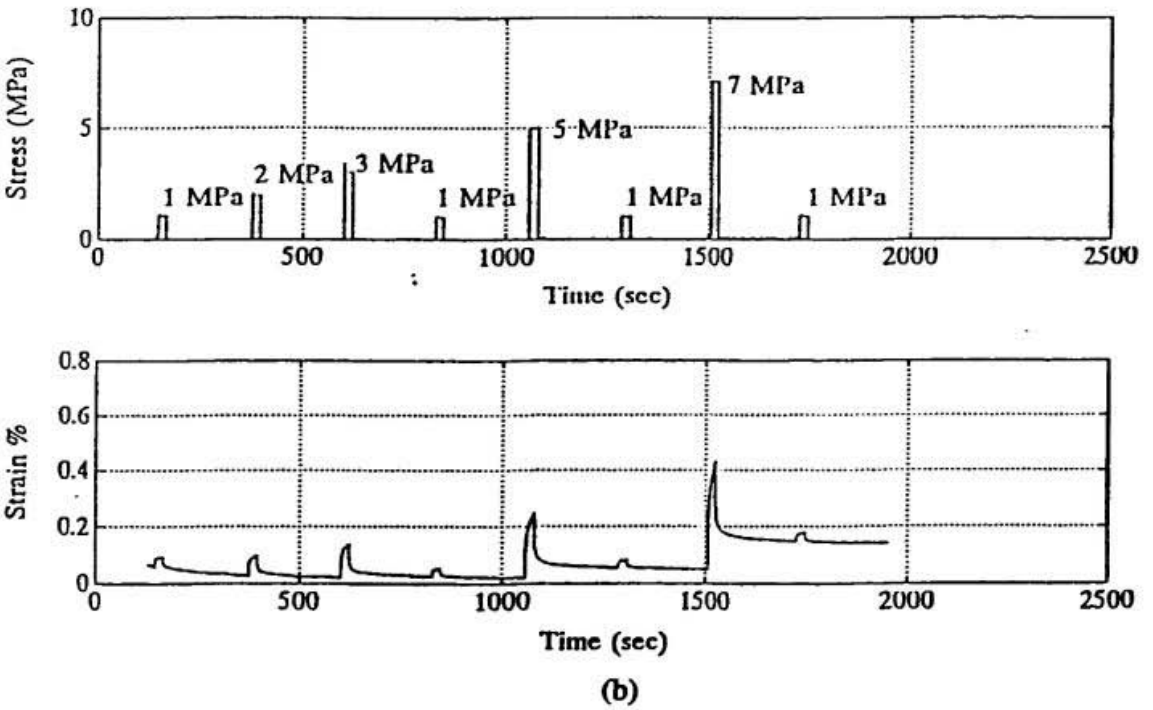

(b)

Figure 3.5: Applied stress history and strain responses of: (a) intact ice (b) damaged ice, for creep tests.

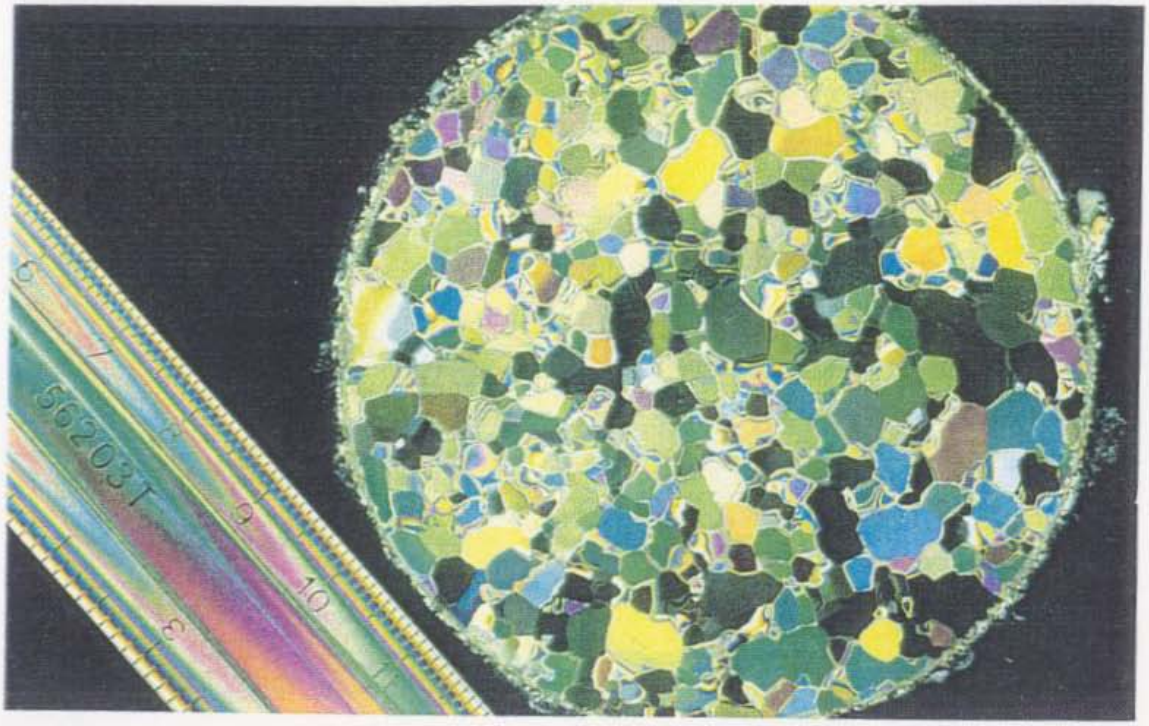

(a)

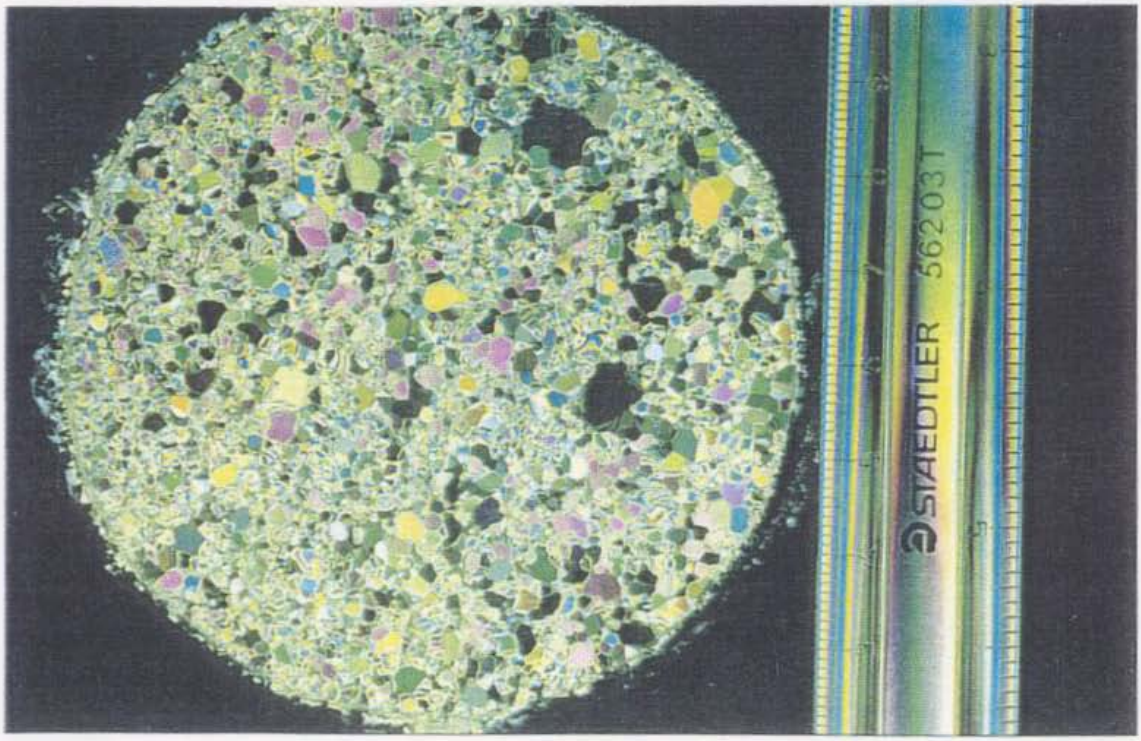

(b)

Figure 3.6: Thin section photos of intact and damaged ice samples: (a) intact ice; (b) damaged ice.

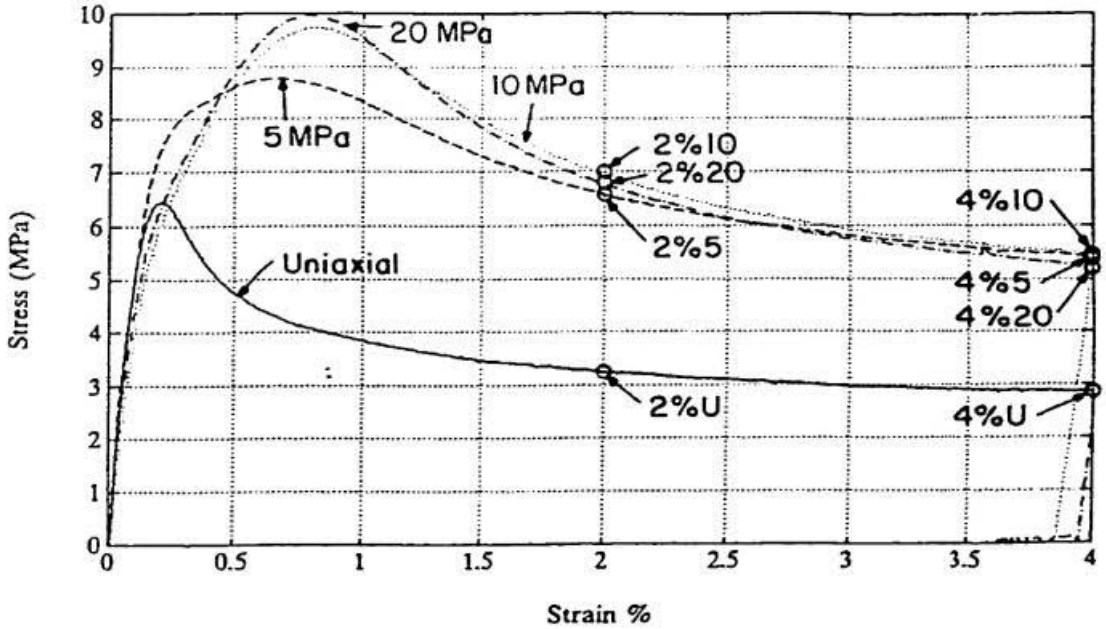

Figure 3.7: Damage states created by compressing undamaged intact samples at a strain rate of 10^{-4} sec^{-1} to a total strain of 2 or 4%.

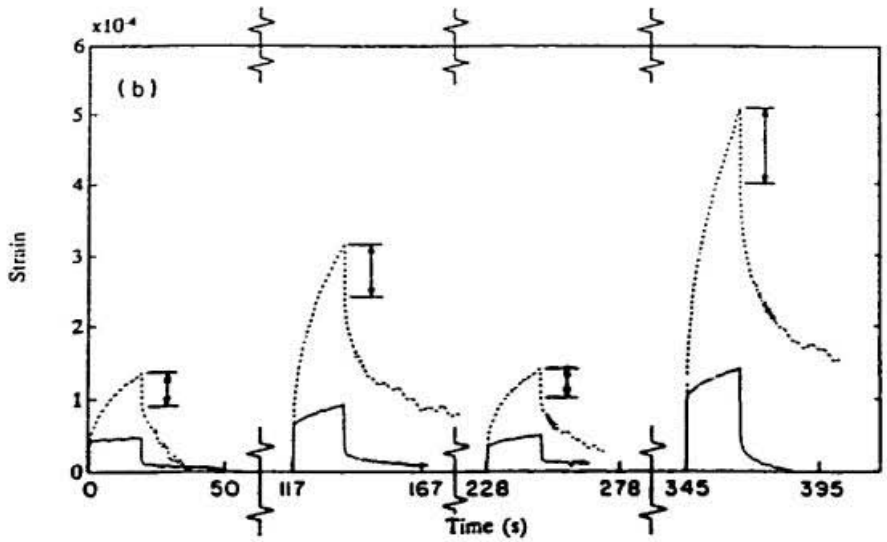

Figure 3.8: Creep response of intact(——) and 2% uniaxially damaged ice (.....) for 20 sec. pulse load sequence of .25/.5/.25/.75 MPa under uniaxial conditions (Jordaan, 1992).

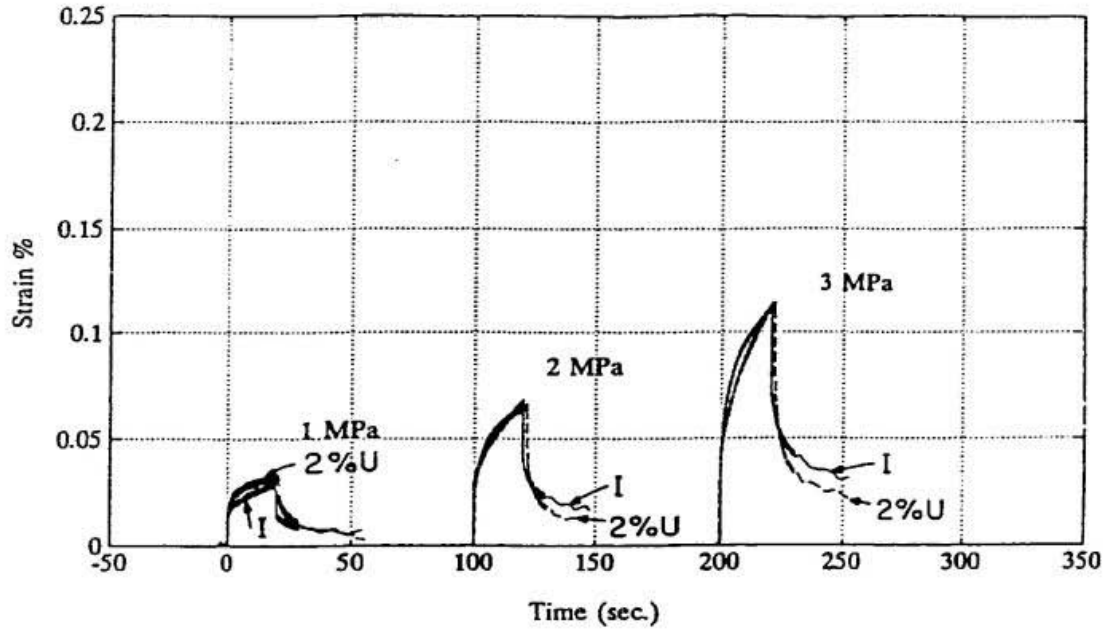

Figure 3.9: Creep response of intact (I) and 2% uniaxially predamaged ice (2% U) under 5 MPa triaxial confinement for 1,2, and 3 MPa 20 sec. pulse loads.

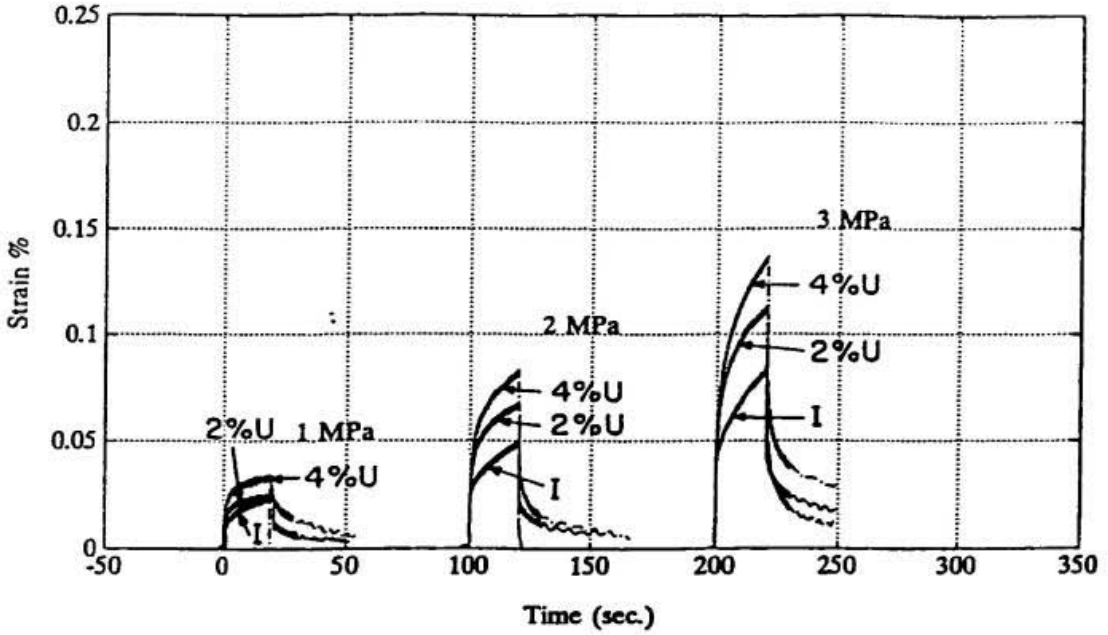

Figure 3.10: Creep Response of intact (I) and 2% and 4% uniaxially damaged ice (2%U, 4%U) under 10 MPa triaxial confinement for 1,2 and 3 MPa 20 sec. pulse loads.

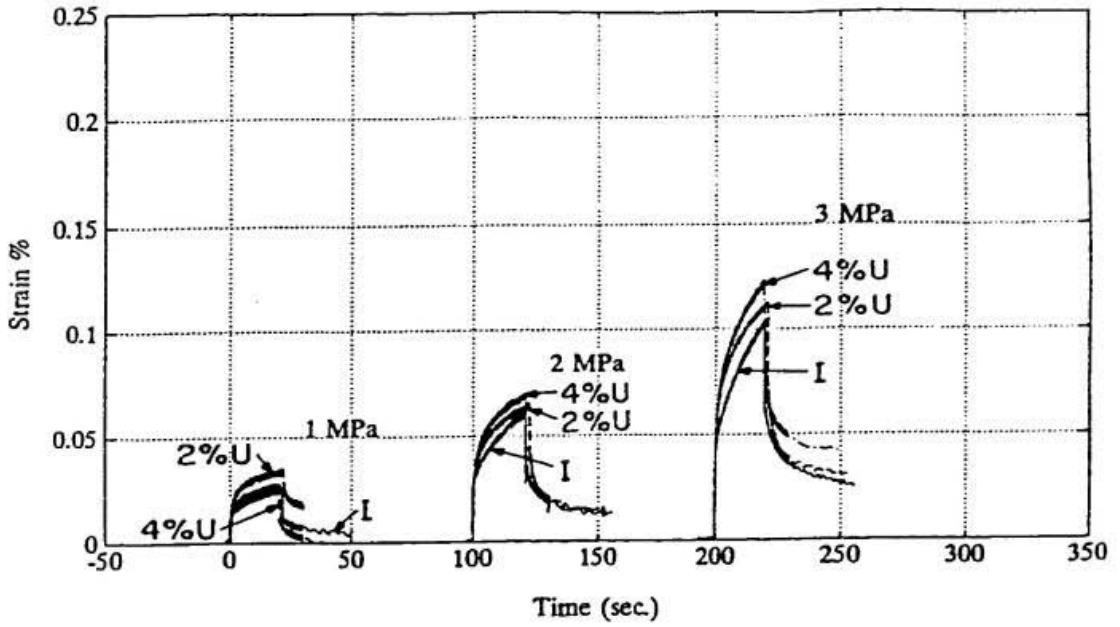

Figure 3.11: Creep Response of intact (I) and 2% and 4% uniaxially predamaged ice (2%U, 4%U) under 20 MPa triaxial confinement for 1,2 and 3 MPa 20 sec. pulse loads.

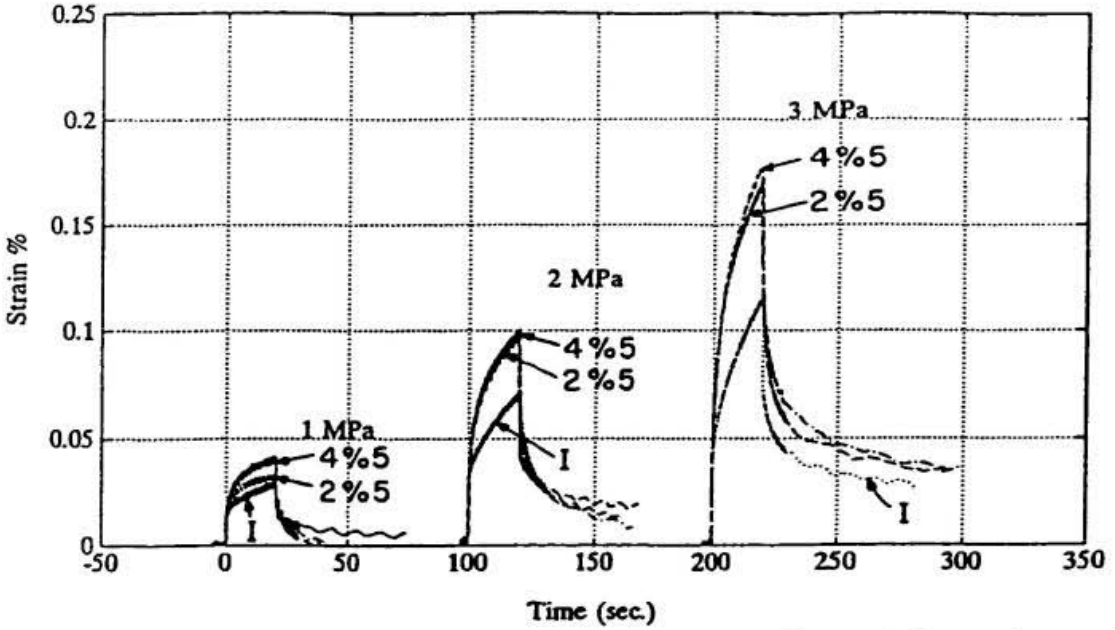

Figure 3.12: Creep response of intact (I) and 2% and 4% triaxially damaged ice (2%5 and 4%5) under 5 MPa triaxial confinement for 1,2 and 3 MPa 20 sec. pulse loads.

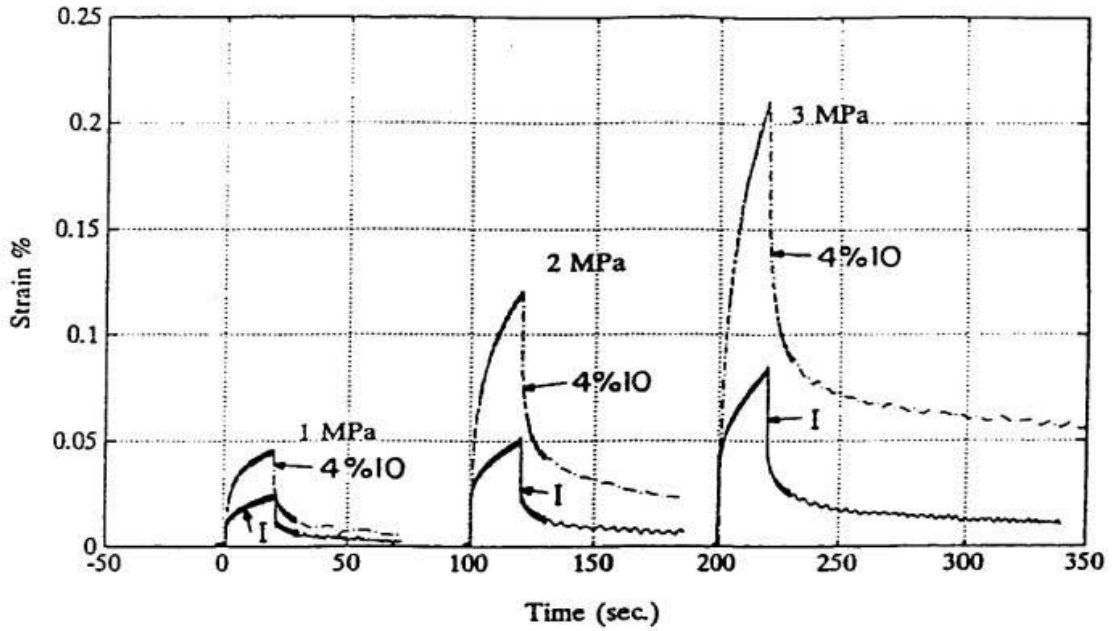

Figure 3.13: Creep response of intact (I) and 4% triaxially predamaged ice (4%10) under 10 MPa triaxial confinement for 1,2 and 3 MPa 20 sec. pulse loads.

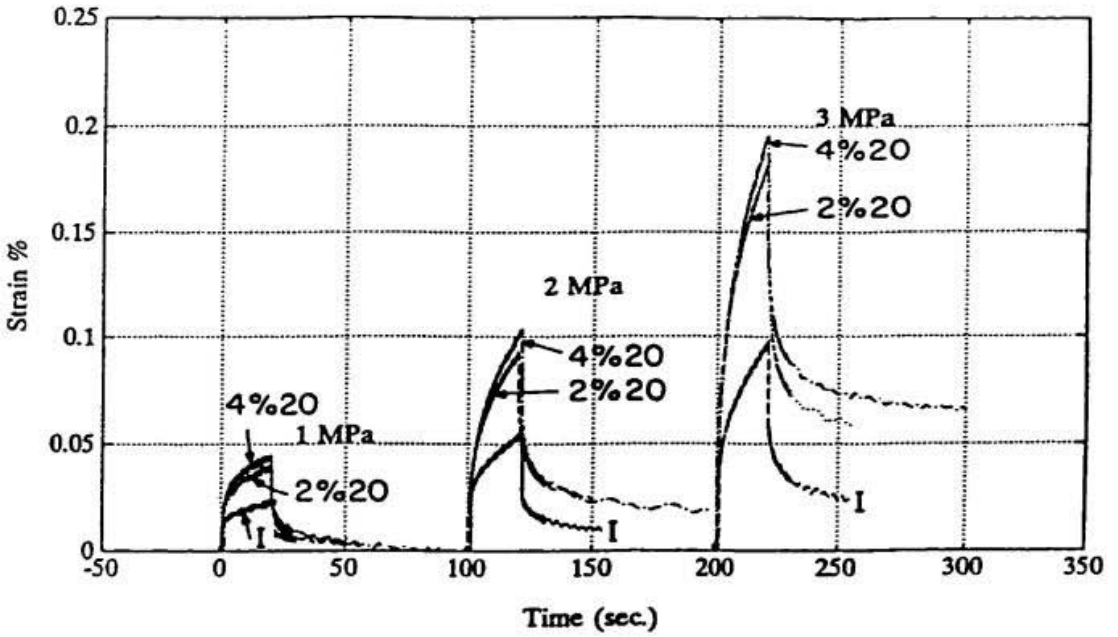

Figure 3.14: Creep response of intact (I) and 2% and 4% triaxially damaged ice (2%20 and 4%20) under 20 MPa triaxial confinement for 1,2 and 3 MPa 20 sec. pulse loads.

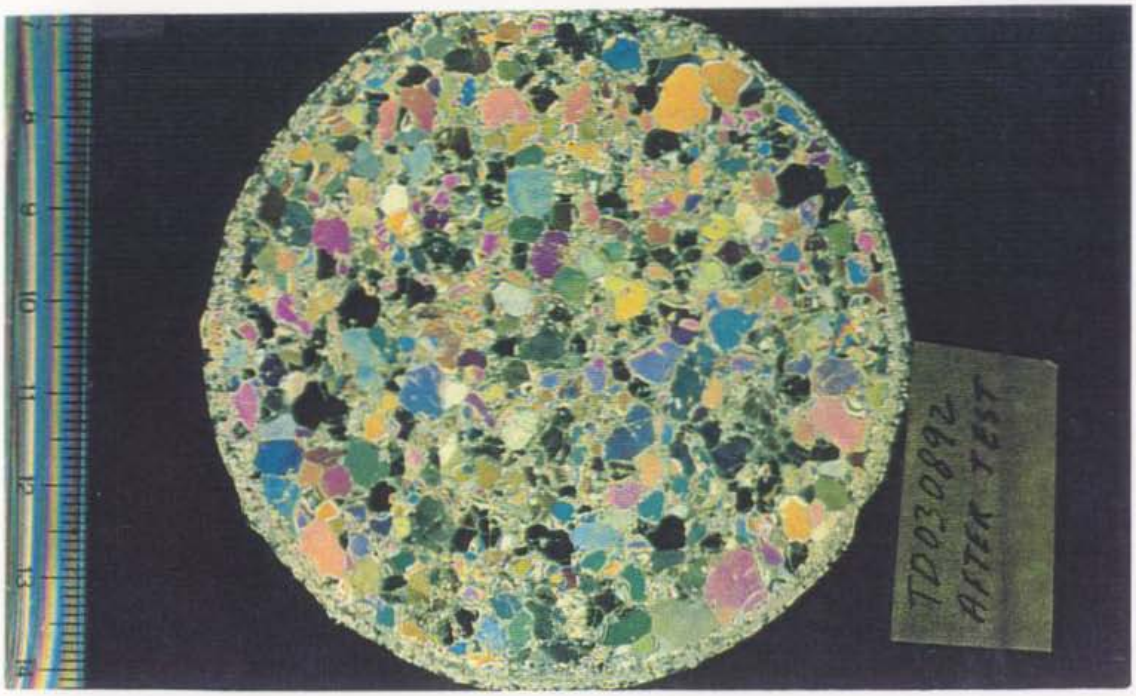

(a)

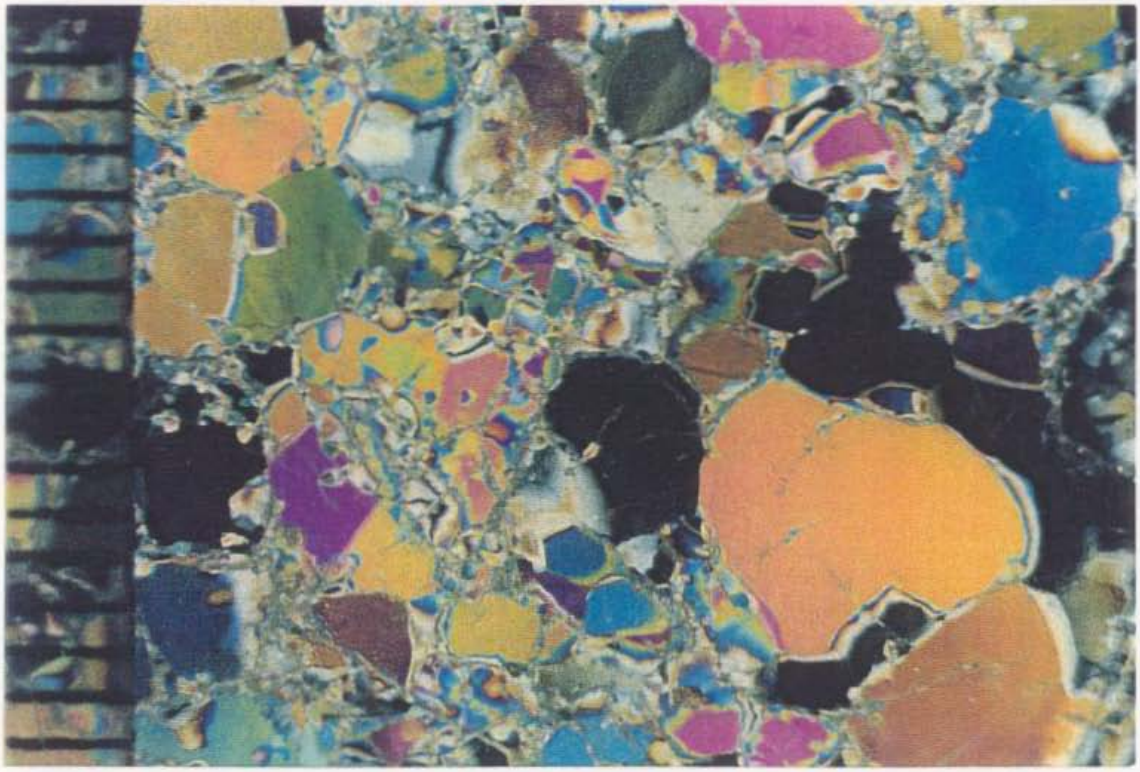

(b)

Figure 3.15: (a) Thin section of a specimen after 2% uniaxial damage (2%U) and a 1,2,3,1 MPa 20 sec. pulse load sequence under triaxial confinement of 10 MPa. (b) Magnification.

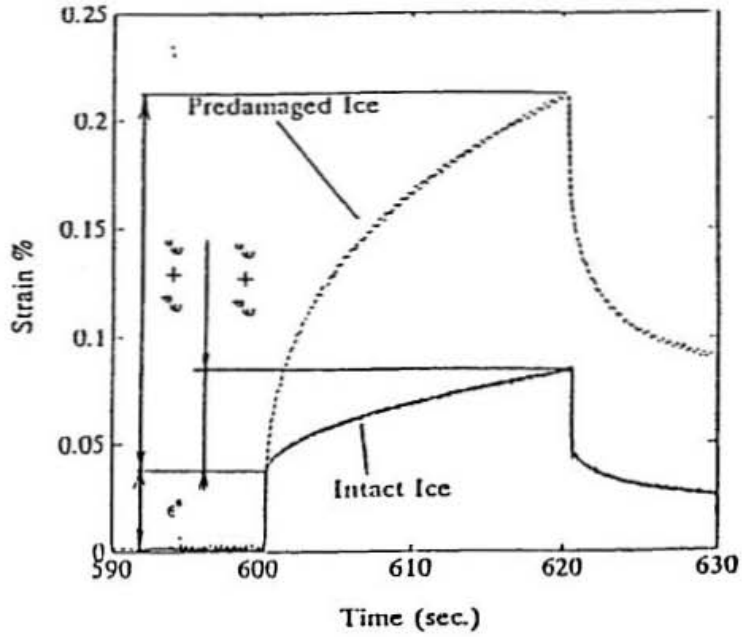

Figure 3.16: Strain response of intact and predamaged ice under a stress difference of 3 MPa and same confinement of 10 MPa.

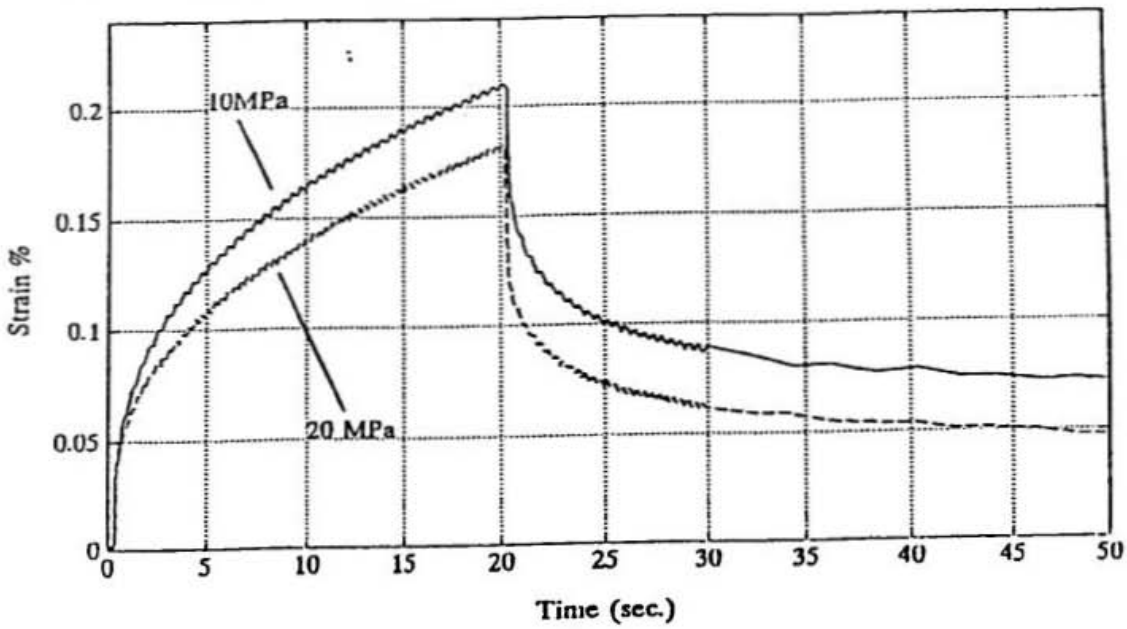

Figure 3.17: Strain response of damaged ice under same stress difference of 3 MPa but with different confinement of 10 and 20 MPa.

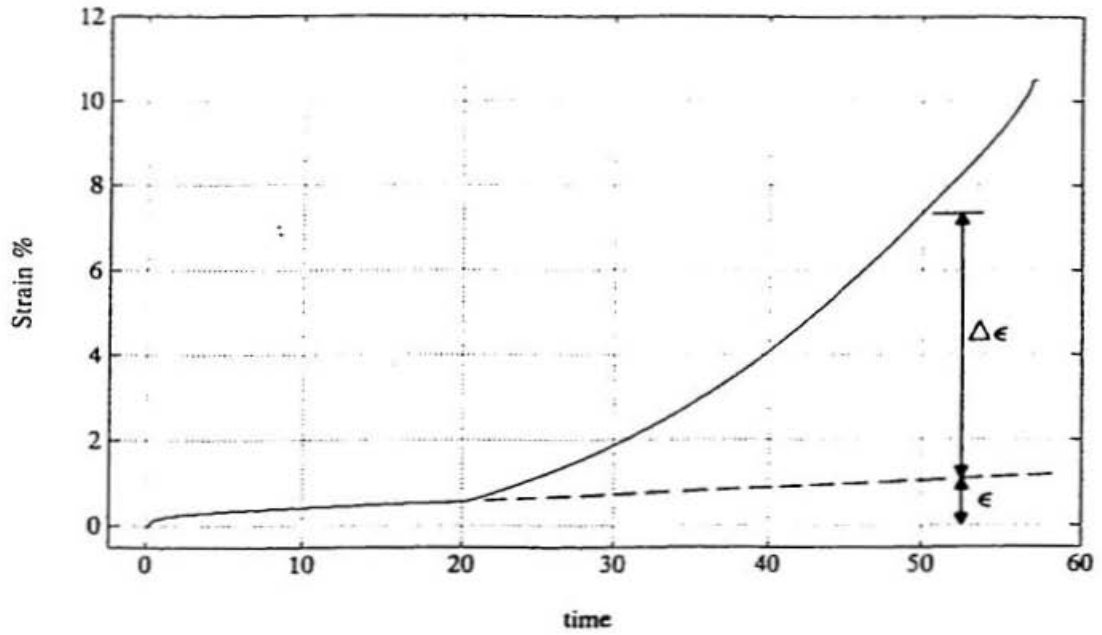

Figure 3.18: Strain-time, 2% triaxial predamage (2%10), 7 MPa load pulse, triaxial confining pressure 10 MPa 0 to 20 sec. 5 MPa 20 sec. to 60 sec.

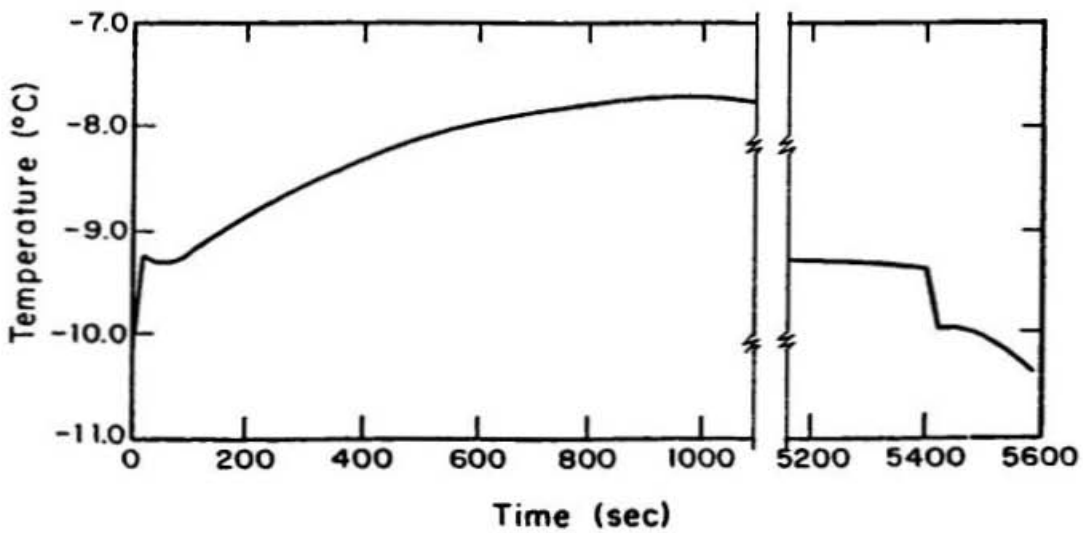

Figure 3.19: Temperature at sample centre upon pressurization to a triaxial confining pressure of 40 MPa.

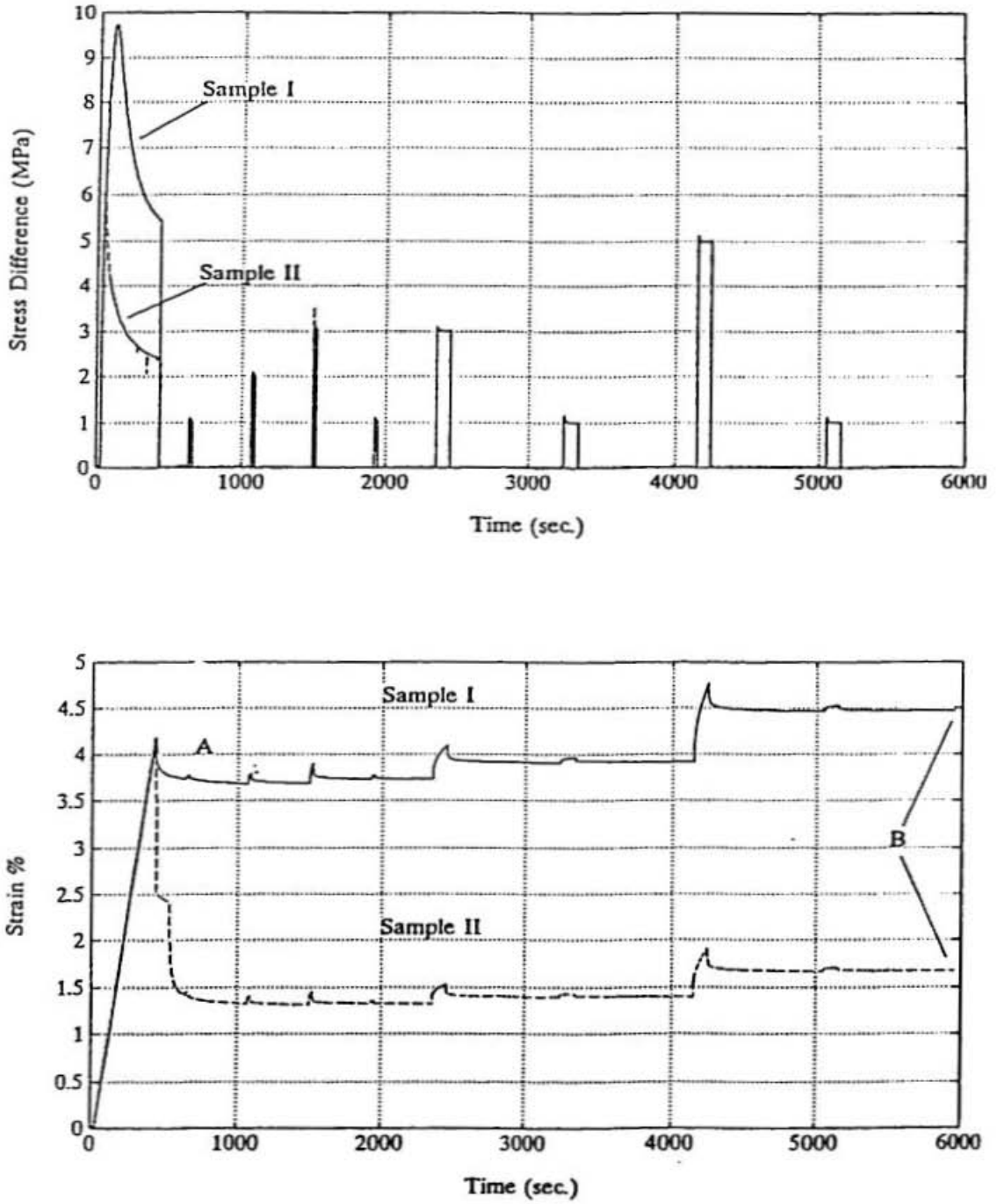

Figure 3.20: Comparison of creep response of uniaxially and triaxially damaged ice under 10 MPa triaxial confinement.

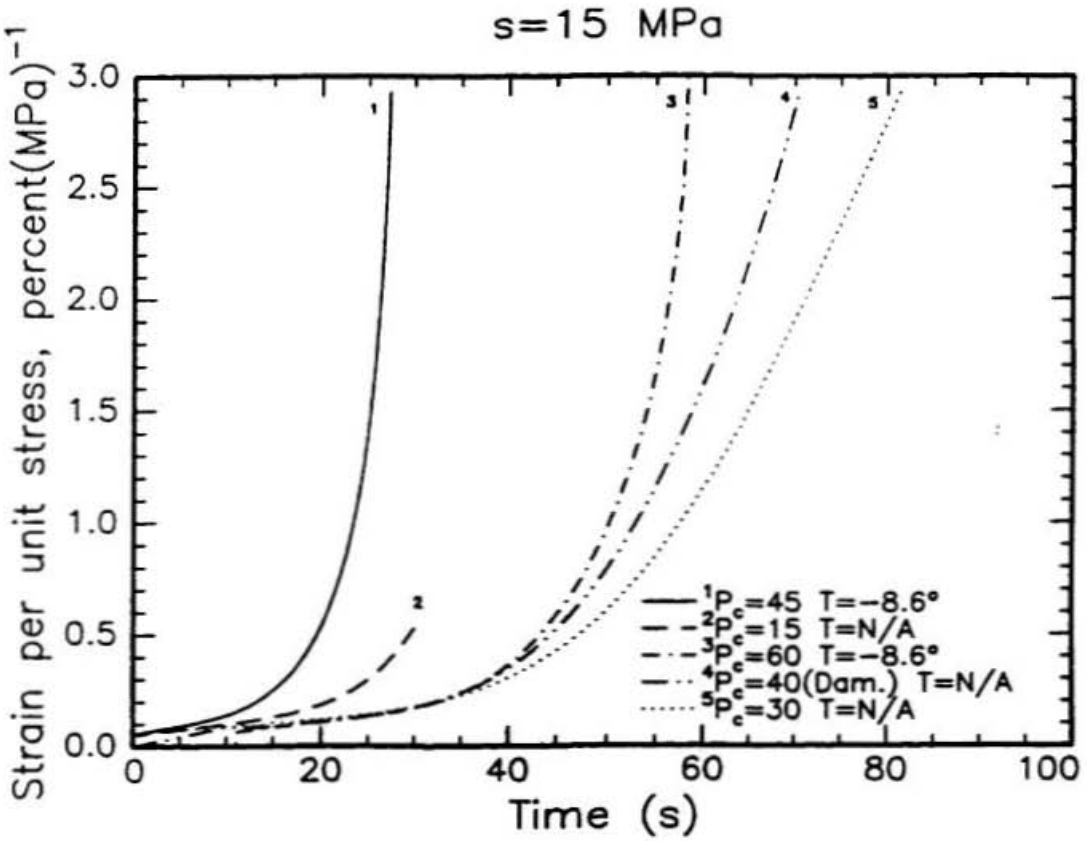

Figure 3.21: Creep tests under 15 MPa deviatoric stress and various confining pressures up to 60 MPa. Temperature in °C (after Meglis et al., 1997).

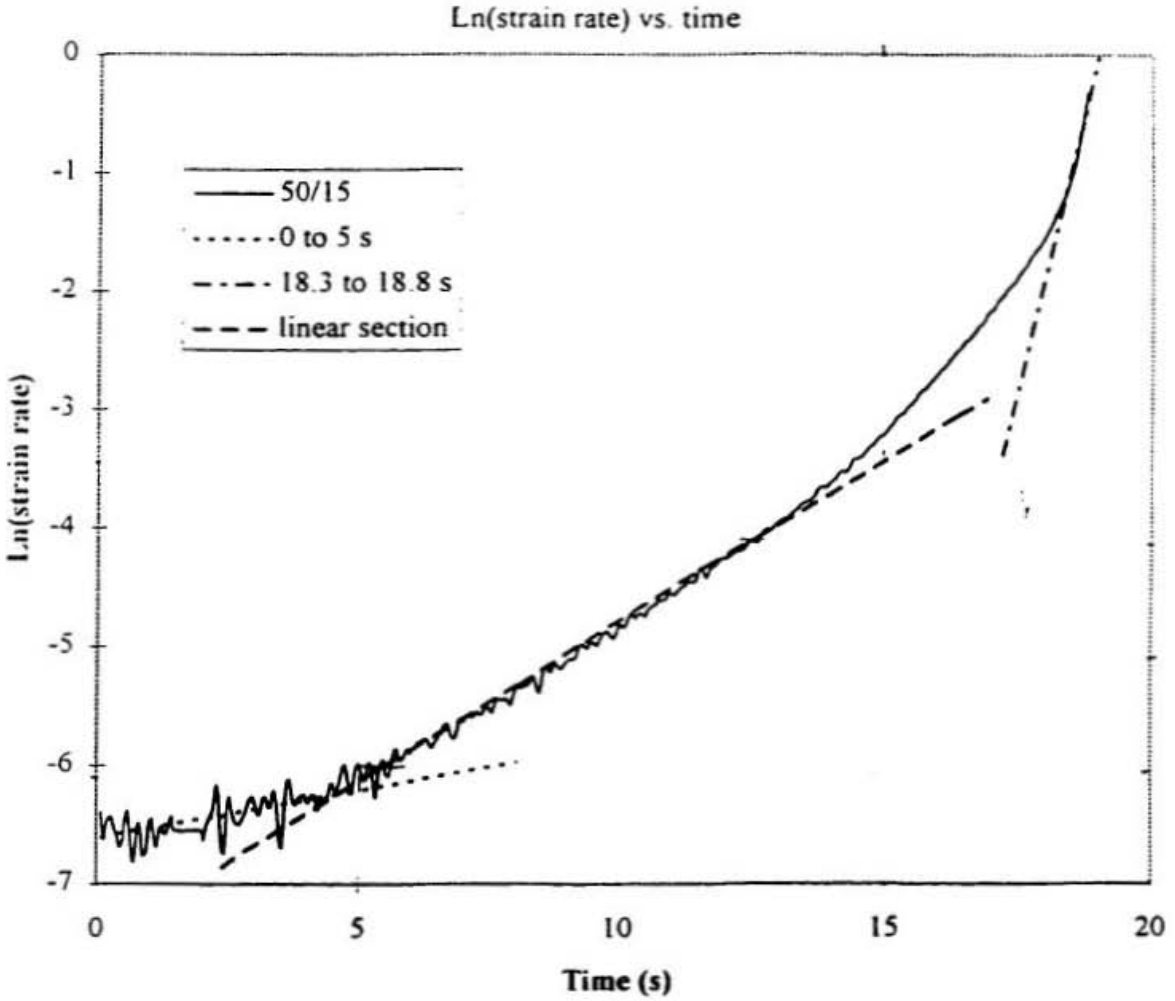

Figure 3.22: Test curve of creep strain rate in logarithm scale versus time, and the linearization of the curve into three portions: minimum, linear and maximum portion, respectively (after Meglis et al., 1997).

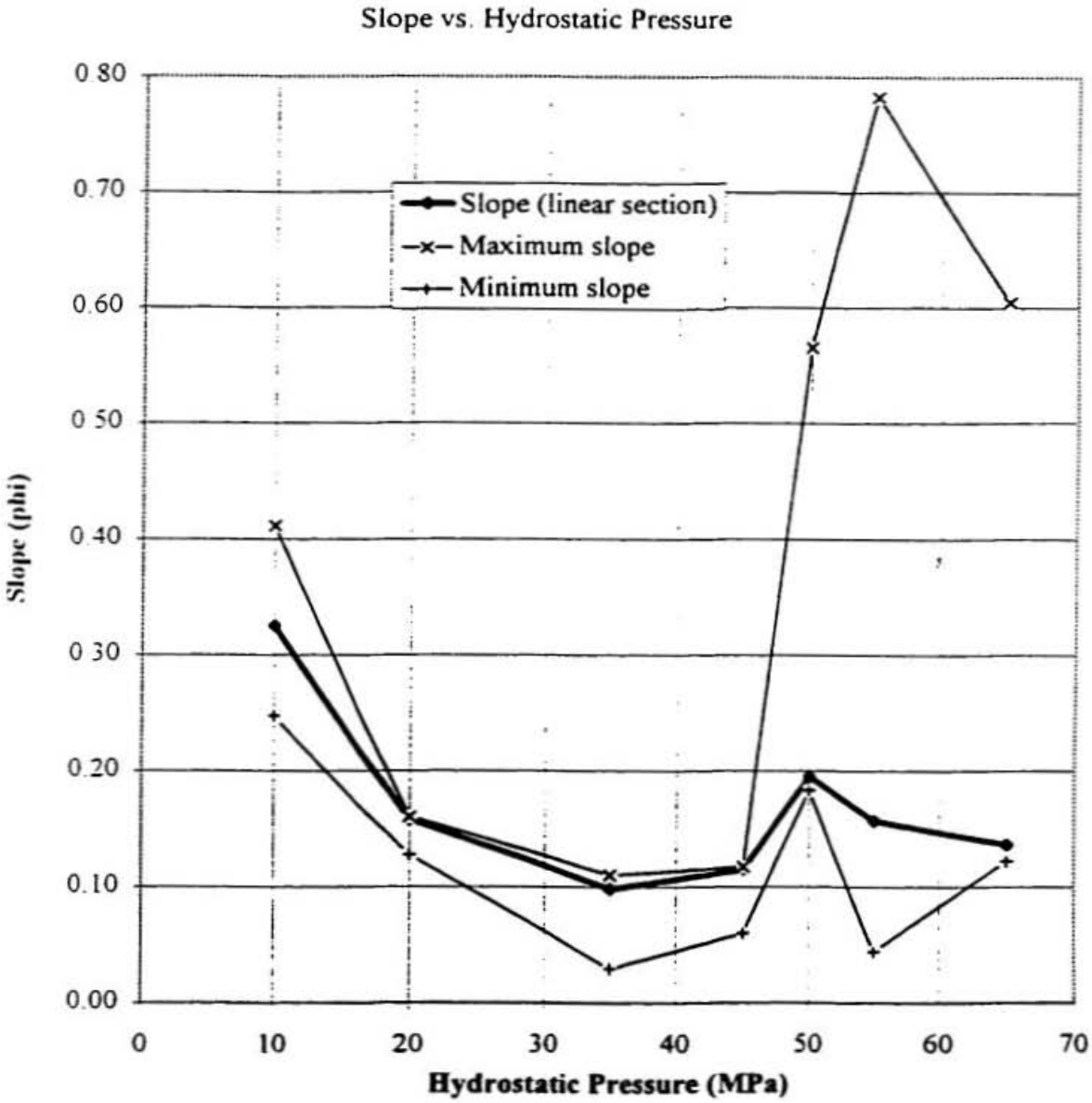

Figure 3.23: The relationship of creep strain rate and hydrostatic pressure. Three strain rates of the minimum, linear and maximum portion are plotted (after Meglis et al., 1997).

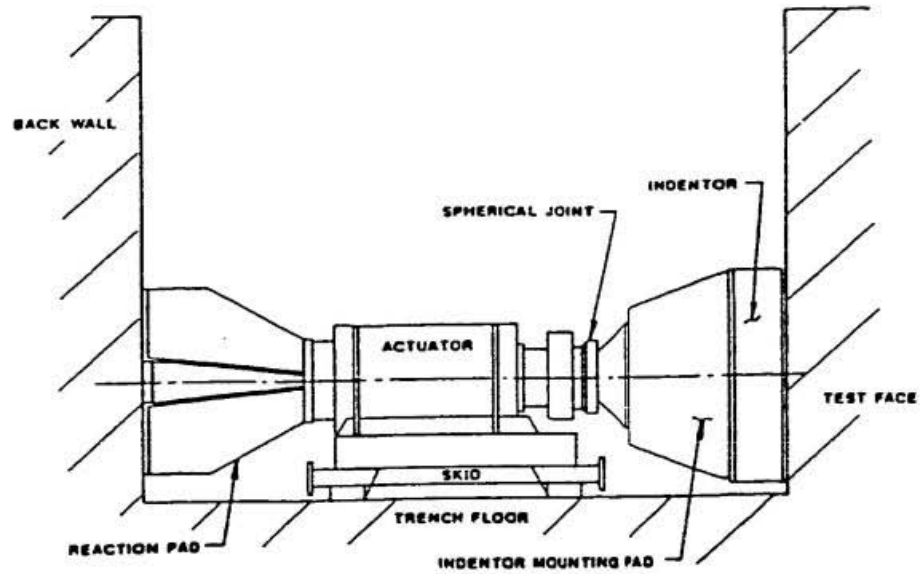

(a)

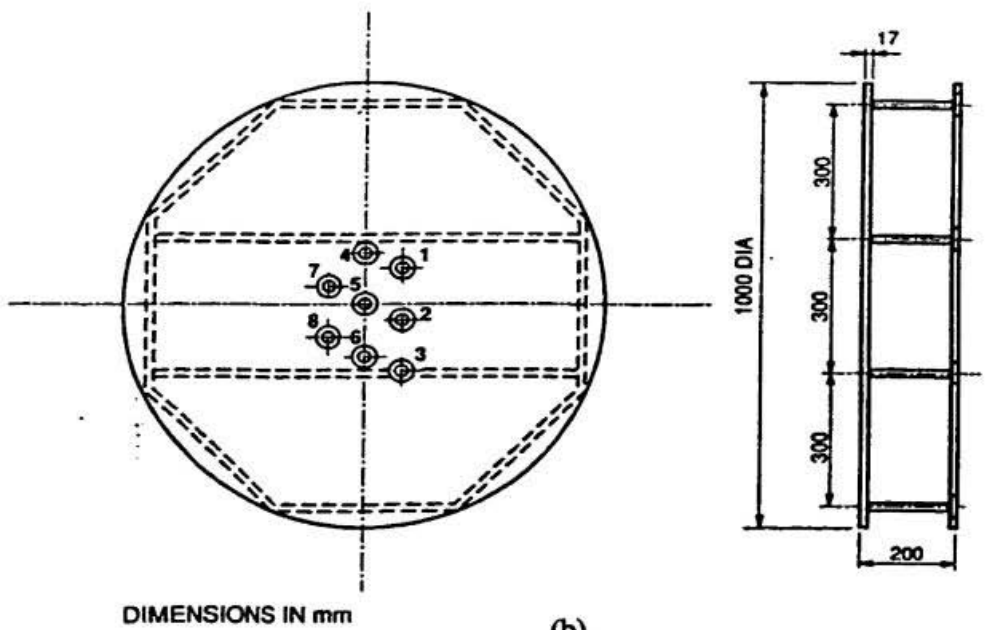

(b)

Figure 3.24: Schematic of: (a) the actuator indenter system; (b) locations of ice pressure cells. (Frederking et al., 1990a).

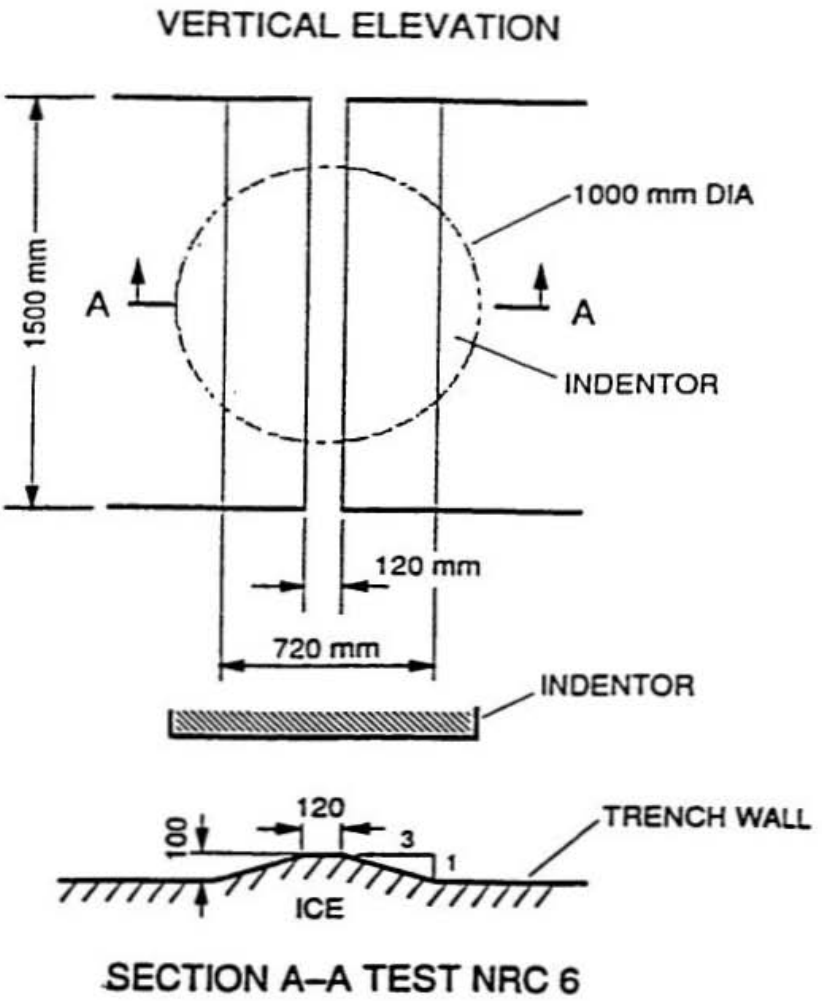

Figure 3.25: Schematic of truncated wedge ice face for Tests NRC06 and NRC07 (Frederking et al., 1990a).

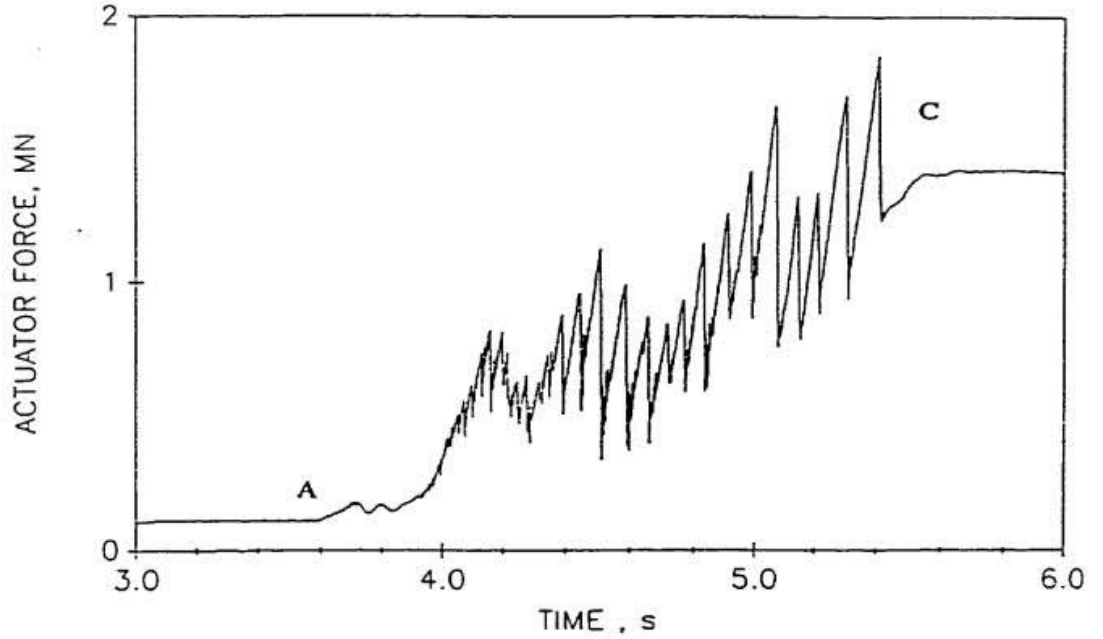

(a)

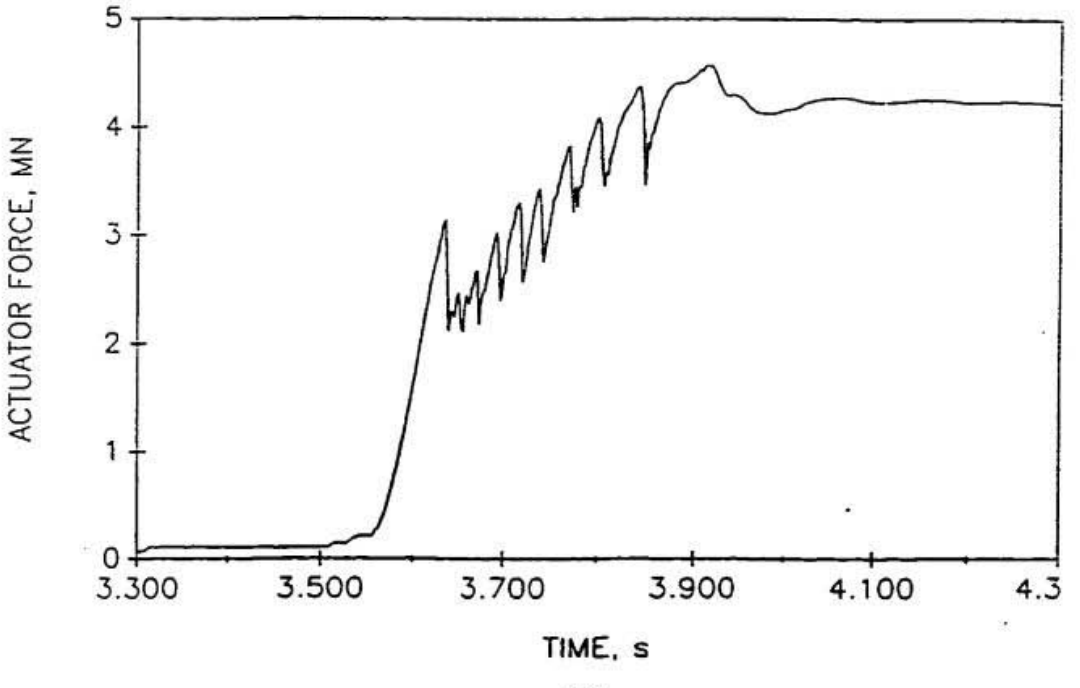

(b)

Figure 3.26: Load time record of: (a) test NRC06, with average indentation rate ≈ 20 mm/s; (b) test NRC07 with loading speed of 68mm/s (Frederking et al., 1990a).

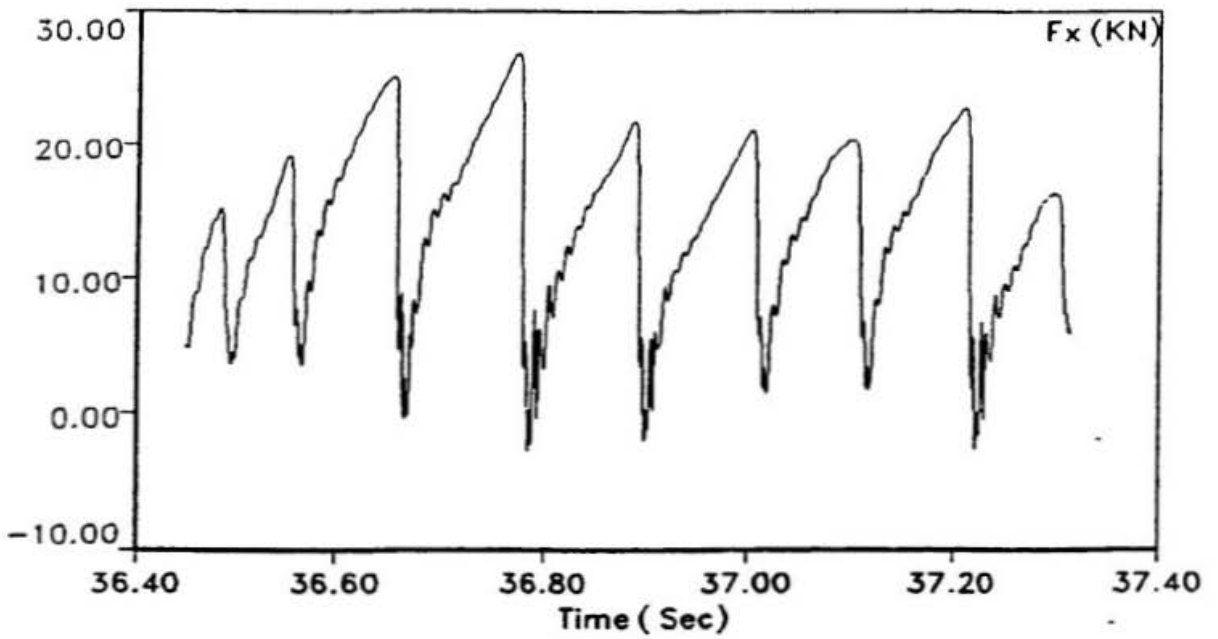

Figure 3.27: Detail from vertical indentation experiment force vs time trace (Fresh6_HI_Run3: ice thickness = 35.6 mm, indentor width = 120 mm, speed = 50 mm/s).

Chapter 4

Constitutive Modelling

In this chapter a three dimensional constitutive model is presented for brittle, viscoelastic materials, based on damage and fracture mechanics, viscoelasticity including Schapery's theory, as well as the broad-spectrum approach. Special attention has been given to the deformation processes of ice under compressive stress states. This model has also been applied to ice indentation problems in the following chapters. These problems are encountered in the determination of ice forces on structures.

4.1 A Mechanical Model

As discussed in the previous chapters, the deformation of brittle, viscoelastic solids, such as ice and rock, is a complex process, especially when cracking and other structural activities take place. The properties of the solid are strongly influenced by the presence of damage. A idealized mechanical model, called Burgers' model (see also Figure 2.2), is practical and applicable to many viscoelastic solids, such as rock, cement, ice and metal. It consists of a combination of a Maxwell and a Kelvin unit, with a nonlinear dashpot in each unit (see also Jordaan and McKenna, 1988b).

A great deal of research work has been done to model the primary and secondary creep in ice and other materials. A Kelvin unit with a power-law stress-dependent

creep compliance, as proposed by Jordaan and McKenna (1988b, 1989), Jordaan et al., (1990a, b), has been shown to be appropriate for describing the initial primary creep under rapid loading. This also provides an expedient computational solution for the primary creep strain. With this model, at the beginning of each time increment, the program only needs to read the stresses, strains and other model parameters which are stored as state variables from the previous state, instead of requiring access to the whole storage of past history. All of the state variables will be updated at the end of each increment.

In the case of uniaxial stress, total axial strain is given in terms of three components, i.e.

$$\epsilon_1 = \epsilon_1^e + \epsilon_1^d + \epsilon_1^c \tag{4.1}$$

where the elastic component is given by

$$\epsilon_1^e = \sigma_1 / E, \tag{4.2}$$

where σ_1 is the axial stress and E is the elastic modulus.

The delayed elastic and secondary creep strain rates are defined as

$$\dot{\epsilon}_1^d = \sigma_1 / \mu_{k1}, \text{ and} \tag{4.3}$$

$$\dot{\epsilon}_1^c = \sigma_1 / \mu_{m1} \tag{4.4}$$

where μ_{k1} and μ_{m1} are the viscosity coefficients of the Kelvin unit and Maxwell unit, respectively. Assuming that the strains of the dashpots in both units follow the power-law relation with stress, the delayed elastic strain rate is given as

$$\dot{\epsilon_1}^d = \dot{\epsilon}_0^d (\sigma_1^d / \sigma_0)^n \tag{4.5}$$

where $\dot{\epsilon}_0^d$ is a creep reference rate; $\sigma_0 = 1$ MPa, is a constant with unit stress; and σ_1^d is the stress in the dashpot in Kelvin unit, which is calculated by

$$\sigma_1^d = \sigma_1 - E_k \epsilon_1^d \tag{4.6}$$

where E_k is elastic stiffness in the Kelvin unit. The accumulated delayed elastic strain ϵ_1^d is given by

$$\epsilon_1^d = \int_0^t \dot{\epsilon}_1^d \, dt. \tag{4.7}$$

Comparing Eq. (4.3) with Eq. (4.5), it is found that

$$\mu_{k1} = (\sigma_1/\dot{\epsilon}_0^d)(\sigma_0/\sigma_1^d)^n. \tag{4.8}$$

Similarly, the secondary creep strain rate is also defined by the power-law as:

$$\dot{\epsilon_1}^c = \dot{\epsilon}_0^c(\sigma_1/\sigma_0)^m \tag{4.9}$$

where m is a constant; $\dot{\epsilon}_0^c$ is a creep parameter, and the viscosity coefficient of Maxwell unit is derived as

$$\mu_{m1} = (\sigma_1/\dot{\epsilon}_0^c)(\sigma_0/\sigma_1)^m. \tag{4.10}$$

For multi-axial stress state, the deformation of a solid is defined as:

$$\epsilon_{ij} = \epsilon_{ij}^e + \epsilon_{ij}^d + \epsilon_{ij}^c \tag{4.11}$$

If the elastic properties of the material are assumed to be isotropic, the elastic strain components ϵ_{ij}^e can be presented by

$$\epsilon_{ij}^e = -\frac{\nu}{E}\sigma_{kk}\delta_{ij} + \frac{1+\nu}{E}\sigma_{ij} \tag{4.12}$$

where ν is Poisson's ratio and δ_{ij} is the delta function.

Both delayed elastic strain and secondary creep strain can be expressed in terms of a strain deviator component e_{ij} and a volumetric strain component ϵ_v, i.e.

$$\epsilon_{ij}^d = e_{ij}^d + \epsilon_v^d, \text{ and} \tag{4.13}$$

$$\epsilon_{ij}^c = e_{ij}^c + \epsilon_v^c. \tag{4.14}$$

Note that the volumetric strains here are not the results of elastic deformation. Assuming creep deformation to be incompressible, it is the nonlinear portion of volumetric strain, which is probably due to the cracking and some other mechanisms. This will be discussed in detail later.

Based on the discussion in the case of uniaxial loading, the deviatoric strain rates of delayed elastic and secondary creep components are assumed to be proportional to the deviatoric stresses and are defined in the forms similar to Eq. (4.3) and Eq. (4.4)

$$\dot{e}_{ij}^d = \frac{3}{2} s_{ij}/\mu_k, \text{ and} \tag{4.15}$$

$$\dot{e}_{ij}^c = \frac{3}{2} s_{ij}/\mu_m \tag{4.16}$$

where $s_{ij} = \sigma_{ij} - \frac{1}{3}\sigma_{ii}$ is the overall stress deviator. These definitions assume that the creep behaviour of the solid is isotropic, and the viscosity coefficient of shear deformation follows the same law as that in the principal directions.

The viscosity coefficients, μ_{k1} and μ_{m1} defined in Eq. (4.3) and Eq. (4.4) are functions of axial stress. In the case of multi-axial loading, the coefficients, μ_k and μ_m are defined as functions of von Mises stress in the similar ways, by substituting the axial stress component with von Mises stress, i.e.

$$\mu_k = (s/\dot{\epsilon}_0^d)(\sigma_0/s^d)^n, \text{ and} \tag{4.17}$$

$$\mu_m = (s/\dot{\epsilon}_0^c)(\sigma_0/s)^m. \tag{4.18}$$

The definition of von Mises stress is given as

$$s = (\frac{3}{2} s_{ij} s_{ij})^{1/2}. \tag{4.19}$$

The internal stress s^d (the von Mises stress in the dashpot in the Kelvin unit), is calculated by

$$s^d = s - E_k e^d \tag{4.20}$$

where e^d is the equivalent (or effective) delayed elastic strain and is calculated by

$$\begin{aligned} e^d &= \int_0^t \dot{e}^d \, dt \\ &= \int_0^t \dot{\epsilon}_0^d (s^d/\sigma_0)^n \, dt. \end{aligned} \tag{4.21}$$

The definition of equivalent strain is given by

$$e = (\frac{2}{3} e_{ij} e_{ij})^{1/2}. \tag{4.22}$$

Reference can be made to Xiao (1991) for more details on the definition of equivalent strain and its relationship with von Mises stress.

Substituting Eq. (4.17), Eq. (4.20) into Eq. (4.15), and Eq. (4.18) into Eq. (4.16), it is found that

$$\begin{aligned} \dot{e}_{ij}^d &= \frac{3}{2} \dot{\epsilon}_0^d \left(\frac{s^d}{\sigma_0} \right)^n \frac{s_{ij}}{s} \\ &= \frac{3}{2} \dot{\epsilon}_0^d \left(\frac{s - E_k e^d}{\sigma_0} \right)^n \frac{s_{ij}}{s}, \quad \text{and} \end{aligned} \tag{4.23}$$

$$\dot{e}_{ij}^c = \frac{3}{2} \dot{\epsilon}_0^c \left(\frac{s}{\sigma_0} \right)^m \frac{s_{ij}}{s}. \tag{4.24}$$

In the case of uniaxial loading, deviatoric stresses $s_{11} = \frac{2}{3}\sigma_1$, $s_{22} = s_{33} = -\sigma_1/3$ and $s_{ij} = 0, (i \neq j)$, so von Mises stress $s = \sigma_1$, therefore, $s^d = \sigma_1^d$; similarly, the deviatoric delayed elastic strains $e_{11}^d = \epsilon_{11}^d - \epsilon_v^d = \epsilon_{11}^d$ (assuming $\epsilon_v^d = 0$), $e_{22}^d = e_{33}^d = \epsilon_{22}^d = -\epsilon_{11}^d/2$, thus $e^d = \epsilon_{11}^d = \epsilon_1^d$. Therefore, the above two equations become

$$\dot{e}_{11}^d = \dot{\epsilon}_0^d \left(\frac{\sigma_1 - E_k \epsilon_1^d}{\sigma_0} \right)^n \text{ and} \tag{4.25}$$

$$\dot{\epsilon}^c_{11} = \dot{\epsilon}^c_0(\sigma_1/\sigma_0)^m. \tag{4.26}$$

These two equations are equivalent to Eq. (4.5) and Eq. (4.9). Thus it is consistent and convenient to assume that in multiaxial stress state the viscosity coefficients, μ_k and μ_m are related to the von Mises stress and equivalent strain in a similar way as the viscosity coefficients, μ_{k1} and μ_{m1} as defined by Eqs. (4.8) and (4.10).

4.2 Damage Evolution Law

This section addresses progressive damage in zones under loading such that large fractures are not active but significant microstructural changes still take place. The model described in the previous section is for intact (undamaged) materials only, and the following is developed in an attempt to address the behaviour of damaged solids. The relation of the extent of damage and the growing network of microcracks has been discussed in Chapter 2.

Based on Budiansky and O'Connell (1976) and Horii and Nemat-Nasser (1983), Xiao (1991) proposed an approximate solution for elastic moduli with damage:

$$G'/G = 1 - \omega D, \text{ and} \tag{4.27}$$

$$K'/K = 1 - \omega D \tag{4.28}$$

where $\omega = 16/9$ in tension; $\omega = 1$ for compressive stress state. The damage measure, $D = a^3N$ (N is the crack density and a is the radius of crack surface), and the crack formation is defined, following McKenna et al. (1990), by a rate expression of

$$\dot{N} = \dot{N}_c\left(\frac{\sigma}{\sigma_0}\right)^r \tag{4.29}$$

where r is a constant.

Kachanov (1993) proposed a 3D solution to approximate the effects of distributed cracks on the elastic properties. His solution is given by Eqs. (2.41) to (2.43) as:

$$\frac{E}{E_0} = (1 + C_1 N)^{-1} \tag{4.30}$$

$$\frac{G}{G_0} = (1 + C_2 N)^{-1} \tag{4.31}$$

$$\frac{\nu}{\nu_0} = \frac{E}{E_0}(1 + C_3 N) \tag{4.32}$$

where C_1, C_2 and C_3 are constants; N is the crack density.

As discussed in the earlier chapters, the reduction of elastic moduli as well as the enhancement of creep deformation were associated with damage processes in the material. These processes include not only microcracking but also other possible microstructural changes, such as, recrystallization and pressure melting depending on the loading stress and confining pressure. For viscoelastic materials involving cracking and damaging, Schapery's continuum damage theory provided a damage measure which was defined as

$$S = \int_0^t f_1 (\frac{\sigma}{\sigma_0})^q dt.$$

Based on this theory, a single scalar damage model was proposed by Singh (1993) which was also adopted by Xiao and Jordaan (1996), to include the effect of confining pressure on damage progress. This model provided good agreement with test results under moderate loading stresses and confining pressures (see also Chapter 2). For high loading stresses and confining pressures, a damage model with two state variables was proposed by Jordaan et al., (1997) and Meglis et al., (1997) as:

$$\begin{aligned} S &= S_1 + S_2 \\ &= \int_0^t (f_1(p)(\frac{\sigma}{\sigma_0})^{q_1} + f_2(p)(\frac{\sigma}{\sigma_0})^{q_2}) dt \text{ where} \end{aligned} \tag{4.33}$$

$$f_1(p) = \begin{cases} 0.712\left(1 - \frac{p}{37}\right)^2 & \text{if } p < 37 \text{ MPa} \\ 0 & \text{if } p \geq 37\text{MPa} \end{cases}, \quad \text{and} \tag{4.34}$$

$$f_2(p) = 0.1\left(\frac{p}{42.8}\right)^r, \tag{4.35}$$

and q_1, q_2 and r are constants. The state variable S_1 is mostly related to microcracking. It can represent the damage progress very well under low confining pressures. The second state variable S_2 is mainly associated with pressure-softening processes, such as recrystallization as well as pressure melting under high confining pressures, as addressed by Jordaan et al., (1997) and Meglis et al., (1997).

Since cracks are one form of damage, in the present study, Equations (4.30), (4.31) and (4.32) have been adopted to define the specifications of elastic moduli as a function of damage. The crack density N has been substituted by αS where α is a constant and S is the damage measure which includes all of the possible microstructural changes.

The derivative of Eq. (4.33) shows that the damage rate:

$$\frac{dS}{dt} = f_1(p)\left(\frac{\sigma}{\sigma_0}\right)^{q_1} + f_2(p)\left(\frac{\sigma}{\sigma_0}\right)^{q_2} \tag{4.36}$$

is a function of stress following the power law.

Jonas and Muller (1969) proposed an expression to take into account of the effect of dynamic recrystallization on the strain rate, in which the strain rate follows an exponential function of stress (see also section 2.2). In this study, it is proposed to substitute the power function with an exponential function to the second term of Eq. (4.36). This means under high confining pressures, the damage rate will increase rapidly following an exponential function with stress. It should be pointed out that the exponential function equals to a series of power functions, thus, it is a more general form of the power functions. Therefore the proposed model using an

exponential function in the second state variable is an extension to the recent work by Jordaan et al., (1997) and Meglis et al., (1997).

The proposed damage function is defined as:

$$S = \int_0^t \{f_1(p)(\frac{\sigma}{\sigma_0})^{q_1} + f_2(p)\exp(\frac{\sigma}{\sigma_0})\}dt \tag{4.37}$$

where $f_1(p)$ and $f_2(p)$ are given by Eqs. (4.34) and (4.35), respectively.

4.3 Creep Enhancement Factor

The effect of damage on the creep deformation was discussed in Chapter 2. An exponential form was proposed by Jordaan and McKenna (1989) and McKenna et al. (1990) to define the creep enhancement factor as a function of damage. This term was also adopted by Xiao and Jordaan (1996). The creep strain rates of damaged material were then defined as

$$\dot{e}_{ij}^{d'} = \dot{e}_{ij}^{d} \exp(\beta_d S), \text{ and} \tag{4.38}$$

$$\dot{e}_{ij}^{c'} = \dot{e}_{ij}^{c} \exp(\beta_c S) \tag{4.39}$$

where S is the damage measure; and the primes refer to the components for damaged material; and β_d, β_c are creep enhancement factors, and $\dot{e}_{ij}^{d}$ and $\dot{e}_{ij}^{c}$ are respectively the delayed elastic strain rate and secondary creep strain rate of the intact material, as given by Eq. (4.23) and Eq. (4.24).

4.4 Dilatation under Compression

In recent years, more and more attention has been paid to the dilatation of solid under loading, especially when cracking and damage is induced. As mentioned in Chapter 2, Resende and Martin (1983, 1984) defined volumetric strain rate (inelastic

portion including compaction and dilatation) as a function of stress, strain, damage for rock-like materials. As addressed in the previous chapter, density of ice in the crushed layer adjacent to the indenter (Frederking et al., 1990a, b) was less than that of parent ice, indicating the presence of dilatation due to the cracking and pulverizing of the ice during the interaction process. The reverse process has also been observed during crushed ice tests, i.e. the crushed ice has been sintered into a hard block of ice mass under high confining pressure (Spencer et. al., 1993). Dilatation (volumetric deformation) was also measured in small scale compressive experiments at constant strain rates by Wang (1981) and Dorris (1989), at constant stress by Sinha (1989), and more recently by Singh (1993), Xiao and Jordaan (1994) and Stone et al. (1994) on intact, damaged and crushed ice.

In the present study, volumetric strain has been measured. Two techniques were used to obtain volumetric strain; (a) measuring the diametral expansion of the sample in two orthogonal directions with three specially designed strain gauges at the center portion of the sample; (b) measuring the fluid volume change within the confining cell. Singh (1993) presented an expression to estimate inelastic dilatation, based on thermodynamics (the method of complementary strain energy) and calibrated with the measurements of volumetric strains for intact, damaged and crushed ice under different confinements. The proposed function was given as

$$\dot{\epsilon}_v = -\frac{f_3}{p}\, s\,(\dot{e} - \dot{e}^e), \quad \sigma_v \leq 0 \tag{4.40}$$

where f_3 is a constant, e and e^e are the equivalent total and elastic strain, respectively. The compaction is defined as being positive while dilatation is negative.

As mentioned earlier in Eq. (4.13) and Eq. (4.14), there are two volumetric strain components ϵ_v^d and ϵ_v^c, which are to related to delayed elastic and secondary creep strain, respectively. They are, again, not the results of elastic bulk deformation,

rather due to nonlinear deformation. The total volumetric strain (nonlinear portion), ϵ_v, as in Eq. (4.40), is assumed to include both ϵ_v^d and ϵ_v^c, i.e. $\epsilon_v = \epsilon_v^d + \epsilon_v^c$.

Finally, the tensor of total strain rate is expressed by

$$\dot{\epsilon}_{ij} = \dot{\epsilon}_{ij}^e + \dot{e}_{ij}^{d'} + \dot{e}_{ij}^{c'} + \delta_{ij}\dot{\epsilon}_v, \tag{4.41}$$

where $\dot{\epsilon}_{ij}^e, \dot{e}_{ij}^{d'}$ and $\dot{e}_{ij}^{c'}$ are elastic, delayed elastic and secondary creep strain tensor, respectively; $\dot{\epsilon}_v$ is the volumetric strain (nonlinear part).

4.5 Finite Element Implementation and Model Verification

The numerical solution of damage equations is performed using an explicit incremental scheme. For an isotropic material, the stress tensor is given by

$$\sigma_{ij} = K_{ijkl}\epsilon_{kl}^e, \tag{4.42}$$

where the stiffness matrix:

$$K_{ijkl} = (K - \frac{3}{2}G)\delta_{ij}\delta_{kl} + G(\delta_{ik}\delta_{jl} + \delta_{il}\delta_{jk}). \tag{4.43}$$

The increment of stress tensor is calculated by

$$\delta\sigma_{ij} = K_{ijkl}\delta\epsilon_{kl}^e + \delta K_{ijkl}\epsilon_{kl}^e \tag{4.44}$$

where the stiffness matrix is given by

$$K_{ijkl} = \begin{Bmatrix} K+4G/3 & K-2G/3 & K-2G/3 & 0 & 0 & 0 \\ & K+4G/3 & K-2G/3 & 0 & 0 & 0 \\ & & K+4G/3 & 0 & 0 & 0 \\ & & & 2G & 0 & 0 \\ & SYMM. & & & 2G & 0 \\ & & & & & 2G \end{Bmatrix}. \tag{4.45}$$

The incremental change in the elastic stiffness tensor δK_{ijkl} is obtained by first calculating the increment in damage with:

$$\begin{aligned} \delta S &= \delta \int_0^t \{f_1(p)(\frac{s}{\sigma_0})^{q_1} + f_2(p)\exp(\frac{s}{\sigma_0})\} d\tau \\ &= \{f_1(p)(\frac{s}{\sigma_0})^{q_1} + f_2(p)\exp(\frac{s}{\sigma_0})\}\,\delta t, \end{aligned} \tag{4.46}$$

where δt is the time increment specified by the user. Summing this to the accumulated total damage and calculating the difference between the elastic moduli for the current and previous state, i.e.

$$G' = G_0[1 + C_2(S + \delta S)]^{-1}$$

$$G = G_0[1 + C_2 S]^{-1}$$

$$\delta G = G' - G$$

similarly, δK can be calculated, therefore

$$\delta K_{ijkl} = \begin{Bmatrix} \delta K + 4\delta G/3 & \delta K - 2\delta G/3 & \delta K - 2\delta G/3 & 0 & 0 & 0 \\ & \delta K + 4\delta G/3 & \delta K - 2\delta G/3 & 0 & 0 & 0 \\ & & \delta K + 4\delta G/3 & 0 & 0 & 0 \\ & & & 2\delta G & 0 & 0 \\ & SYMM. & & & 2\delta G & 0 \\ & & & & & 2\delta G \end{Bmatrix}. \tag{4.47}$$

The increment of elastic strain components $\delta\epsilon_{ij}^e$ is calculated by

$$\delta\epsilon_{ij}^e = \delta\epsilon_{ij} - \delta e_{ij}^{d'} - \delta e_{ij}^{c'} - \delta\epsilon_v\,\delta_{ij} \tag{4.48}$$

where the total strain increment $\delta\epsilon_{ij}$ is defined in the boundary conditions, e.g. the indentation speed or strain rate $\dot{\epsilon}$ and the time increment δt; δ_{ij} is the delta function. The delayed elastic strain increment of intact material, δe_{ij}^d, is calculated by

$$\delta e_{ij}^d = \frac{3}{2}\dot{\epsilon}_0^d \left(\frac{s - E_k e^d}{\sigma_0}\right)^n \frac{s_{ij}}{s}\,\delta t. \tag{4.49}$$

Substituting this equation into Eq. (4.38), the delayed elastic strain increment of damaged material is found to be

$$\delta e_{ij}^{d'} = \dot{\epsilon}_0^d \left(\frac{s - 2G_k\, e^d}{\sigma_0} \right)^n \exp(\beta_d S)\, \frac{s_{ij}}{s}\, \delta t. \tag{4.50}$$

Similarly, the secondary creep strain increment $\delta e_{ij}^{c'}$ can be obtained from Eq. (4.24) and Eq. (4.39), i.e.

$$\delta e_{ij}^{c'} = \dot{\epsilon}_0^c \left(\frac{s}{\sigma_0} \right)^m \exp(\beta_c S)\, \frac{s_{ij}}{s}\, \delta t. \tag{4.51}$$

The volumetric strain increment $\delta\epsilon_v$ is given by Eq. (4.40),

$$\delta\epsilon_v = -\frac{f_3}{p}\, s\, (\dot{e} - \dot{e}^e)\, \delta t;\ \sigma_v \leq 0. \tag{4.52}$$

The elastic strain components ϵ_{ij}^e are defined as

$$\epsilon_{ij}^e = C_{ijkl}\, \sigma_{ij}$$

where C_{ijkl} is the compliance matrix which is the inverse of stiffness matrix.

In the above equations, the stresses s, s_{ij}, σ_v, strain e^d and damage S are stored as state variables from previous states, and at the end of each increment, these variables will be updated as

$$\sigma_{ij}^* = \sigma_{ij} + \delta\sigma_{ij}, \tag{4.53}$$

$$\vdots$$

$$S^* = S + \delta S. \tag{4.54}$$

The complete multiaxial model has been developed in FORTRAN code and implemented as a user material specification in the ABAQUS finite element structural analysis program for numerical computation. The parameters of the damage model are all calibrated from the triaxial test results. By fitting the time-strain record of

Table 4.1: Parameters Used in the Mechanical Model

Description	Parameter	Value
Elastic Modulus	E	9500MPa
Elastic Stiffness in Kelvin Unit	E_k	9500MPa
Poisson's Ratio	ν	0.3
Primary Creep Reference Rate	$\dot{\epsilon}_0^d$	$1.0\times10^{-5}s^{-1}$ at -10°C
Creep Exponent for Kelvin unit	n	1.0
Secondary Creep Ref. Rate	$\dot{\epsilon}_0^c$	$1.76\times10^{-7}s^{-1}$ at -10°C
Creep Exponent for Maxwell unit	m	2.5
Volumetric Constant	f_3	0.11
Reference Stress	σ_0	15 MPa
Damage Parameter	α	5.0
Creep Enhancement Parameter	β_d	1.0
Creep Enhancement Parameter	β_c	1.0

creep test on intact ice (see Figure 4.1), the primary and secondary creep reference rates, $\dot{\epsilon}_0^d$ and $\dot{\epsilon}_0^c$, and the creep exponents, n, m can be estimated. Then, by fitting creep test on damaged ice (see Figure 4.2a, b), the damage exponents, q_1, q_2, and the creep enhancement parameters, β_d and β_c can be obtained. Figure 4.3 shows the predictions of strain response of damaged ice under the same loading conditions except the confinement. The test result of volumetric strain is compared with the model prediction in Figure 4.4. The stress-strain relation predicted by the model is then compared with the result of constant strain rate test, as shown in Figure 4.5. Once the model predictions can fit the results of these three types of test, the model verification has been accomplished. All parameters are listed in Table 4.1. Note that for low stress tests, The parameter f_2 is insignificant, thus the second state variable S_2 can be ignored. Vice verser, when stress is high, S_1 can be ignored.

4.6 The Broad-Spectrum Approach

As discussed in Chapter 2, a model with chains of Maxwell or Kelvin units can be a rigorous representation of the behaviour of viscoelastic materials. But the disadvantage is its complexity. A broad-spectrum approach proposed by Schapery (1962) can somewhat overcome this difficulty. Based on this approach, a modified constitutive model is proposed by introducing a chain of Kelvin units to replace the single Kelvin unit in the model presented in the previous sections. Assuming all the Kelvin units have linear springs and nonlinear dashpots following the power-law. The creep compliance of a Kelvin unit under constant stress can be derived from Eq. (2.14):

$$D_k(t) = \frac{1}{E_k}\{1 - [(n-1)\omega_k t + 1]^{1/(1-n)}\} \tag{4.55}$$

where, $\omega_k = E_k/\mu_{k0}$. Similar to Eq. (2.4) the total creep compliance can be expressed:

$$D(t) = \frac{1}{E_1} + \frac{t}{\mu_1} + \sum_{i=2}^{N} \frac{1}{E_i}\{1 - [(n_i-1)\omega_i t + 1]^{1/(1-n_i)}\} \tag{4.56}$$

where E_1 is the elastic modulus and assumed to be 9500 MPa.

By choosing a set of collocation points for t, such as $t_1 = 0$ and $t_j = 10^{(j/4-3)}$, (j=2, 3, ... n), and letting $\omega_i = c/t_i$, i.e. $\omega_i = c/10^{(i/4-3)}$, ($i$=1, 2, 3, ... n), where c is a constant, a set of n linear algebraic equations for the unknown variables of E_j (j=1, 2, 3, ... n), can be defined similar to Eq. (2.17) as:

$$\{b_j\} = \{a_{ij}\}\{1/E_j\} \tag{4.57}$$

where $b_j = D(t_j) - 1/E_1$ and $a_{ij} = \{1 - [(n_i-1)\omega_i t_j + 1]^{1/(1-n_i)}\}$. At present, n_i=3 (i=1, 2, 3, ... n) are assumed. By solving the above equation, the values of E_j can be calculated. Substituting E_j into Equation (4.56), the model response can be evaluated by comparing with the experimental results. A few iterations may be needed by adjusting t_j and ω_i to achieve satisfactory results.

An example of such a model with three Kelvin units has been implemented into a finite element model. As shown in Figure 4.6, the model results are compared with the same test data as shown in Figure 4.1 with good agreement.

This broad-spectrum approach can be explored further. As discussed in Chapter 2, the creep compliance of a viscoelastic material can be expressed as:

$$D(t) = D_1 + D_2(t) + D_3(t) \tag{4.58}$$

where $D_1 = 1/E_1$, $D_2(t) = t/\mu_1$, and

$$D_3(t) = \sum_{i=2}^{N} \frac{1}{E_i}\{1 - \exp(-\frac{E_i}{\mu_i}t)\}. \tag{4.59}$$

This expression is the same as Eq. (2.4). Assuming the spring in the ith Kelvin unit breaks at time t_i^0, i.e. $E_i \to 0$ at $t = t_i^0$, then the ith component of $D_3(t)$, $\frac{1}{E_i}\{1 - \exp(-\frac{E_i}{\mu_i}t)\}$ will reduce to $1/\mu_i$, i.e. $\frac{1}{E_i}\{1 - \exp(-\frac{E_i}{\mu_i}t)\} \to 1/\mu_i$. This event can be related to a structure break-down of some local high stress zones, such as the triple point in polycrystalline ice. Such a break-down can be due to microcracking, dynamic recrystallization and/or pressure melting. As a result, it will reduce the overall viscosity, and soften the material. With increasing number of structure break-downs, it may lead to a domino effect, so that all the springs in the Kelvin units will be broken after time t_{max}^0, here $t_{max}^0 = max\{t_i^0, (i = 1, 2, ...n)\}$. Therefore the creep compliance $D(t)$ can be reduced to:

$$D(t) = 1/E_1 + \sum_{i=1}^{N} \frac{1}{\mu_i}t \ \ (t > t_{max}^0). \tag{4.60}$$

This means the creep model will be reduced to a spring plus a series of dashpots, or simply, one spring and one equivalent dashpot (which represents the series of dashpots and it has much lower viscosity), which means the material has been significantly softened. Thus the Kelvin chain becomes a Maxwell unit. This simplified model can be very useful in practice to model the crushed layer at the contact interface. This will be discussed later.

4.7 A Constitutive Model Using Three Kelvin Units

As discussed in Chapter 3, high loading stress and confinement can significantly soften the material. A typical test curve of time versus strain rate in logarithm scale is shown in Figure 3.22. The curve can be linearized into three portions, minimum, linear and maximum portion, respectively. It can be assumed that each portion represents a different stage of damage progress in the material. For example, the minimum portion may represent the initial stage of increasing damage. The linear portion can represent the stable stage of damage progress. The maximum portion will be the unstable stage when damage reaches a critical value and leads to a rapid change in the structure of the material. This structure change can be a shear or fracture failure under high deviatoric stress and low confinement, or it can be the formation of pulverized material under high loading stress and confinement. In this study, it is proposed to model the deformation of materials under high loading stresses using a combination of three Kelvin units and a Maxwell unit. With an increase of damage, the springs in the Kelvin units will be broken. Assume that the break-down events will occur in sequence. Each such event will change a Kelvin unit into a dashpot, thus will reduce the overall viscosity and lead to a higher strain rate. In this way, the three stages of the damage progress can be represented by means of three Kelvin units, respectively. The tensor of the total strain rate is given by Eq. (4.41), $\dot{\epsilon}_{ij} = \dot{e}^{e}_{ij} + \dot{e}^{d'}_{ij} + \dot{e}^{c'}_{ij} + \delta_{ij}\dot{\epsilon}_v$, here $\dot{e}^{d'}_{ij}$ will be modified and expressed as a sum of three terms (each represents one Kelvin unit):

$$\dot{e}^{d'}_{ij} = \dot{e}^{d1'}_{ij} + \dot{e}^{d2'}_{ij} + \dot{e}^{d3'}_{ij}, \text{ and} \tag{4.61}$$

$$\dot{e}^{dk'}_{ij} = \frac{3}{2}\dot{\epsilon}^{dk}_{0}\left(\frac{s - E_k e^{dk}}{\sigma_0}\right)^{n_k}\frac{s_{ij}}{s}\exp(\beta_{dk}S), \quad (\text{k=1,2,3}) \tag{4.62}$$

This is the same as Eq. (4.38). Figure 3.22 shows that there are three significant increases in strain rate at time of 4.5 second, 13 second and 18 second, respectively.

Based on Eq. (4.37), the calculated damage levels at these three points of time are 2.0, 5.85 and 8.1, respectively. Assume that each jump in strain rate can be related to a break of a spring in one of the Kelvin units at these damage levels. Therefore, near the end of the test, when all of the three springs are broken, i.e. $E_k \to 0\,(k = 1, 2, 3)$, the above equations reduce to:

$$\dot{e}_{ij}^{dk'} = \frac{3}{2}\dot{\epsilon}_0^{dk}\left(\frac{s}{\sigma_0}\right)^{n_k}\frac{s_{ij}}{s}\exp(\beta_{dk}S), \quad \text{(k=1,2,3)}. \tag{4.63}$$

This means the whole model can be reduced to a spring plus four dashpots.

For triaxial creep tests, the deviatoric stress $S_{11} = (2/3)s$, therefore, the deviatoric strain rates can be expressed by

$$\dot{e}_{11}^{dk'} = \dot{\epsilon}_0^{dk}\left(\frac{s}{\sigma_0}\right)^{n_k}\exp(\beta_{dk}S), \quad \text{(k=1,2,3)}. \tag{4.64}$$

Under constant stress states, by taking the natural logarithm and substituting Eq. (4.37) for S, the above equations can be expressed in much simpler forms:

$$\ln(\dot{e}_{11}^{dk'}) = \phi_k t + I_k \tag{4.65}$$

where the slopes ϕ_k are given as:

$$\phi_k = \beta_{dk}(f_1(p)(\frac{s}{\sigma_0})^{q_1} + f_2(p)\exp(\frac{s}{\sigma_0})). \tag{4.66}$$

The zero-intercepts I_k of the linear curves are given by:

$$I_k = n_k \ln\left(\frac{s}{\sigma_0}\right) + \ln\dot{\epsilon}_0^{dk} \tag{4.67}$$

The constants in the above equations can be calculated based on test results, as shown in Figure 3.22. Here $\dot{\epsilon}_0^{dk}$ are assumed to be the same as $\dot{\epsilon}_0^{d}$ as listed in Table 4.1. Figure 4.7 shows the comparison of model result and test result shown in Figure 3.22. In addition to Table 4.1, some more constants are listed in Table 4.2.

It is worth noting that the above approach is similar to the idea of back-stress stated in many earlier works, such as Jonas and Muller (1969), Sunder and Wu (1989) to name a few examples. In their work, the deformation or stain rate is not just a function of applied stress, it also depends on the so-called internally generated back-stress. The back-stress will be reduced as the deformation progresses. This in turn will enhance the subsequent deformation. The term $E_k e^{dk}$ in the above equations represents the stress in the spring of the Kelvin units. This is equivalent to the back-stress. When stress in the spring reduces, more stress is transferred to the dashpot which will result in the acceleration of deformation.

This broad-spectrum model will be used later in the finite element analyses. This model is a modification and extension of the model given by Jordaan et al., (1997). It includes three Kelvin units. An exponential function is used to define the second state variable for damage. These enables the model to provide a better prediction of large deformation and high strain rates for viscoelastic materials under extreme loading conditions. The model was initially calibrated by three types of tests: creep test on intact ice, on damaged ice and constant strain rate test. Due to the discrepancies in test results, which can be caused by a number of reasons, e.g. sample discrepancies and test conditions, for each type of test, one set of test data was selected to be the best representation of all the tests. Due to limited resources and time, this was considered as a reasonable approach. The second reason is that these are all low stress tests with short loading time, the deformation and rates are small. For practical application of the model, such as medium scale indentation tests, the loading stress and rates are very high and beyond the range of these low stress tests. Thus the accuracy of modeling low stress tests is less critical if the goal is to simulate field tests. High stress tests were conducted by Meglis et al., (1997) to provide information to calibrate the damage model under extreme loading conditions.

Table 4.2: Parameters Used in the Constitutive Model

Description	Parameter	Value
Creep Exponent for Kelvin unit 1	n_1	3.38
Creep Exponent for Kelvin unit 2	n_2	2.98
Creep Exponent for Kelvin unit 3	n_3	0.57
Creep Enhancement Parameter 1	$\beta_d 1$	0.2
Creep Enhancement Parameter 2	$\beta_d 2$	0.78
Creep Enhancement Parameter 3	$\beta_d 3$	2.86

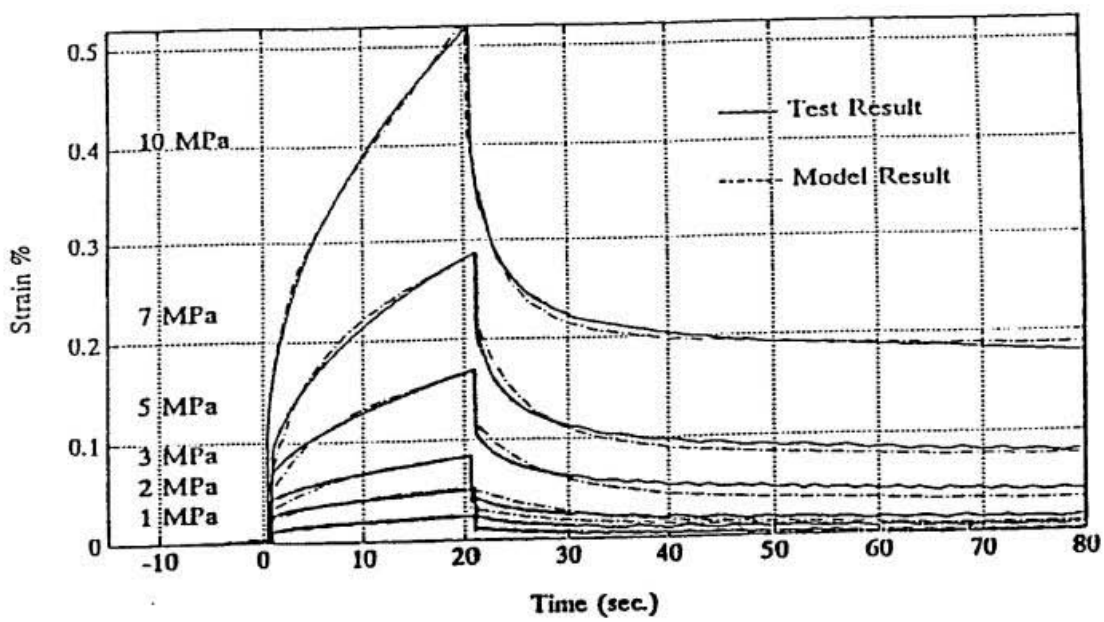

Figure 4.1: Comparison of creep test results with model results on intact ice under stress differences from 1 to 10 MPa and confinement of 10 MPa.

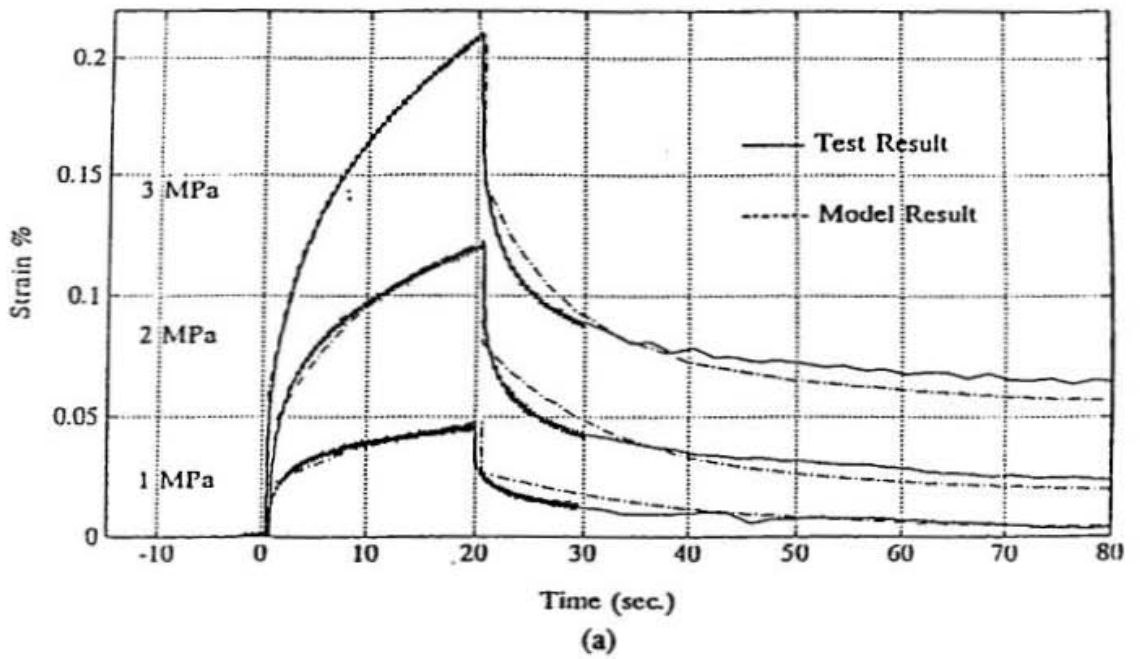

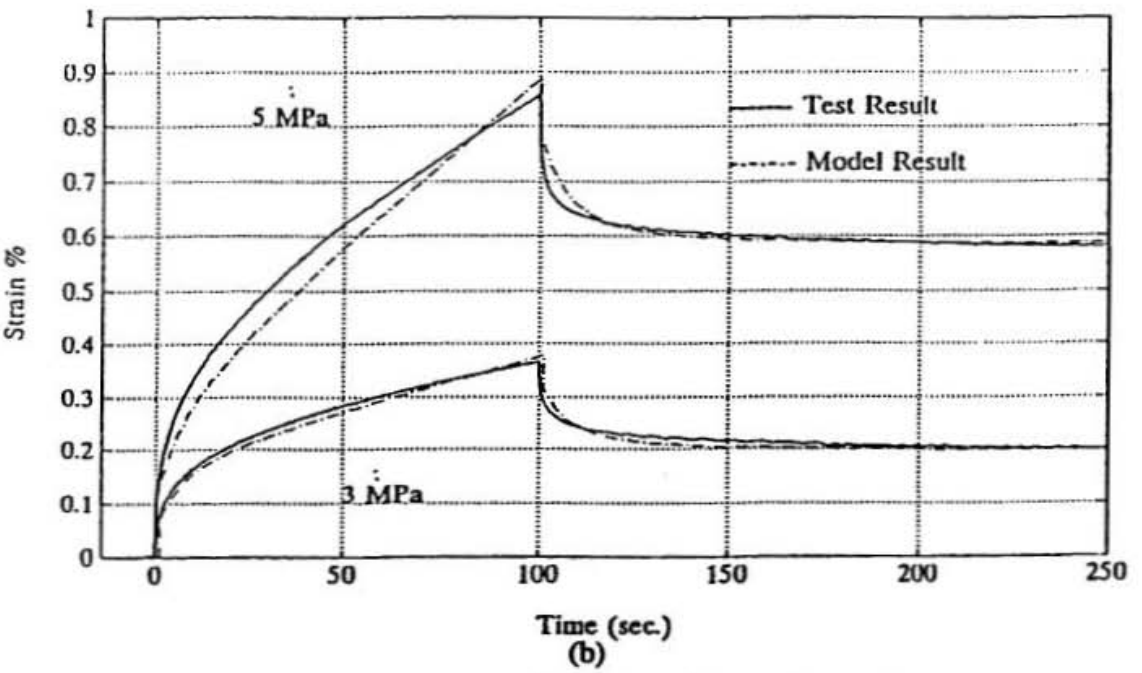

Figure 4.2: Comparison of creep test results with model results on damaged ice, under stress differences from 1 to 5 MPa and confinement of 10 MPa, for a loading period of: (a) 20 seconds (b) 100 seconds.

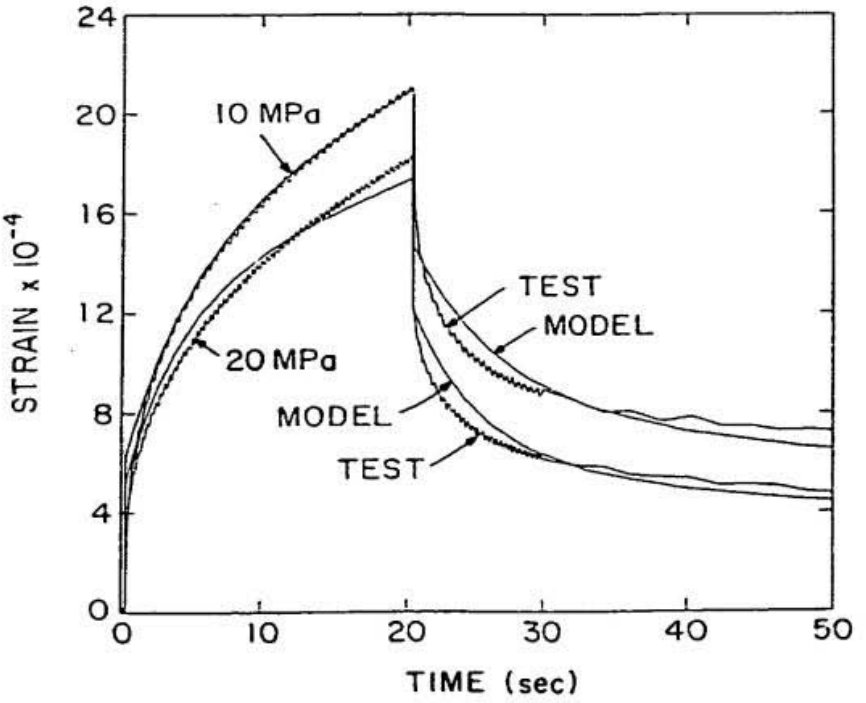

Figure 4.3: Comparison of test and model results on the strain response of damaged ice under same stress difference of 3 MPa but with different confinement of 10 and 20 MPa.

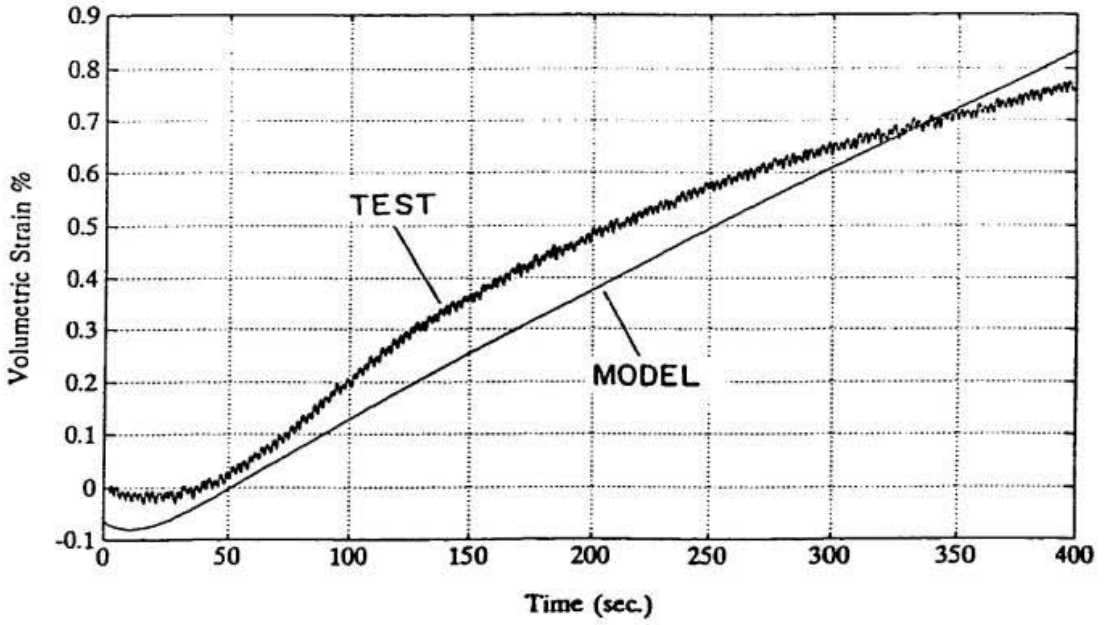

Figure 4.4: Comparison of test and model results on the volumetric strain response of constant strain rate test under 5 MPa confinement

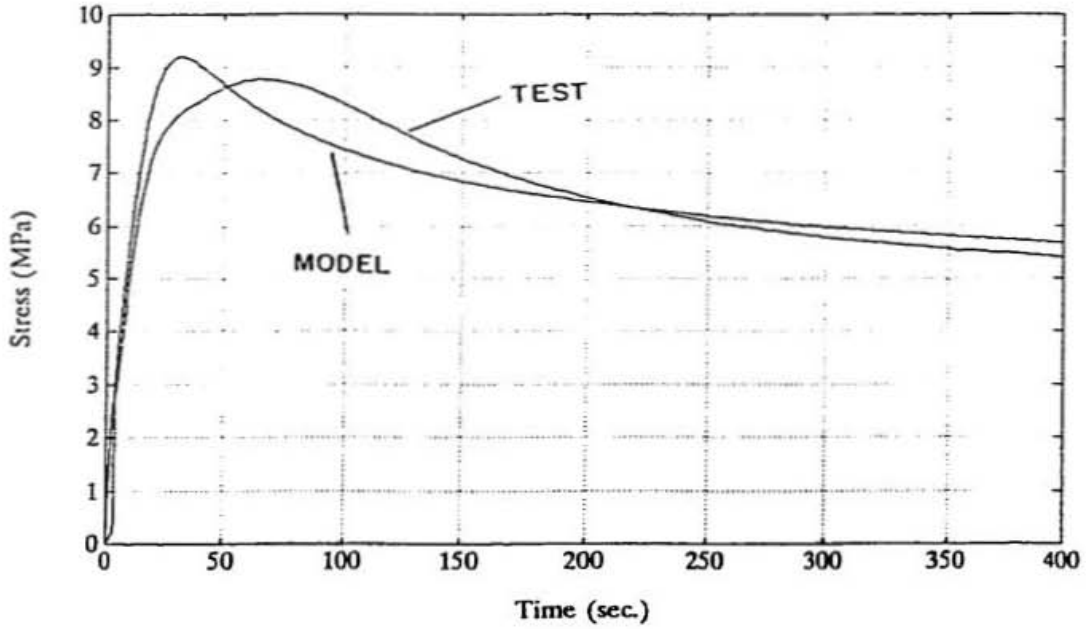

Figure 4.5: Comparison of constant strain rate test results with model results.

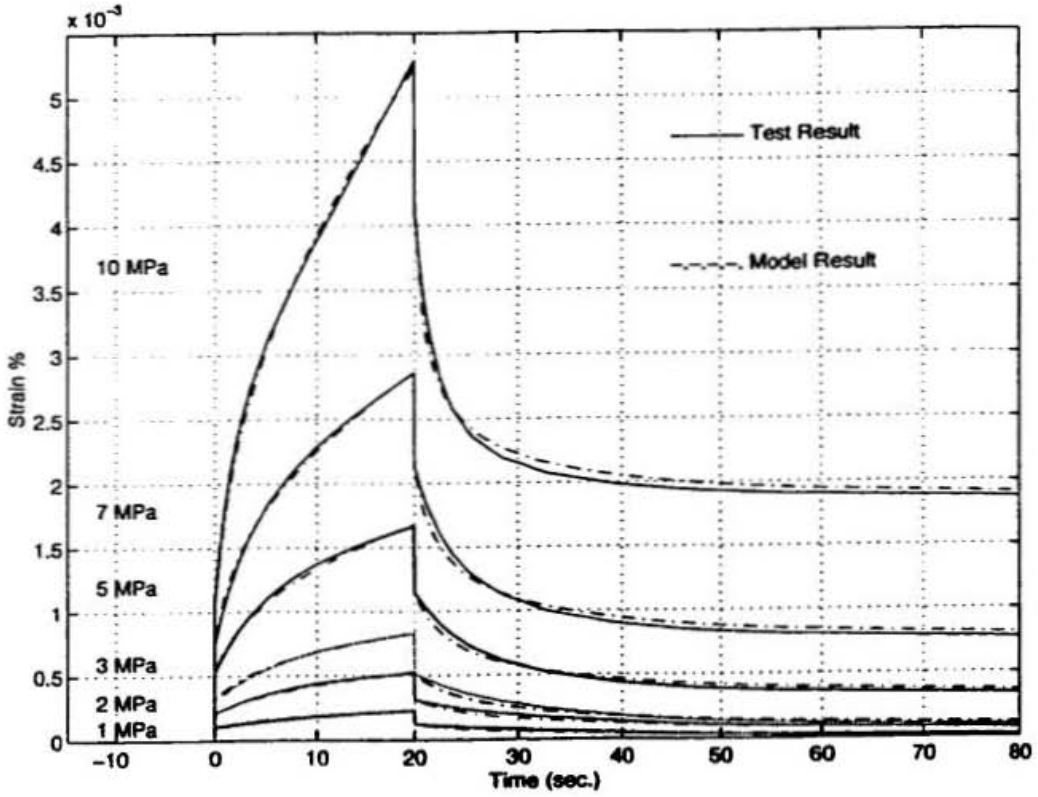

Figure 4.6: Comparison of creep test results with the broad-spectrum model results.

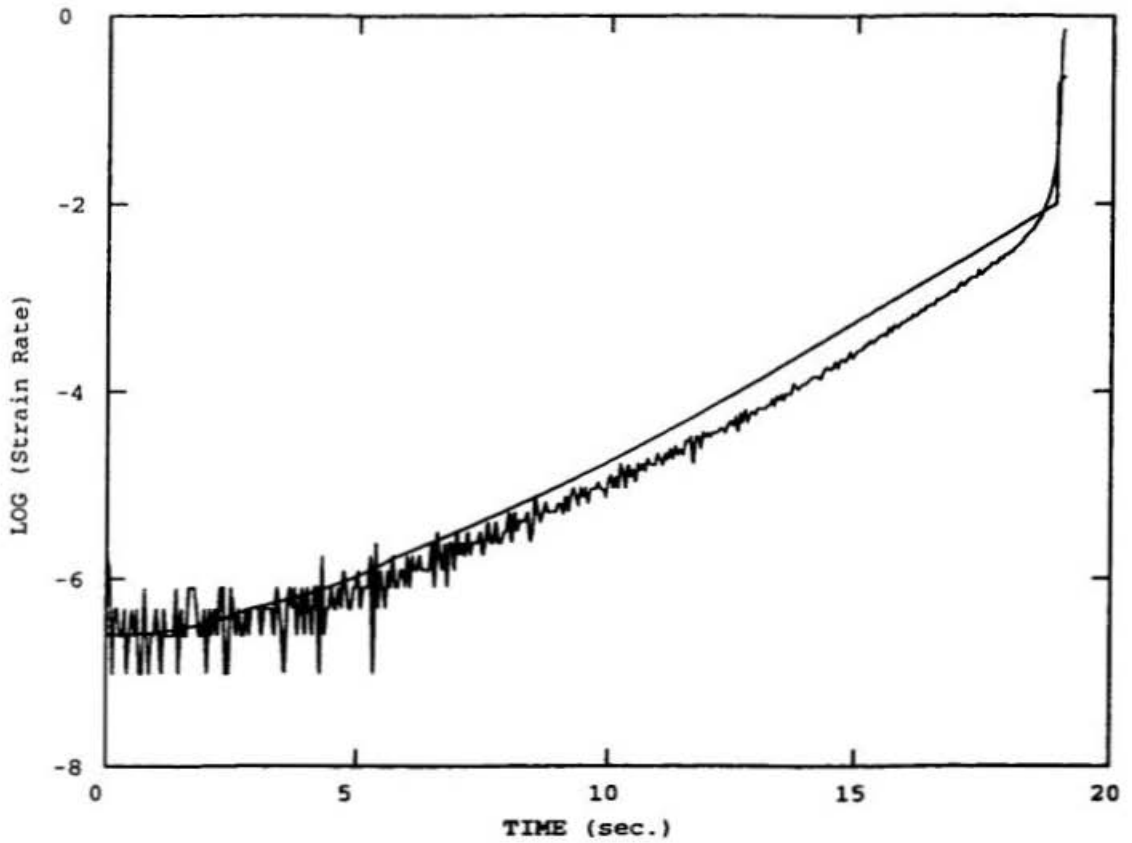

Figure 4.7: Comparison of test and model result on the strain rate response of a creep test under 50 MPa confinement.

Chapter 5

Finite Element Analysis of Indentation Problems

5.1 Introduction

Brittle, viscoelastic solids under stress can fail in a variety of mechanisms. In this work, the typical failure mechanisms are related to creep deformation, dynamic recrystallization, or microcracking as well as collapsing due to fracture, depending on the loading conditions. In contact problems, the failure mode can be a combination of the above mechanisms. In the ice environment, indentation problems are very common and they present a great challenge in the design of offshore structures. Estimation of ice forces on the structure is the essence of engineering design.

5.2 Two Modelling Tools

In this study, two theoretical modeling tools, damage mechanics and fracture mechanics, have been developed and implemented in the numerical analysis (finite element analysis). Damage mechanics does not deal with each individual crack or failure event, rather it takes into account the averaged effect of all the cracks and damage processes on the properties at a point in the material, for instance an average elastic modulus or viscosity. It is not possible to obtain details of crack sizes or the progress

of each failure event based on analysis using damage theory. Fracture mechanics on the other hand, can be used to analyze an individual crack. It can predict the propagation and trajectory of the crack, as well as the size of pieces fractured off. It is conceivable to implement both tools into one numerical model to simulate the complex failure processes occurring during ice structure interactions. In such cases, both micro-scale damage processes and macro-scale fracture failures can take place simultaneously. The two failure mechanisms will also in turn affect and enhance each other during the failure process.

5.3 Implementation of Damage Models

5.3.1 Modelling of Medium Scale Indentation Tests

As discussed in Xiao (1991) and Jordaan and Xiao (1992), damage analysis can provide accurate predictions in terms of force-time curves for medium scale indentation tests under low loading rates (until the occurrence of a spall). The associated damage distribution as well as the pressure distribution at the interface predicted by the analysis are also in good agreement with the observations from the tests. Figure 5.1 shows the modelling results of two spherical indentation tests. The test speeds were 0.3 mm/s and 3 mm/s, respectively. The associated damage distribution for the slower test is shown in Figure 5.1a (The unit for time in all the figures is second).

As noted earlier, stress concentrations play an important part in the analysis of crack initiation. From the test results (see Figure 3.26), the saw-tooth pattern of load curves indicate that crushing and possible fracture events were taking place.

In this section, the damage constitutive models described in the previous chapters, are implemented in finite element models to simulate the ice indentation tests as discussed in Chapter 3. Figure 3.25 shows a cross-section of a test with a flat

indenter against an ice wall (Test 07 from Frederking et al, 1990 a,b). The situation corresponds essentially to plane strain with extrusion to the left and the right of the interface. A symmetric finite element model is shown in Figure 5.2.

First the damage model proposed by Jordaan et al., (1997) has been implemented in the finite element model shown in Figure 5.2. The damage model was described in Chapter 2 and given by Eq. (2.84). Different combinations of the power functions were used as experimental runs to study the influence of the damage parameters on the results of numerical modelling. Load histories of the simulation results are shown in Figure 5.3. These results are similar to what were presented by Jordaan et al., (1997). The damage distributions for the trial runs are shown in Figure 5.4 and Figure 5.5. The figures show clearly the development of a layer of damaged material near the indenter.

The damage model proposed in this study (see Chapter 4) and given by Eq. (4.37) to Eq. (4.41) was then implemented in the same finite element model. As discussed in the earlier chapters, the first term of the damage function (state variable S_1 in Eq. (2.84)) which was directly adopted in this study, can represent the damage progress very well under low to moderate confining pressures. In this pressure range, damage is mostly related to microcracking, therefore it will be suppressed under pressure, and the strain rate will drop with increasing pressure (see also chapter 3). The second term of the damage function (state variable S_2 in Eq. (2.84)) represents the damage progress under high confining pressures. In this case the development of damage as well as the strain rate will be enhanced by the increase of pressure. An exponential function was proposed to substitute the power function in Eq. (2.85) to define the rapid growth of damage, under both high shear stresses and high confining pressures. The effect of high confining pressures on the progress of damage has been taken into account by a power function $f_2(p)$ as given by Eq. (2.87). To study the influence of

confining pressure on damage growth as well as the modeling results, different values of the exponent r have been applied. The model results of the force-time curves are shown in Figure 5.6. It shows that when the exponent r is larger than 10, the total force on the indenter will drop rapidly after the peak, which implies a sharp increase of damage in the material. The model results for exponent r larger than 20 also show a reasonable agreement with the test results, including the peak load and the frequency for the first load cycle. Fig. 5.7 shows the comparison of model and test results. Model result is stiffer than the test result. This is due to that the model with a rigid indenter has not taken into account the flexibility of the indentation system.

To illustrate the important role of pressure softening on the development of rapid load drops, two cases were studied: (1) the exponent r in function $f_2(p)$ was set to zero, therefore no pressure softening is included; (2) the exponents in both functions $f_1(p)$ and $f_2(p)$ were set to zero to exclude the effects of pressure softening as well as hardening. The two force-time curves C1 and C7 are shown in Figure 5.6 for the two cases respectively. Curve C1 shows that the total load drops only slightly after the peak. Curve C7 shows that the total load peaks at about 2.4 MN, lower than all the other cases, in which the peaks are in the range of 3 to 3.6 MN. This shows that without pressure hardening ($f_1(p)$) damage develops faster resulting in a lower peak load. Also without pressure softening, no fast load drops will occur, instead, the total load will go up as contact area increases. It was also found that the damage for both cases was concentrated near the edge of the interface.

Model results of damage distributions at the end of the analyses are shown in Figure 5.7 to Figure 5.9 (r ranges from 5 to 25). The figures show a thin layer of highly damaged material in contact with the indenter ($r \geq 15$). For the case of $r = 35$, figures 5.10a, b and 5.11 show the progress of damage at the peak load, after the load drop and at the end of the analysis, respectively. It can be seen that the damage

starts at the edge of the interface. It then begins to develop towards the center of the interface. This development of damage leads to the downswing of the total load. After the load drop, the damage zone will form a crushed layer at the interface. The center area has higher damage due to high confining pressure. A tensile zone with tensile stresses higher than 1-2 MPa (this is the typical range of ice tensile strength) is shown in Figure 5.12 ($r = 35$). This indicates that possible fractures may occur in this area. Without modeling of the removal of the crushed material and possible failures due to fractures (both of which will result in the removal of materials from the contact surfaces), it is difficult to model further load oscillations. This analysis shows that the damage and its enhancement of creep deformation can result in sharp load drops and the formation of highly damaged thin layer of material at the interface.

Figure 5.13 shows that development of viscosity, damage and hydrostatic pressure in the crushed layer (for the case of $r = 35$). It shows that the viscosity is reduced as much as 1,000 to 10,000 times after the load drops. The viscosity near the edge and in the center areas has been reduced most. The whole process takes place in a very short time. When load drop occurs, the damage level is between 3 to 4 and the pressure is in the range of 45 to 50 MPa. These values are important in the development of a simple model later. It was also found that when the exponent $15 \leq r \leq 25$ the development of viscosity, damage and hydrostatic pressure in the crushed layer is similar to the case of exponent $r = 35$. This can be seen in Figure 5.6 as well from the load curves. Therefore an exponent of $r = 20$ will be sufficient in future modeling.

It is worth pointing out that based on the analytical and testing results discussed in the previous chapters (see also Xiao, 1991), it was found that the elastic strain is small, less than 10% of the total strain, as is the delayed elastic strain. The specifications of elastic and delayed elastic strain are less important than the secondary creep strain, as far as accuracy is concerned. The creep strain dominates the deformation process.

But once the "structure break-down" occurs, the three Kelvin units will break into three dashpots and make significant contributions to the reduction of viscosity, as well as the total deformation. They will play a important role after the peak load, therefore they can not be ignored. A simplified model is proposed later by converting the three Kelvin units into one equivalent dashpot.

5.3.2 Modelling of Ice Sheet Indentation Test

In this section, a 3-D finite element model is developed to simulate the ice sheet indentation test as discussed in chapter 3 and Finn (1991). It is believed that dynamic ice forces can result from constant or near constant relative velocities between ice and structure; far field ice velocities need not vary with time. Consistent with the analysis discussed in the previous section, constant displacement rate loadings will be addressed. Two cases are considered; the first assumes a rigid structure, while the second uses a measured value of the stiffness of the indenter so that the ice is not subject to a constant loading rate.

Assuming that the structure is rigid, the indentation test is modelled using the finite element geometry shown in Figure 5.14, which is a view from the top, onto the plane of the ice sheet, with the indenter moving upwards. The modelled conditions have been set up to duplicate as closely as possible the conditions of the experiment denoted as Fresh6_HI_Run3 where the indentation speed was 50 mm/s. The ambient temperature was -5^{0}C. The indenter width and the ice thickness were 120 mm and 35.6 mm, respectively.

First, the indentation of the intact ice sheet is modelled to obtain the stress, the damage development and its distribution. The change in viscosity of ice is also examined, which is a function of stress and damage. The total load vs time history is plotted in Figure 5.15. It can be seen that after the peak load at about 0.06 second,

the total load drops rapidly as a result of damage progressing into the ice adjacent to the indenter. The predicted peak load is about 34 KN. This is in line with the measurements of 20 to 30 KN as shown in Figure 3.27. Two points should be noted. First, the force-time curve shows that after the first load peak, the total force drops to about two third of the peak value, it then followed by a load build-up instead of continuous dropping as damage progresses. From the test results it shows in many cases the load would drop to zero. This is due to the facts that (a) the viscosity of the material will increase once the pressure is reduced; (b) no removal of material (extrusion of crushed ice) is modelled in this simulation, while during the tests, a large amount of crushed ice was extruded out from the interface, which could result in no direct contact between the indenter and the ice. Therefore zero contact forces can be measured during the tests. In the modeling, there is always material in contact with the indenter and the calculated forces can not be zero without removal of material (elements) from the interface. The second point is that as shown in Figure 5.15, the slope of the load build-up during the second loading cycle is not as steep as in the first cycle. This is due to first, the indenter is still directly in contact with highly damaged material (no material had been removed from the previous load cycle); secondly, the hardening process is not included in this model, while in reality, a sintering process can occur at the center of the interface.

The damage distribution shown in Figure 5.16 indicates that most of the damage occurs adjacent to the indenter in the center of the interface where confining pressure is high, as well as near the edge of the indenter where the shear stress is greatest and the mean pressure is least. The pressure distribution in the contact interface changes as damage progresses. It is initially high at the edge due to stress concentration and decreases when the ice is highly damaged. High pressure then moves to the center of the interface due to high confining pressure. The distribution of maximum principal

stress (or alternately, the maximum tensile stress) in the X-Y plane (the plane of the ice sheet) is given in Figure 5.17. It can be seen that in-plane tensile stresses which are much higher than 2 MPa have been developed in the area near the edge of the indenter, so tensile cracks could occur in this area, therefore resulting in radial fractures. Figure 5.18 shows the tensile stress in Z direction (vertical to the plane of the ice sheet). It shows that high tensile stress could result in spalling failures from the top and bottom of the ice sheet near the indenter. These failures, in association with the extrusion of the crushed ice, would lead to sudden load drops and regular saw-tooth pattern of load oscillations, in many cases the load can drop to zero.

It is assumed in the above model that the indenter is rigid and moving at a constant speed and the analyses were static. But the indentation system in the experiments was measured to have a static stiffness of about 9.4 MN/m. The measured displacements of the indenter relative to the carriage of the indentation system were in the range of 1 mm to 2 mm. Accounting for other factors in the measurement of these displacements, these values are then lower bounds on the actual displacements. A spring of stiffness of 9.4 MN/m was added to the rigid indenter model as shown in Figure 5.19. Since the constant speed was measured at the carriage of the indentation system, the actual speed of the indenter can vary due to the flexibility of the system. In this case, it is point B that is moving at a constant speed. Load-time curves are shown in Figure 5.20. It shows that the peak load of model result is higher than the test. This could be due to the nonlinearity in stiffness of the indentation suystem (which was assumed to be linear static). The load peaks at about 0.1 second and then drops much more rapidly. It takes more time to reach the peak load due to the flexibility of the system. Calculated displacements of the indenter and the carriage are shown in Figure 5.21. The maximum relative displacement, i.e. the difference between the displacements at point A and point B, was calculated to be 2 mm. The measured peak load was about

the maximum value calculated corresponding to the relative displacement of 2 mm, so the calculated displacement is not far off the measured values noted above. As shown in the figure, at the point of load drop, the indenter (point A) moves forward much rapidly at the speed of about 500 mm/second, 10 times faster than the carriage (point B) (note that point B is still moving at the constant speed of 50 mm/second). This fast movement of the indenter is the result of rapid growth of damage in the ice adjacent to the indenter, therefore leading to the clearance (extrusion) of the highly damaged (crushed) material from the interface. At the valley of the load drop, the applied force and the reaction force on the indenter will lose its balance. One of the reason is that the material (elements) in contact with the indenter has been highly damaged and has very low stiffness. The indenter is pushed forward by the spring which has stored a large amount of energy during the load build-up phase. When encountering soft material which means low resistance, the movement of the indenter will be accelerated resulting in very large deformation in the elements near the interface. These elements will become highly distorted. Therefore the finite element model will become unstable. Further simulation is very difficult.

In reality, the indentation is a dynamic interaction process. The structure and ice both have mass, viscosity (damping) and other related properties. It is very important to include the dynamic characteristics of the indentation system as well as the ice mass in the study of ice-structure interactions. For example, the speed of the indenter after the load drop should be much slower due to the effects of inertia and damping of the structure and ice mass, and the analysis should be much more stable. During the load build-up phase, the indentation process can be regarded as quasi-static. When the load drops, the process becomes dynamic. Therefore, to fully capture the behaviour of this complex process, a dynamic analysis is recommended.

Damage distribution near the indenter is shown in Figure 5.22. Calculated maxi-

mum principal stress near the interface is shown in Figure 5.23. It shows that tensile stress higher than 2 MPa has occurred. The tensile strength of ice is usually 1 to 2 MPa, therefore crushing failures as well as tensile fractures should have taken place even before the load has reached the peak. Since no fracture analysis is included in this analysis, no cut-off values were used for fracture failures. It only shows that spalls or cracks can be developed along with crushing failures. Note that the measured frequency of load oscillation is about 10 Hz. The calculated first load drop in Figure 5.20 is also about 0.1 second.

5.4 Analysis of Fracture and Spalling

5.4.1 Introduction

The analysis of fracture is carried out in ABAQUS (Hibbitt et al. 1997, version 5.6). The direction of virtual crack advance is specified in ABAQUS by means of a vector **n**. This makes it possible to consider various angles of crack propagation. The estimation of the ratio of K_I and K_{II} can also be made in linear elastic materials; two J integral requests are made, one in the crack direction (J_x) and the other in the perpendicular direction (J_y). This gives

$$J_x = \frac{K_I^2 + K_{II}^2}{E'} \tag{5.1}$$

$$J_y = -\frac{2}{E'} K_I K_{II} \tag{5.2}$$

where $E' = E/(1-\nu^2)$ for plane strain. From these two equations, the ratio of K_I and K_{II} can be estimated by

$$\frac{K_I}{K_{II}} = (\frac{J_x^2}{J_y^2} - 1)^{1/2} - \frac{J_x}{J_y} \tag{5.3}$$

A second method of estimating the ratio of K_I and K_{II} is based on the ratio of displacements in the direction of and perpendicular to the crack direction, taken at

a pair of nodes near the crack tip. This ratio will be used to estimate the direction of crack growth later.

5.4.2 Initial Fracture Analysis

A trial case was considered to conduct an initial fracture analysis. Due to the common existence of flaws in ice features, the geometry and the initial crack are shown in Figure 5.24. In the initial analysis, linear elastic material behaviour with plane strain condition was considered. A parabolic load distribution was assumed to be applied at the contact surface. This is consistent with the kind of load distribution found in the field tests after some damage has been developed at the ice-structure interface.

The finite element model is shown in Figure 5.25(a). More details of the area around the crack are shown in Figures 5.25(b) and 5.25(c). The elements around the crack tips included a singularity (on the order of 1/r, where r is the distance to the crack tip), which assists in obtaining accurate values of J. The initial crack length was 40 mm, and the crack orientation angle was $\alpha = 0°$. First, J values are calculated with increasing loads. When the J reaches its critical value. The stress intensity factors at the crack tips are calculated to find out the direction of crack propagation. The calculation of K_I and K_{II} showed that K_{II} predominated, i.e. the crack tips were in almost pure shear. The values of K_I and K_{II} at both crack tips were almost equal. The load on the interface was 3.6 MN when critical $K_{II} = 0.82K_I$ was reached. Based on Figure 2.7, the propagation would be at an angle of 75° to the original crack surface, and Figure 5.26 shows the area remeshed for the first crack extension. Remeshing is necessary after the crack extension, which would lead to rather unsatisfactory finite element meshes. A further analysis using the remeshed model showed that J values at both ends of the crack were more than doubled as extension proceeded. This means the crack would propagate at an accelerated rate.

Table 5.1: Details of Crack Extension

Total Load	Crack	J Value at Left Tip	J Value at Right Tip	K_I/K_{II}	Crack Extension Angle θ
3.6 MN	Initial Crack (40 mm)	0.82	0.83	0	75°
3.6 MN	First Crack Extension (5 mm)	1.90	1.87	1.6	45°

Based on the analysis similar to that described above, a second crack extension would propagate at an angle of 45° to the original crack surface (Figure 5.27). The analysis results are summarized in Table 5.1. The evaluation of J integral at the crack tips of second extension has shown a significant increase in J values, which will lead to very unstable crack propagation. The J values for the second extension have therefore been omitted from Table 5.1; further investigation and analysis of the path of crack extension would be very difficult.

The ratio of K_I to K_{II} shows a significant increase after the second crack extension, which means that K_I became dominant and the crack tips were approaching the tensile zones. The cracks would follow a trajectory similar to that for "wing" cracks; after the second extrusion, it was assumed that the cracks continued on the same trajectory as in the second extension; this was approximately in the direction perpendicular to that of maximum tensile stress in the areas near the crack tips. On this basis, elements were removed which simulates a spall, see Figure 5.28a. The results of the loading curve with elements removed are shown in Figure 5.28b.

5.4.3 Analysis Based on Damage and Fracture

In this analysis, the finite element models in the previous section were adopted. Instead of the parabolic loading, a flat rigid indenter was applied at the contact

Table 5.2: Details of Crack Extension

Total Load	Crack	J Value at Left Tip	J Value at Right Tip	K_I/K_{II}	Crack Extension Angle θ
11 MN	Initial Crack (20 mm)	0.85	0.85	0	75°
11 MN	First Crack Extension (5 mm)	2.19	2.19	3.0	32°

interface. This is to simulate the ice-structure interaction (see Figure 5.29). A crack orientation angle of α= -10^0 was assumed based on a few trial runs at different angles. This angle gives higher J values for the given loads. The structure was moving at 100 mm/s. A friction coefficient of 0.3 was applied between the structure and ice.

The analysis of the crack propagation (leading to a spall) is similar to the previous section. Table 5.2 summarizes results regarding crack extensions. Due to stress redistribution caused by the spall, high stress concentration will be developed near the contact surface which will in turn trigger one or more spalls, most likely in the area opposite to the initial spall. Further analysis shows that right after the first spall, a crack or flaw of size as small as 5 mm (on the order of microcracks) which most certainly will exist, would (almost) simultaneously grow and extend to the surface leading to a second spall. Figure 5.30 shows the resulting configuration of finite element mesh after two spalls. In reality more spalling failures would also be developed due to further stress concentration so that the combined effect should be considered in future analyses. It is worth noting that even without crack propagation (leading to a spall failure), damage alone can cause high tensile stress zones resulting in fractures, as discussed in earlier sections.

Figure 5.31 shows the force-time curve after two spalls. Although the immediate

effect of spalls is relatively small compared with some field test results in terms of total load drops after spalls, the cumulative effect is quite significant. Figure 5.32 shows the load history of a damage analysis on the same finite element model without modelling spalls. The peak load from the spall analysis is about 11 MN compared to 28 MN with the damage analysis only. It should be pointed out that the movement rate of the structure is 100 mm/s, the divisions of the horizontal axis of Figure 5.31 correspond to 50, 100 and 150 mm displacement, etc. The pressure distribution at the ice-structure interface is shown in Figure 5.33 for various displacements. The localization of pressure is illustrated. Before the spalls, contact pressure is relatively low and uniform (when indentation distance is less than 10 mm). After the spalls (indentation is larger than 12 mm), the pressure is initially high at the edges and gradually decreases as damage progresses. Eventually, high pressure moves to the center of the contact surface due to confinement (indentation is between 25 mm to 60 mm).

The above is a preliminary analysis of fractures in ice-structure interaction. It shows that fracture spalls can be easily developed under impact conditions. The sources of the spalls can be the existing flaws in the ice with a dimension of a few centimeters. The propagation of cracks can be very fast. The locations of flaws are random. Although in this analysis, two flaws were assumed to be near the top and bottom surfaces of the ice sheet, which result in a symmetric wedge sharp ice profile after two spalls. No symmetric conditions were used due to the random locations of flaws. Fractures will result in stress concentration, which will further enhance the development of damage in the material. The progress of damage will also create more opportunities for crack growth, which in turn will develop more spalls. Therefore these two processes will mutually co-exist and lead to load oscillations.

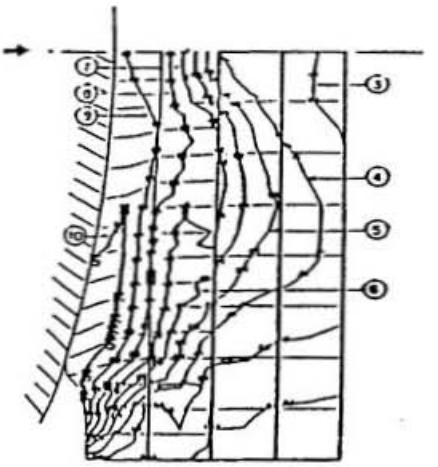

(a) Damage of Half of Spherical Indentation Zone, Test 01. Damage Level of 10 Corresponds to Significant Material Softening, and Reduction of Elastic Modulus of 50% with Linear Damage Scale.

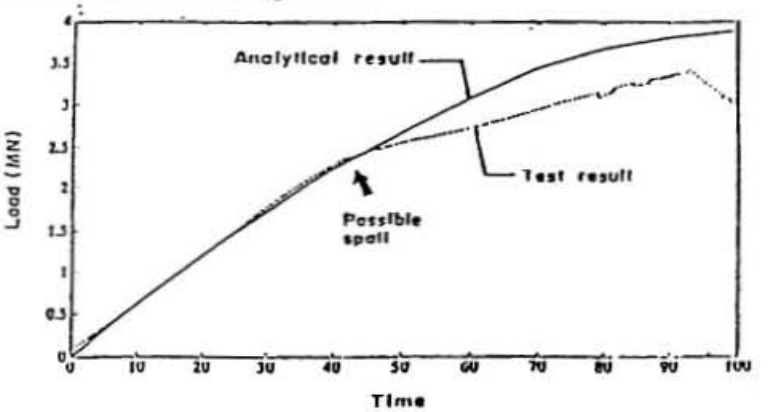

(b) Force-time Curves, Test 01.

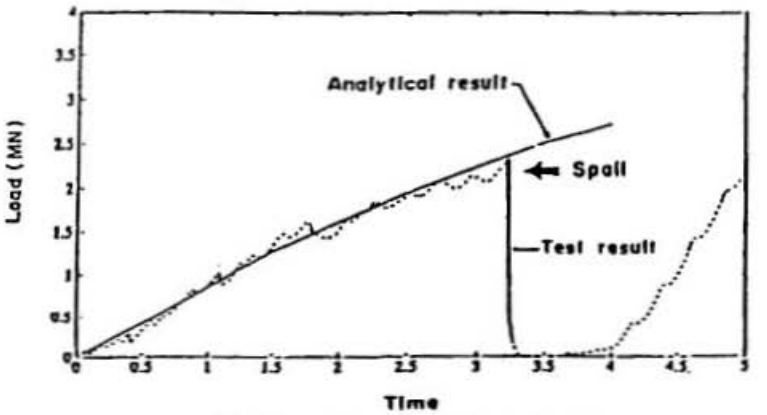

(c) Force-time Curves, Test 02.

Figure 5.1: Simulation of Test 01 and 02 of 1989 test program (Xiao, 1991; Frederking et al., 1990).

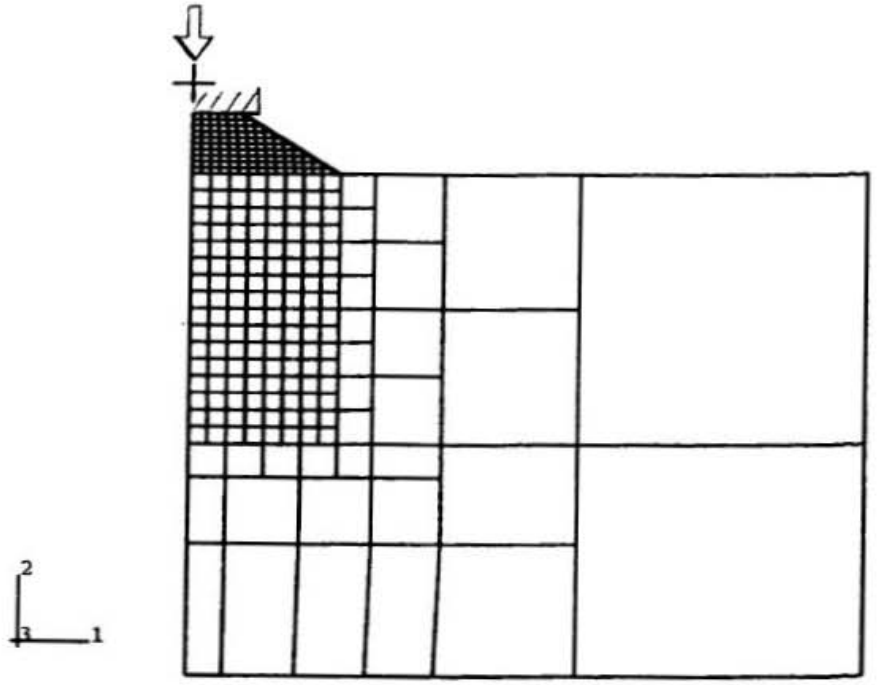

Figure 5.2: Finite Element Idealization of Test 07.

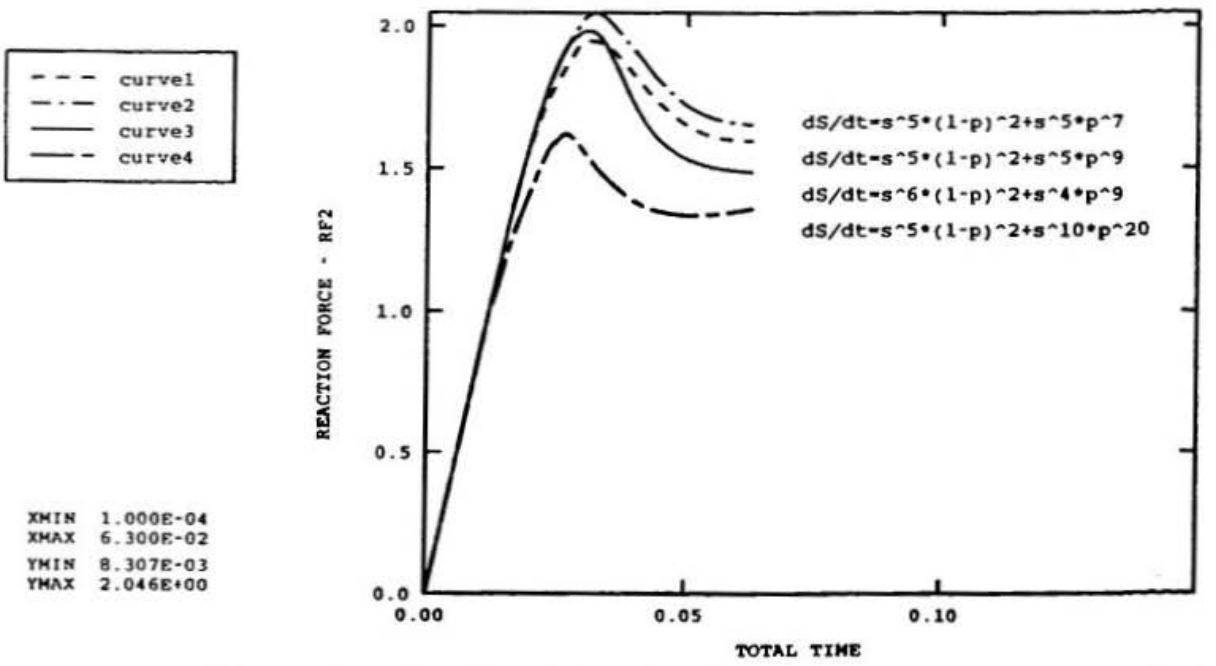

Figure 5.3: Force-time Curves for Analyses with the Damage Model Proposed by Jordaan et al., (1997).

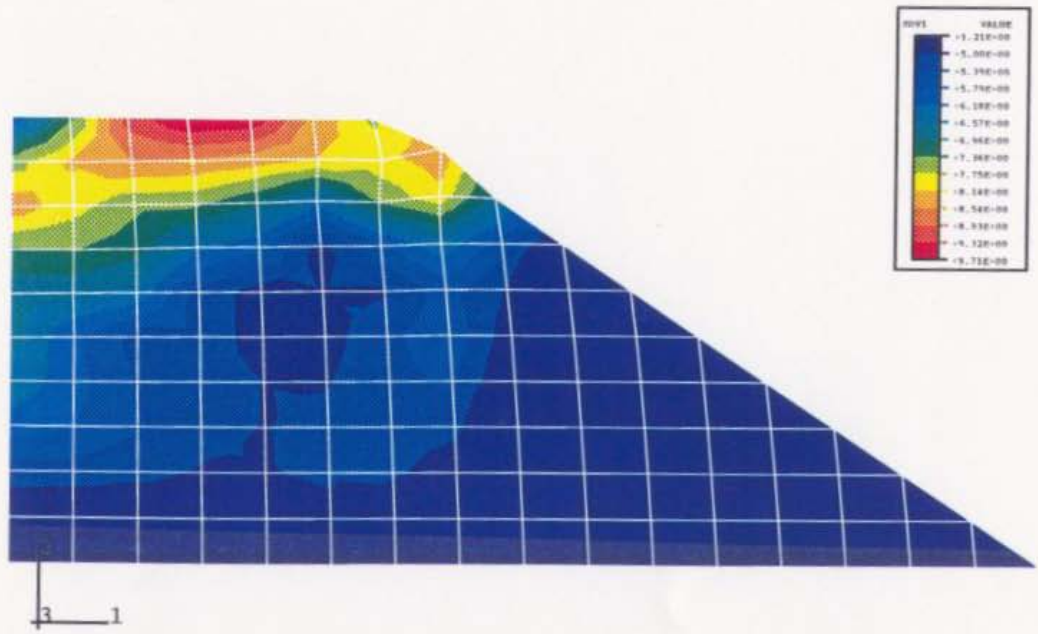

Figure 5.4: Damage Distribution for $dS/dt = s^6(1-p)^2 + s^4p^9$.

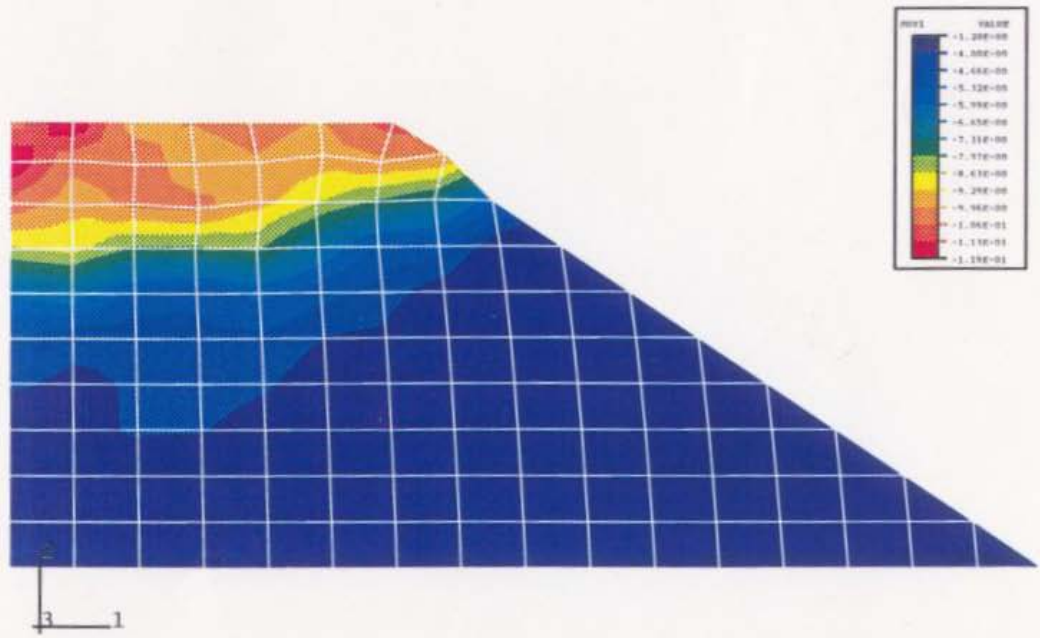

Figure 5.5: Damage Distribution for $dS/dt = s^5(1-p)^2 + s^{10}p^{20}$.

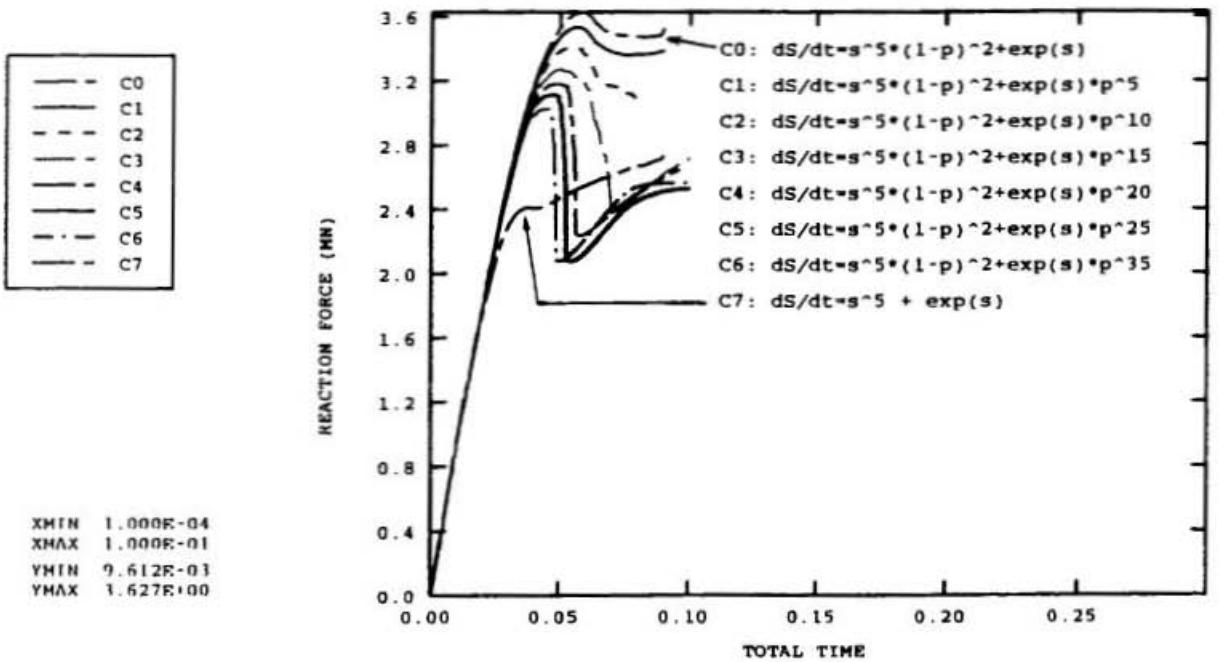

Figure 5.6: Force-time Curves for Analyses with the Damage Model Proposed in This Study.

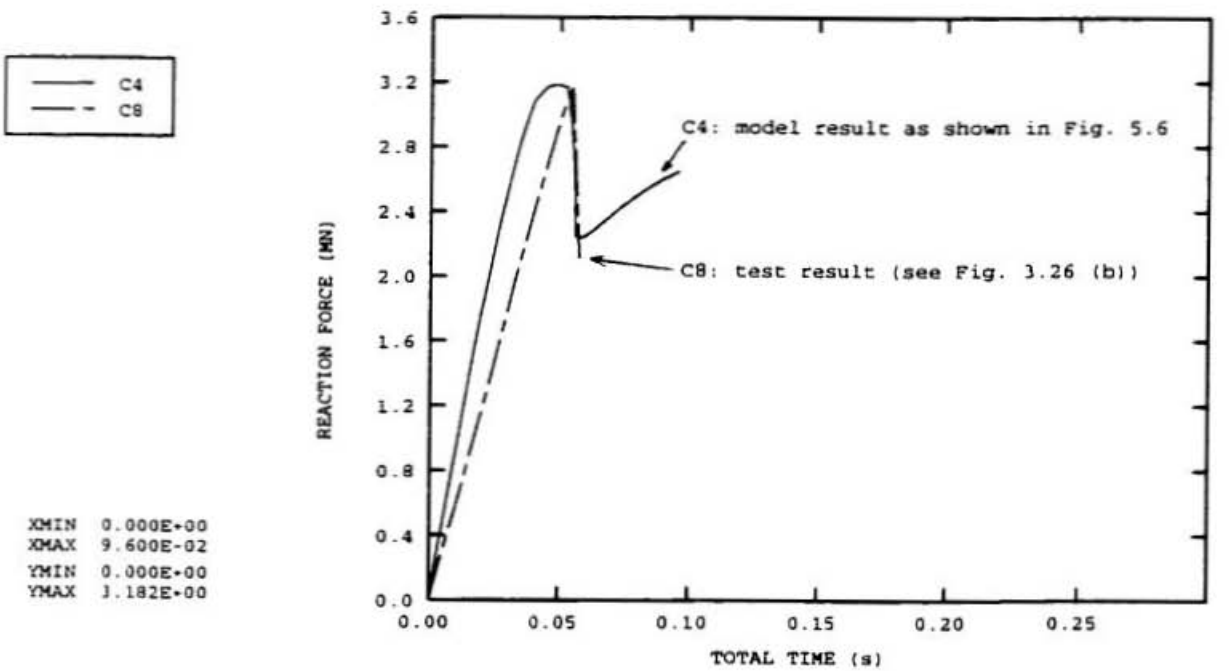

Figure 5.7: Force-time Curve Comparison of Model and Test Results.

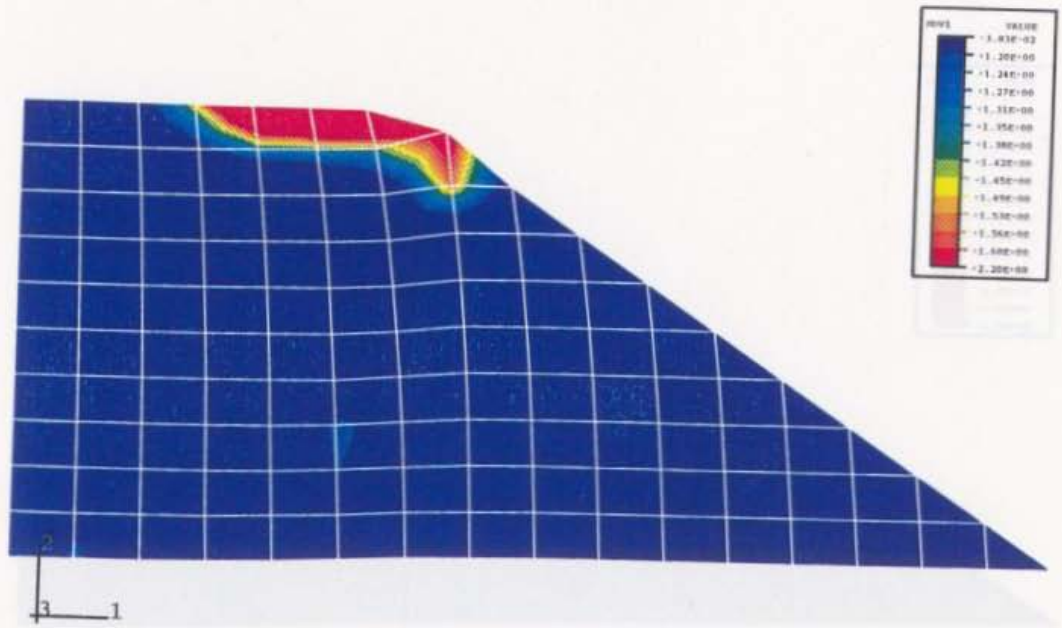

(a)

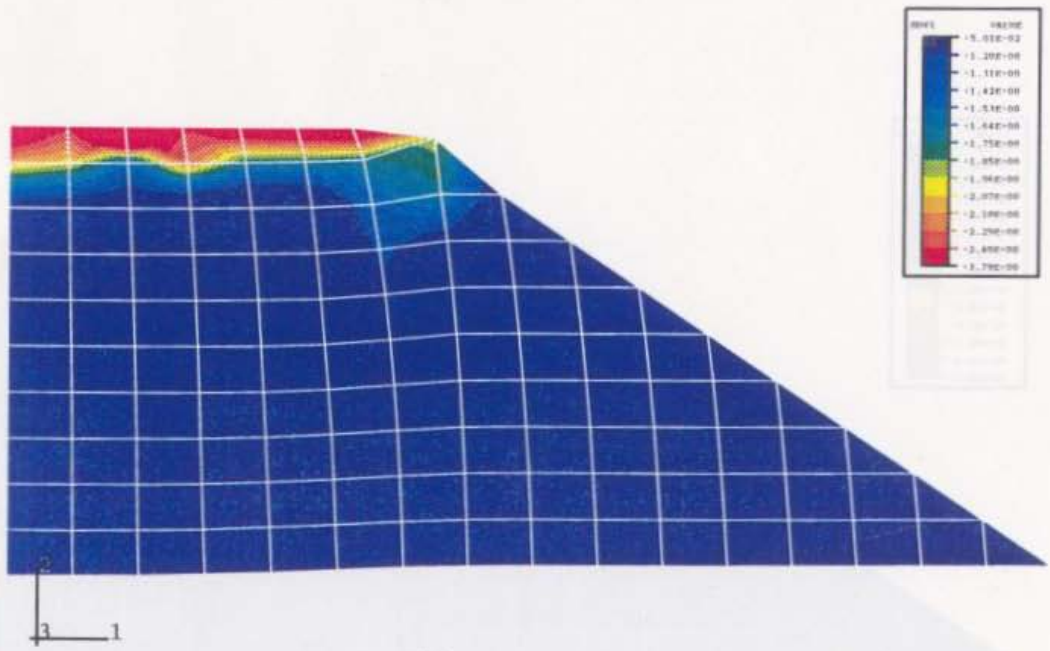

(b)

Figure 5.8: Damage Distribution for: (a) $dS/dt = s^5(1-p)^2 + \exp(s)p^{10}$; (b) $dS/dt = s^5(1-p)^2 + \exp(s)p^{15}$.

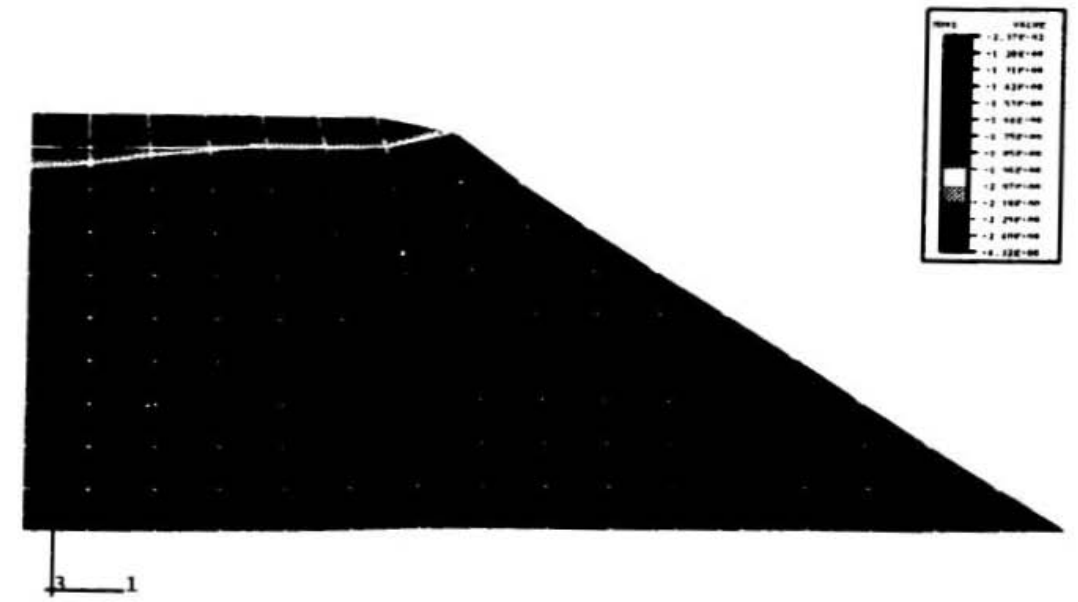

(a)

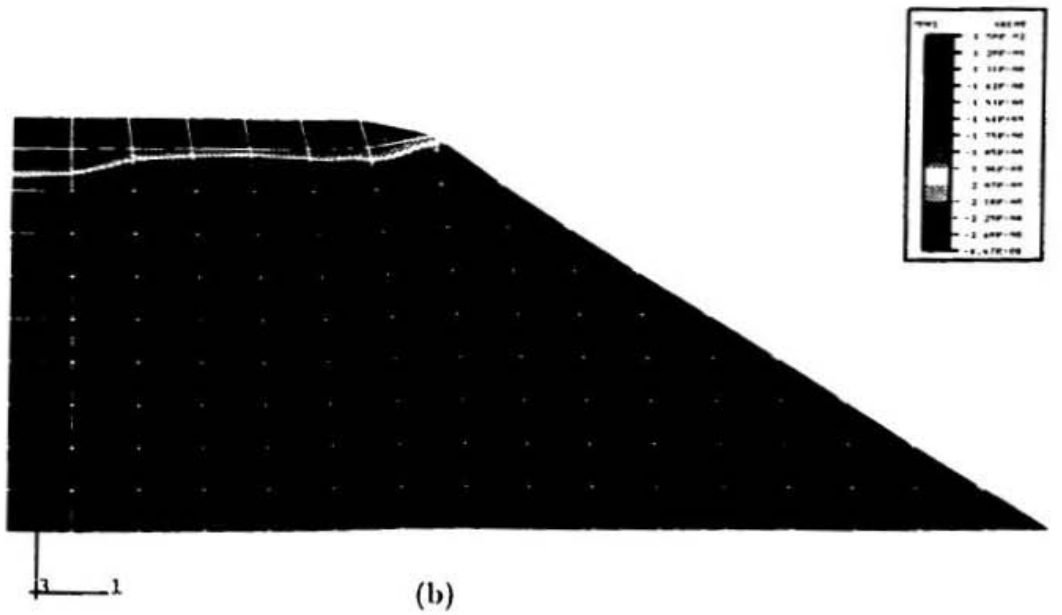

(b)

Figure 5.9: Damage Distribution for: (a) $dS/dt = s^5(1-p)^2 + \exp(s)p^{20}$; (b) $dS/dt = s^5(1-p)^2 + \exp(s)p^{25}$.

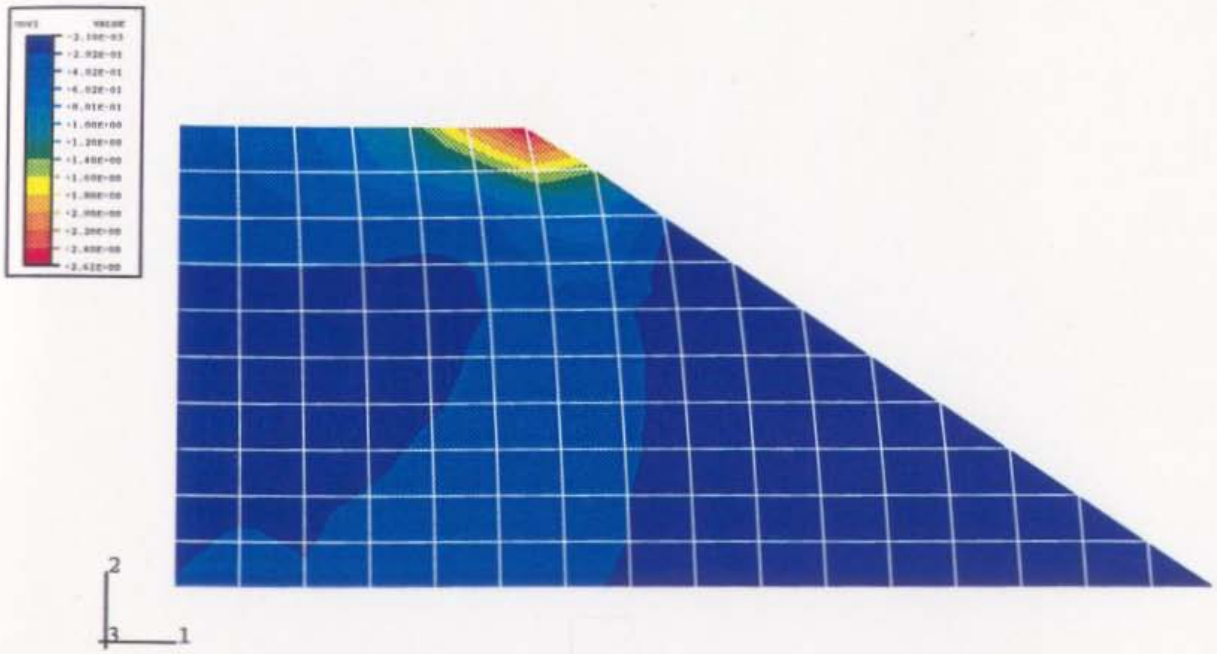

(a)

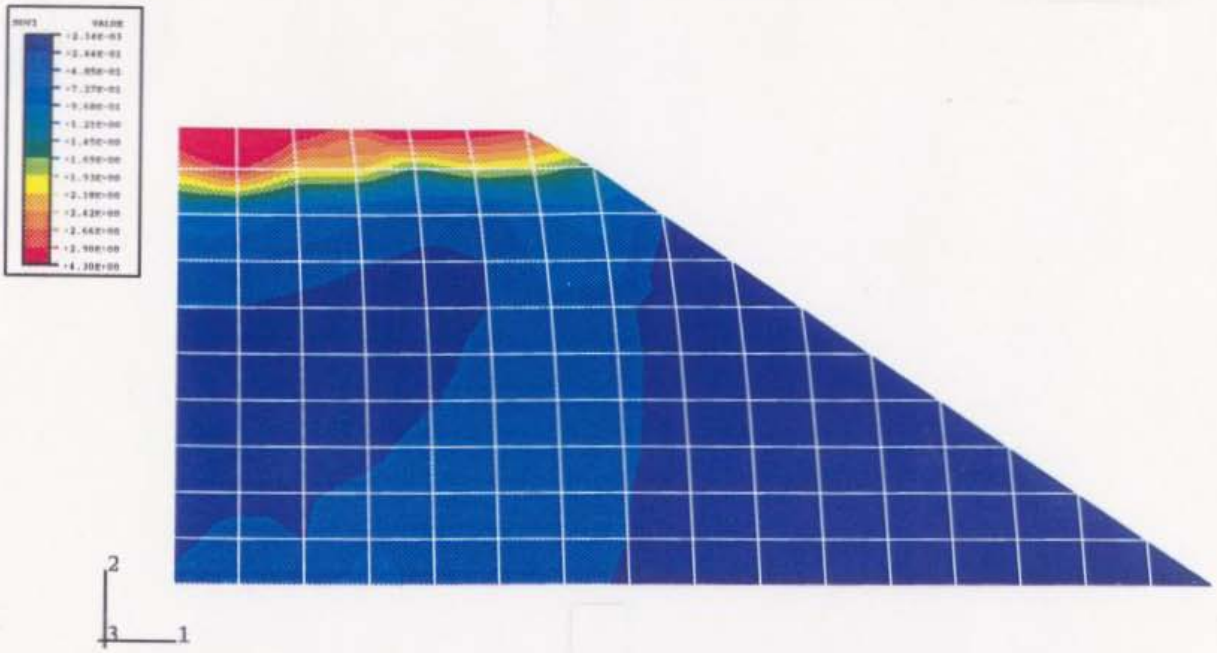

(b)

Figure 5.10: Damage Distribution for $dS/dt = s^5(1-p)^2 + \exp(s)p^{35}$: (a) at the peak load; (b) after the load drop.

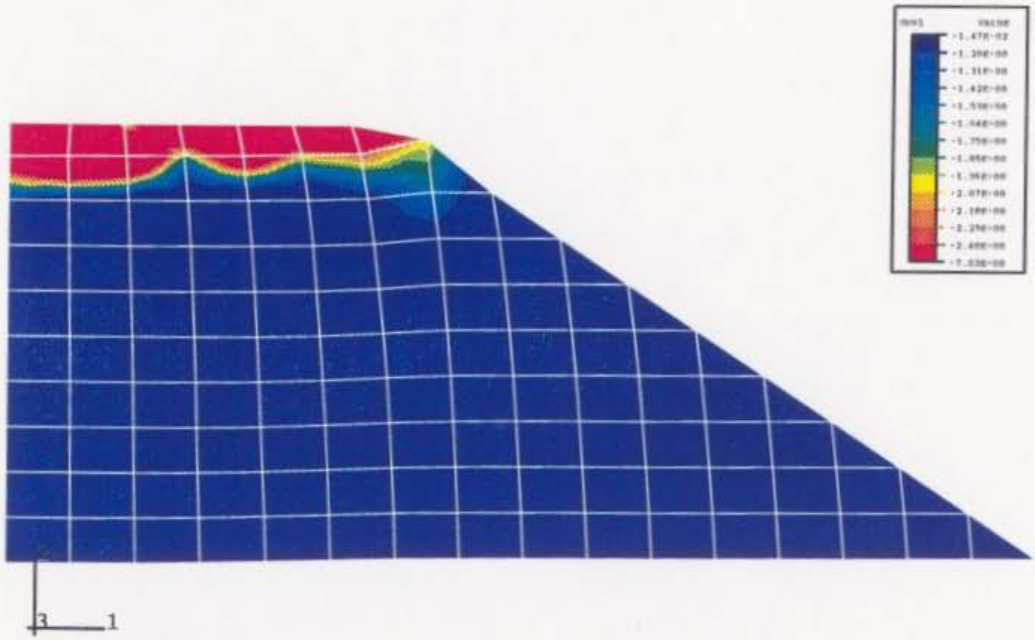

Figure 5.11: Damage Distribution for $dS/dt = s^5(1-p)^2 + \exp(s)p^{35}$ at the end of the analysis.

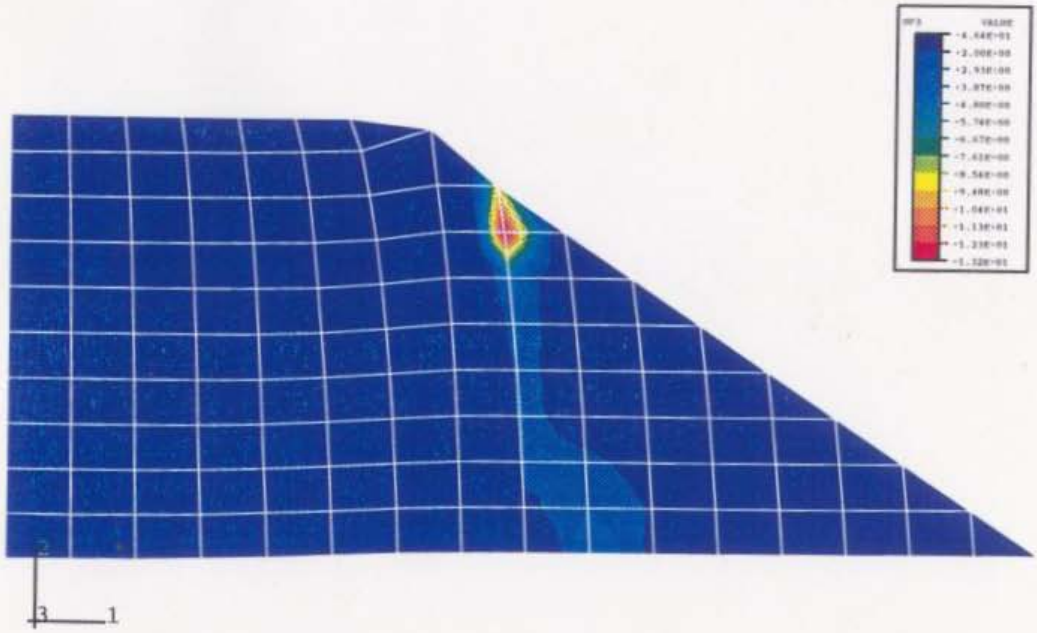

Figure 5.12: Tensile Zone near the Contact Surface.

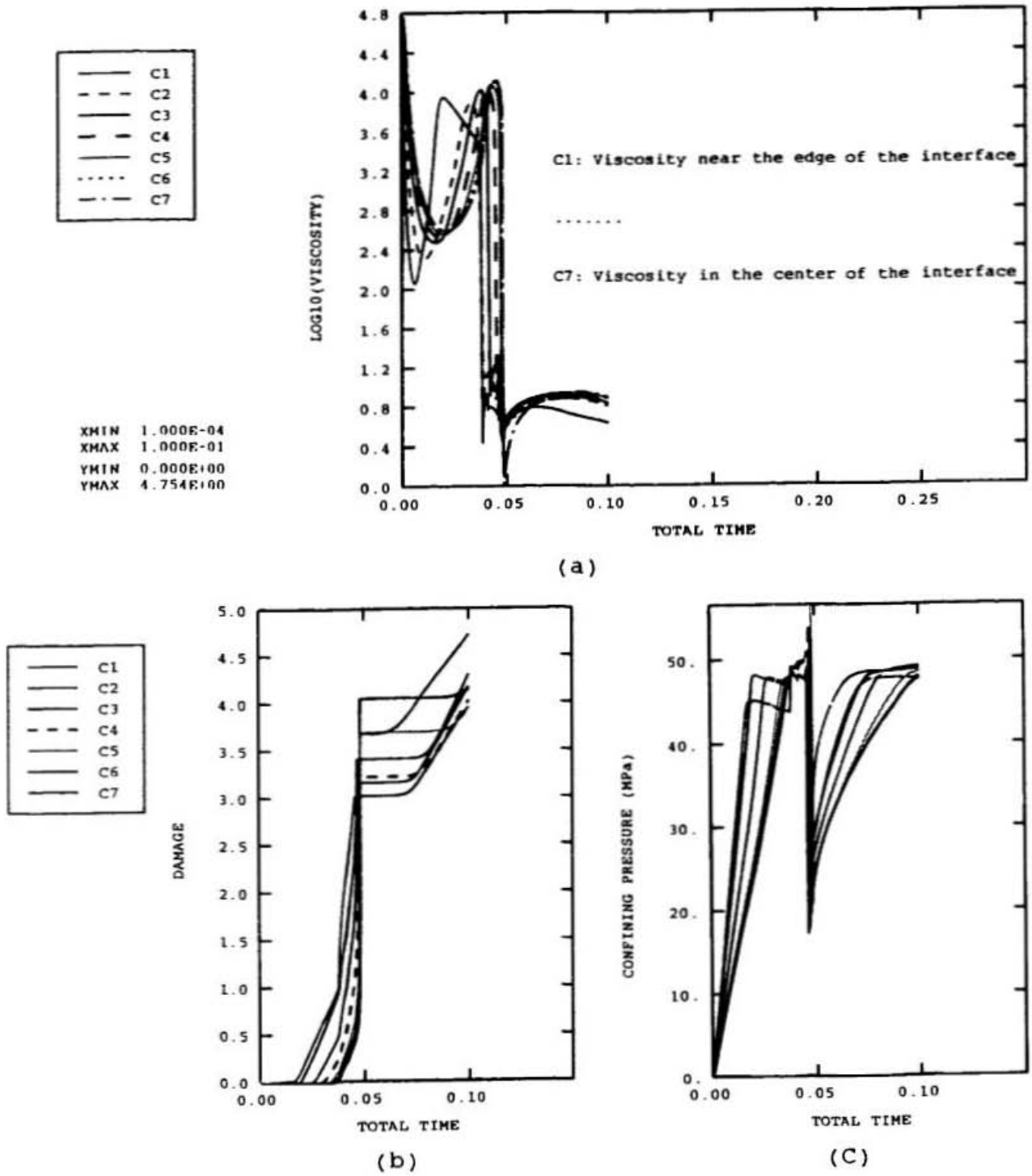

Figure 5.13: The Development of (a) Viscosity, (b) Damage, (c) Confining Pressure for $dS/dt = s^5(1-p)^2 + \exp(s)p^{35}$.

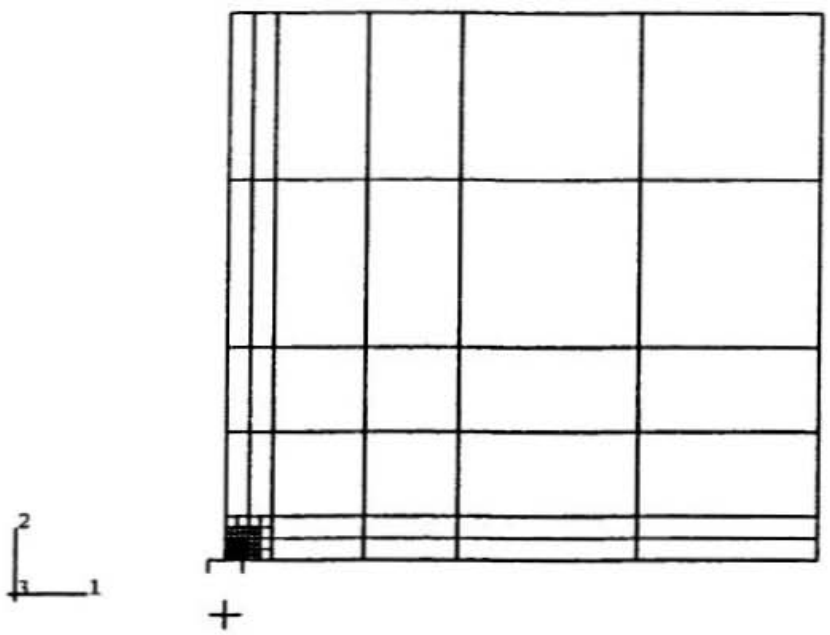

Figure 5.14: Finite Element Mesh for the Ice Sheet Indentation Test with Rigid

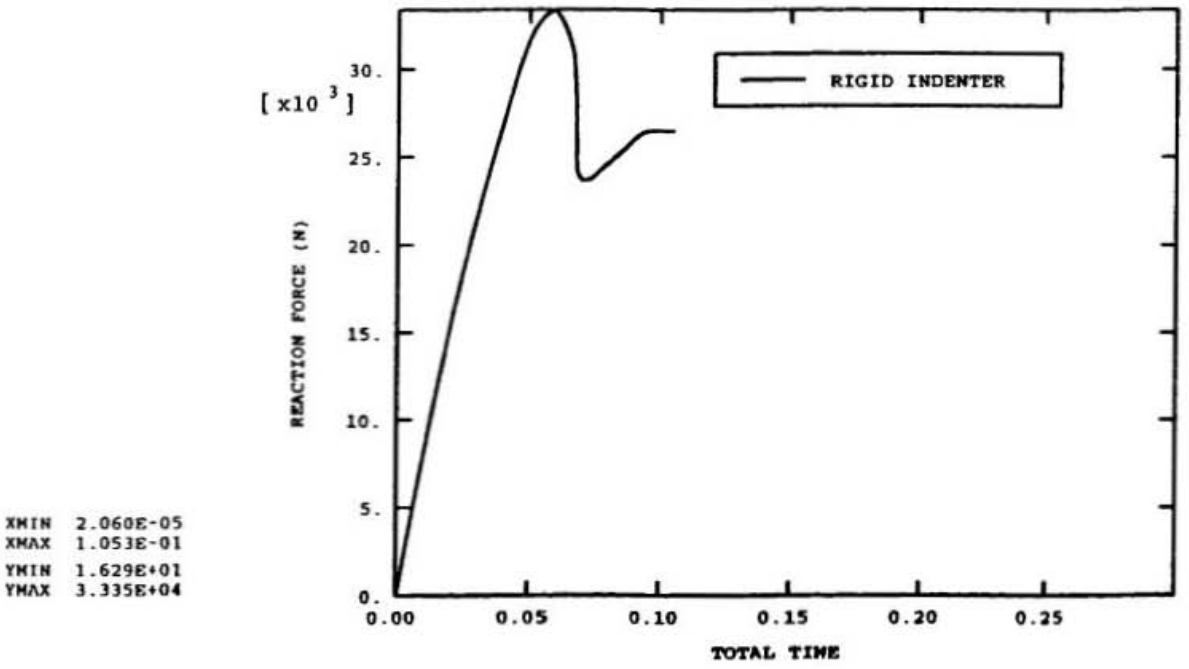

Figure 5.15: Total Load versus Time Relation for the Ice Sheet Indentation Test with Rigid Indenter.

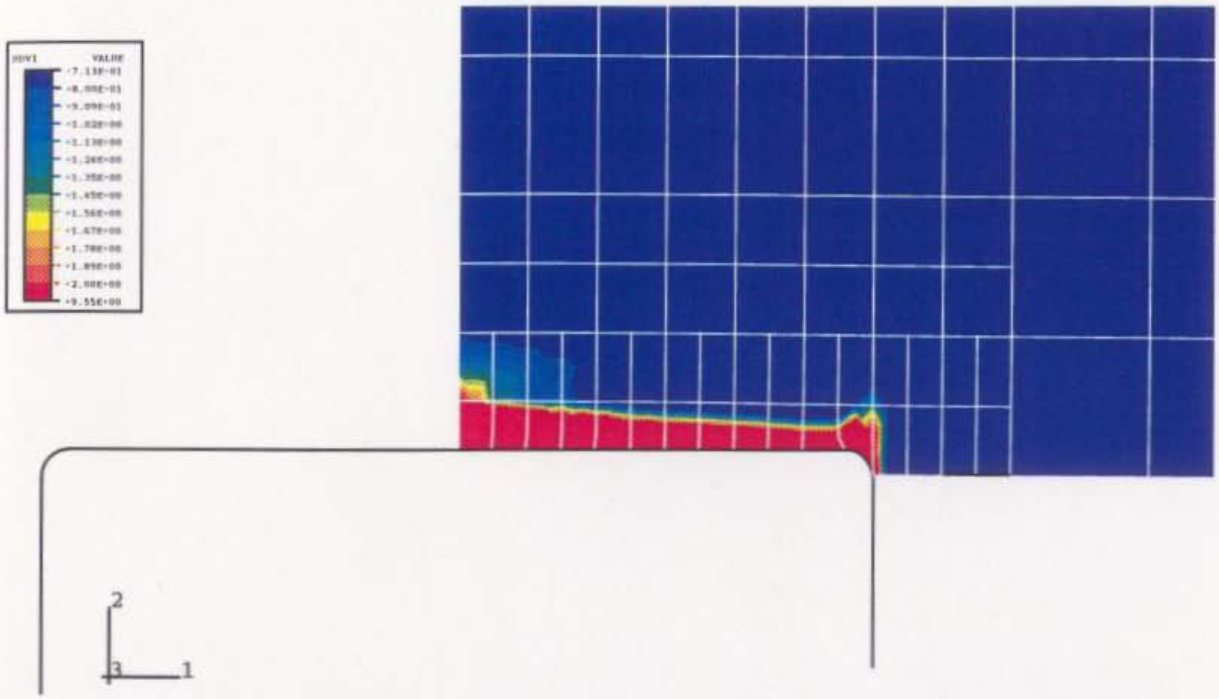

Figure 5.16: Damage Distribution in the Ice Sheet near the Indenter.

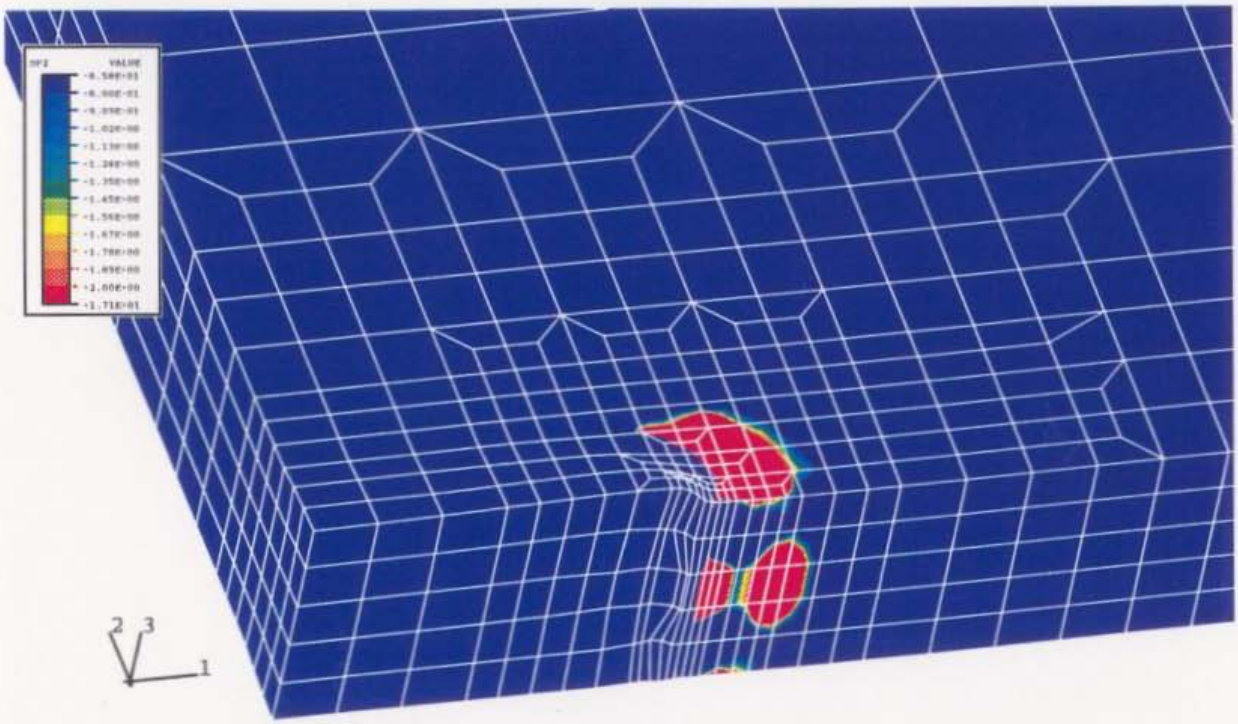

Figure 5.17: Tensile Stress Distribution near the Indenter in the Plane of the Ice Sheet.

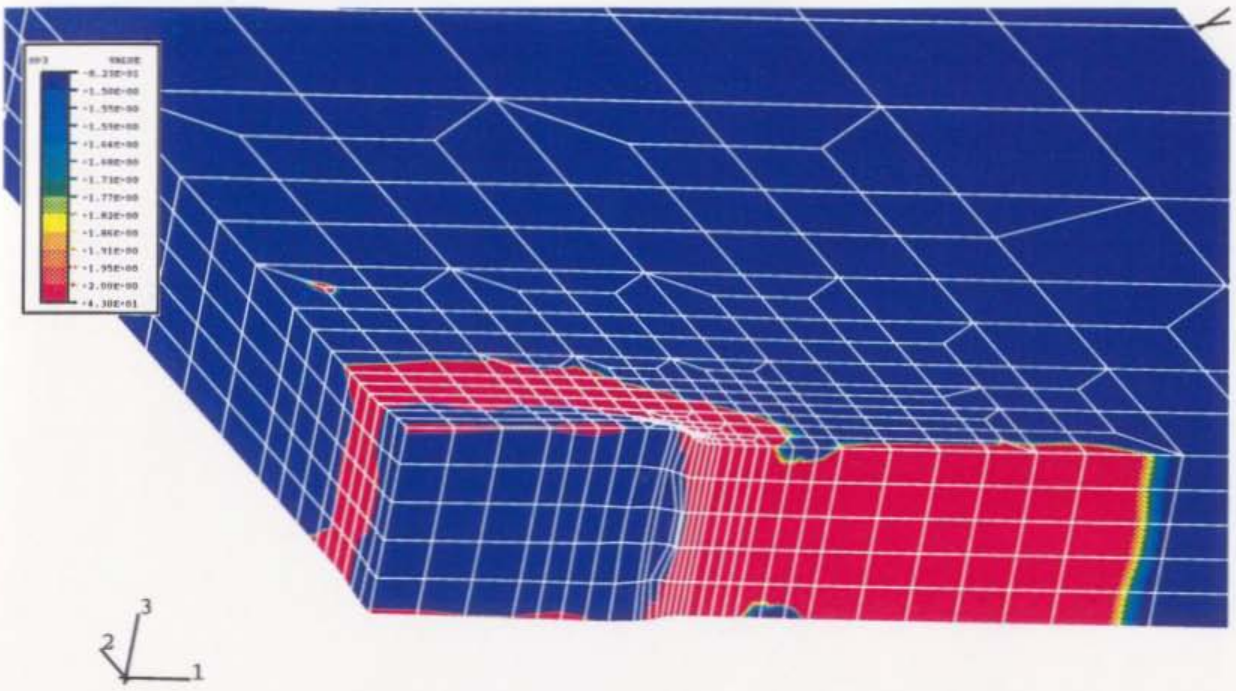

Figure 5.18: Tensile Stress Distribution near the Indenter in the Direction Normal to the Plane of the Ice Sheet.

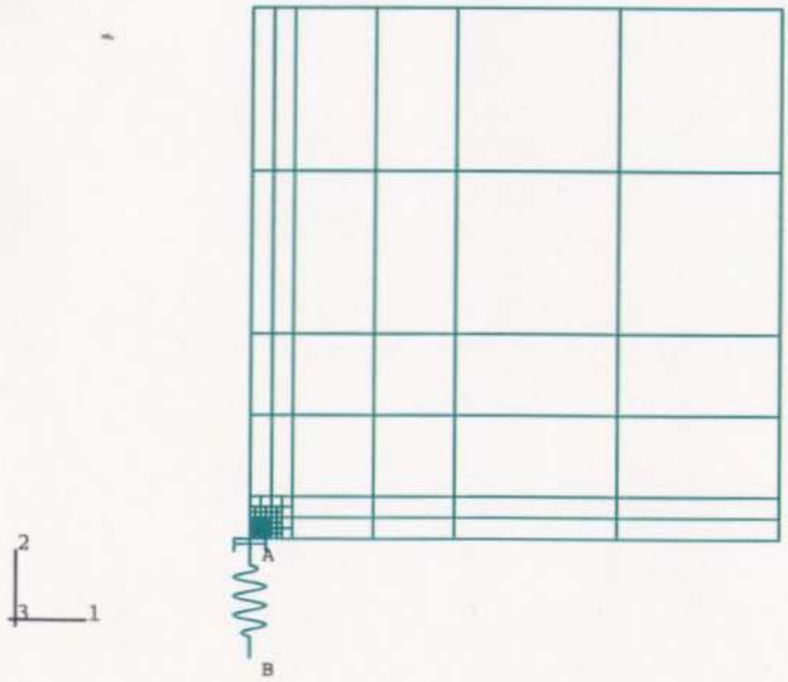

Figure 5.19: Finite Element Mesh for the Ice Sheet Indentation Test with Flexible Indenter.

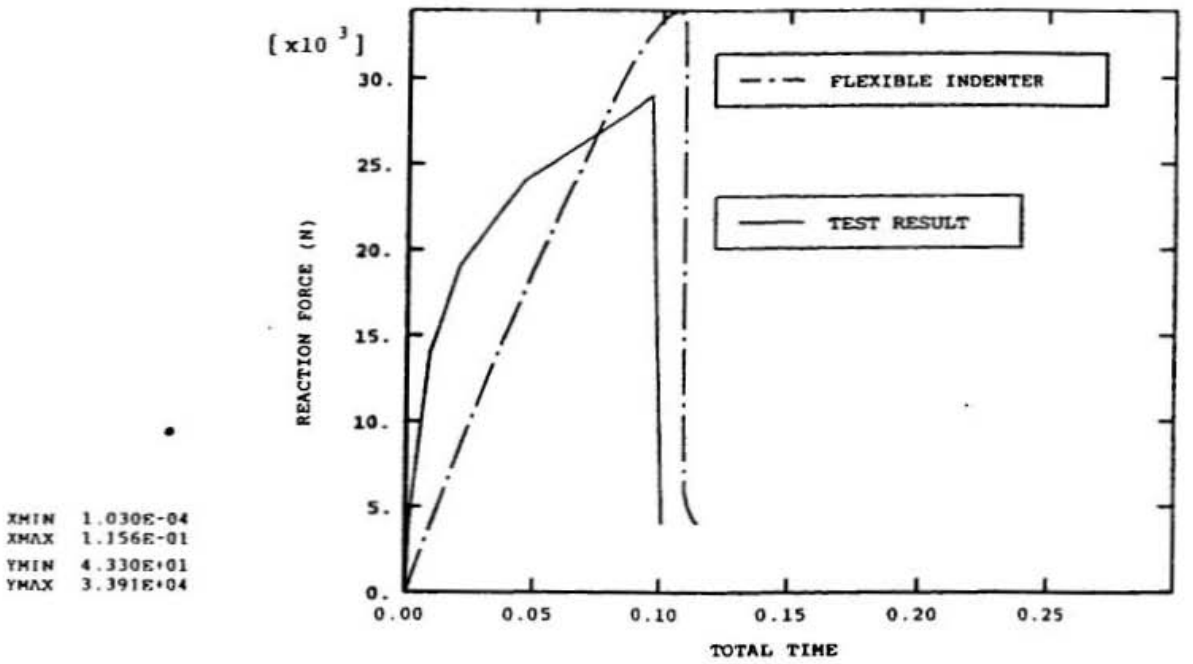

Figure 5.20: Total Load versus Time Relation for the Ice Sheet Indentation Test with Flexible Indenter.

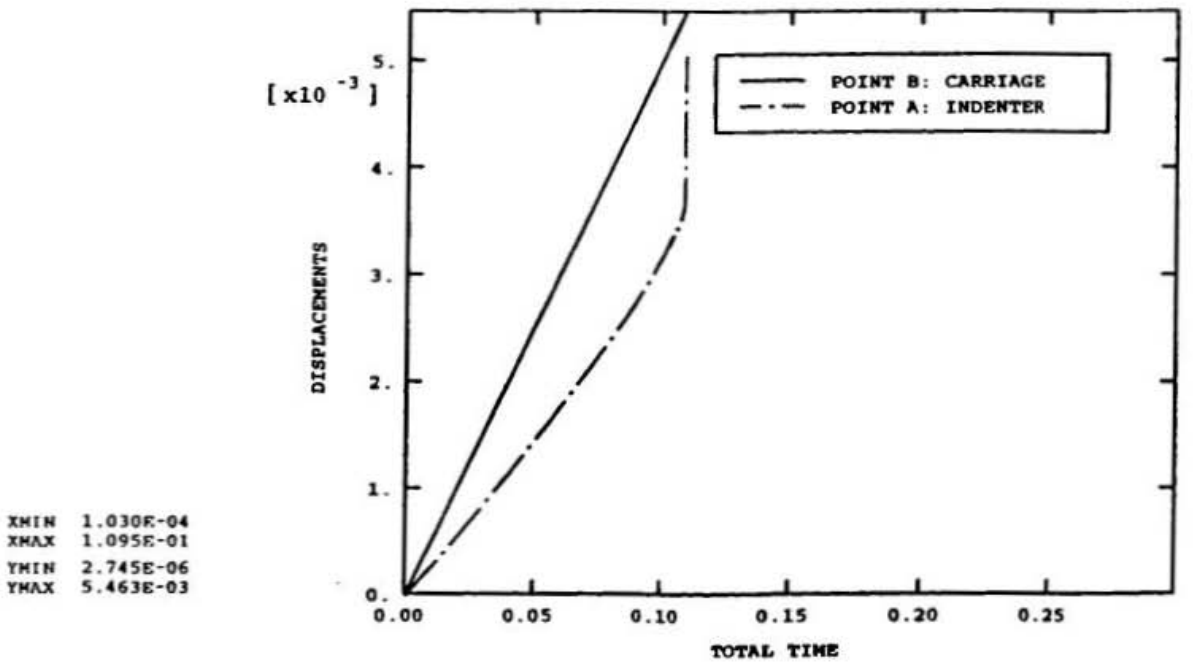

Figure 5.21: Calculated Displacements for Point A and Point B.

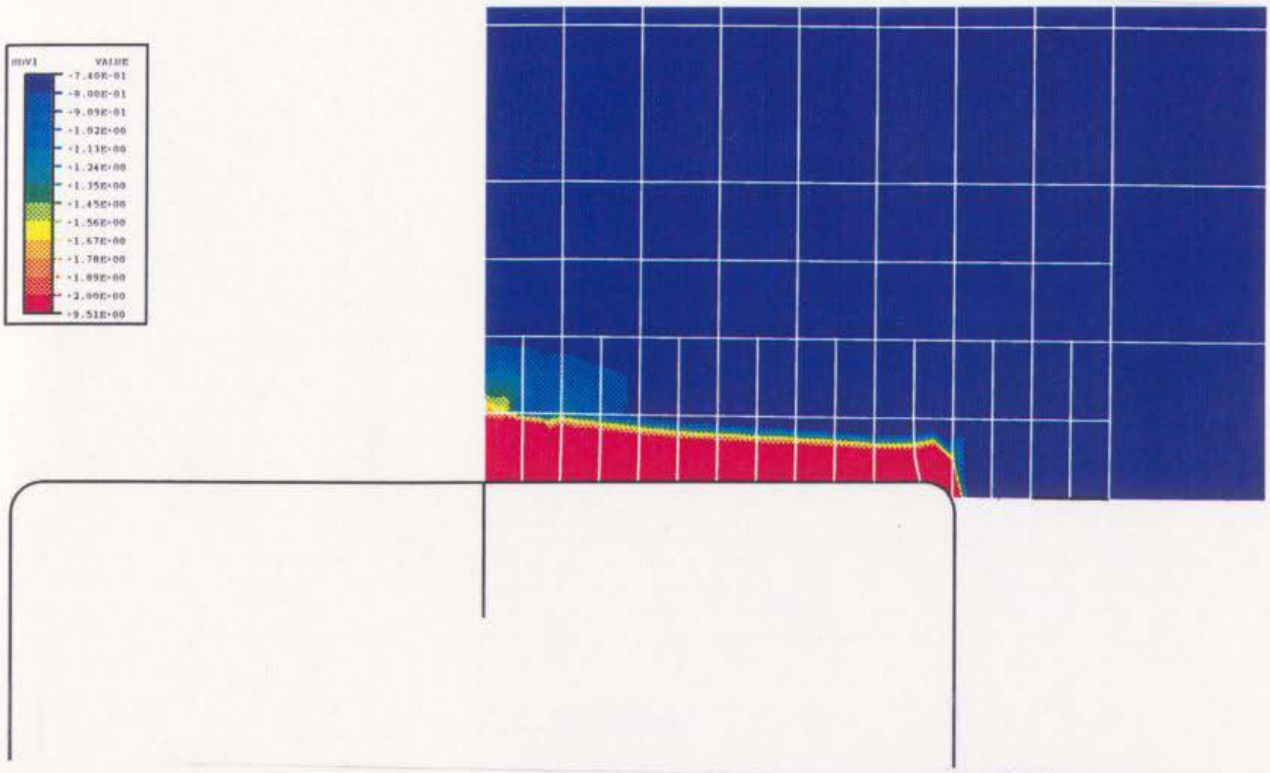

Figure 5.22: Damage Distribution in the Ice Sheet near the Indenter.

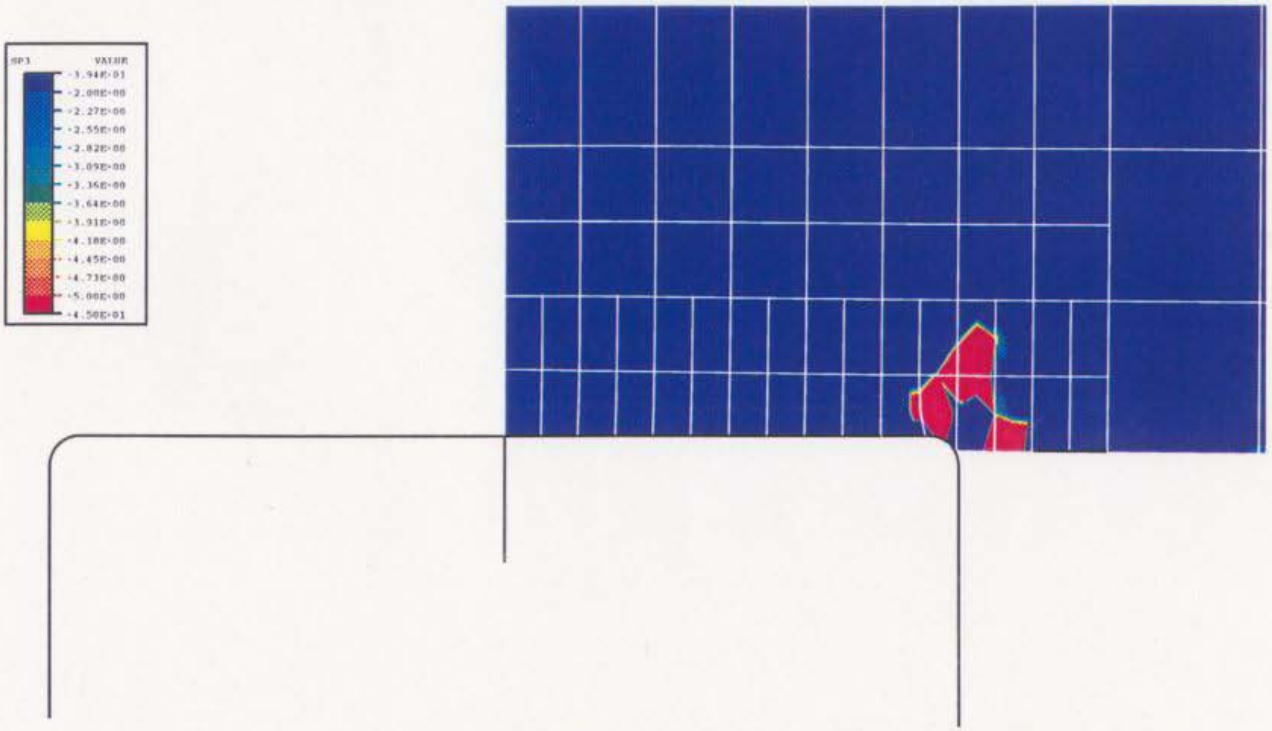

Figure 5.23: Tensile Stress Distribution near the Indenter in the Plane of the Ice Sheet.

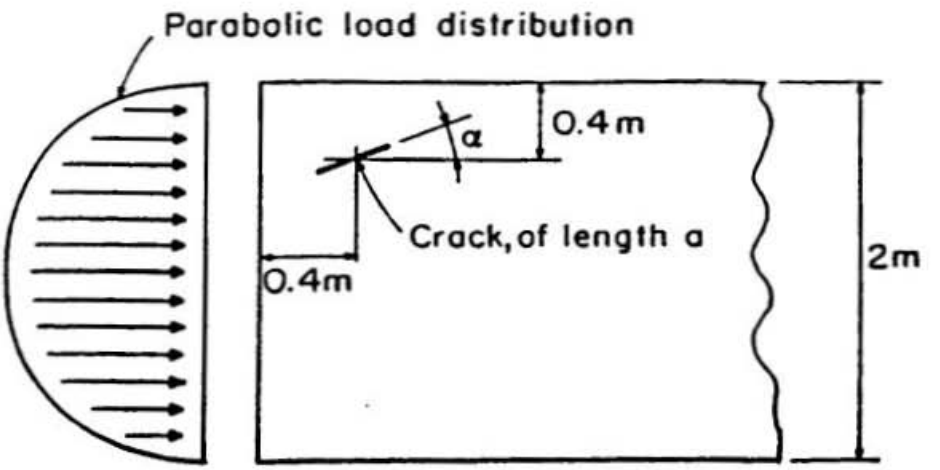

Figure 5.24: Position of Initial Crack: Typical Value of Crack Length of 40 mm, α Varied from Approximately 0^o to 30^o.

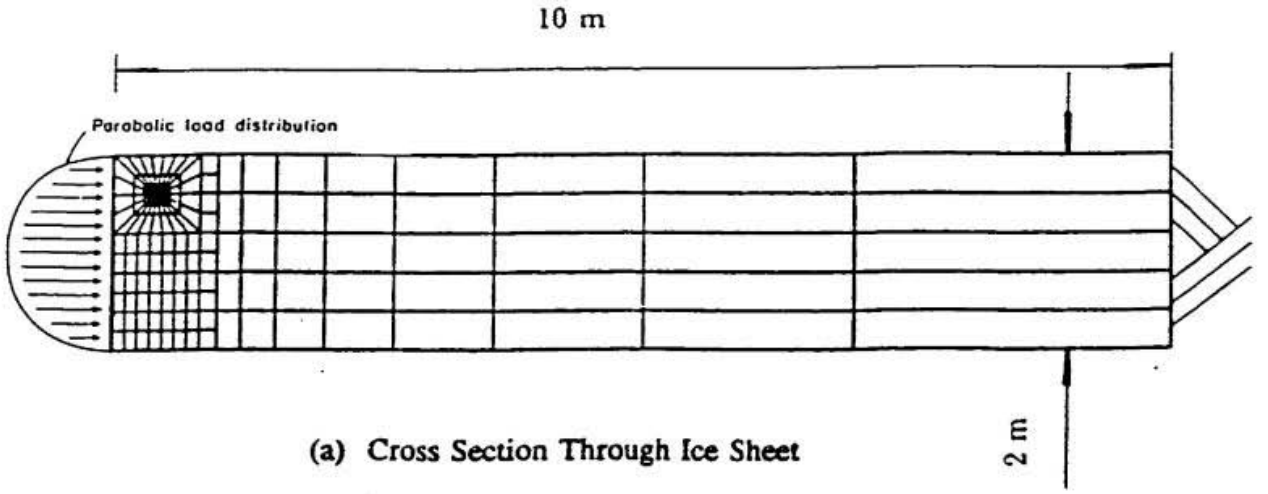

(a) Cross Section Through Ice Sheet

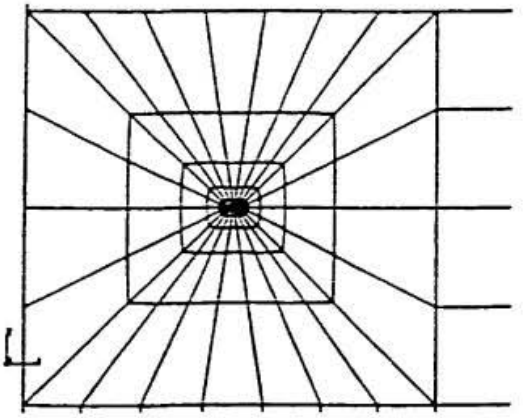

(b) Region Near Crack

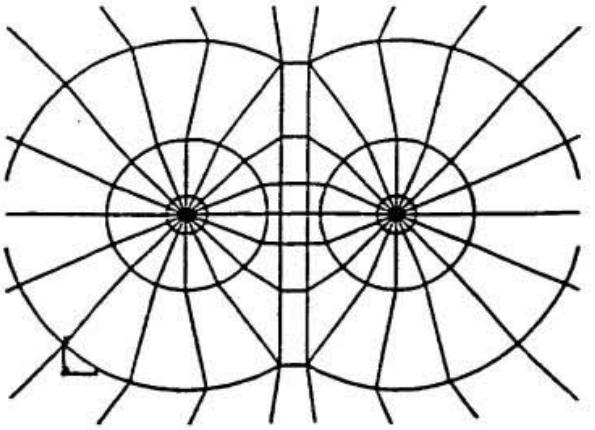

(c) Close-up of Crack

Figure 5.25: Finite Element Idealization of Trial Test Case with a Crack.

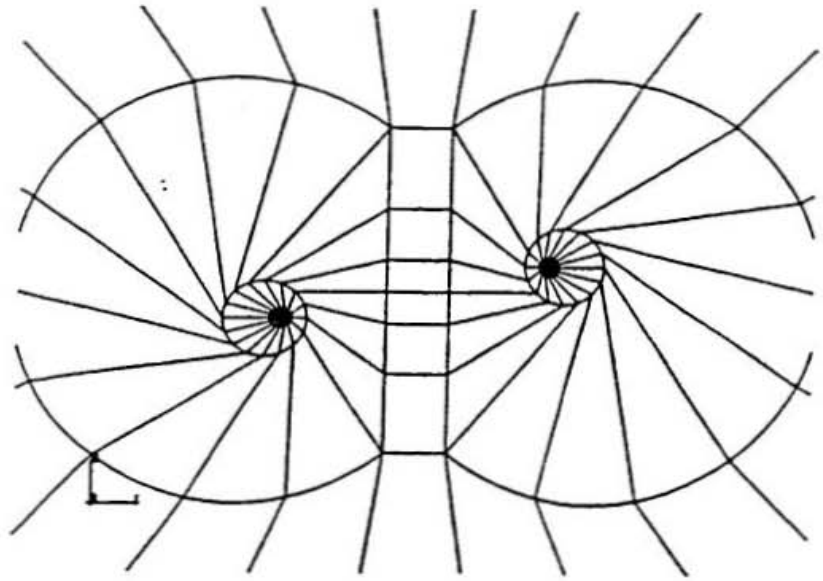

Figure 5.26: Extension of Initial Crack along Maximum SERR Line.

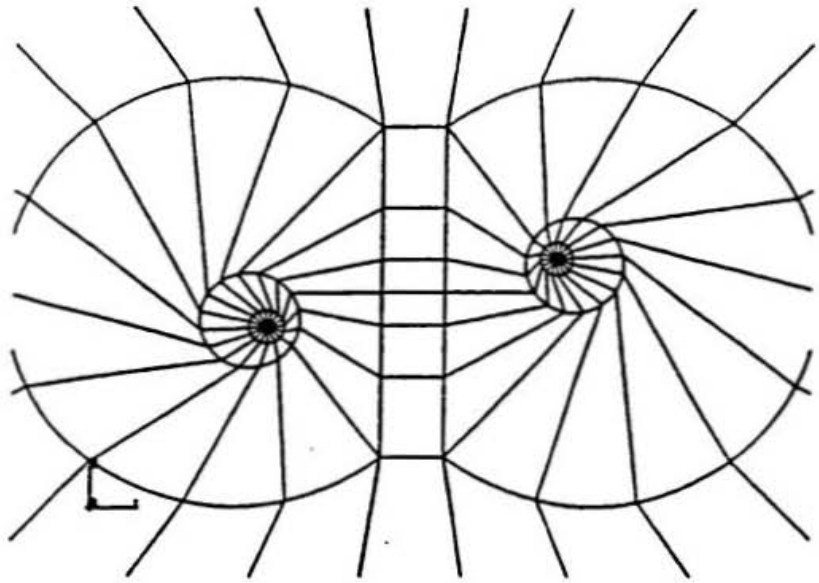

Figure 5.27: Mesh for Second Crack Extension.

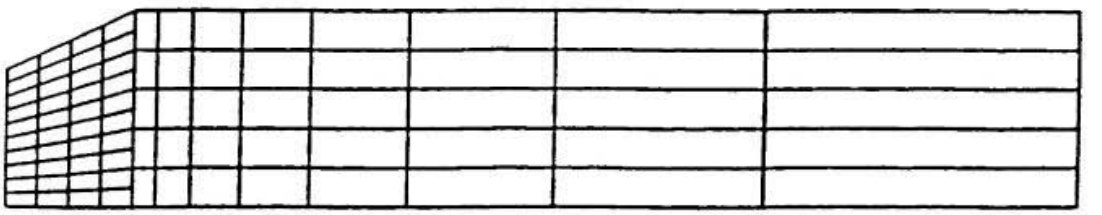

(a) Finite Element Mesh and the Locations of the Points at the Contact Face

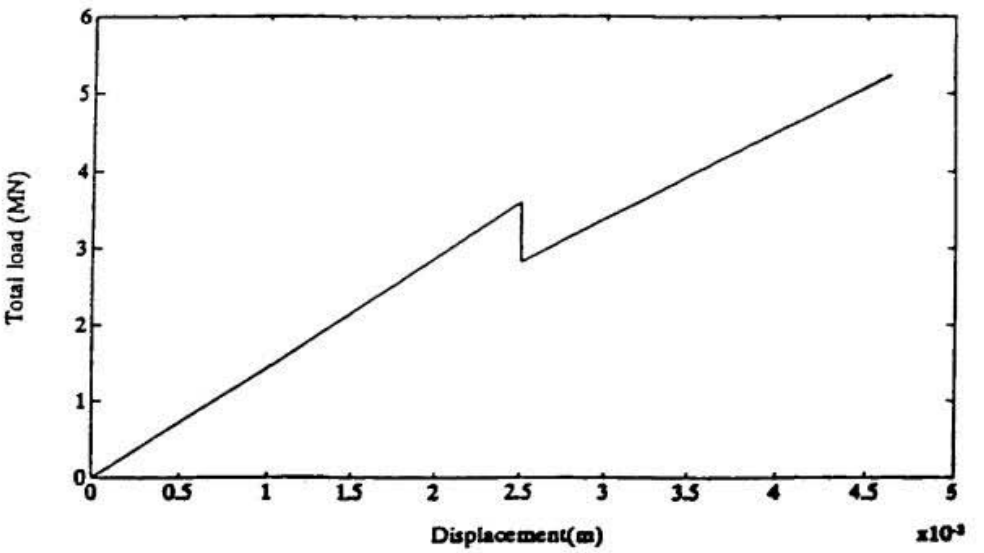

(b) Force-displacement Curve

Figure 5.28: Removal of Elements Due to a Spall.

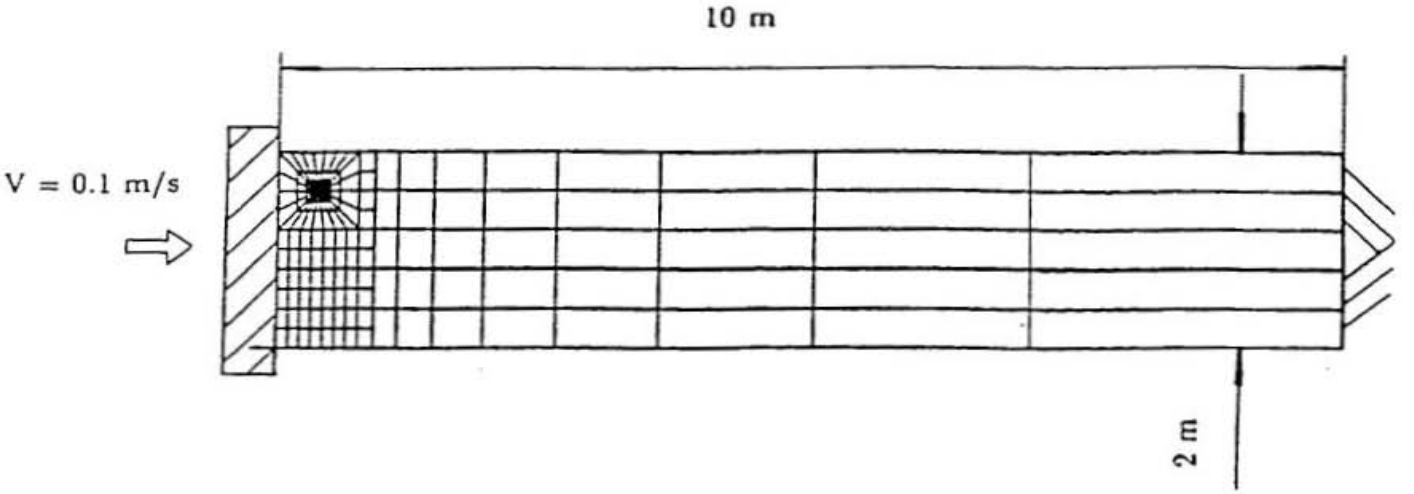

Figure 5.29: Finite Element Mesh for the Ice Sheet.

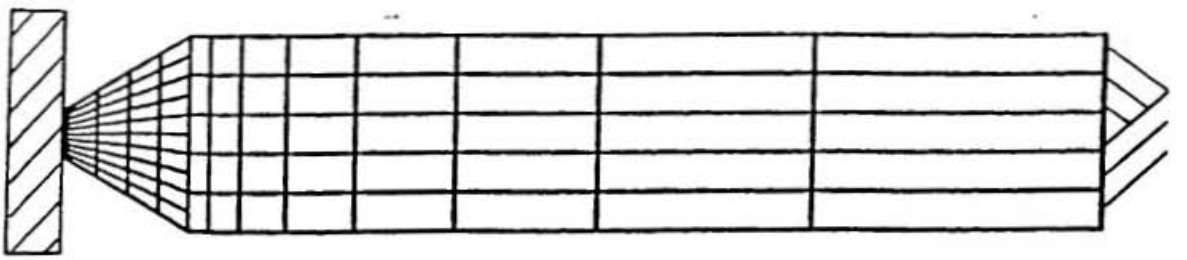

Figure 5.30: Finite Element Mesh after Spalling.

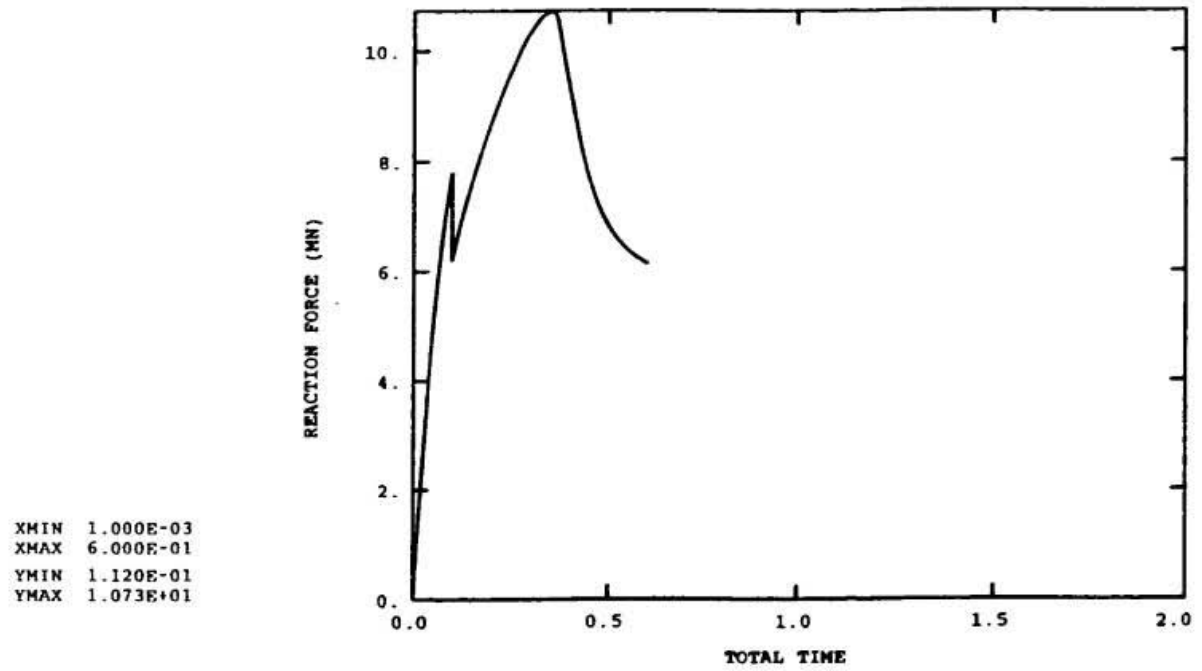

Figure 5.31: Model Results: Effects of Spalls on Total Force.

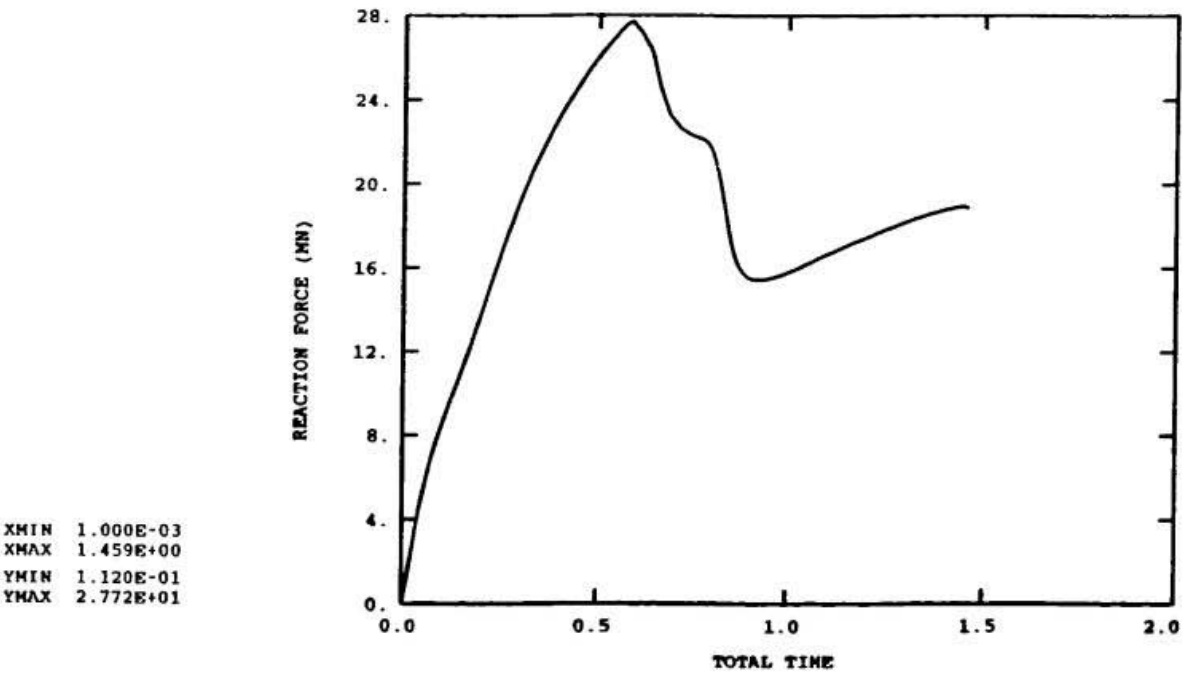

Figure 5.32: Model Results: Load History with Damage Analysis Only.

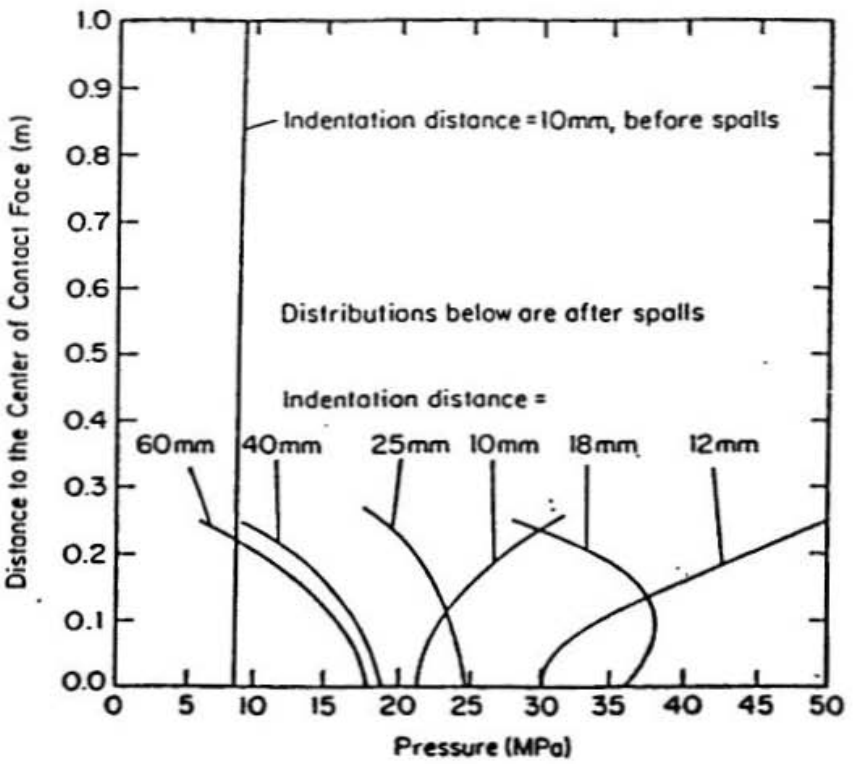

Figure 5.33: Stress Redistribution at Different Indentation Distances (Spalls occur after 10 mm).

Chapter 6

A Simple Model for Ice-Structure Interaction

6.1 Introduction

During ice-structure interaction, regular repeated oscillations in load occur at certain loading rates. Spalling of large pieces of ice near the contact zone will result in a load decrease as the contact area is reduced. Such events do not explain the regularity of the oscillations, nor do they account for the occurrence of oscillations observed in a thin layer of compressed crushed ice particles confined between two plates (Spencer et al., 1992).

In the medium scale field indentation test program on Hobson's Choice Ice Island (Frederking et al., 1990), temperature was measured at the ice-indenter interface (Gagnon and Sinha, 1991). Regular decreases in temperature occurred during increases in load and vice-versa. Evidence of melting has also been presented. This observation requires a thermomechanical explanation of the indentation process. The possibility of pressure melting in such situations was raised three decades ago by Barnes and Tabor (1966) and Kheisin and Cherapanov (1970). In full scale ice interactions, although the global measured pressures are usually low, pressure melting could still take place in the local high pressure zones, the so-called, hot spots (Jor-

daan et al., 1997). Laboratory indentation and impact tests performed on freshwater ice by Gagnon and Mølgaard (1990) have also shown evidence of pressure melting. Triaxial tests in the laboratory (Meglis et al., 1997) including the measurement of ice temperature under high triaxial confinement (up to 60 MPa) have also provided similar evidence, as discussed in chapter 3. As shown in Figure 3.22, the measured strain rate increased more than 600 times from the beginning to the end of the test. This implies that the material has been highly softened and the overall viscosity of the material has been reduced significantly, since the strain rate $\dot{\epsilon} = \sigma/\mu$, here the stress is constant during the test. The calculated damage enhancement factor for this test is about 665, which means the viscosity is reduced by 665 times. This is consistent with the test results. As discussed in earlier chapters, the softening of the material is mostly due to the combined effects of microcracking, dynamic recrystallization and pressure melting. When the damage level is high, the structure break-down in the material will occur. As a result, the Kelvin units can be equivalent to a single dashpot. This means a spring plus a dashpot (a Maxwell unit) should be a sufficient idealization for highly damaged (crushed) materials. At this stage of material deformation, dynamic recrystallization and pressure melting should dominate the development of damage. In this study, a simplified damage model with only one Maxwell unit is proposed to model viscoelastic materials, especially under conditions of high loading stress and high confining pressure, which will result in extensive damage to the material. One example of such conditions is in the crushed layer near the contact interface in ice-structure interaction.

6.2 A Simplified Damage Model

As described in the previous chapters, when the structure break-down in the material occurs, the broad-spectrum damage model with three Kelvin units can be replaced by a simple model with one Maxwell unit. It is proposed to use this simple model to represent viscoelastic materials under intact or damaged conditions, as long as the material will be undergoing extreme loads and will suffer extensive damage after initial loading. By doing so, the initial loading curve near the origin may not be accurate. But in many cases, especially under extreme loading conditions, one would be more interested in the peak loads, the frequency of the load oscillations as well as the stress and damage distributions when the failure of the material occurs. The predictions for initial loading period should not affect the final results significantly. The benefits of using this simple model is that (1) due to much fewer parameters and variables in the model, it is much easier to calibrate the model with laboratory high stress test results; (2) without the delayed elastic term, the model can reach the convergent solution much easier and faster, thus saving computation time.

A trial test case is considered. The damage evolution law given by Eq. (4.37) and the creep enhancement factors given by Eqs. (4.38) and (4.39) are used in the simple damage model. This damage model is implemented into the finite element model used in Chapter 5, as shown in Figure 5.2. As discussed in Section 5.3.1, when load drops occur, the viscosity in the crushed layer has been reduced as much as 1000 to 10000 times with the edge and center areas of the interface being reduced most. The damage level is between 3 to 4 and the hydrostatic pressure is in the range of 45 to 50 MPa at the interface. Experimental results in the laboratory and theoretical analyses on these tests have also shown a reduction in viscosity of more than 600 times (665 times from analysis), as mentioned earlier. Therefore in the simple model,

it is proposed to reduce the viscosity of the material by a factor of 1000, when either damage reaches 3.0 or the hydrostatic pressure reaches 50 MPa. A test case without the reduction in viscosity is also conducted to show the significance of such a reduction on the development of the total load.

Figure 6.1 shows the force-time curves (The unit for time in all the figures is second). Curve C1 is calculated using the simple damage model with viscosity reduction; curve C3 is using the same model without viscosity reduction; and curve C2 is based on the broad-spectrum model as shown in Figure 5.6 (curve C4). It can be seen that C1 and C3 are identical before the peak load. When damage and/or hydrostatic pressure reach the critical values, the viscosity of the material will be reduced resulting in the load dropping. This also shows the effect of the reduction in viscosity on the total load. Curves C1 and C2 are also matching closely, which means, for simplicity, the simple damage model with viscosity reduction can be used to replace the broad-spectrum model with satisfactory results. The difference between these two models is that the simple model has only two components, elastic and secondary creep; the broad-spectrum model has these two terms plus a delayed elastic component, which is represented by three Kelvin units. Before the loads drop, the difference between C1 and C2 is due to the delayed elastic component in C2. This also indicates that the delayed elastic component is less significant in terms of the total load. Curve C3 represents the broad-spectrum model without the delayed elastic component. In general, the model results do not give as sharp load drops as shown in the test results. As discussed in Chapter 5, the indentation process is a dynamic process. The dynamic effects and the flexibility of the structure and the whole system lead to sharper load drops. The indentation process also involves the extrusion and clearance processes, which also results in sharp load drops. The present study does not include elements removal.

Figure 6.2 shows the damage distribution at the peak load for the simple model with viscosity reduction. Figures 6.3, 6.4 and 6.5 show the damage distributions at the half way of the load drop, at the bottom of the load drop and at the end of the analysis, respectively. Figure 6.6 shows a tensile zone with tensile stresses higher than 2 MPa. Figure 6.7 shows the development of viscosity, damage and hydrostatic pressure in the crushed layer. This is similar to what is shown in Figure 5.13.

6.3 The Role of Pressure Melting

The above analysis shows the effects of the reduction in viscosity on the development of the total load. The rebound in viscosity as well as total load are not included. The recovery in loads in Figure 6.1 are mostly due to the increase in contact area. Field tests show regular variation of total load, pressure as well as temperature. Evidence of pressure melting has been presented in both field and laboratory. The melting and refreezing processes may play an important role in the load oscillations.

Pressure melting will develop a layer of lubricating liquid between the grains of solid material or particles in the crushed layer, as well as the solids and the contacting structure, which will reduce both viscosity and friction of the material. The lubricating liquid can be considered as a dashpot in series to the dashpot of the solid, thus reducing the total viscosity. It will also change the structure of the material (or in other term, damaging the material).

The role of pressure melting in the processes noted above may well be significant with regard to the oscillations within a layer. Two hypotheses are explored as follows:

- pressure melting affects the viscosity in the damaged layer, accelerating the processes noted above, and

- pressure melting results in a reduction of friction which is a function of pressure,

i.e. basically stick-slip motions.

These hypotheses incorporating the simplified damage model (with only one Maxwell unit) are investigated using numerical models, which are developed and implemented into the ABAQUS finite element program.

6.4 Experimental Observations

The sawtooth pattern of oscillations in loads is generally evident in laboratory tests (Spencer et al., 1992), in medium-scale field indentation tests (GEOTECH, 1985; Frederking et al., 1990), as well as in full-scale interactions (Jefferies and Wright, 1988). Typically, the frequency range of vibrations is about 20-30 Hz for the medium scale. Figure 6.8 shows a force-time curve from the 1985 Pond Inlet medium scale test series, where spherical indenters penetrated a prepared test face, with a loading speed variation from 100 mm/s to 0 following a sine wave function. A possible spall event is indicated in the figure by means of an arrow. It is not a reasonable inference that each drop in load in the high frequency oscillations is associated with a spall. Spencer et al. (1992) conducted extrusion tests on crushed ice to investigate ice-induced vibrations. Crushed ice particles of about 1 mm in size were compressed and squeezed out between two rigid rectangular platens (see Figure 6.9a). The test speed ranged from 2.5 mm/s to 160 mm/s. In these tests, oscillations in pressure have been observed (see Figure 6.9b). These observations showed that the repetitive cycling of load can occur in a thin layer of crushed ice with no evidence of spall failure.

Friction between ice particles, and between ice and indenter may play an important role in the ice indentation process. Video records of both indentation and crushed ice tests have shown the sudden forward movement of the indenter as the ice failed in the layer and extruded out of the interface. This suggests that the viscosity or friction

coefficient of the ice could also vary during the indentation process.

6.5 The Effects of Pressure Melting on the Viscosity and Friction of Ice

The hypotheses of viscosity and friction variation during ice indentation are based on the above observations and theories on pressure melting and ice friction. Suppose that during an upswing in load, the local pressure is high enough so that the melting point is less than the local ice temperature, i.e. $T_m < T$. Then the ice will start to melt, taking heat from the surrounding ice. This causes a drop in temperature as the load increases. Meanwhile the water produced in this process will reduce the viscosity of the ice, and will also lower the friction between ice particles and the interface of ice and the indenter. This is equivalent to a reduction of the lateral confinement within the crushed layer, and the pressure on the indenter will drop rapidly. As the pressure reduces, the melting temperature increases. The ice will thus refreeze by releasing heat and the local ice temperature will start to rise. This pattern of temperature fluctuations opposite to the changes in load was observed during the field tests (Gagnon and Sinha, 1991). After the load (pressure) drops, the lateral sliding speed of the ice relative to the indenter will also be reduced along with refreezing of the ice. Hence, the viscosity and friction of the ice will rebound and the same processes will repeat. This is illustrated in Figure 6.10.

The release of elastic strain energy when the load drops was found to be about 25 - 40% of the load per cycle (Jordaan and Timco, 1988). The general conclusion based on the medium scale indentation tests using "Sandwell" apparatus is that roughly equal amounts of energy are imparted to the ice during upswings and downswings of load. Since the time periods of downswings are usually shorter than that of the upswings, the power imparted to the ice during the periods of downswings is higher than that

of the upswings. Although frictional heating will also affect the processes mentioned above, a sound thermodynamic analysis is required to explain these processes in detail.

6.6 Finite Element Implementation

The assumption that viscosity and friction vary as a result of pressure melting has been implemented in finite element models. Two trial test cases have been made to simulate the crushed ice tests and indentation tests. The simplified constitutive damage model proposed in this chapter is applied to represent the behaviour of crushed ice. Damage evolution is related to the micro-structural changes. The development of damage will effectively reduce the elastic modulus of ice, and also strongly enhance the creep process. This damage model has been developed in FORTRAN code and implemented as a user subroutine in the ABAQUS finite element program. The representation of the viscous and frictional coefficients are included in this user subroutine as a function of pressure.

6.7 Modelling of the Crushed Ice Test

Because of the geometrical symmetry in crushed ice tests, only one half of the structure has been idealized into a finite element mesh, with the abscissa and ordinate as the symmetrical axes (see Figure 6.11). The test speed was constant at 125 mm/s (test 982). Since the modulus (or more precisely, the compressive strength) of the crushed ice is a function of confining pressure and varies during the compaction, the only possible way to get the value was to measure the modulus of the compacted ice after tests, which was estimated to be about 1100 MPa. The stiffness of the test frame was about 7140 MN/m, and the hydraulic loading system had a minimum stiffness of about 3000 MN/m; the combined stiffness of the whole test system was calculated to

Table 6.1: Parameters Used in the Model

Description	Value
Elastic Modulus	9500 MPa
Poisson's Ratio	0.3
Initial Damage for Crushed Ice	1.0
Initial Friction Coefficient	0.25
Reduced Friction Coefficient	0.05
Viscosity Reduction Factor	1000
Ice Temperature	-10°C

be 2100 MN/m. A spring element is introduced to represent the structure stiffness. Plane strain conditions are assumed in this analysis. At the ice-indenter interface, an initial friction coefficient of 0.25 is applied using interface elements. The material properties and constants used in the model are listed in Table 6.1.

The simulation using the first hypothesis, i.e. changing of viscosity due to pressure melting, is illustrated in Figure 6.12. The viscosity of the ice is assumed to be reduced by a factor of 665, once pressure melting occurs. Pressure oscillations were obtained at a frequency of about 100 Hz. Note that measured average frequency of pressure oscillation for test 982 is about 130 Hz (see Figure 6.9). It is found that the magnitude and frequency of the load fluctuations are dependent on the reduction of viscosity. Peak pressures of about 3 to 3.5 MPa were obtained which are not far off the measured values. Due to the lack of the physical measurements, only preliminary results are presented in this work.

It is conceivable that pressure melting could also affect the frictional properties of ice as previously mentioned. As the pressure at the interface is building up, the ice may start to melt. Note that the pressure along the interface is not uniformly distributed. The center portion of the interface will start to melt first due to higher

confining pressure. Once melting occurs, the friction coefficient will drop rapidly from the center towards the edges. For simplicity, the friction reduction is assumed to be simultaneous along the interface to a value of 0.05, since this value is common for high speed friction between ice and metals (a layer of water lubricates the interface for high speed friction tests). As shown in Figure 6.13, the mean pressure on the platen drops rapidly. Upon reaching the valley of the pressure, the friction at the interface will be recovered, and the mean pressure will rebound as shown in the figure. Repeating the same processes the load oscillation occurs. A frequency of about 120 Hz was obtained which is very close to the measured value. Calculated peak pressures were about 3 to 5 MPa which are more in the line with the measured values (see also Figure 6.9). It is worth mentioning that without the recovery of the friction, the computation shows that pressure curve will drop and remain flat at the valley as indicated by the dotted line in Figure 6.13. This shows the important role of friction on the load fluctuations during ice indentation.

6.8 Simulation of Ice Sheet Indentation Test

Figure 6.14 shows the initial finite element idealization of the trial test case for ice sheet indentation. The mesh is on the order of 1.0 m × 1.0 m × 10.0 m. Loading speed is 0.1 m/s. At the far end, the ice sheet was supported on an elastic foundation. At the interface, a layer of crushed ice of 0.1 m in thickness is defined between the indenter and the solid ice sheet. Interface elements have been defined between the indenter and the crushed layer, and between the crushed layer and the solid ice sheet. In this analysis, the crushed layer is modeled using the simplified damage model. The solid ice sheet is modeled as elastic material without damage, since most of the damage and deformation progresses are occurred in the crushed layer. Figure 6.15

shows the calculated load-time curve. The frequency of load oscillation is about 6 Hz. The Peak loads are about 8 MN, which give the average pressures about 8 MPa on the indenter, with a contact area of 1 m^2. These are in the range of the results from medium scale indentation tests. Again, as shown in the figure, without variation in viscosity after the third load oscillation, the load curve remains flat without rebound.

The analyses presented in this Chapter are a few trial test cases, not intended to simulate certain field experiments. The purpose is to try to find a simpler way to model ice loads based on the analyses using the full scale model, the broad-spectrum model. By assuming the viscosity of the material will be reduced when either damage or the hydrostatic pressure reaches a critical value, the full scale model is simplified to just one Maxwell unit. This will result in an easier model correlation with tests and saving computation work. Analyses were also performed to specifically investigate the effects of pressure melting on ice load oscillations. All of the analyses have shown promising results. More laboratory high pressure tests are recommended to provide detailed information on the effects of damage (structural changes) on the deformation processes, e.g. the specific roles of cracking, recrystallization and pressure melting on the creep responses, at what stage of deformation, and on what kind of loading and boundary conditions. With these information, the damage model can be better calibrated against certain loading conditions. Finite element analyses can then be performed to investigate the ice loads for a variety of loading and boundary conditions, as well as the geometry of ice and structure. These may lead to a better understanding of ice structure interactions. A semi-empirical formulation may be derived by correlating the analysis results with field observations and test results. This will be the ultimate goal of finite element analysis to develop a simple formulation for practical applications.

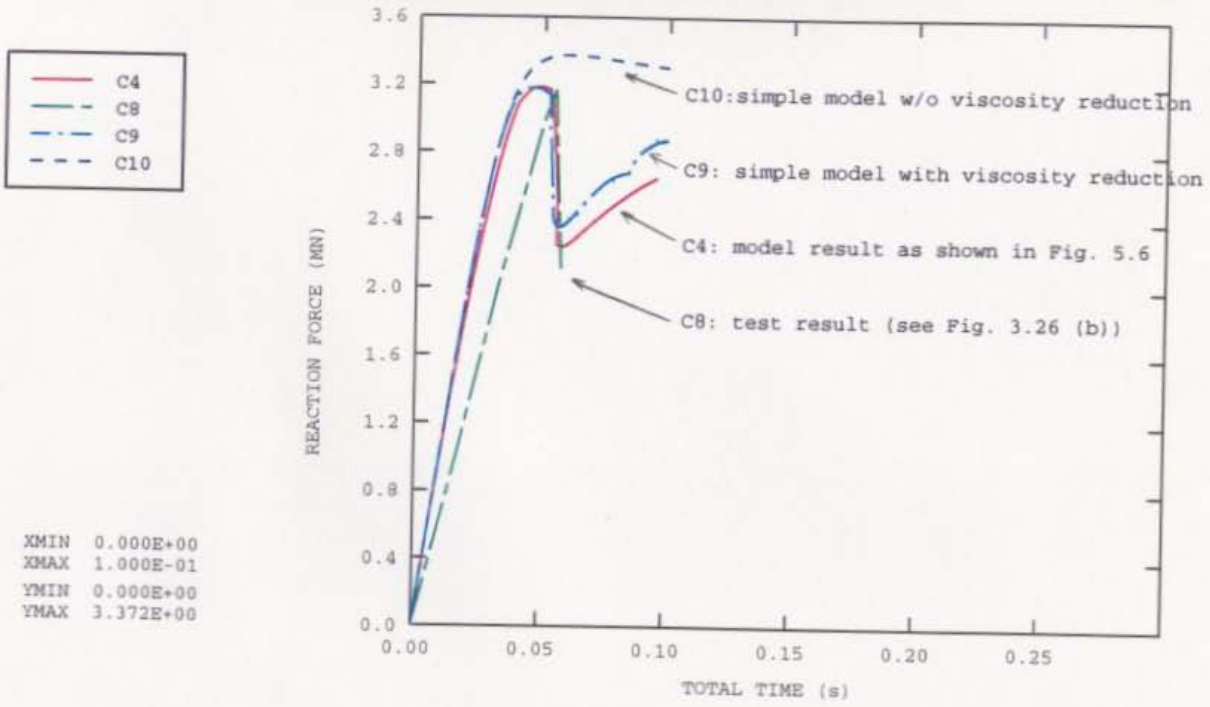

Figure 6.1: Force-time Curves for the trial test case.

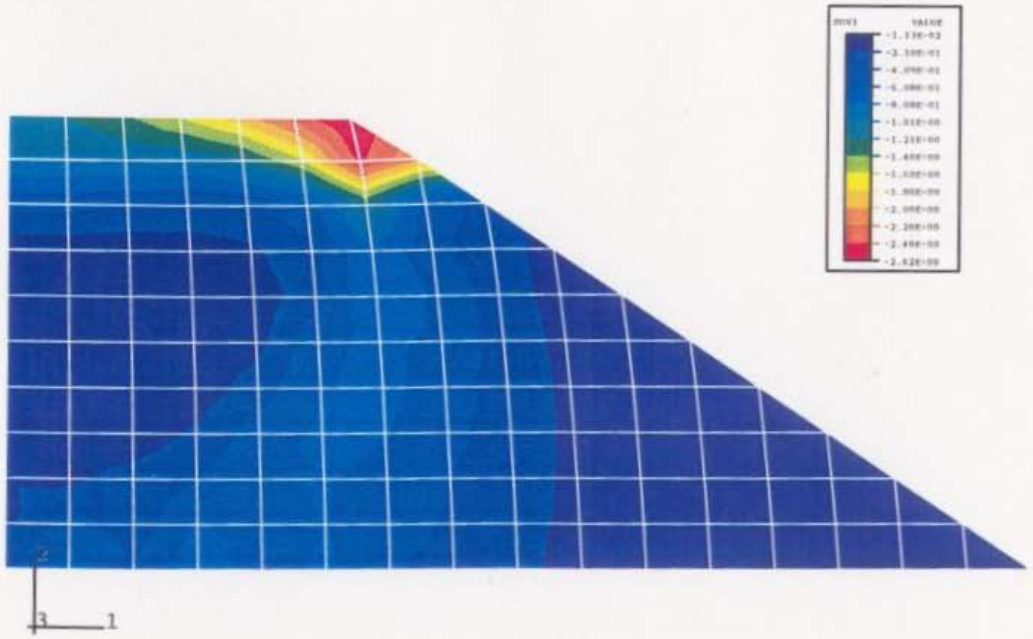

Figure 6.2: Damage Distribution for the simple damage model at the peak load.

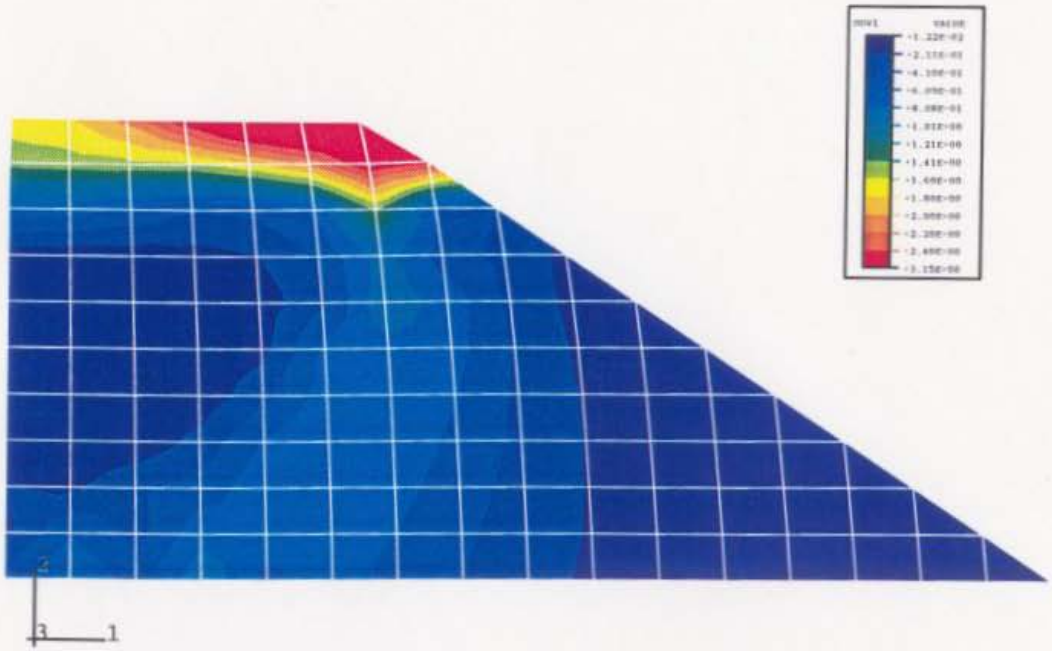

Figure 6.3: Damage Distribution for the simple damage model at the half way of the load drop.

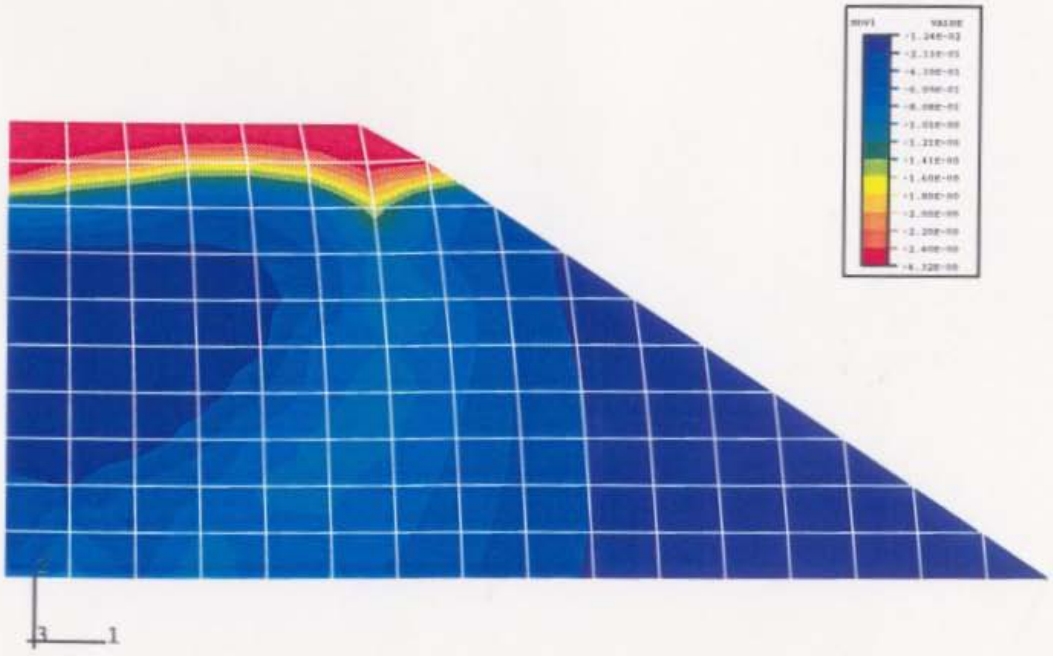

Figure 6.4: Damage Distribution for the simple damage model after the load drop.

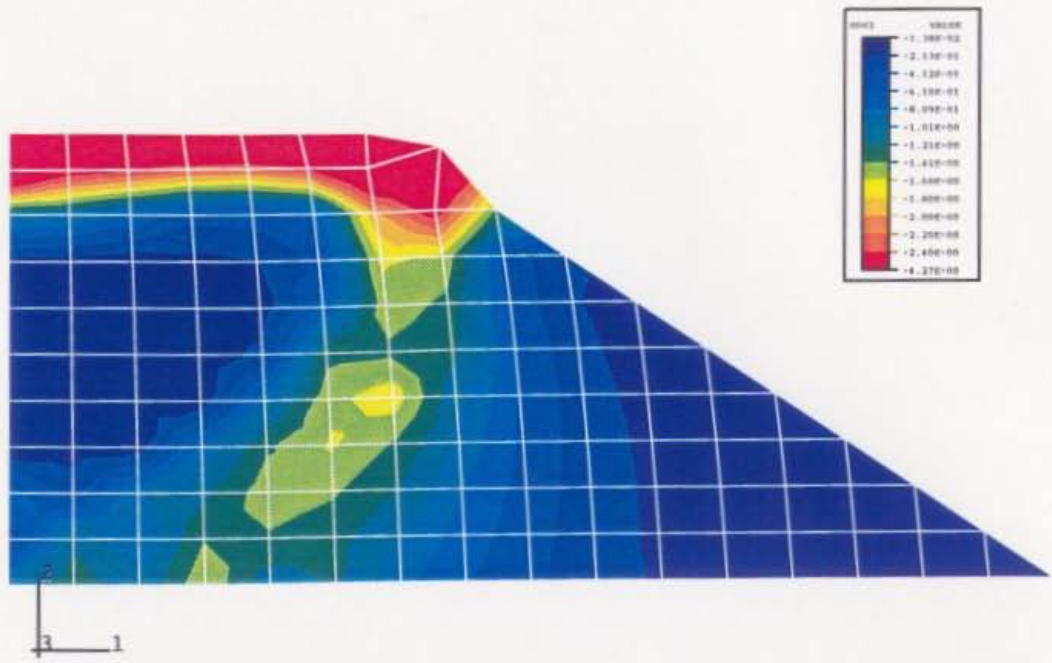

Figure 6.5: Damage Distribution for the simple damage model at the end of the analysis.

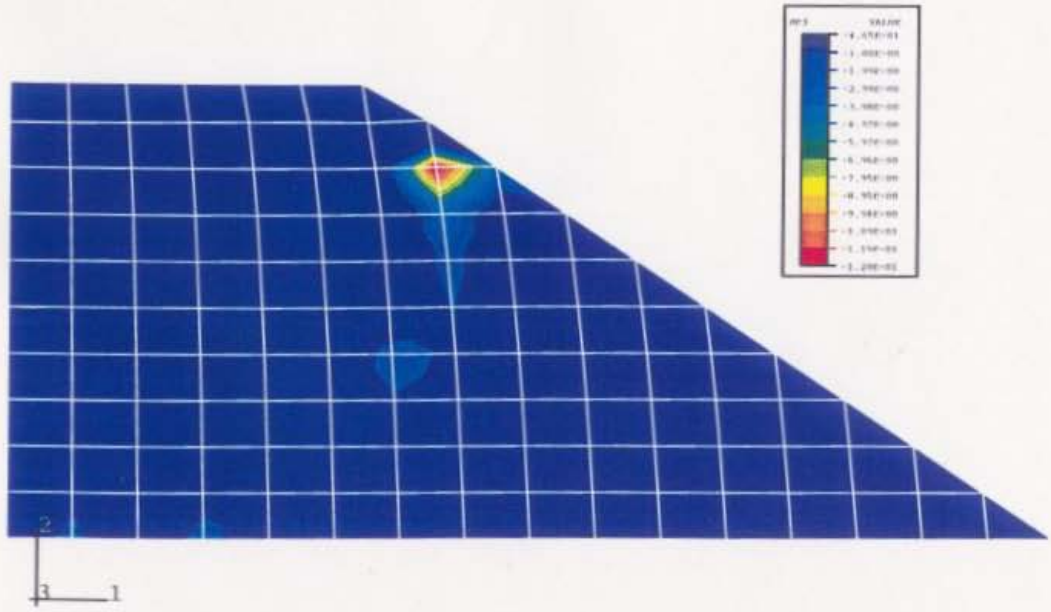

Figure 6.6: Tensile Zone near the Contact Surface.

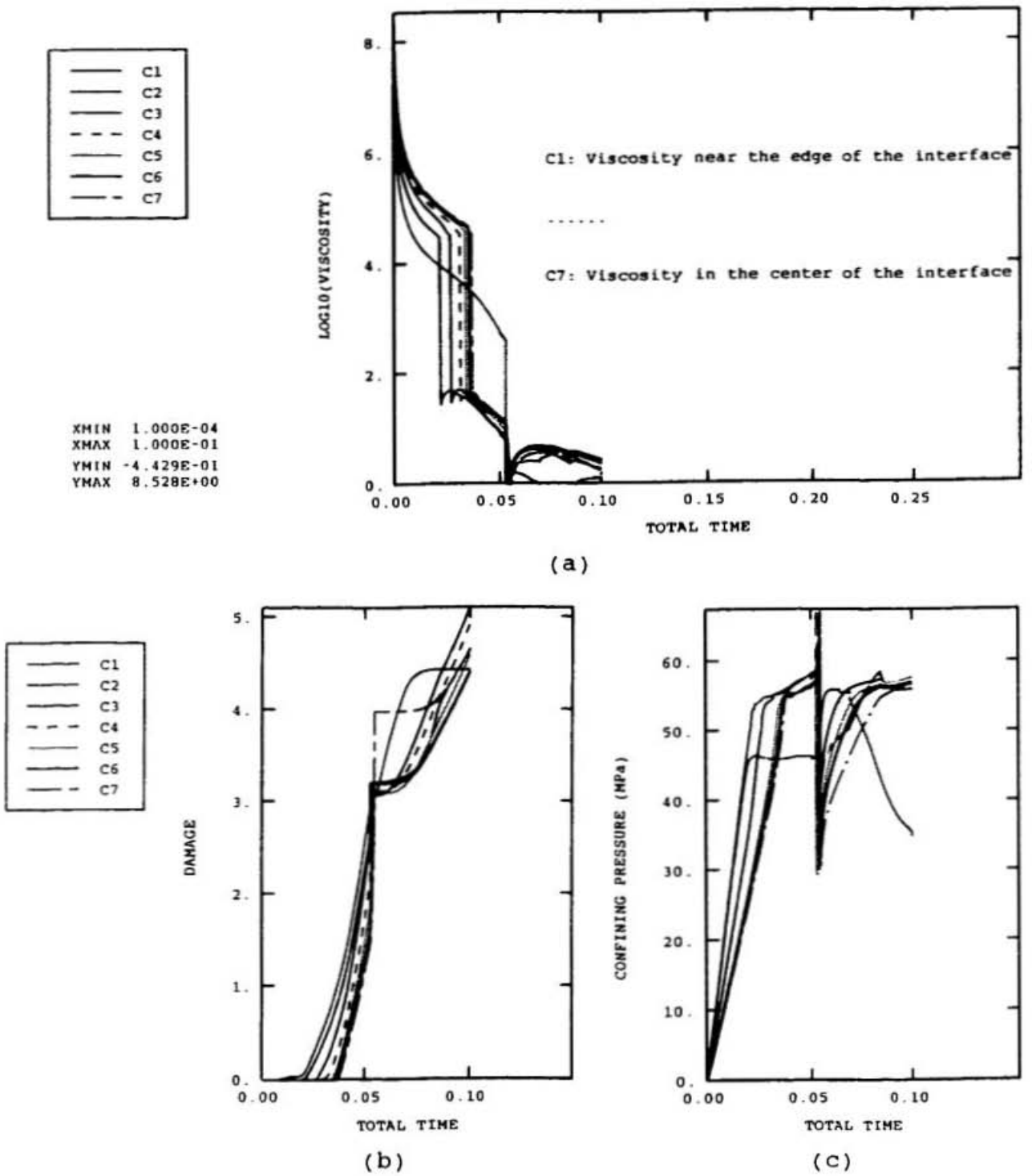

Figure 6.7: The Development of (a) Viscosity, (b) Damage, (c) Confining Pressure.

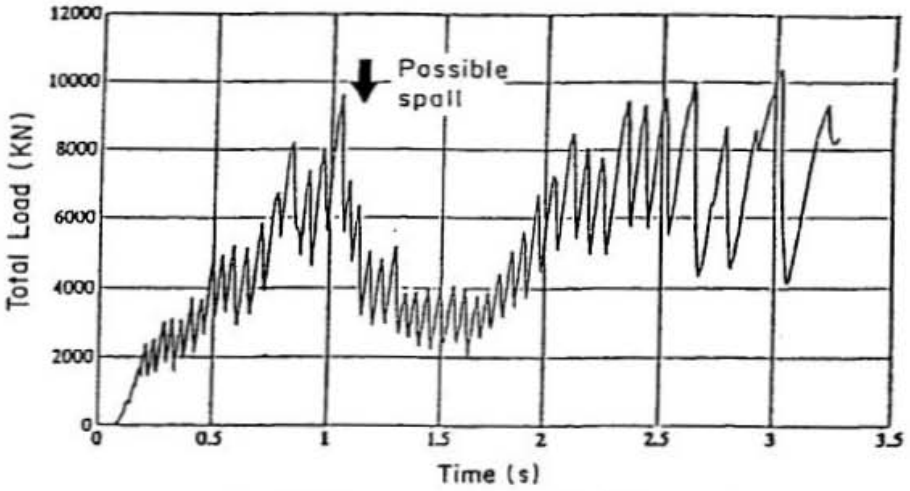

Figure 6.8: Result of the Pond Inlet test Series with 3.0 m^2 Spherical Indenter (test T1T5) (GEOTECH, 1985).

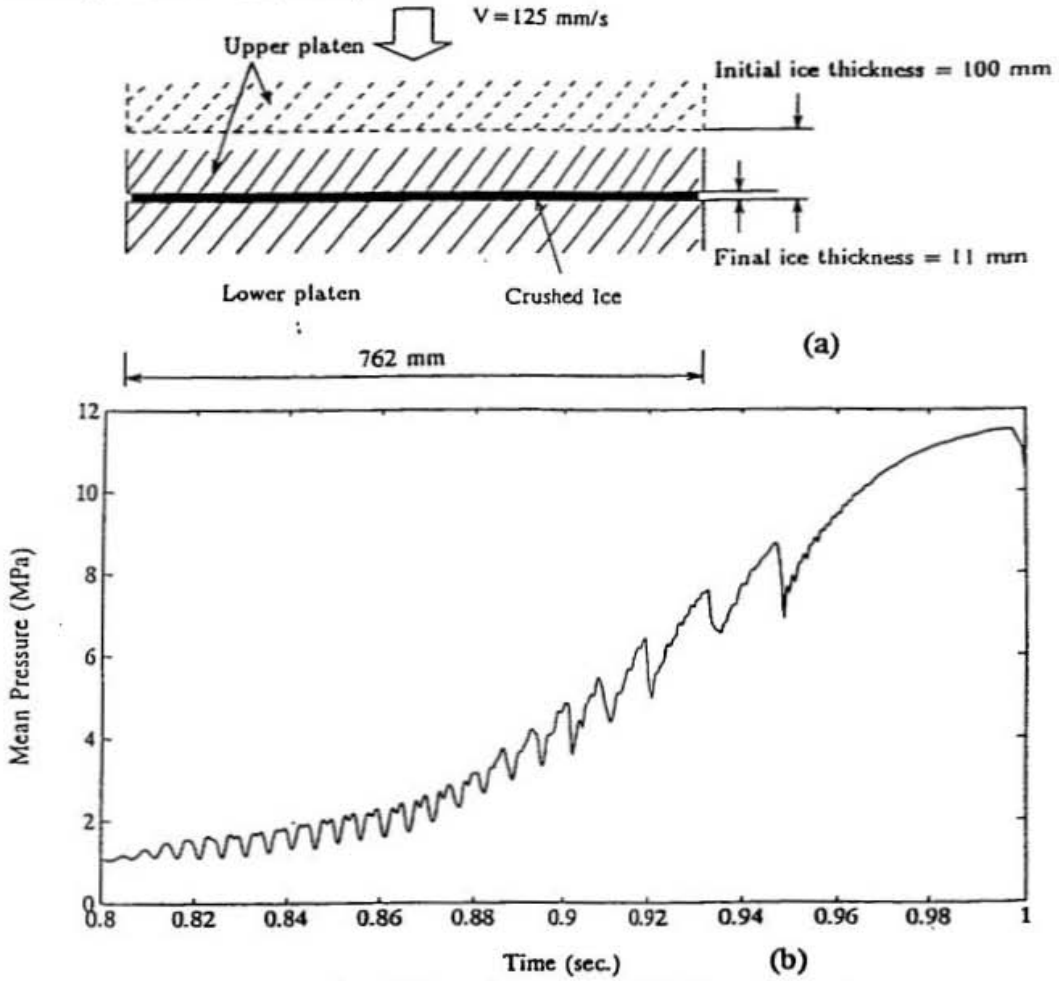

Figure 6.9: (a) Schematic of Test Setup and (b) Result of Crushed Ice test Series (test 982).

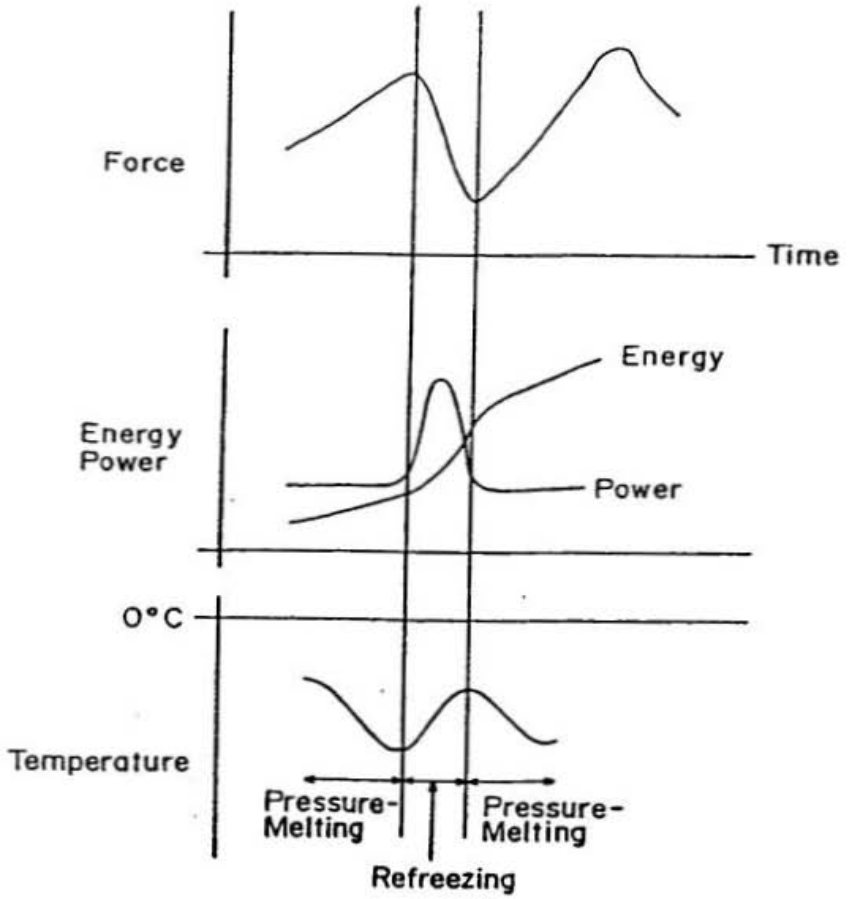

Figure 6.10: Idealization of the Pressure melting Process in Ice-Structure Interaction.

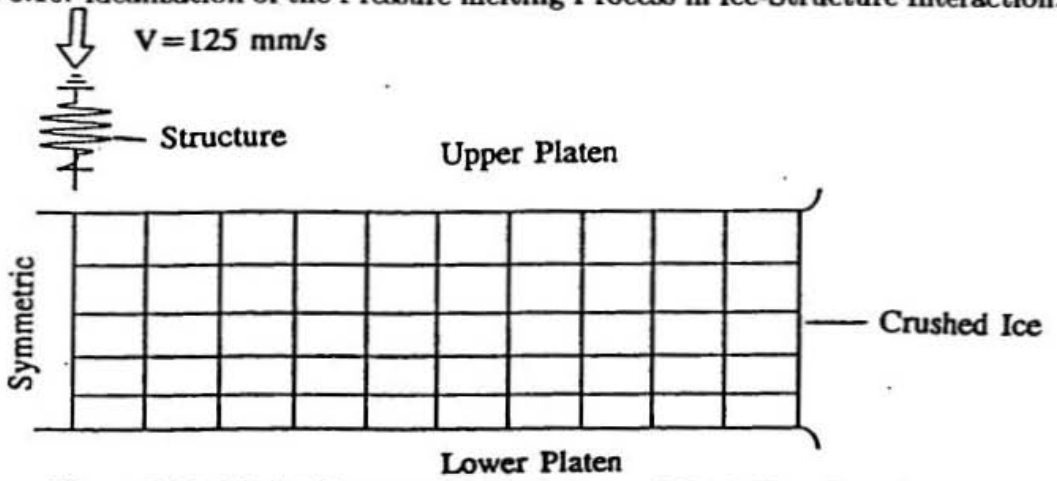

Figure 6.11: Finite Element Discretization of Trial Test Case I.

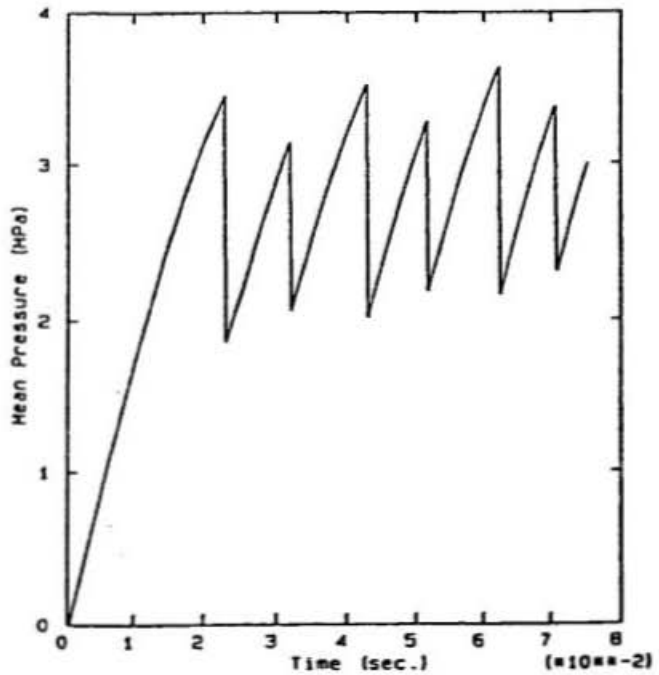

Figure 6.12: Mean Pressure-Time Curve for Analysis with Variation of Viscosity (Hypothesis I).

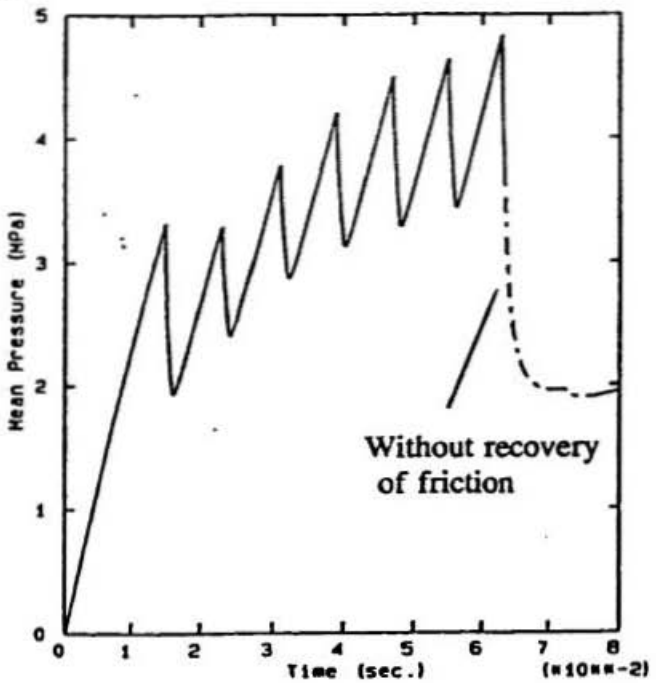

Figure 6.13: Mean Pressure-Time Curve for Analysis with Variation of Friction (Hypothesis II).

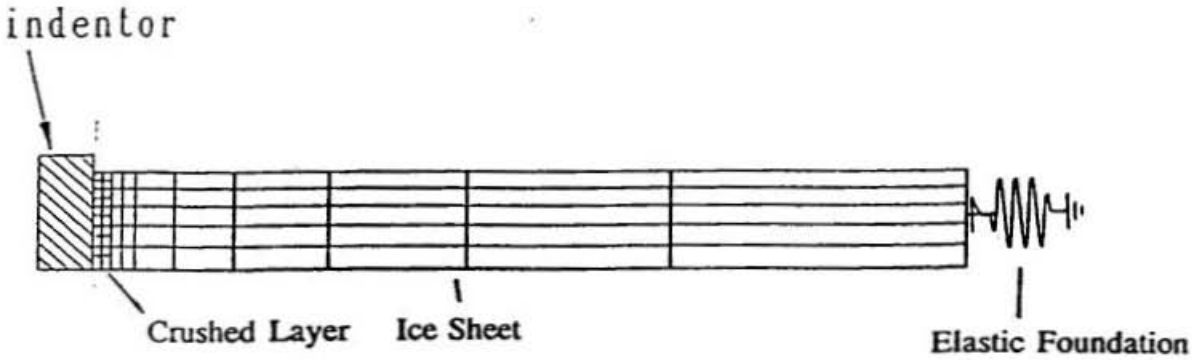

Figure 6.14: Finite Element Discretization of Trial Test Case II.

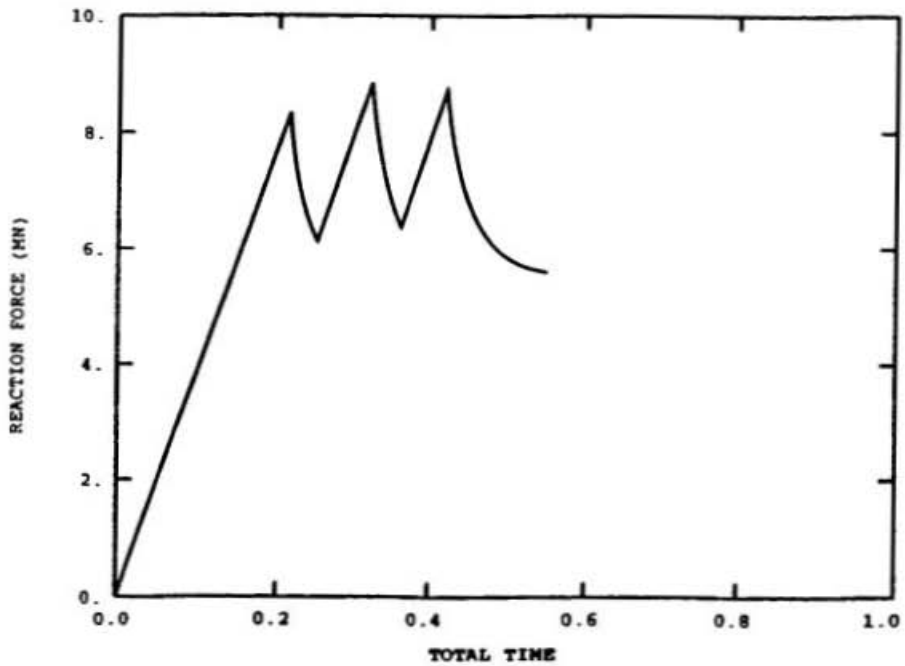

Figure 6.15: Calculated Force-Time Curve for Analysis with Variation of Viscosity (Hypothesis I).

Chapter 7

Conclusions and Recommendations

The present study is a comprehensive examination of the role of damage and fracture processes in brittle, viscoelastic materials. The development and implementation of the constitutive damage model have been documented. Triaxial compressive tests on both intact and damaged ice, as well as medium-scale ice indentation experiments on Hobson's Choice Ice Island (1989, 1990) have been described. Investigations on the test results have shown clear evidence of softening of the material and the enhancement on the creep strain due to micro-structure changes (damage). These changes include microcracking, dynamic recrystallization and pressure melting, which would also be influenced by the confinement. Special attention was given to the effects of high shear stress and high confinement on the development of damage.

A multiaxial constitutive theory for brittle, viscoelastic materials is presented based on viscoelasticity, continuum damage theory and fracture mechanics. The microstructural nature of the material and micromechanical processes have been modelled by damage mechanics using averaging procedures with a finite collection of state variables. The change in the state variable is directly related to the individual deformation process. Damage evolution is based on Schapery's approach using the generalized J integral theory. In the work of Xiao (1991) and Xiao and Jordaan (1996), a damage model which is related to crack density was presented. The model

could provide reasonable predictions for tests under low loading stress and confinement. Jordaan et al., (1997) proposed a damage model which includes two state variables. The second state variable is related to the damage processes under high loading stress and confinement. In this study, the second state variable is modified by using an exponential function to model the rapid growth of damage under high loading stress (or loading rates) and high confinement. Based on the broad-spectrum approach, a constitutive model using three Kelvin units was developed. The constitutive model includes the effects of microcracking, dynamic recrystallization and pressure melting on the reduction in elastic modulus and the enhancement in creep deformation. The model predictions of the strain-stress relation for triaxial tests, as well as the total load versus time histories for medium scale indentation tests show good agreement with the measured results. Both the magnitude and distribution of the contact pressure calculated from the model are realistic. The model predictions also show clearly thin layers of highly damaged material near the contact surfaces. Further research is recommended to investigate the effect of each individual microprocess, such as pressure melting and recrystallization on the mechanical properties of the material.

A theoretical framework for analysis of fractures has been presented. The propagation of flaws and cracks is included in the finite element model, which is also consistent with the damage analysis. The modelling approach is based on the observations in the field and laboratory, particularly the medium-scale field tests in which measurements have been made under controlled conditions.

The analysis of damage showed that, if damage alone occurred, for medium and high loading speeds, the average stresses are much higher than those found in practice. The damage analysis does not provide detailed information on the distribution of piece sizes. Separate analysis could be conducted: for example, an upper bound could be

found on the number of pieces by considering that the energy released upon fracture was consumed entirely in creating surfaces.

The initial numerical analysis of fractures is believed to be a promising approach. Propagation of cracks has been studied in terms of initiation and direction, and spall pieces have been removed from the ice mass. The analysis has been combined with the viscoelasticity and damage mechanics that were previously formulated and implemented. Calibration will require further effort; there is a complex interaction between damage, spalling and the associated stress distribution. Further exercising of the model to calibrate with respect to crack growth, size of spalls and associated load reduction, scale effects, force-time curves (including slope), states of stress, and frequency of the various activities is needed.

Initial indications are positive: a crack of 40 mm long was found to propagate at less than one-half of the load found if damage only took place. Localization of damage was found to follow naturally in geometries where the stress is concentrated; such geometries would result from spalls.

Approximate solutions for spalling are seen as important. Solutions to the problem of spalling of ice sheets have been given by Evans et al. (1984) and by Wierzbicki (1985), the latter based on the well-known solution of Kendall (1978). These solutions are very useful in that they are in closed form; by the same token, the range of situations for which answers are provided is limited. In the long term, it is important to extend such solutions to cover a broader range of practical implementations. The shear cracks found in the initial computer experiments are good candidates for exploitation in this regard. Figure 7.1 illustrates a possible idealisation; further numerical work is advocated before such idealisations are finally decided upon.

A simplified damage model using one Maxwell unit is proposed to model viscoelastic materials under both intact and/or damaged conditions. With the reduction in

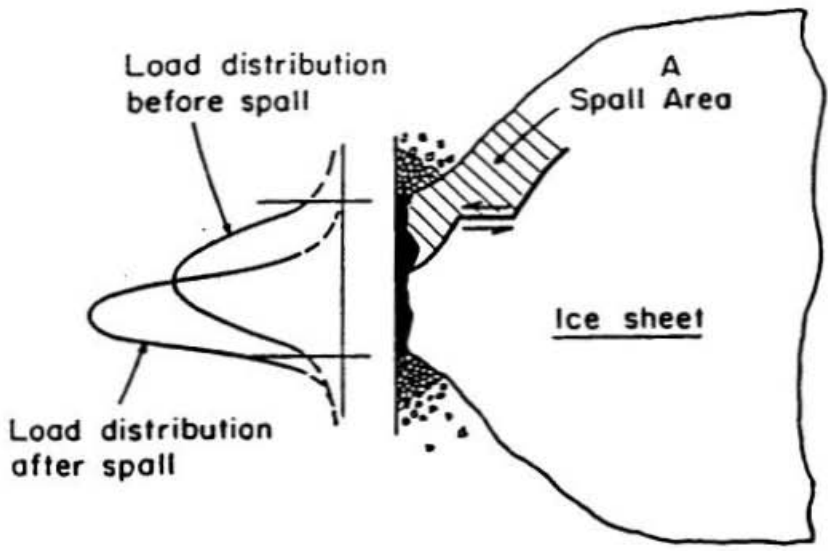

Figure 7.1: Shear Crack near Critical Zone, Suggested by Numerical Analysis.

viscosity when either damage or the confining pressure reaches a critical value, the simple model can provide very similar results as given by the broad-spectrum model in terms of total load, damage and pressure distributions.

Fluctuations in load during ice-structure interaction arise for several reasons, but mainly as a result of the crushing and brittle failure processes in ice. Results of tests in the medium-scale as well as full-scale observations have shown regular force-time patterns, as well as less regular ones. The regularity is partly related to the structure response, but also to the failure processes in the ice. The evidence points to activity in the "crushed layer" as being responsible for the regular variations (about 25 Hz in the medium scale and 1 Hz in full scale). Spalling and fracturing of large pieces of ice cause less frequent drops in load.

The physical mechanism of vibration in the crushed layer has been investigated by means of numerical analyses using finite element models. Two hypotheses have

been explored, i.e (1) the variation of viscosity as a result of pressure melting; (2) the variation of friction as a result of pressure melting. Two trial test cases have been studied. Initial analysis shows that the variation of viscosity or friction due to pressure melting can result in load (pressure) oscillation. The magnitude and frequency of the load fluctuations are influenced by the reduction of viscosity and friction. These initial results are very promising for a realistic analysis of ice-structure interaction events. Further exercising of the models, and a linking to the fracture analysis on spalling and production of discrete ice pieces (as discussed in chapter 5) is advocated. A detailed thermodynamic analysis is recommended to achieve a sound basis and more experimental evidence regarding pressure melting are required to verify the hypotheses noted above.

Based on the analysis of the experimental results and the model simulations detailed in this work, some general conclusions can be made as follows:

1. The presence of cracks and damage significantly enhances the creep responses (delayed elastic strain plus secondary strain). The creep strain of damaged ice can be several times larger than that of intact ice.

2. The idealized damage model, consisting of combination of a Maxwell unit and three Kelvin units with a nonlinear dashpot in each unit, has been shown to be appropriate for describing the ice behaviour under certain loading conditions, such as compressive loading.

3. Due to the domination of creep strain for a high degree of damage, the determination of viscosities becomes significant. This is influenced by the existence of damage, confining pressure and loading rate.

4. This damage model based on the proposed constitutive theory can provide good

agreement on time-strain, strain-stress histories, damage progression, as well as pressure distribution, under different loading conditions, such as loading rates, confinement, stress and initial damage levels.

5. Fracture analysis incorporating damage theory has been implemented into finite element models, which can provide realistic results on load-time histories, damage distribution and progression, as well as contact pressure distribution and progression. The peak load predicted by this approach is much smaller than that of damage analysis alone, and realistic comparisons were made with test measurements. The estimation of crushed ice layer thickness can be made possible when more measurements on the distribution of damage are obtained.

6. Analyses using a simplified damage model incorporating the effects of pressure melting in ice-structure interaction have been shown to be very promising. The simple model can predict very similar results to those given by the broad-spectrum model in terms of total load, damage and pressure distributions. Both the frequency of load oscillation as well as the magnitudes of the peak loads are in the range of field measurements. The effects of pressure melting on the structure and mechanical properties of ice can be considered as one particular type of damage process and require further research.

References

Ashby, M.F. and Duval, P., 1985. The Creep of Polycrystalline Ice, Cold Regions Science and Technology, Vol. 11, pp. 285-300.

Atkins, A.G. and Mai, Y.W., 1985. Elastic and Plastic Fracture, Ellis Horwood.

Barenblatt, G.I., 1962. The Mathematical Theory of Equilibrium Cracks in Brittle Fracture, Advances in Applied Mechanics, Vol.7, pp.55-111, Academic Press.

Barnes, P. and Tabor, D., 1966. Plastic Flow and Pressure Melting in the Deformation of Ice I, Nature, Vol. 210, pp. 878-882.

Barnes, P., Tabor, D. and Walker, J.C.F. 1971. The Friction and Creep of Polycrystalline Ice, Proceedings of the Royal Society of London, Vol. 324A, pp. 127-155.

Biot, M.A., 1954. Theory of Stress-Strain Relations in Anisotropic Viscoelasticity and Relaxation Phenomena, J. Applied Physics, Vol. 25, pp.1385-1391.

Broek, D., 1986. Elementary Engineering Fracture Mechanics, Martinus Nijhoff.

Budiansky, B. and O'Connell, R.J. 1976. Elastic Moduli of a Cracked Solid, International Journal of Solids and Structures, Vol.12, pp.81-97.

Chen, A.C.T. and Lee, J., 1986. Large-Scale Ice Strength Tests at Slow Strain Rates,Proceedings Fifth International Offshore Mechanics and Arctic Engineering (OMAE) Symposium, ASME, Tokyo, Japan, Vol.IV, pp.374-378.

Cole, D.M., 1986. Effect of Grain Size on the Internal Fracturing of Polycrystalline Ice, CRREL Report 86-5.

Cole, D.M., 1988. Crack Nucleation in Polycrystalline Ice. Cold Regions Science and Technology, Vol. 15, pp. 79-87.

Cole, D.M., 1989. Microfracture and the Compressive Failure of Polycrystalline Ice. Proceedings IUTAM/IAHR Symposium on Ice-Structure Interaction, St. John's, Newfoundland, Canada, pp. 231-250.

Conrad, N., 1976. On Microcrack Growth and Arrest in Simulated Fibrous Compsites, Mechanics and Materials Research Center, Texas A&M University, College Station, Report MM 3168-76-10.

Cormeau, A., Jordaan, I. J., and Maes, M., 1986. Development of a model for progressive damage in ice. Det norske Veritas (Canada) Ltd. Calgary, Alberta.

Currier, J.H. and Schulson, E.M., 1982. The Tensile Strength of Ice as a Function of Grain Size. Acta Metallurgica. Vol. 30, pp. 1511-1514.

DeFranco, S.J. and Dempsey, J.P., 1990. Crack Growth Stability In S2 Ice, IAHR Symposium, Espoo.

Dorris, J.F. 1989. A Plasticity Model for the Crushing of Ice, Proceedings IUTAM/IAHR Symposium on Ice-Structure Interaction, St. John's, Newfoundland, Canada, pp. 311-338.

Duval, P., 1981. Creep and Fabrics of Polycrystalline Ice under Shear and Compression, J. of Glaciology, Vol. 27, No. 95, pp.129-140.

Duval, P., Ashby, M.F. and Anderman, I., 1983. Rate-Controlling Processes in the Creep of Polycrystalline Ice, J. Phys. Chem., Vol 87, pp4066-4074.

Evans, A.G., Palmer, A.C., Goodman, D.J., Ashby, M.F., Hutchinson, J.W., Ponter, A.R.S. and Williams, G.J., 1984. Indentation Spalling of Edge-Loaded Ice Sheet, IAHR Ice Symposium, Hamburg.

Finn, D.W., Jordaan, I.J., Singh, S.K. and Spencer, P., 1989. Flow of Crushed Ice: Physical and Mechanical Properties and Behavior, Ocean Engineering Research Centre, Memorial University of Newfoundland, St. John's, NF (proprietary).

Finn, D., 1991. M. Eng. Thesis, Memorial University of Newfoundland.

Frederking, R.M.W. et al., 1990a. Field Tests on Ice Indentation at Medium Scale, Ice Island, April 1989. National Research Council of Canada Report CR 5866.1.

Frederking, R., Jordaan, I.J. and McCallum, J.S. (1990) Field Tests of Ice Indentation at Medium Scale, Hobson's Choice Ice Island, Proceedings of the 10th IAHR Symposium on Ice, Espoo, Finland, Vol. 2, pp. 931-944.

Gagnon, R.E. and Molgaard, J., 1990. Evidence for Pressure Melting and Heat Generation by Viscous Flow of Liquid in Indentation and Impact Experiments on Ice. Presented at the IGS Symposium on Ice-Ocean Dynamics and Mechanics, Dartmouth College, Hanover, New Hampshire.

Gagnon, R.E. and Sinha,N.K., 1991. Energy Dissipation Through Melting in Large Scale Indentation Experiments on Multi-Year Sea Ice, Proceedings, OMAE, Vol. IV, pp. 157-161.

GEOTECH (GEOTECHnical resources Ltd.), 1985. Medium Scale Iceberg Impact Simulation Test Program, report prepared for Mobil Oil Canada Ltd..

Glen, J.W., 1955. The Creep of Polycrystalline Ice, Proceedings Royal Society of London, Piccadilly, London, W., Ser. A, Vol. 228, pp. 519-538

Glen, I.F. and Blount, H., 1984. Measurements of Ice Impact Pressures and Loads Onboard CCGS Louis S. St. Laurent, Offshore Mechanics and Arctic Engineering (OMAE) Symposium, New Orleans, Vol. III, pp. 246-252.

Gold, L.M., 1970. Process of Failure in Ice. Canadian Geotechnical Journal, Vol. 7, pp. 405-413.

Gold, L.M., 1972. The Failure Process in Columnar-grained Ice, Technical Paper No. 369, Division of Building Research, NRC.

Hallam, S.D., 1986. The Role of Fracture in Limiting Ice Force, Proceedings of IAHR Ice Symposium, Iowa City, Iowa, pp. 287-319.

Hallam, S.D., Duval, P. and Ashby, M.F., 1987. A study of Cracks in Polycrystalline Ice Under Uniaxial Compression, J. de Physique, Tome 48, pp. C1-303-311.

Hibbitt, D. et al., 1987. ABAQUS Manual. Hibbitt, Karlsson and Sorensen Inc.

Hobbs, P.V. (1974). Ice Physics, Clarendon Press, Oxford.

Horii, H. and Nemat-Nasser, S. 1983. Overall Moduli of Solids with Microcracks: Load-Induced Anisotropy, Journal of Mechanics and Physics of Solids, Vol.31, No.2, pp.155-171.

Jefferies, M.G. and Wright, W.H. 1988. Dynamic Response of Molikpaq to Ice-Structure Interaction, Proceedings Offshore Mechanics and Arctic Engineering Symposium, OMAE, Houston, Vol. IV, pp. 201-220.

Jonas, J.J. and Muller, F., 1969. Deformation of Ice under High Shear Stress, Canadian Journal of Earth Sciences, Vol. 6.

Jones, D.E., Kennedy, F.E. and Schulson, E.M. (1991). The Kinetic Friction of Saline Ice Against Itself at Low Sliding Velocities, Annals of Glaciology, Vol. 15, pp. 242-246.

Jones, S.J. and Chew, H.A.W., 1983. Creep of Ice as a Function of Hydrostatic Pressure, J. Phys. Chem., Vol 87, pp4064-4066.

Jordaan, I.J. and Timco, G.W., 1988. Dynamics of the Ice Crushing Process, Journal of Glaciology, Vol. 34, No. 118, pp. 318-326

Jordaan, I.J., Maes, M. and Nadreau, J.P., 1988. The Crushing and Clearing of Ice in Fast Spherical Indentation Tests, OMAE '88, Proceedings of the Seventh International Offshore Mechanics and Arctic Engineering Symposium, Vol. 4, New York, American Society of Mechanical Engineers, pp. 111-116

Jordaan, I.J. and McKenna, R.F., 1988a. Modelling of Progressive Damage in Ice, IAHR Symposium on Ice, Sapporo, Japan, August, Proceedings Vol. II, pp. 585-624

Jordaan, I.J. and McKenna, R.F. 1988b. Constitutive Relations for Creep of Ice, Proceedings International Association for Hydraulic Research (IAHR) Ice Symposium, Sapporo, Japan, Vol.3, pp.47-58.

Jordaan, I.J. and McKenna, R.F. 1989. Processes of Deformation and Fracture of Ice in Compression, Proceedings IUTAM/IAHR Symposium on Ice-Structure Interaction, St. John's, Newfoundland, Canada, pp. 283-310.

Jordaan, I.J., Stone, B.M., McKenna, R.F. and Fuglem, M.K. 1990a. Effect of Microcracking on the Deformation of Ice, Proceedings of the 43rd Canadian Geotechnical Conference, Quebec, pp. 387-393.

Jordaan, I.J., McKenna, R.F., Duthinh, D., Fuglem, M.K, Kennedy, K.P., Maes, M.A. and Marshall, A., 1990b. Development of New Ice Load Models, report for Canada Oil and Gas Lands Administration (COGLA) by (C-CORE), Memorial University, St, John's, NF.

Jordaan,I.J. and Xiao, J. (1992) Interplay Between Damage and Fracture in Ice-Structure Interaction, to be presented at the 11th IAHR Ice Symposium, Banff, Alberta, June 15-19, 1992.

Jordaan, I.J., Xiao, J., Zou, B., 1993, Fracture and Damage of Ice: Towards Practical Implementation, MEET'N 93 of AMSE, AMCE and SES, Charlottesville, Varginia.

Jordaan, I.J., Matskevitch, D. and Meglis, I., 1997. Disintegration of Ice under Fast Compressive Loading, Int. J. Frac. (submitted).

Kachanov, L.M., 1958. On the Creep Rupture Time. Izv. AN SSSR, Ofd. Tekhn. Nauk., No. 8, pp. 26-31.

Kachanov, L.M., 1986. Introduction to Continuum Damage Mechanics. Martinus Nijhoff Publishers.

Kachanov, M., 1993. Elastic Solids with Many Cracks and Related Problems. Advances in Applied Mechanics, V. 30, Academic Press.

Kalifa, P., Duval, P. and Ricard, M., 1989. Crack Nucleation in Polycrystalline Ice Under Compressive States, Proceedings, OMAE, A.S.M.E., Vol. 4, pp 13-21.

Karna, T., Muhonen, A. 1990. Preliminary Results From Ice Identation Tests Using Flexible and Rigid Indentors, IAHR Ice Symposium. Proceedings, 9th, Espoo, Finland, 1990, v.3., pp.261-275.

Karr, D. G., 1985. A damage mechanics model for uniaxial deformation of ice. OMAE'85, Vol. 2, pp. 227-233.

Karr, D.G. and Choi, K., 1989. A Three-Dimensional Constitutive Damage Model for Polycrystalline Ice, Mechanics of Materials, Vol. 8, pp. 55-66.

Kendall,K., 1978. Complexities of Compression Failure, Proceedings of the Royal Society of London, Vol. A361, 1978, pp. 245-263.

Kennedy, K.P., 1990. M. Eng. Thesis, Memorial University of Newfoundland.

Kheisin, D.E. and Cherepanov, N.V. (1970) Change of Ice Structure in the Zone of Impact of a Solid Body Against the Ice Cover Surface, Problemy Arktiki i Antarktiki, Vol. 34.

Krajcinovic, D., and Fonseka, G. U., 1981. The continuous damage theory of brittle materials, Journal of Applied Mechanics, Vol. 48, pp. 809-824.

Krajcinovic, D., 1983. Constitutive equations for damage materials, Journal of Applied Mechanics, Vol. 50, pp. 355-360.

Leckie, F.A., 1978. The Constitutive Equations of Continuum Creep Damage Mechanics. Phil. Transactions of the Royal Society, London, Series A, 288, pp. 27-47.

Maes, M.A., Jordaan, I.J. and Cormeau, A., 1986, Probabilistic Theories For the Failure of Sea Ice, International Conference on Ice Technology, MIT, Boston, pp. 37-54.

McKenna, R.F., Meyssonnier, J. and Jordaan, I.J., 1989. Peak Pressures from a Damage Model for Ice in Compression, Proceedings of the Eighth International Conference on Offshore Mechanics and Arctic Engineering, the Hague, Netherlands, Vol. IV, pp. 67-73.

McKenna, R.F., Jordaan, I.J. and Xiao, J., 1990. Analysis of Damage and Energy Flow in the Crushed Layer during Rapid Ice Loading, Proceedings of IAHR Symposium on Ice, Espoo, Finland, Vol. 3, pp. 231-245.

Meaney, R., Jordaan, I.J. and Xiao, J., 1996. Analysis of Medium Scale Ice-Indentation Tests, Cold Regions Science and Technology, Vol. 24, pp. 279-287.

Meglis, I., Matskevitch, D., Melanson, P., Jordaan, I.J., Finlay, P., Fuglem, M., Muggeridge, K. and Stone, B., 1997. The Failure of Ice under Impact Conditions, a report for National Energy Board by OERC, Memorial University, St. John's, NF.

Mellor, M. and Cole, D. M., 1982. Deformation and Failure of Ice under Constant Strain-Rate, Cold Regions Science and Technology, Vol. 5, pp. 201-219.

Mellor, M., 1983. Mechanical Behaviour of Sea Ice, U.S. Army Cold Region Research and Engineering Lab,Hanover, CRREL Report 83-1.

Michel, B., 1979. Ice Mechanics, Universite Laval Press.

Moran, B., and Shih, C.F., 1986. Crack Tip and Associated Domain Integrals from Momentum and Energy Balance, Brown University Report.

Nordell, B. (1990) Measurement of P-T Coexistence Curve for Ice-Water Mixture, Cold Regions Science and Technology, Vol. 19, pp. 83-88.

Ohno, N., Murakami, S. and Ueno, T., 1985. A Constitutive Model of Creep Describing Creep Recovery and Material Softening Caused by Stress Reversals, Journal of Engineering Materials and Technology, Vol. 107, pp. 1-6.

Parks, D.M., 1977. The Virtual Crack Extension Method for Nonlinear Material Behaviour, Computer Methods in Appl. Mech. and Eng., 12, pp. 353-364.

Palmer, A.C. et al., 1982. Fracture and Ice Forces on Offshore Structures, Symposium on Applied Glaciology, Hanover, NH.

Palmer, A.C., Goodman, D.J., Ashby, M.F., Evans, A.G., Hutchinson, J.W. and Ponter, A.R.S., 1983. Fracture and Its Role in Determining Ice Forces on Offshore Structures, Annals of Glaciology, Vol.4, pp.216-221.

Palaniswamy, P. and Knauss, W.G., 1974. On the problem of Crack Extension in Brittle Solids Under General Loading, California Institute of Technology, SM-74-8.

Resende, L. and Martin, J.B., 1983. Damage Constitutive Model for Geotechnical Applications. Technical report No. 44, Dec. 83.

Resende, L. and Martin, J.B., 1984. A Progressive Damage Continuum Model for Granular Materials. Computer Methods in Applied Mech. and Eng. 42, 1-18 North Holland.

Rice, J.R., 1986a. A Path Independent Integral and the Approximate Analysis of StrainConcentration by Notches and Cracks. Journal of Applied Mechanics, Vol.35, pp. 379-386.

Rice, J.R., 1986b. Mathematical Analysis in the Mechanics of Fracture, Chapter 3 in "Fracture, An Advanced Treatise", Edited by H. Liebowitz, Academic Press.

Saeki, H., Ono, T., Nakazawa, N., Sakai, M. and Tanaka, S. (1986). The Coefficient of Friction between Sea Ice and Various Materials Used in Offshore Structures, Journal of Energy Resources Technology, Vol. 108. pp. 65-71.

Sanderson, T.J.O. 1988. Ice Mechanics–Risks to Offshore Structures, Graham and Trotman.

Schapery, R.A., 1962. A Simple Collocation Method for Fitting Viscoelastic Models to Experimental Data, GALCIT SM 61-23 A. California Institute of Technology.

Schapery, R.A., 1968. On a Thermodynamic Constitutive Theory and Its Application to Various Nonlinear Materials, Procs. IUTAM Symp., East Kilbride, June, 1968, pp.259-283.

Schapery, R.A., 1969. On the Characterization of Nonlinear Viscoelastic Materials, Polymer Eng. Sci., Vol. 9, pp.295-310.

Schapery, R.A., 1981. On Viscoelastic Deformation and Failure Behaviour of Composite Materials with Distributed Flaws. Advances in Aerospace Structures and Materials. The American Society of Mechanical Engineers, pp. 5-20.

Schapery, R.A., 1984a. Time-dependent Fracture: Continuum Aspects of Crack Growth, Encyclopedia of Materials Science and Engineering, pp.5043-5053.

Schapery, R. A., 1984b. Correspondence Principles and a Generalized J Integral for Large Deformation and Fracture analysis of Viscoelastic Media. Int. Journal of Fracture, Vol. 25, pp. 195-223.

Schapery, R. A., 1988. A theory of mechanical behaviour of elastic media with growing damage and other changes in structure, Mechanics and Materials Center, Texas A and M Univ., College Station, Texas, Report No. MM. 5762-88-1.

Schapery, R. A., 1989. Models for the Deformation Behavior of Viscoelastic Media with Distributed Damage and Their Applicability to Ice, Proceedings IUTAM/IAHR Symposium on Ice-Structure Interaction, St. John's, Newfoundland, Canada, pp. 191-230.

Schapery, R.A., 1990a. A Theory of Mechanical Behavior of Elastic Media with GrowingDamage and Other Changes in Structure, Journal of the Mechanics and Physics of Solids, Vol.38, pp.215-253.

Schapery, R.A., 1990b. Simplifications in the Behavior of Viscoelastic Composites withGrowing Damage, IUTAM Symposium on Inelastic Deformation of Composite Materials, Troy, New York, Springer-Verlag, 1991.

Schulson, E.M. and Cannon, N.P., 1984. The Effect of Grain Size on the Compressive Strength of Ice. IAHR Ice Symp. Hamburg. pp. 24-38.

Schulson, E.M., 1987. The Fracture of Ice Ih, J. de Physique, 48: C1-207-220.

Schulson, E.M., 1989. The Tensile and Compressive Fracture of Ice, Proceedings IUTAM/IAHR Symposium on Ice-Structure Interaction, St. John's, Newfoundland, Canada, pp. 165-184.

Schulson, E.M., Hoxie, S.G. and Nixon, W.A., 1989. The Tensile Strength of Cracked Ice. Phil. Mag., Vol. 59, pp. 303-311.

Seng-Kiong, T. and Shyam Sunder, S., 1985. Constitutive Modelling of Sea Ice with Applications to Indentation Problems, CSEOE Research Report No. 3, MIT, Cambridge, Massachusetts.

Shen, W. and Lin, S.Z., 1986. Fracture Toughness of Bohai Bay Sea Ice, Proceedings of the Fifth International Conference on Offshore and Arctic Engineering (OMAE), Vol. IV, pp.354-357.

Shyam Sunder, S. and Wu, M.S. 1990. Crack Nucleation due to Elastic Anisotropy in Polycrystalline Ice, Cold Regions Science and Technology.

Sih, G.C., 1973. A Special Theory of Crack Propagation, in Mechanics of Fracture, 1,Methods of Analysis and Solutions of Crack Problems, Ed. G.C.Sih, Nordhoff, Leyden, pp.XXI-XLV.

Sih, G.C. and Tzou, D.Y., 1983. Mechanics of Nonlinear Crack Growth: Effects of Specimen Size and Loading Step, Conference on Modelling Problems in Crack Tip Mechanics.

Singh, S.K., 1993. Ph. D. Thesis, Memorial University of Newfoundland.

Sinha, N.K., 1978. Rheology of Columnar-Grained Ice, Experimental Mechanics, Vol. 18, No. 12, pp. 464-470.

Sinha, N.K., 1981. Deformation Behaviour of Ice-Like Materials in Engineering Applications, Proc. International Symposium on Mechanical Behaviour of Structured Media, Ottawa, pp. 419-430.

Sinha, N.K., 1982. Delayed Elastic Strain Criterion for First Cracks in Ice, Proc. of the Symposium on Deformation and Failure of Granular Materials, pp. 323-330. Rotterdam: Balkema.

Sinha, N.K., 1983. Creep Model of Ice For Monotonically Increasing Stress, Cold Regions Science and Technology, Amsterdam, Vol. 8, No. 1, pp. 25-33.

Sinha, N.K. 1984. Intercrystalline Cracking, Grain-Boundary Sliding, and Delayed Elasticity at High Temperatures, Journal of Material Science, London, Vol.19, pp. 359-376.

Sinha, N.K., 1988. Crack-Enhanced Creep in Polycrystalline Material: Strain-Rate Sensitive Strength and Deformation of Ice, J. of Materials Science, Vol. 23, No. 12, pp. 4415-4428.

Sinha, N.K., 1989a. Elasticity of Natural Types of Polycrystalline Ice. Cold Regions Science and Technology, Vol. 17, pp. 127-135.

Sinha, N.K. 1989b. Kinetics of Microcracking and Dilatation in Polycrystalline Ice, Proceedings IUTAM/IAHR Symposium on Ice-Structure Interaction, St. John's, Newfoundland, Canada, pp. 69-87.

Sinha, N.K. 1990. In Situ Multiyear Sea Ice Strength and Deformation using NRCC Borehole Indentor. To be presented at OMAE, 1991.

Sjölind, S.G., 1987. A Constitutive Model for Ice as a Damaging Visco-Elastic Material. Cold Regions Science and Technology, No. 41, pp. 247-262.

Spencer, P.A., Masterson, D.M., Lucas, J. and Jordaan, I.J. (1992) The Flow properties of Crushed Ice I: Experimental Observation and Apparatus, to be presented at the 11th IAHR Ice Symposium, Banff, Alberta, June 15-19, 1992.

Stone, B.M., Jordaan, I.J., Jones, S.J. and McKenna, R.F. 1989. Damage of Isotropic Polycrystalline Ice Under Moderate Confining Pressures, Proceedings of the 10th International Conference on Port and Ocean Engineering under Arctic Conditions, Lula, Sweden, Vol.1, pp.408-419.

Stone, B.M., Jordaan, I.J., Jones, S.J. and Xiao, J., 1997. Experiments on the Damage Process in Ice under Compressive States of Stress, J. of Glaciology, Vol. 43 (in press).

Timco, G.W., 1986. Indentation and Penetration of Edge-Loaded Freshwater Ice Sheets in the Brittle Range, Fifth OMAE Symposium, Proceedings Vol. IV, pp. 444-452

Timco, G.W. and Jordaan, I.J., 1988. Time-Series Variations in Ice Crushing, POAC '87, Proceedings of the 9th International Conference on Port and Ocean Engineering Under Arctic Conditions, Fairbanks, Alaska, pp. 13-20.

Tomin, M., Cheung, M., Jordaan, I.J. and Cormeau, A., 1986. Analysis of Failure Modes and Damage Processes of Freshwater Ice in Indentation Tests. Proc. of 5th OMAE Symp., Tokyo, Vol. IV, pp. 453-460.

Urai, J.L., Humphreys, F.J. and Burrows, S.E., 1980. In-situ Studies of the Deformation and Dynamic Recrystallization of Rhombhedral Comphor, J. Materials Science, Vol. 15, pp.1231-1240.

Vernon, R.H., 1981. Optical Microstructure of Partly Recrystallized Calcite in Some Naturally Deformed Marbles, Tectonophysics, Vol. 78, pp.601-612.

Volterra, V., 1909. Sulle Equazioni integro-differenziali della Teoria dell' Elasticita. Atti della Reale Academia dei Lencei, Vol. 18, pp. 295.

Wang, Y.S., 1979a. Sea Ice Properties. Technical Seminar. Exxon Company, USA.

Wang, Y.S., 1979b. Crystallographic Studies and Strength tests of Field Ice in the Alaskan Beaufort Sea. In POAC 79, pp. 651-655.

Wang, Y.S., 1981. Uniaxial Compression Testing of Arctic Sea Ice. Proc. of 6th POAC, Vol. 1, pp. 346-355.

Wang, Y. and Poplin, J.P., 1986. Laboratory Compression Tests of Sea Ice at Slow Strain Rates From a Field Test Program, Proceedings Fifth International Offshore Mechanics and Arctic Engineering (OMAE) Symposium, ASME, Tokyo, Japan, Vol.IV, pp.379-384.

Weeks, W.F. and Assur, A., 1967. The Mechanical Properties of Sea Ice. CRREL Monograph II-C3.

Weertman,J., 1969. Effects of Cracks on Creep Rate, Transactions Quarterly, Transactions of the ASM, Vol. 62, No. 2, pp. 502-511.

Wierzbicki, T., 1985. Spalling and Buckling of Ice Sheets, Civil Engineering in The Arctic Offshore, Proc. of ASCE Conf., Arctic 85, San Francisco, pp. 953-962.

Xiao, J., 1991. M.Eng. Thesis, Faculty of Engineering and Applied Science, Memorial University of Newfoundland, St. John's, Newfoundland.

Xiao, J. and Jordaan, I.J., 1991. Modelling of Fracture and Production of Discrete Ice Pieces, a report prepared for Canada Oil and Gas Lands Administration (COGLA).

Xiao, J., Jordaan,I.J., McKenna, R.F. and Frederking, R.M.W., 1991. Finite Element Modelling of Spherical Indentation Tests on Ice. Proc. of the 11th International Conference on Port and Ocean Engineering under Arctic Conditions, Sept., 1991, St. John's, NFLD.

Xiao, J. and Jordaan, I.J., 1996. Application of Damage Mechanics to Ice Failure in Compression, Cold Regions Science and Technology, Vol. 24, pp. 305-322.